MYCOBACTERIAL DRUG TARGET DECONVOLUTION USING COMPUTATIONAL, GENETIC, PHENOTYPIC AND PROTEOMIC APPROACHES

by

ALEXANDER DAVID HARRY KINGDON

A thesis submitted to the University of Birmingham for the degree of

DOCTOR OF PHILOSOPHY

Institute of Microbiology and Infection
School of Biosciences
College of Life and Environmental Sciences
University of Birmingham
February 2023

UNIVERSITY OF BIRMINGHAM

University of Birmingham Research Archive
e-theses repository



This unpublished thesis/dissertation is under a Creative Commons Attribution 4.0 International (CC BY 4.0) licence.

You are free to:

Share — copy and redistribute the material in any medium or format

Adapt — remix, transform, and build upon the material for any purpose, even commercially.

The licensor cannot revoke these freedoms as long as you follow the license terms.

Under the following terms:



Attribution — You must give appropriate credit, provide a link to the license, and indicate if changes were made. You may do so in any reasonable manner, but not in any way that suggests the licensor endorses you or your use.

No additional restrictions — You may not apply legal terms or technological measures that legally restrict others from doing anything the license permits.

Notices:

You do not have to comply with the license for elements of the material in the public domain or where your use is permitted by an applicable exception or limitation.

No warranties are given. The license may not give you all of the permissions necessary for your intended use. For example, other rights such as publicity, privacy, or moral rights may limit how you use the material.

Unless otherwise stated, any material in this thesis/dissertation that is cited to a third-party source is not included in the terms of this licence. Please refer to the original source(s) for licencing conditions of any quotes, images or other material cited to a third party.

Abstract

Mycobacterium tuberculosis has burdened humanity for centuries, remains one of the largest global killers, and causes over ten million tuberculosis infections yearly. Resistance to the current treatment regimen is growing and new treatment options are required. Work was undertaken to target the essential *M. tuberculosis* protein, AroB, and study the mechanism of action of a recently discovered antimycobacterial compound, vanoxerine (GBR12909). Several tools were developed to allow the rapid screening of potential inhibitors against the AroB protein, including biochemical, biophysical, and *in vitro* assays. Computational screening identified potential inhibitors of AroB, however, no compounds showed activity *in vitro* or *in vivo* against AroB or mycobacteria. In contrast, screening a drug repurposing library identified the antimycobacterial activity of vanoxerine, but no known target. Previous work suggested vanoxerine targeted AroB, however, this work has demonstrated it is not the target. Evidence provided herein highlights vanoxerine is a disruptor of the membrane electric potential, with downstream inhibition of efflux and membrane transport. A more potent analogue of vanoxerine was also developed, retaining its mechanism of action, but possessing lower activity against the known human target. Vanoxerine also targeted the pathogenic *Enterococcus faecium*, suggesting routes for future development against multiple pathogenic species. Overall, this work provides a strong foundation for future drug discovery studies targeting *M. tuberculosis*.

Acknowledgments

This thesis would not have been possible without the support of numerous individuals across the past four years.

I would like to thank all members of the Birmingham Tuberculosis labs, who provided a really supportive environment and made the past four years a much more enjoyable experience. Specifically, the former members of the Alderwick lab: Ian, Bala, Alice and Parisa for helping me settle into the lab and being a great help throughout my PhD. I'd also like to thank members of the Besra lab: Sarah, Natacha, Alice, Kat, Ed, and Mamata for welcoming me and all their support and encouragement. Finally, the wider members of the TB labs, Asti, Helen, Clare, Greg, Sam, Abi, Albel, and Rudi for the great conversations and sharing of food.

This thesis would not have been possible without Prof. Gurdyal Besra, who was incredibly helpful while I was finishing off my PhD. Being able to remain in the same laboratory and have someone read my thesis was incredibly useful. I would like to thank my previous supervisor, Dr Luke Alderwick, for his support and guidance, while he was at the University, and allowing me to develop independence over the course of my PhD.

I'd like to thank my roommate and fellow PhD student Stanley for stopping me becoming a workaholic and getting me to see more of Birmingham.

I'd like to thank my summer project student Asti for bringing enthusiasm to the lab and contributing towards part the vanoxerine project. I also want to thank the wider IMI community for their advice and friendship across the years.

I want to thank the Wellcome Trust for their sponsorship of my PhD.

Finally, I want to thank my friends: Flora, Arved, Josh, Katie, Lizzie, Nicki, and Daisie for providing welcome breaks from the PhD; and my family for their unending support, even if they didn't understand what I was doing.

Published Work:

One research article (also online as a pre-print) and one review paper were published prior to writing of this thesis and hence there may be some similarity to these works:

Kingdon, A.D.H. and Alderwick, L.J. (2021) Structure-based *in silico* approaches for drug discovery against *Mycobacterium tuberculosis*. *Computational and Structural Biotechnology Journal*, 19: 3708–3719. doi:10.1016/j.csbj.2021.06.034.

Kingdon, A.D.H., Meosa John, A.-R., Batt, S.M. and Besra, G.S. (2022) Repurposing Vanoxerine as a new antimycobacterial drug and its impact on the mycobacterial membrane. *bioRxiv*. doi:10.1101/2022.11.29.517118.

Kingdon, A.D.H., Meosa-John, A.-R., Batt, S.M. and Besra, G.S. (2023) Vanoxerine kills mycobacteria through membrane depolarization and efflux inhibition. *Frontiers in Microbiology*, 14: 1112491. doi:10.3389/fmicb.2023.1112491.

The review article will have similarities to pages 29 to 35 in the introduction and the article on vanoxerine will have similarities to chapter 3.

In relation to both of these works, I was the first author, and I am corresponding author for the vanoxerine paper. I wrote the initial draft of both manuscripts, including deciding on the order arguments/evidence was introduced, and produced all the figures presented in both manuscripts. For the review article, L.J. Alderwick suggested some changes to the initial draft, which were minor in nature. For the vanoxerine work, S.M. Batt and G.S. Besra critically reviewed the manuscript and made some suggestions for changes, but these were minor alterations. Author A.-R. Meosa-John performed preliminary experiments on vanoxerine, however, no data directly generated by this author was included in the manuscript or this thesis, and they did not suggest changes to the manuscript. The vast majority of these works were my own production, hence leading to similarities within this thesis.

Table of Contents

1.1. *Mycobacterium tuberculosis* 1
1.1.1. Impact 1
1.2.1. Infection 1
1.2.3. *Mycobacterium* 2
1.2. Tuberculosis Drug Treatments 5
1.2.1. Front-line Treatment Regimen 5
1.2.1.1. Isoniazid 6
1.2.1.2. Pyrazinamide 6
1.2.1.3. Ethambutol 7
1.2.1.4. Rifampicin 7
1.2.2. Second-line Treatment Regimen 7
1.2.2.1. Aminoglycosides 9
1.2.2.2. Quinolones 9
1.2.2.3. Oral Agents 10
1.2.2.4 Oxazolidinones 10
1.2.2.5. Newest Approved Agents 11
1.2.3. Future Drug Treatments 12
1.2.3.1 Clofazimine 13
1.2.3.2. DprE1 inhibitors 14
1.2.3.2. Other Phase II Clinical Trial Agents 15
1.2.3.3. Other Agents in Development (Phase I or Pre-clinical) 16
1.3. Tuberculosis Drug Resistance 17
1.3.1. Mycobacterial Cell Envelope 18
1.3.2. Mycobacterial Latency 22
1.3.3. Mycobacterial Efflux 23
1.3.4. Specific Resistance Mechanisms 26
1.4. Drug Discovery & Development Approaches 29
1.4.1. High-throughput Screening 29
1.4.1.1. Drug to Target Approach 29
1.4.1.2. Target to Drug Approach 30

1.4.2. Natural Products & Semi-synthetic Approaches 31
1.4.3. Drug Repurposing 32
1.4.4. Computational Approaches 33
1.4.5. Hit to Lead Optimisation 35
1.4.5. Thesis Outlook 36
2. Targeting AroB, an Essential TB Protein 37
2.1. Introduction 37
2.1.1. Shikimate acid pathway 37
2.1.2. AroB 39
2.2. Results 44
2.2.1. Tools to study AroB 44
2.2.1.1. Expression/Purification of MtAroB 44
2.2.1.2. MtAroB activity assay 47
2.2.1.3. Fluorimetry on MtAroB 50
2.2.1.4. Differential scanning fluorimetry (DSF) to assess compound binding 53
2.2.1.5. Protein crystallography and crystal structure 54
2.2.1.6. MD simulations of AroB protein 57
2.2.1.7. Clustering of MD MtAroB simulations 61
2.2.1.8. Principal component analysis (PCA) on MD simulation trajectories 66
2.2.1.9. CRISPR-interference of AroB in *M. smegmatis* 69
2.2.1.10. Generating mutants of MtAroB 71
2.2.1.11. Activity of MtAroB mutants 74
2.2.1.12. CD spectra of mutant MtAroB proteins 77
2.2.1.13. MtAroB-GFP fusion protein 78
2.2.1.14. Microscale thermophoresis (MST) 80
2.2.2. Finding drugs to target AroB 82
2.2.2.1. XCHEM 82
2.2.2.2. Docking of the Prestwick library 85
2.2.2.3. Virtual screening against MtAroB 90
2.2.3. Testing hits from virtual screening 93
2.2.3.1. Whole cell inhibition data – against *M. smegmatis* and *M. bovis* BCG 93
2.2.3.2. AroB protein inhibition assay 95

2.2.3.3. MST initial binding test 97
2.2.3.4. DSF for compound binding....98
2.2.3.5. MtAroB fluorimetry binding 100
2.3. Discussion 103
3. Mode of Action Determination of Vanoxerine Against Mycobacteria....110
3.1. Introduction 110
3.2. Results 113
3.2.1. MtAroB overexpression did not affect vanoxerine resistance....113
3.2.2. *aroB* mutations are unlikely to cause resistance 114
3.2.3. Minimum Inhibitory Concentrations (MICs) 116
3.2.4. Monitoring killing of mycobacteria 119
....123
3.2.5. Monitoring ATP levels in response to vanoxerine treatment 123
3.2.6. Resistance to vanoxerine could not be developed in mycobacteria 126
3.2.7. Homologues of human targets of vanoxerine....127
3.2.8. Propidium iodide uptake in mycobacteria is increased by vanoxerine....131
3.2.9. Ethidium bromide accumulation is increased, and efflux inhibited in mycobacteria....136
3.2.10. Disruption of the electric potential by vanoxerine 139
3.2.11. Vanoxerine does not potentiate the activity of other antimycobacterial drugs 142
3.2.12. RNA-Sequencing following treatment of *M. bovis BCG* with vanoxerine 144
3.2.13. Testing *M. bovis* BCG Danish transposon mutants....149
3.2.14. Testing over-expressor strains for vanoxerine resistance 150
3.2.15. Testing CRISPRi strains for vanoxerine susceptibility....152
3.2.16. Trehalose mono-mycolate (TMM) is lost following treatment of *M. smegmatis*....159
3.2.17. Overexpression of mycolic acid biosynthesis pathway....162
3.2.18. Vanoxerine analogues....164
3.2.19. Vanoxerine analogues – MICs 165
3.2.20. Vanoxerine analogues – accumulation/efflux of ethidium bromide....167
3.2.21. Vanoxerine analogues – $DiOC_2(3)$ dye disruption....171

3.2.22. Vanoxerine analogue 482 – protein pull-down 174
3.2.23. Dopamine transporter inhibition study 176
3.2.24. Vanoxerine targets the cell envelope in *B subtilis* 177
3.2.25. Vanoxerine caused accumulation of ethidium bromide in *E. faecium* and *B. subtilis* 178
3.2.26. Vanoxerine impacted *B. subtilis* efflux, but not *E. faecium* efflux 181
3.2.27. Vanoxerine disrupted the electric potential of *E. faecium* and *B. subtilis* 183
3.2.28. Resistance development in *E. faecium* E745 185
3.3. Discussion 189
4. Discussion and Future Work 202
5.1. General Experimental Methods 206
5.1.1. Media preparation 206
5.1.1.1. Luria – Bertani (LB) Broth 206
5.1.1.2. Luria – Bertani (LB) Agar 206
5.1.1.3. Terrific Broth 206
5.1.1.4. Brain-Heart Infusion (BHI) Broth 206
5.1.1.5. Brain-Heart Infusion (BHI) Agar 206
5.1.1.6. 7H9 Broth 206
5.1.1.7. 7H11 Agar 207
5.1.1.8. Tween-80 (20%) 207
5.1.1.9. Transformation Buffers 207
5.1.1.10. Protein Purification Buffers 208
5.1.1.11. SDS-Blue 209
5.1.1.12. Assay Buffers 209
5.1.2. Bacterial Strains and Growth Conditions 209
5.1.2.1. Bacterial Strains 209
5.1.2.2. Broth Growth Conditions 213
5.1.2.3 Agar Growth Conditions 213
5.1.2.4. Glycerol Stocks 214
5.1.2.5. Growth Curve Analysis 214
5.1.3. Competent Cell Preparation 214

5.1.3.1. Chemically Competent *E. coli* XL10 cells 214
5.1.3.2. Electrocompetent *M. smegmatis cells* 215
5.1.3.3. Electrocompetent *M. bovis BCG* cells 215
5.1.4. Polymerase Chain Reactions (PCR) 215
5.1.4.1. Gene Amplification PCR 216
5.1.4.2. PCR for HiFi Cloning 216
5.1.4.3. PCR for Q5 Mutagenesis 217
5.1.4.4. Colony PCR 218
5.1.5. Miraprep Plasmid Purification 218
5.1.6. Agarose Gel DNA Extraction 219
5.1.6.1. Agarose Gels 219
5.1.6.2. DNA Gel Extraction 219
5.1.7. Traditional Cloning 220
5.1.7.1. Digestion (insert and plasmid) 220
5.1.7.2. Alkaline phosphatase (plasmid only) 220
5.1.7.3. Ligation 220
5.1.8. Transformation 221
5.1.8.1. Chemical Transformation of *E. coli* 221
5.1.8.2. Electroporation Transformation of *M. smegmatis* 221
5.1.8.3. Electroporation Transformation of *M. bovis BCG* 221
5.1.9. HiFi Cloning 222
5.1.10. Q5 Mutagenesis 222
5.1.11. DNA/Plasmid Sequencing 223
5.1.12. CRISPR interference gene knockdowns 223
5.1.12.1. sgRNA sequence selection 224
5.1.12.2. Oligo annealing 226
5.1.12.3. Digestion and Ligation 226
5.1.12.4. Exonuclease (RecBCD) Treatment 226
5.1.12.5 Transformation and Confirmation 226
5.1.13 SDS-PAGE Gels 227
5.1.14. Minimum Inhibitory Concentration (MIC) Testing 227
5.1.14.1 Drug Compounds 227

5.1.14.2. Planktonic MICs 228
5.1.15. Figure Production 228
5.2. Chapter 2 Methods 229
5.2.1. AroB Protein Expression and Purification 229
5.2.1.1. MtAroB and MtAroB-GFP Protein Expression 229
5.2.1.2. MtAroB Protein Purification 229
5.2.1.3. MtAroB Mutant Protein Purification 229
5.2.1.4. MtAroB-GFP Protein Purification 230
5.2.2. Protein Crystallography 230
5.2.2.1. MtAroB Protein Crystallography 230
5.2.2.2. Optimisation for XCHEM 231
5.2.3. MtAroB Activity Assay 231
5.2.4 Circular Dichroism Spectroscopy 232
5.2.5. Fluorimetry Assay for MtAroB Binding 233
5.2.5.1 Cuvette-based Fluorimetry 233
5.2.5.2 Plate-reader Fluorimetry 233
5.2.6. Microscale Thermophoresis (MST) 233
5.2.6.1. Protein and Ligand check 233
5.2.6.2 Binding analysis 234
5.2.7. Differential Scanning Fluorimetry 234
5.2.8. BlueBEAR 234
5.2.9. Molecular Docking 235
5.2.9.1. Classical Molecular Docking 235
5.2.9.2. Cluster Ensemble docking 235
5.2.9.3. Virtual Screening (work by Dr Daniel Moscoh (University of Ghana)) 236
5.2.10. Molecular Dynamic Simulations 236
5.2.10.1. Classical Molecular Dynamic Simulations 236
5.2.10.2. Accelerated Molecular Dynamic Simulations 237
5.2.11. Molecular Dynamic Trajectory Analysis 237
5.2.11.1. VMD Analysis 237
5.2.11.2. Cluster analysis 238
5.2.11.3. Principal Component Analysis 238

5.2.12. Compound Property Correlations....239
5.3. Chapter 3 Methods....239
5.3.1. Resistant Mutant Generation....239
5.3.1.1 Spontaneous resistant mutants....239
5.3.1.2 Induced resistant mutants (Agar method)....239
5.3.1.3. E. faecium resistant mutants....240
5.3.1.4. Genome sequencing....240
5.3.2 MICs Methods....240
5.3.2.2. Checkerboard MICs....241
5.3.3. RNA Sequencing....241
5.3.4. Propidium Iodide Membrane Permeabilisation Assay....241
5.3.5. Ethidium Bromide Assays....242
5.3.5.1. Accumulation Assay....242
5.3.5.2. Efflux Assay....242
5.3.6. Membrane Potential Assay....243
5.3.6.1. $DiOC_2(3)$ concurrent drug treatment....243
5.3.6.2. $DiOC_2(3)$ pre-incubation, then drug treatment....243
5.3.7. Real Time Glo™ Assay....244
5.3.8. ATP monitoring using Firefly Luciferase....244
5.3.9. Protein pull-down assay using 482....245
5.3.10. Lipid Extraction and TLC analysis....246
5.3.10.1. Drug Treatment....246
5.3.10.2. Total Lipid Extractions....246
5.3.10.3. Thin-Layer Chromatography (TLC) analysis systems....246
5.3.10.4. C^{14} labelling of lipids....247
5.3.11. Dopamine Transporter assay....247
5.3.12. *B. subtilis* reporter strain assay....248
6. References....249
Appendix 1....278
Molecular cloning of plasmids....278
Appendix 2....281
Vanoxerine's interactions with DPH....281

Appendix 3 282
Crystallographic parameters for MtAroB structure 282
Appendix 4 283
Docking scores for top 31 AroB hit compounds 283
Appendix 5 284
List of SNPs present in laboratory *M. smegmatis* strain compared to reference . 284
Appendix 6 287
Vanoxerine's impact on other Mycobacterial lipids..... 287
Appendix 7 290
Percentage survival or growth curves following vanoxerine analogue treatment 290
Appendix 8 292
Comparison of lab *E. faecium* E745 WGS to reference strain..... 292

List of Figures

Figure 1.1: Phylogenetic tree of *Mycobacterium* 3

Figure 1.2: Structures of front-line antimycobacterial drugs 5

Figure 1.3: Structures of second-line antimycobacterial drugs....8

Figure 1.4: Structure of antimycobacterial drugs in clinical or pre-clinical trials....12

Figure 1.5: Structure of the mycobacterial cell envelope....19

Figure 1.6: Types of efflux pumps found in mycobacteria, showing cellular location and examples....24

Figure 2.1: Diagram of the shikimate acid pathway, with the *M. tuberculosis* enzymes highlighted....38

Figure 2.2: MtAroB enzymatic mechanism converting DAHP into 3-dehydroquinate 40

Figure 2.3: Conservation of the AroB protein across bacterial species 41

Figure 2.4: SDS-PAGE gel showing the initial purification of MtAroB (39 kDa) using a nickel column....45

Figure 2.5: SDS-PAGE gel showing the final purification of MtAroB (39 kDa) using a size-exclusion column 46

Figure 2.6: MtAroB activity assay reaction scheme....47

Figure 2.7: The development and testing of the MtAroB activity assay 49

Figure 2.8: Fluorimetry using the tryptophan fluorescence of purified MtAroB protein against increasing compound concentration 51

Figure 2.9: Differential scanning fluorimetry of MtAroB with DMSO, DAHP, NAD and vanoxerine....53

Figure 2.10: Structure of MtAroB crystallised within this work....56

Figure 2.11: RMSD of MtAroB α-carbons across 120-nanosecond of MD simulation 58

Figure 2.12: RMSF of each backbone α-carbon atom, following MD simulation for 120 ns, projected onto each residue of the MtAroB protein....60

Figure 2.13: Coordination of the active site zinc ion in MtAroB 61

Figure 2.14: Comparison of the twenty MtAroB trajectory clusters by RMSD and principal component analysis 65

Figure 2.15: MtAroB total trajectory evaluation by principal component analysis and final splitting into clusters 68

Figure 2.16: MtAroB structure with residues selected for mutation highlighted..... 72

Figure 2.17: SDS-PAGE gels showing the purification of mutant versions of MtAroB, using nickel resin 73

Figure 2.18: Activity of MtAroB mutant proteins..... 76

Figure 2.19: CD Spectra of MtAroB wild-type and mutants in the near-UV..... 77

Figure 2.20: SDS-PAGE gel showing the purification of MtAroB-GFP (67.4 kDa) using nickel resin 79

Figure 2.21: MST response of MtAroB-GFP in the presence of DAHP, NAD or Vanoxerine..... 81

Figure 2.22: Comparison of the planned vs actual XCHEM process for MtAroB crystallographic fragment screening 84

Figure 2.23: Scheme for computational drug discovery virtual screening..... 85

Figure 2.24: Best docked poses of NAD and carbaphosphonate compared to the crystal structure binding poses 88

Figure 2.25: Correlogram showing the correlations between molecular properties, whole cell efficacy against mycobacteria and docking scores against MtAroB..... 89

Figure 2.26: Top 31 molecules from virtual screening effort against MtAroB 91-92

Figure 2.27: Testing of the docked AroB hits indicates they lack whole-cell activity against mycobacteria..... 94

Figure 2.28: MtAroB inhibition assay to assess putative hit compounds 96

Figure 2.29: MST binding check analysing of MtAroB-GFP with hit compounds..... 98

Figure 2.30: Differential scanning fluorimetry to assess compound binding and stabilisation of MtAroB 99

Figure 2.31: Tryptophan fluorescence binding analysis of AroB hit compounds..... 101

Figure 2.32: Structures of proposed MtAroB inhibitor, alongside tested inhibitor IMB-T130..... 108

Figure 3.1: Structure of vanoxerine (GBR12909)..... 110

Figure 3.2: Percentage survival curves of *M. smegmatis* overexpressing MtAroB, showing no shifts in MIC_{99} compared to empty vector controls..... 113

Figure 3.3: Overlay of MtAroB and MsAroB structures, highlighting the resistant mutant residues in MsAroB and equivalent MtAroB residues 114

Figure 3.4: Vanoxerine treated cells %Survival or %Growth..... 117

Figure 3.5: Vanoxerine percentage growth curves of *A. baumannii, K. pneumoniae* and *P. aeruginosa*, either untreated or following EDTA-mediated permeabilisation 119

Figure 3.6: Growth curves of mycobacteria expressing GFP, grown in the presence of vanoxerine, showing growth inhibition 121

Figure 3.7: RealTime Glo™ MT Cell viability assay 123

Figure 3.8: ATP levels spiked in a concentration dependent manner following vanoxerine treatment 125

Figure 3.9: Overexpression of the predicted structural homologues of human targets of vanoxerine had limited effect on the survival of *M. smegmatis* 130

Figure 3.10: Development of propidium iodide assay 132

Figure 3.11: Vanoxerine treatment increased the propidium iodide fluorescence of *M. smegmatis* and *C. glutamicum* at 0.5x MIC_{99} and *M. bovis* BCG at 2x MIC_{99}. 135

Figure 3.12: Vanoxerine treatment leads to increased accumulation of ethidium bromide and prevents its efflux from mycobacteria 138

Figure 3.13: Vanoxerine disrupts the partitioning of the $DiOC_2(3)$ dye, suggesting membrane electric potential dissipation 141

Figure 3.14: Vanoxerine does not potentiate the effects of other antimycobacterial drugs 143

Figure 3.15: Vanoxerine induces many transcriptional changes in *M. bovis* BCG, following 8-hours of drug treatment 145

Figure 3.16: Limited shift in MIC occurred in BCG Danish mutants compared to the wild-type strain 150

Figure 3.17: Overexpression of *bcg0727, clgR, narK2, ribC* and *whiB3* had a limited impact on the vanoxerine MIC 151

Figure 3.18: Growth curves of *M. bovis* BCG CRISPRi strains, showing that only *mmpL3+10* and *pknB+50* strains are affected by addition of ATc 153

Figure 3.19: Percentage survival curves of *M. bovis* BCG CRISPRi strains following vanoxerine treatment, in the presence/absence of ATc 158

Figure 3.20: Loss of TMM occurred in *M. smegmatis* following drug treatment but does not appear to be cause of killing 161

Figure 3.21: Overexpression of mycolic acid biosynthetic enzymes did not affect the resistance to vanoxerine 163

Figure 3.22: Structural analogues of vanoxerine 165

Figure 3.23: Comparison of the effect of compounds 482, 486, 488, and vanoxerine on the accumulation and efflux of ethidium bromide by *M. smegmatis* 170

Figure 3.24: Vanoxerine analogues can disrupt the *M. bovis* BCG membrane electric potential 173

Figure 3.25: The fusion of compound 482 to agarose resin did not allow a mycobacterial protein target to be selected 175

Figure 3.26: Vanoxerine caused accumulation of ethidium bromide, shown by an increase in fluorescence 180

Figure 3.27: Vanoxerine prevented ethidium bromide efflux in *B. subtilis* but has limited effect on efflux in *E. faecium* 182

Figure 3.28: Disruption of the electric potential of the membrane, indicated by the change in red fluorescence of $DiOC_2(3)$ 184

Figure 3.29: Vanoxerine resistance up to 2x MIC_{99} could be acquired following four days of sub-culture and translated into a shift in the MIC_{99}..... 186

Figure 3.30: Overall summary of vanoxerine mechanism of action 197

Figure 3.31: Correlogram showing the correlations between MIC_{99}, ethidium bromide influx/efflux and electric potential formation/disruption across the vanoxerine analogues 200

List of Tables

Table 2.1: *M. smegmatis* CRISPRi strains targeting AroB growth curve start and endpoints, in the presence or absence of ATc 70

Table 2.2: Evaluation of docked control compounds against both g_cluster and PCA derived conformations of MtAroB 87

Table 3.1: Comparison of aroB mutations in the *M. smegmatis* lab strain and 'resistant mutants' to vanoxerine found in *M. smegmatis* 116

Table 3.2: Minimum inhibitory concentrations (MIC_{99}s) of vanoxerine against representative species 118

Table 3.3: *M. tuberculosis* predicted structural homologues of vanoxerine's human targets 129

Table 3.4: Significantly dysregulated genes comparing treatment of *M. bovis* BCG following treatment of 15 and 30 µg/ml of vanoxerine 147-148

Table 3.5: Genes of interest from the RNA-sequencing 149

Table 3.6: *M. bovis* BCG CRISPRi strains growth curve start and endpoints, in the presence or absence of ATc 155

Table 3.7: Vanoxerine MICs of *M. bovis* BCG CRISPRi strains, in the presence or absence of ATc 156

Table 3.8: Gene expression of mycolic acid biosynthesis genes, comparing no drug to 30 µg/mL vanoxerine 159

Table 3.9: MIC_{99} values determined for vanoxerine analogues 166

Table 3.10: Rates of accumulation and efflux of ethidium bromide in *M. smegmatis* and the impact of vanoxerine analogues 168

Table 3.11: Inhibitory impact of vanoxerine analogues on the dopamine transporter uptake 176

Table 3.12: Responses of *B. subtilis* reporter strains due to vanoxerine treatment 177

Table 3.13: Missense mutations in *E. faecium* E745 grown in 2x MIC_{99} vanoxerine 188

Table 3.14: Comparison of transcriptional responses of *M. tuberculosis* to CCCP, 2B8 and verapamil with the response of *M. bovis* BCG to vanoxerine 195-196

Table 5.1: List of strains used 210-213

Table 5.2: Primer sequences used for gene amplification PCRs 216
Table 5.3: Primer sequences for HiFi cloning PCRs 216-217
Table 5.4: Primer sequences for Q5 mutagenesis PCRs 217
Table 5.5: Table of colony PCR primers 218
Table 5.6: Table of sequencing primers 223
Table 5.7: Primers for CRISPR interference 224-225
Table 5.8: Crystallography conditions tested for reproducibility 231
Table 5.9: TLC solvent systems 247

List of Abbreviations

ABC – ATP-binding cassette

$AcPIM_2$/Ac_2PIM_2 – Acyl/diacyl phosphatidylinositol dimannosides

$AcPIM_6$/Ac_2PIM_6 – Acyl/diacyl phosphatidylinositol hexamannosides

ADMET – Absorption, distribution, metabolism, excretion, and toxicity

ADP – Adenosine di-phosphate

aMD – Accelerated molecular dynamic

Araf – Arabinofuranose

Arg – Arginine

Asn – Asparagine

Asp – Aspartic acid

ATc – Anhydrotetracycline

ATP – Adenosine triphosphate

BCG - Bacillus Calmette-Guérin

BHI – Brain heart infusion

BLAST – Basic local alignment search tool

BSA – Bovine serum albumin

CCCP – Carbonyl cyanide *m*-chlorophenylhydrazone

CD – Circular dichroism

CL – Clarified lysate

cMD – Classical molecular dynamic

COVID-19 – Coronavirus disease 2019

CRISPR – Clustered regularly interspaced short palindromic repeats

CRISPRi – Clustered regularly interspaced short palindromic repeats interference

DAHP – 3-Deoxy-D-*arabino*-heptulosonic acid 7-phosphate

DAT – Diacyltrehalose

DHQS – 3-dehydroquinate synthetase

DMSO – Dimethyl sulfoxide

DNA – Deoxyribose nucleic acid

DSF – Differential scanning fluorimetry

EDTA – Ethylenediaminetetraacetic acid

FDA – Food and Drug Administration

FIC – Fractional inhibitory concentration

Fnorm – Normalised fluorescence

fs – femtosecond

FT – Flow through

g – gram

GFP – Green fluorescent protein

GlcNAc – *N*-acetylglucosamine

Glu – Glutamic acid

GPL – Glycopeptidolipids

HEPES – 4-(2-hydroxyethyl)-1-piperazineethanesulfonic acid

His – Histidine

IC_{50} – Inhibitory concentration (50% inhibition)

IPTG – Isopropyl β-d-1-thiogalactopyranoside

Kd – Binding constant

LAM – Lipoarabinomannan

LB – Luria-Bertani

LM – Lipomannan

LogP – Logarithm of the partition coefficient

Lys – Lysine

M – Molar

MATE – Multi-drug and toxic compound extrusion

MD – Molecular dynamic

*m*DAP – *meso*-diaminopimelate

MDR – Multi-drug resistant

MESG – 6-mercapto-7-methylguanosine

MFS – Major facilitator superfamily

mg – milligram

MIC – Minimum inhibitory concentration

mL – millilitre

mol – mole

mM – millimolar

MPM – Mannosyl-β-1-phosphomycoketides

MsAroB – *Mycobacterium smegmatis* AroB

MST – Microscale thermophoresis

MtAroB – *Mycobacterium tuberculosis* AroB

MTBC – *Mycobacterium tuberculosis* complex

MurNAc/MurNGlyc – *N*-acetylmuramic acid/*N*-glycolylmuramic acid

NAD/NAD+ – Nicotinamide adenine dinucleotide

nL – nanolitre

ns – nanosecond

NTA – Nitrilotriacetic acid

NTM – non-tuberculosis mycobacteria

OD_{600} – Optical density at 600 nm

OADC – Oleic acid albumin dextrose catalase

PAGE – Polyacrylamide gel electrophoresis

PAS – Para-amino salicylic acid

PAT - Polyacyltrehalose

PC – Principal component

PCA – Principal component analysis

PCR – Polymerase chain reaction

PDB – Protein data bank

PDIM – Phthiocerol dimycocerosate

PE – Phosphatidylethanolamine

PEG – polyethylene glycol

PGL – Phenolic glycolipids

PI – Propidium iodide

PIMs – Phosphatidylinositol mannosides

PMF – Proton motive force

PNP – Purine nucleoside phosphorylase

PO_4 – Inorganic phosphate

RFU – Relative fluorescent units

RLU – Relative luminescence units

RMSD – Root mean square deviation

RMSF – Root mean square fluctuation

RNA – Ribonucleic acid

RND – Resistance nodule division

SDS – Sodium dodecyl sulphate

SDS-PAGE – Sodium dodecyl sulphate-polyacrylamide gel electrophoresis

sgRNA – small guide RNA

SL – Sulfolipid

SMR – Small multi-drug resistance

TB – Tuberculosis

TDM – Trehalose dimycolates

TFB – Transformation buffer

TLC – Thin layer chromatography

Tm – Melting temperature

TMM – Trehalose monomycolates

UV – Ultra-violet

v/v – volume/volume

WGS – Whole genome sequencing

WHO – World Health Organisation

WT – Wild type

w/v – weight/volume

XDR – Extensively-drug resistant

Zn – Zinc

Å – Angstrom

°C – Degrees Celsius

% - Percentage

ΔFluorescence – Change in Fluorescence

$\Delta\psi$ - Electric potential

ΔpH – Proton gradient

µg/mL – microgram per millilitre

µM – micromolar

µL – microlitre

1. Introduction

1.1. *Mycobacterium tuberculosis*

1.1.1. Impact

Mycobacterium tuberculosis is the causative agent of tuberculosis (TB) and led to between 1.5 to 1.7 million deaths in 2020, with between ten to eleven million new infections in the same year (WHO, 2022a). The burden of TB is localised to low and middle-income countries, with India, China, Pakistan, Indonesia, the Philippines, Bangladesh, Nigeria, and the Democratic Republic of the Congo accounting for two thirds of the total incidences (WHO, 2022a). The impact of *M. tuberculosis* cannot be overstated, this pathogen appears to have infected early hominids up to 15,000 years ago and has continued to infect and kill humans ever since (Barberis et al., 2017). During the late 18th century, TB was killing one in four individuals in North America and Europe (Barberis et al., 2017). While the advent of the combination therapy for TB managed to greatly reduce incidence rates and deaths in North America and Europe during the 19th century, this impact was not seen globally. Much more work is required to combat this global epidemic, with *M. tuberculosis* remaining the largest global killer for a single infectious agent from 2014 to 2019 (only surpassed by COVID-19 in 2020 and 2021), despite well-defined treatment options (WHO, 2015, 2022b).

1.2.1. Infection

The primary route of *M. tuberculosis* transmission is air droplet dispersal from infected individuals, with droplets reaching the alveoli of the lungs most likely to cause an infection (Pai et al., 2016; Barry III et al., 2009; Bañuls et al., 2015; Coleman et al., 2022). A long-held belief is that transmission of *M. tuberculosis* only occurs from patients with active symptomatic TB, however, more recent evidence has suggested

that ‘subclinical’ symptomless but culture positive TB infections also contribute to its spread (Coleman et al., 2022; Williams et al., 2020; Patterson and Wood, 2019). The major chains of transmission are still unknown in high incidence settings, with known contacts representing a small proportion of linked cases using whole-genome sequencing (Glynn et al., 2015).

Upon reaching the site of infection in the lungs, the bacteria can either cause an active or latent TB infection. Latent TB is a symptomless infection, where *M. tuberculosis* is isolated within lesions in the lungs and has reduced metabolic activity (Barry III et al., 2009; Pai et al., 2016). This is suggested to occur through macrophage-mediated, granuloma formation and hypoxia induced latency (Barry III et al., 2009; Keane et al., 1997; Dulberger, Rubin and Boutte, 2020). Active TB develops in one-tenth of the population infected with latent TB, immunosuppression being a major risk factor (Barry III et al., 2009; Pai et al., 2016). Symptoms include: fatigue, fever, weight loss, a persistent cough and haemoptysis (Pai et al., 2016), although up to 25% culture-positive infected patients displayed no symptoms, more recently being named as subclinical TB (Hoa et al., 2010; Coleman et al., 2022).

1.2.3. *Mycobacterium*

Mycobacterium fall within the Actinobacteria phylum, which represents mostly Gram-positive bacteria. Mycobacteria is Gram-indeterminate, as its cell envelope is unique and does not consistently retain Gram stain. The order *Mycobacteriales* are the only order to all produce arabinogalactan (Vincent et al., 2018), exemplifying its unique cell envelope. The genus *Mycobacterium* comprises many different species, which are characterised by their mycolic acid rich cell envelope. However, genotypically, there

are large differences between these strains, as displayed in Figure 1.1, (O'Neill, Mortimer and Pepperell, 2015). The human and animal-adapted lineages of *M. tuberculosis* are referred to as the *Mycobacterium tuberculosis* complex (MTBC).

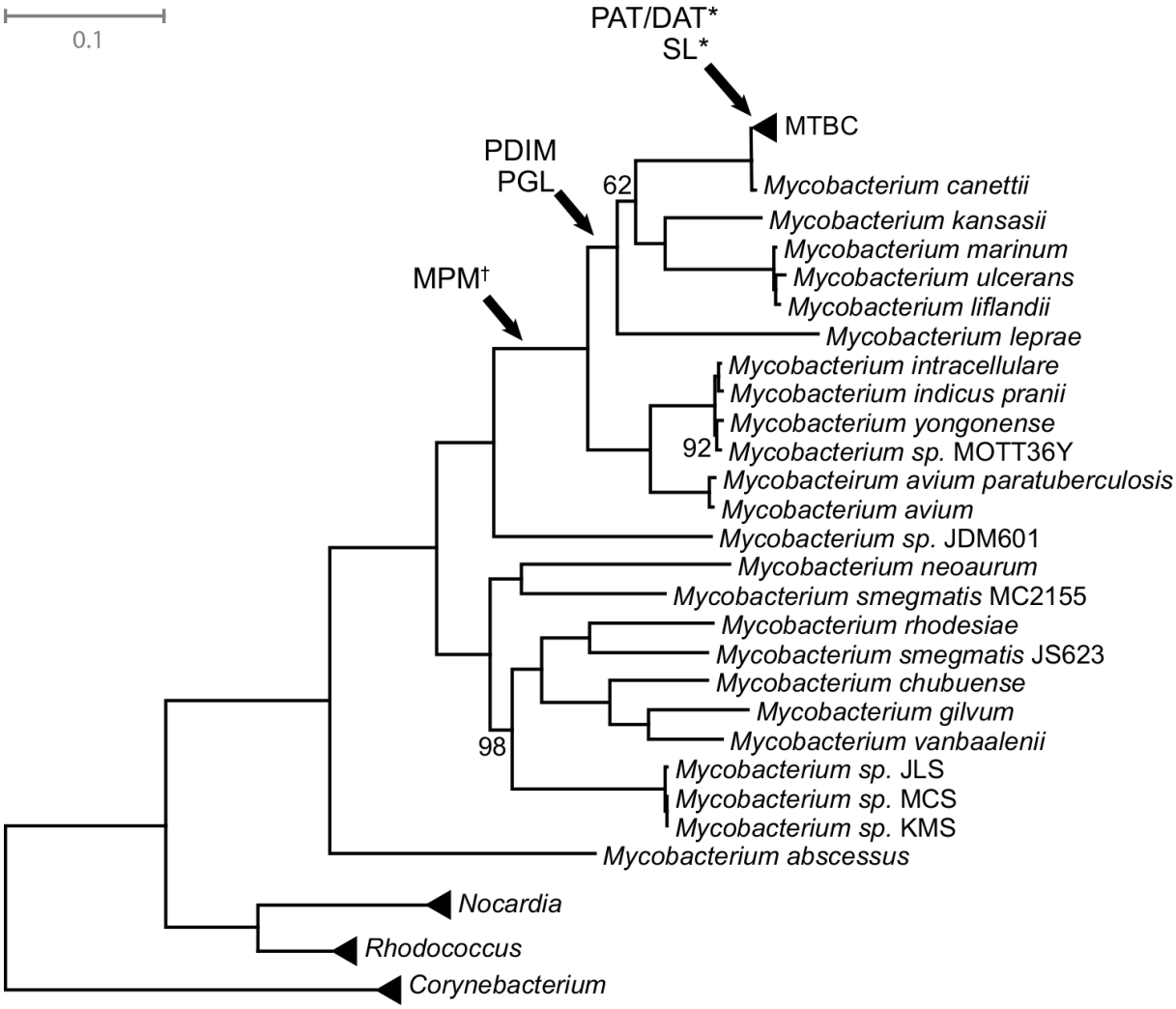


Figure 1.1: Phylogenetic tree of *Mycobacterium* – taken from O'Neill, Mortimer and Pepperell, (2015). Core genome alignment of 57 strains. Scale bar is mean number of substitutions per site. *Lipids present in *M. tuberculosis* human-adapted lineages, but not the remainder of MTBC. PAT/DAT – polyacyltrehalose/diacyltrehalose; SL = sulfolipids; PDIM = phthiocerol dimycocerosate; PGL = phenolic glycolipids and MPM = mannosyl-β-1-phosphomycoketides.

Mycobacteria can generally be split into slow and fast-growing species, with *M. tuberculosis* and *M. leprae* being key examples of slow-growing species and *M. smegmatis* and *M. abscessus* being examples of fast-growing species. For example,

M. tuberculosis has a doubling time of 24-hours *in vitro*, whereas *M. smegmatis* has a doubling time of 2-3 hours *in vitro*. In relation to infections, species are generally grouped into the MTBC*, M. leprae and* non-tuberculosis mycobacteria (NTM).

Due to the fast-growing nature of *M. smegmatis*, but its similarity to *M. tuberculosis*, it is commonly used as a model organism. This has included its use for screening compounds for antimycobacterial properties and their development to target *M. tuberculosis* (Andries et al., 2005; Kanvatirth et al., 2019). *M. smegmatis* is missing several components of the outer mycolic acid membrane which are present in *M. tuberculosis* (Figure 1.1). In addition, *M. smegmatis* is non-pathogenic, with fewer virulence factors than *M. tuberculosis*. A recent study identified transporter proteins, including amino acid and ion transporters to be conserved and enriched in fast growing mycobacteria, but absent in slow-growing mycobacteria (Bachmann et al., 2020).

In addition to the naturally occurring relatives of *M. tuberculosis*, a vaccine strain, *M. tuberculosis variant bovis* Bacillus Calmette-Guérin (BCG) was developed, which had reduced virulence and hence could be administered to protect individuals against virulent *M. tuberculosis* (Calmette, 1931; Mangtani et al., 2014). The vaccine strain has some efficacy, especially in children under 5 years, but fails to provide adequate protection in high-burden environments or in adults (Mangtani et al., 2014; Pai et al., 2016). BCG differs from TB, it is missing regions of the genome associated with virulence (Mahairas et al., 1996; Lewis et al., 2003). The cell envelope is also distinct, with sulfolipids not being produced in BCG and certain lipids involved in virulence also missing from the outer mycolic acid membrane. Despite these differences, BCG retains the ability to survive within macrophages, at least *in vitro*, allowing more accurate modelling of infections compared to other species (Medley et al., 2022; Singh, Netea

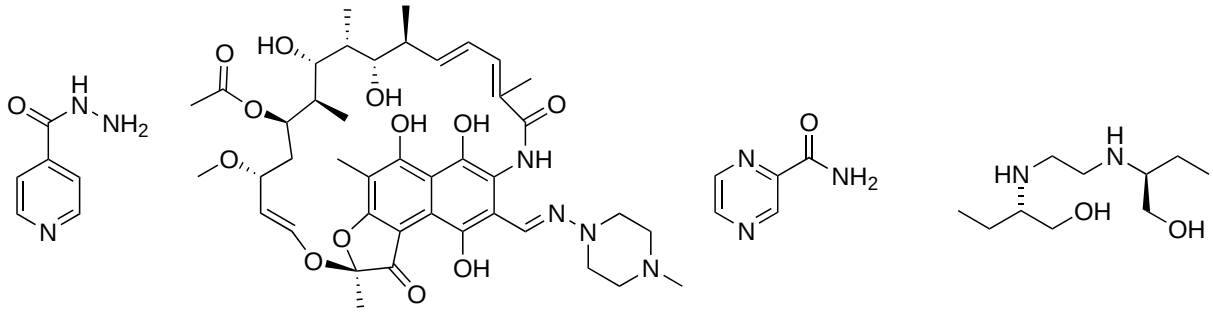
and Bishai, 2021). There are some differences in drug tolerance, with BCG being resistant to D-cycloserine (Chen et al., 2012), although many antimycobacterial drugs show similar efficacy.

Both *M. smegmatis* and *M. bovis BCG* are used extensively as model organisms, due to maintaining similar physiology to *M. tuberculosis*, but with vastly reduced safety concerns. *M. smegmatis* is a biosafety level one pathogen, *M. bovis BCG* is a biosafety level two pathogen, whilst *M. tuberculosis* is a biosafety level three pathogen, requiring substantially more protective infrastructure. Within this work, both *M. smegmatis*, as a representative fast-growing mycobacteria, and *M. bovis BCG*, a representative slow-growing mycobacteria, were used.

1.2. Tuberculosis Drug Treatments

1.2.1. Front-line Treatment Regimen

The current TB treatment regimen, for drug-susceptible *M. tuberculosis*, lasts for 6 months (WHO, 2022a) and includes four 'front-line' antimycobacterial drugs: isoniazid, rifampicin, pyrazinamide and ethambutol (Figure 1.2), the latter two drugs being only used for the first two months (Nahid et al., 2016). All these front-line drugs were developed over 40 years ago and no new drugs have been able to replace these in



Isoniazid Rifampicin Pyrazinamide Ethambutol

Figure 1.2: Structures of front-line antimycobacterial drugs.

clinical use (Chakraborty and Rhee, 2015). This is due to the difficulty of running clinical trials to prove increased efficacy while replacing one of the original drugs (Barry III, 2009). However, levels of resistance are growing, representing 3-4% of all new TB infections and 18-21% of all re-infections (WHO, 2021), requiring the use of second-line drug treatments and development of novel drugs.

1.2.1.1. Isoniazid

The antimycobacterial activity of isoniazid was discovered following chemical modification of nicotinamide, by three independent groups (Bernstein et al., 1952; Offe, Siefken and Domagk, 1952; Fox, 1952). Isoniazid is a pro-drug, which is activated by KatG (Zhang et al., 1992) and goes on to react with NAD, forming an adduct which inhibits the essential enzyme InhA (Banerjee et al., 1994; Rozwarski et al., 1998). Alongside inhibiting mycolic acid biosynthesis through InhA, reactive oxygen species produced during isoniazid activation can also damage many cellular macromolecules and perturb NAD metabolism (Rohde and Sorci, 2021).

1.2.1.2. Pyrazinamide

Pyrazinamide was also discovered following chemical modifications of nicotinamides (Malone et al., 1952; Zhang, 2005) and is also a pro-drug, activated by PncA, producing pyrazinoic acid (Scorpio and Zhang, 1996). The exact mechanism of action of pyrazinoic acid is still under debate. Initial models proposed cytoplasmic acidification and disruption of membrane potential/energy production (Zhang et al., 2003, 2014), however, these methods have been disproven (Peterson et al., 2015). More recently, pyrazinoic acid targeting degradation of the essential protein PanD has been proposed (Gopal et al., 2020).

1.2.1.3. Ethambutol

The antimycobacterial activity of polyamines led to further chemical modifications of this group of compounds and the discovery of ethambutol (Zhang, 2005; Thomas et al., 1961). Ethambutol has been shown to interfere with the biosynthesis of arabinogalactan and lipoarabinomannan (LAM), essential cell envelope components (Takayama and Kilburn, 1989; Goude et al., 2009). Specifically, ethambutol is involved in binding and inhibiting EmbB and EmbC (Goude et al., 2009; Zhang et al., 2020), which are involved in the elongation and branching of the cell wall arabinogalactan and LAM, respectively (Batt et al., 2020).

1.2.1.4. Rifampicin

Rifampicin was developed following a screen for natural products with antibiotic activity (Margalith and Beretta, 1960), which identified rifamycin (Sensi, 1983). This was followed by structural alterations to increase the activity and generate semi-synthetic compounds, including rifampicin (Sensi, 1983). The activity of rifamycin was first described as inhibiting DNA-dependent RNA synthesis (Hartmann et al., 1967; Umezawa et al., 1968), later the direct mechanism of action was identified as rifampicin binding to the β-subunit encoded by *rpoB* (Campbell et al., 2001).

1.2.2. Second-line Treatment Regimen

If *M. tuberculosis* is resistant to both isoniazid and rifampicin, then it is classified as multi-drug resistant *M. tuberculosis* (MDR-TB). Originally, treatment for patients infected with MDR-TB was more complex, requiring a longer treatment regimen of at least 9-months but up to 20-months in duration (WHO, 2019). This consisted of at least six drugs, always the front-line drugs for which *M. tuberculosis* is still susceptible, with at least two second-line drugs, including: aminoglycosides; fluoroquinolones;

cycloserine, ethionamide, para-amino salicylic acid (PAS) and bedaquiline (Figure 1.3) (Nahid et al., 2016; Centers for Disease Control and Prevention, 2013). Generally, a combination of an aminoglycoside, a fluoroquinolone and an oral agent will be utilised (CDC, 2003; Centers for Disease Control and Prevention, 2013). Extensively drug resistant (XDR) *M. tuberculosis* is also resistant to an aminoglycoside and at least one fluoroquinolone. More recently, newer antimycobacterial drugs, bedaquiline,

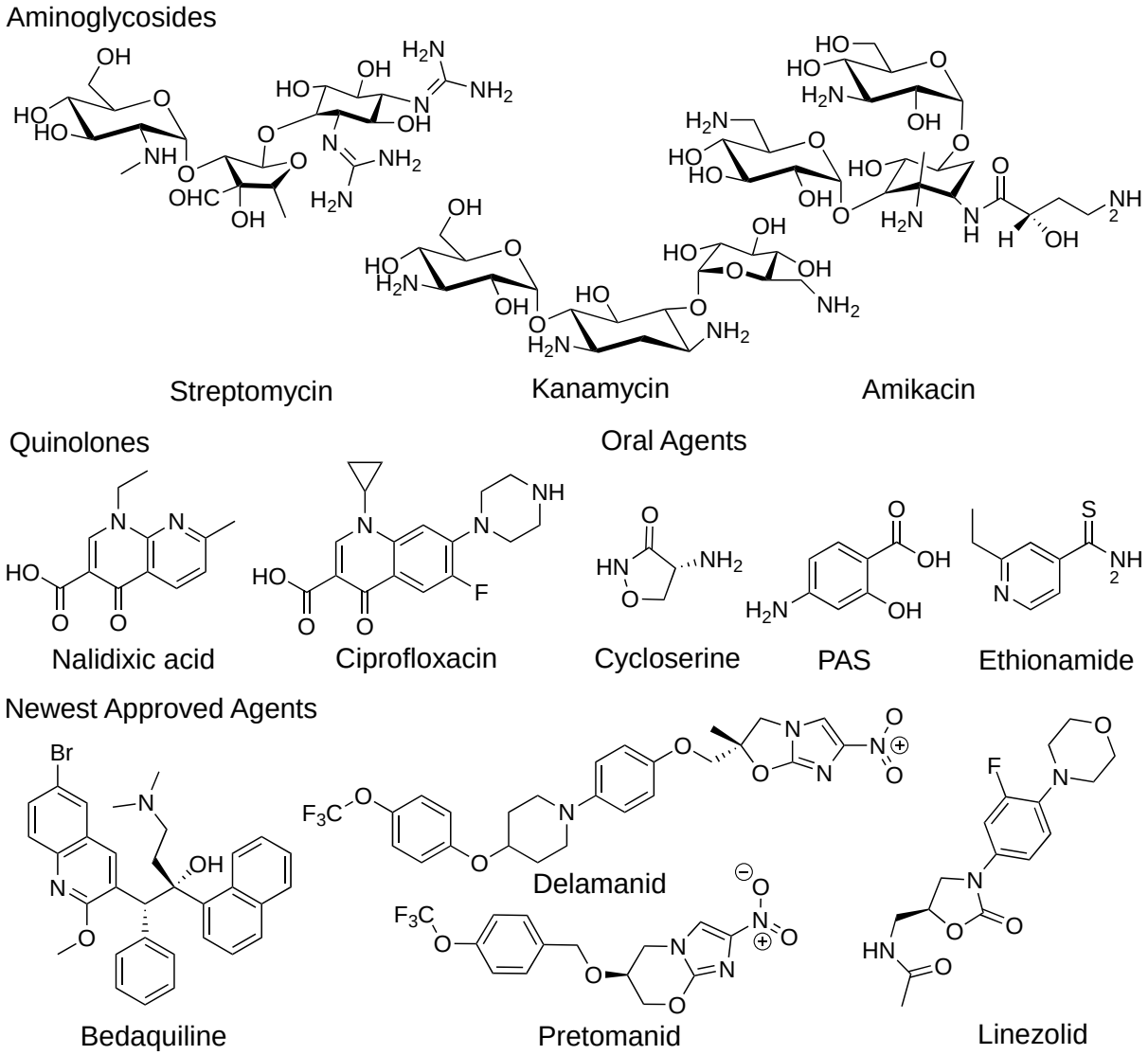


Figure 1.3: Structures of second-line antimycobacterial drugs. PAS = para-amino salicylic acid.

delamanid and pretomanid (Figure 1.3) have been developed (WHO, 2022a; Matsumoto et al., 2006; Stover et al., 2000; Andries et al., 2005). This has allowed shortening of the treatment for MDR and XDR TB to six months, with a regimen involving bedaquiline, pretomanid, linezolid and moxifloxacin (Conradie et al., 2020; WHO, 2022b).

1.2.2.1. Aminoglycosides

Streptomycin was one of the original drugs first used to treat TB, and is sometimes used as a front-line drug, but it was originally used in single application therapy and was the benchmark for treatment efficacy (Fox, 1952). It was discovered as a natural product with a broad spectrum of activity against both Gram-positive and Gram-negative species (Schatz, Bugle and Waksman, 1944). Streptomycin was the first member of the aminoglycosides, which all target protein synthesis, specifically through binding to the 16S rRNA and RpsL protein (Davis, 1987; Telenti, 1998; Garvin, Biswas and Gorini, 1974). More active aminoglycosides have been developed, including kanamycin and amikacin (Figure 1.3), which are also used to treat TB (CDC, 2003).

1.2.2.2. Quinolones

Quinolones, such as nalidixic acid, were developed for their antibacterial properties, and structural modifications have led to fluoroquinolones being synthesised, such as ciprofloxacin (Figure 1.3). These compounds have been repurposed for the treatment of TB. They target both subunits, *gyrA* and *gyrB* of DNA gyrase and inhibit DNA unwinding, with higher drug concentrations releasing DNA with double-stranded breaks, leading to cell death (Blower et al., 2016).

1.2.2.3. Oral Agents

While aminoglycosides and older quinolones could only be administered intravenously, other antimycobacterial agents have always been orally available and hence allow easier administration. These include D-cycloserine, ethionamide and PAS (Figure 1.3). PAS was discovered before isoniazid and used for TB treatment, however, it was later replaced due to better patient tolerance of ethambutol (Ferebee, Doster and Murray, 1966). Recent evidence suggests PAS is a prodrug, which is incorporated into the folate biosynthetic pathway instead of para-aminobenzoic acid, being catalysed by FolP1 and FolC (Minato et al., 2015; Zheng et al., 2013). The activated form then inhibits dihydrofolate reductase (DHFR, DfrA) (Zheng et al., 2013), preventing one-carbon metabolism in *M. tuberculosis* (Minato et al., 2015).

Ethionamide was also discovered based on modification of nicotinamide (Libermann et al., 1956). Similar to isoniazid, it also targets InhA and inhibits mycolic acid biosynthesis (Banerjee et al., 1994). However, it is activated by EthA instead, forming an adduct with NAD (Baulard et al., 2000; DeBarber et al., 2000). This allows it to overcome KatG-linked isoniazid resistance, hence its use as a second-line drug.

D-Cycloserine was discovered as a natural product produced by *Streptomyces* with antimycobacterial activity (Zhang, 2005). As an D-alanine analogue, its main mechanism of action *in vivo* involves inhibiting D-alanine-D-alanine ligase (Ddl), but it can also target alanine racemase (Alr), both proteins are involved in peptidoglycan biosynthesis (Bruning et al., 2011; Prosser and de Carvalho, 2013).

1.2.2.4 Oxazolidinones

Oxazolidinones, which have broad-spectrum antibacterial activity, have been repurposed for the treatment of TB. Linezolid (Figure 1.3) in particular has been the focus for incorporation into combination therapy (Conradie et al., 2020). They inhibit

protein synthesis through 23S rRNA binding and preventing formation of the translation initiation complex (Swaney et al., 1998).

1.2.2.5. Newest Approved Agents

Bedaquiline is another example of a drug that was developed from a structural analogue, identified through a high-throughput screen against *M. smegmatis*, followed by structural optimisation (Andries et al., 2005). Bedaquiline has been shown to bind to the c and ε subunits of ATP synthase, inhibiting ATP generation (Biuković et al., 2013; Andries et al., 2005) and has validated inhibition of energy metabolism as a drug target.

The nitroimidazoles were initially tested as radiosensitising agents and were then repurposed to target TB following antimicrobial testing (Nagarajan et al., 1989). Following initial identification, other groups synthesised structural analogues, identifying pretomanid (Stover et al., 2000) and delamanid (Matsumoto et al., 2006), with more potent antimycobacterial activity. Despite the discovery of pretomanid being published several years earlier, delamanid was approved for clinical use in 2014, whereas pretomanid was not approved until 2019. Both compounds are pro-drugs which are activated by Rv3547 (Manjunatha et al., 2006). The exact target of the nitroimidazoles is unknown, however the conversion of hydroxymycolate to ketomycolate or methoxymycolate was reduced following drug treatment (Stover et al., 2000; Matsumoto et al., 2006). As the nitroimidazoles are also active against non-replicating TB, under which metabolic processes, such as mycolic acid synthesis are reduced, this cannot be the only target (Manjunatha, Boshoff and Barry, 2009; Boshoff and Barry, 2006). Further work has suggested pretomanid generates reactive nitrogen species during prodrug activation, which might lead to respiratory poisoning of non-

replicating cells, leading to a drop in ATP levels and cell death (Manjunatha, Boshoff and Barry, 2009).

1.2.3. Future Drug Treatments

New antimycobacterial drugs are needed to replace the current front-line drugs, which could reduce the length of treatment, combat resistance, decrease cost and increase

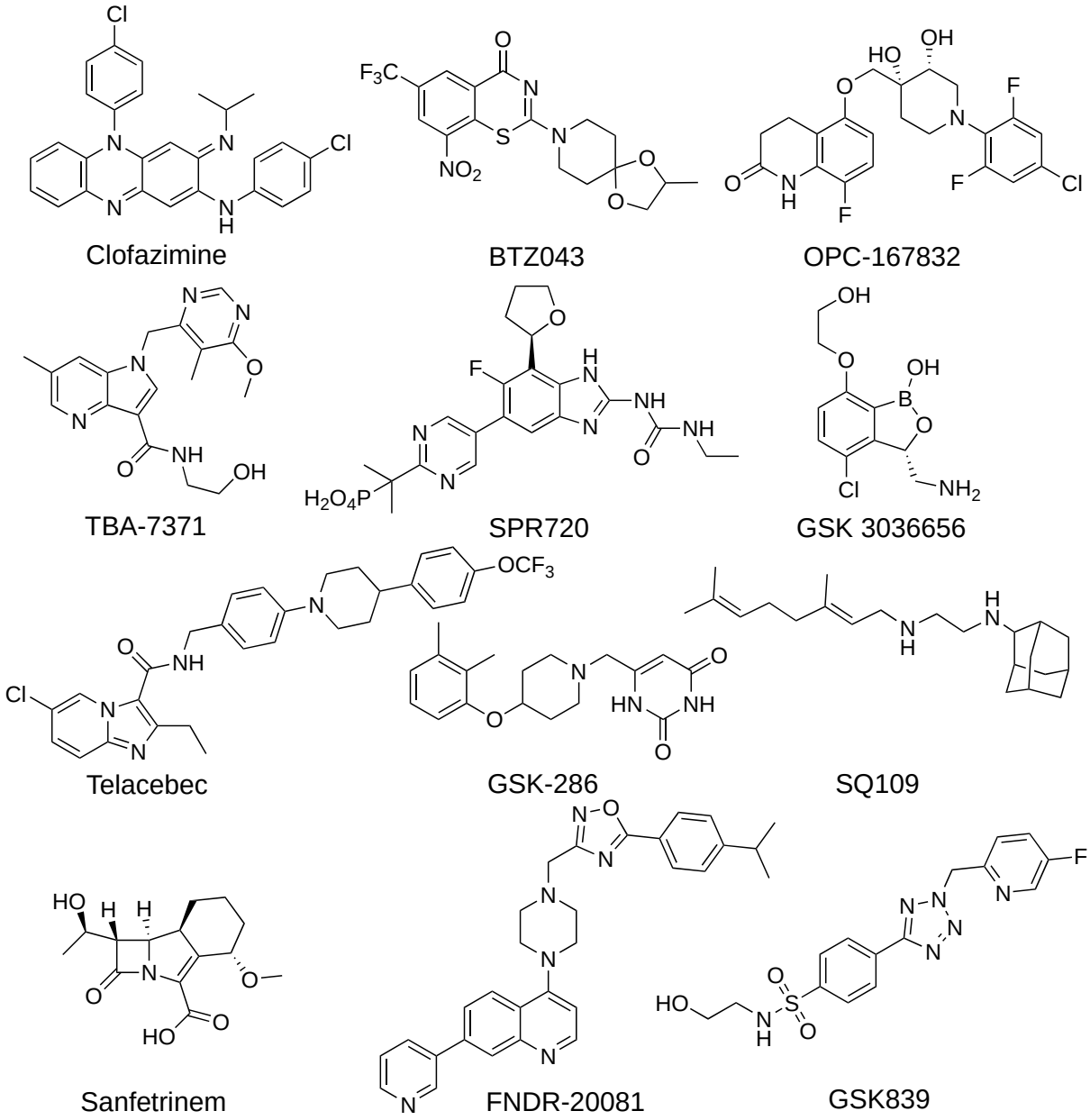


Figure 1.4: Structure of antimycobacterial drugs in clinical or pre-clinical trials

adherence to the drug regimen (WHO, 2019). In addition, resistance has been identified to all known anti-TB drugs, hence, continual drug discovery and development is needed to maintain a pipeline of novel drugs. As a supplement to novel discovery, repurposed drugs represent a viable option, especially as mycobacteria do not take up foreign DNA, so any plasmid-borne resistant mechanisms will not be gained by *M. tuberculosis* (Hatfull, 1993; Parish, 2021). An exception is *Mycobacterium canettii*, which can take up foreign DNA (Madacki et al., 2021). Repurposed drugs represent one-quarter of all the new TB drugs currently in clinical trials (WHO, 2022a).

Focussing on the clinical pipeline of novel anti-mycobacterial drugs (Figure 1.4), a majority are currently in phase II clinical trials, meaning many are not currently validated as true treatment options. In addition, the pre-clinical landscape of anti-mycobacterial drugs is sparce, hence, more research is required to fill the pipeline of upcoming drug compounds. During this section on future treatment options, analogues of previously mentioned antimycobacterial drugs will not be included, the focus will be upon novel mechanisms of action.

1.2.3.1 Clofazimine

Clofazimine is an antimycobacterial compound which was derived following structural alterations of natural products derived from lichens, and initially developed for its activity against *M. tuberculosis* (Bvumbi, 2020; Barry et al., 1957) (Figure 1.4). However, it displayed low efficacy against *M. tuberculosis* in guinea pig models and hence was not developed further; concurrently, it showed efficacy against *M. leprae in vivo* and hence was developed for this clinical application (Barry and Conalty, 1965). More recently, the clinical efficacy of clofazimine against *M. tuberculosis* has been re-evaluated and used to successfully treat MDR-tuberculosis (Gopal et al., 2013).

Clofazimine appears to have pleiotropic effects on mycobacteria, both disrupting the electron transport chain and membrane destabilisation, leading to reactive oxygen species production and inhibition of potassium transport, ultimately leading to cell death (Cholo et al., 2012).

1.2.3.2. DprE1 inhibitors

Many classes of molecules have been found to inhibit DprE1, an enzyme involved in the biosynthesis of arabinofuranose precursors, which are essential for the biosynthesis of arabinogalactan and LAM. The inhibition of these polymers for TB treatment has already been validated by ethambutol, leading to many molecules being developed. Three compounds are currently in phase II clinical trials to prove their efficacy against TB in humans, BTZ043 (NCT04044001), OPC-16783 (NCT05221502), and TBA-7371 (NCT04176250) (Figure 4).

BTZ043 is a benzothiazinone, this class of compounds were shown to have potent whole-cell antimycobacterial activity and then proven to target DprE1 (Makarov et al., 2009; Batt et al., 2012). For OPC-167832, a carbostyril hit was discovered following a whole-cell screen for antimycobacterial activity and identified to target DprE1 through resistant mutant generation (Naik et al., 2014). Structural modifications were then undertaken, leading to OPC-167832, which had increased potency (Hariguchi et al., 2020). In contrast TBA-7371 was identified through ‘scaffold-morphing’ of a telacebec analogue (see below) to identify a drug with potent bactericidal activity, followed by lead optimisation (Shirude et al., 2013; Chatterji et al., 2014). Again, inhibition of DprE1 was later confirmed by spontaneous resistant mutant generation (Shirude et al., 2013).

1.2.3.2. Other Phase II Clinical Trial Agents

Several other drugs are currently undergoing phase II clinical trials to prove efficacy against TB, the drugs outlined herein are all first-in class inhibitors, rather than analogues of previously mentioned drugs. These will be mentioned in the order that each discovery was published.

The discovery of SQ109 was based on a combinatorial chemistry screening approach using ethambutol as the starting point, its diamine structure being used to design and screen a library of 63,238 compounds, with SQ109 being the best compound identified (Lee et al., 2003; Protopopova et al., 2005). Despite being developed as an ethambutol analogue, the two structures are distinct and SQ109 has been shown to be an MmpL3 inhibitor, preventing the transport of mycolic acids across the membrane (Tahlan et al., 2012; Sacksteder et al., 2012).

A high-throughput screen against a TB infected-macrophage model was used to identify hits which were non-cytotoxic but had efficacy at killing *M. tuberculosis* inside macrophages (Pethe et al., 2013). Two hits were selected to follow-up through medicinal chemistry and this led to the synthesis of Telacebec (Q203) as the most efficacious compound (Pethe et al., 2013). The target of Telacebec was identified as QcrB, the cytochrome bc_1 oxidase, a protein in the electron transport chain and its inhibition would prevent ATP synthesis (Abrahams et al., 2012; Pethe et al., 2013).

The aminocoumarin class of natural products were already known to have antibacterial activity, through targeting DNA gyrase (both GyrB and ParE) (Bellon et al., 2004), however, they had mammalian toxicity and rapid resistance development (Grossman et al., 2007). Hence, a structure-based drug design approach was used to produce the aminobenzimidazole class of compounds, targeting the same enzyme with better

properties (Grossman et al., 2007). These were further optimised, and a prodrug, SPR720, was designed which was then found to have activity against *M. tuberculosis* (Grillot et al., 2014; Locher et al., 2015).

GSK3036656 has a convoluted history of discovery. The compound was based on the discovery of benzoxaboroles (Baker et al., 2006), which were shown to have antifungal activity by targeting Leucyl tRNA synthetase (LeuRS) (Rock et al., 2007). The benzoxaboroles themselves were structural analogues of borinic acid quinolone esters which possessed antibacterial properties, as synthetic substrate analogues of methyltransferases CcrM and MenH (Benkovic et al., 2005). Analogues of the benzoxaboroles were tested for antimycobacterial activity and confirmed to still be LeuRS inhibitors of *M. tuberculosis* (Palencia et al., 2016). Further structural analogues were synthesised to improve pharmacokinetics and potency *in vivo*, leading to GSK3036656 (Li et al., 2017).

1.2.3.3. Other Agents in Development (Phase I or Pre-clinical)

Currently in a Phase I clinical trial, GSK-286 is a novel antimycobacterial compound which was identified from a high-throughput screen, looking at efficacy of compounds against *M. tuberculosis* growing within human macrophages, similar to Telacebec's discovery (Nuermberger et al., 2022). Although, the mechanism of action is unknown, it is only active against *M. tuberculosis* using cholesterol as its sole carbon source (Nuermberger et al., 2022).

FNDR-20081 was synthesised alongside a small library of analogues on the basis of antimycobacterial literature highlighting quinoline, 1,2,4-oxadiazoles and a piperazine linker as important functional groups for antimycobacterial activity (Shruthi et al., 2019). The mode of action of this novel compound is currently unknown, resistant mutants

generated signal this compound is likely subject to MmpL5 efflux (Kaur et al., 2021). This compound is currently undergoing pre-clinical trials.

Another compound currently undergoing pre-clinical trials is GSK839, no information about its method of discovery have been described, however, it is patented as a TrpAB inhibitor (Alemparte-Gallardo, Encinas and Esquivias Provencio, 2021). Compound analogues have been shown to target the subunit interface of TrpAB (Abrahams et al., 2017).

Finally, Sanfetrinem was identified as the most active β-lactam against *M. tuberculosis* infected macrophages, from a panel of 2,000 β-lactams and was originally developed for antibacterial activity in the 1990s (Ramón- García et al., 2019; Di Modugno et al., 1994). This screen was undertaken following successful use of meropenem for the clinical treatment of TB (Diacon et al., 2016). β-lactams inhibit the synthesis and remodelling of peptidoglycan, specifically by binding to the penicillin-binding proteins and L,D-transpeptidases, preventing cross-link formation, which weakens the cell envelope and prevents cell growth/division (Maitra et al., 2019).

1.3. Tuberculosis Drug Resistance

M. tuberculosis drug resistance can be split into two general groups, its inherent mechanisms of resistance and its acquired resistance. The inherent mechanisms of resistance include the mycobacterial cell envelope, its ability to enter a hypoxia-induced non-replicating persister state, and the many efflux systems for drug removal. Mycobacteria do not take up extracellular DNA under normal conditions, only electroporation can be used within the lab for transformations (Hatfull, 1993; Parish,

2021); hence, the only mechanism of resistance acquisition is random mutations and their environmental selection.

1.3.1. Mycobacterial Cell Envelope

Mycobacteria are surrounded by a complex cell envelope structure, composed of mycolic acids, modified peptidoglycan, arabinogalactan, and LAM (Figure 1.5, (Batt, Minnikin and Besra, 2020)), which provides a waxy hydrophobic barrier, preventing the penetration of many antibiotics (Maitra et al., 2019; Dulberger, Rubin and Boutte, 2020). This is highlighted by the majority of anti-mycobacterial drugs possessing physiochemical properties which are distinct from general 'drug-like' properties (Motamen and Quinn, 2020; Fullam and Young, 2021).

The inner membrane of mycobacteria is composed of modified phospholipids (Batt, Minnikin and Besra, 2020; Bansal-Mutalik and Nikaido, 2014; Minnikin et al., 2015). The inner leaflet of this membrane is composed of a mix of acyl and diacyl phosphatidylinositol dimannosides ($AcPIM_2$ and Ac_2PIM_2) (Bansal-Mutalik and Nikaido, 2014; Batt, Minnikin and Besra, 2020; Minnikin et al., 2015). The outer leaflet of this membrane then contains acyl and diacyl phosphatidylinositol hexamannosides ($AcPIM_6$ and Ac_2PIM_6), alongside more familiar phospholipids including phosphatidylinositol, phosphatidylethanolamine (PE) and cardiolipin (Bansal-Mutalik and Nikaido, 2014; Batt, Minnikin and Besra, 2020; Minnikin et al., 2015). The $AcPIM_{2/6}$ and $Ac_2PIM_{2/6}$ lipids contain three and four acyl lipid chains, respectively, compared to the two acyl lipid chains found in most phospholipid membranes. The higher number of acyl lipids increases the fatty acid content of the membrane and has been proposed to reduce membrane fluidity, potentially then impeding drug permeability (Bansal-Mutalik and Nikaido, 2014). The unusual mix of both mono and di-acetylated PIMs has

recently been proposed to allow a rapid response to membrane fluidisation, through inositol acetylation in response to external factors (Nguyen et al., 2022).

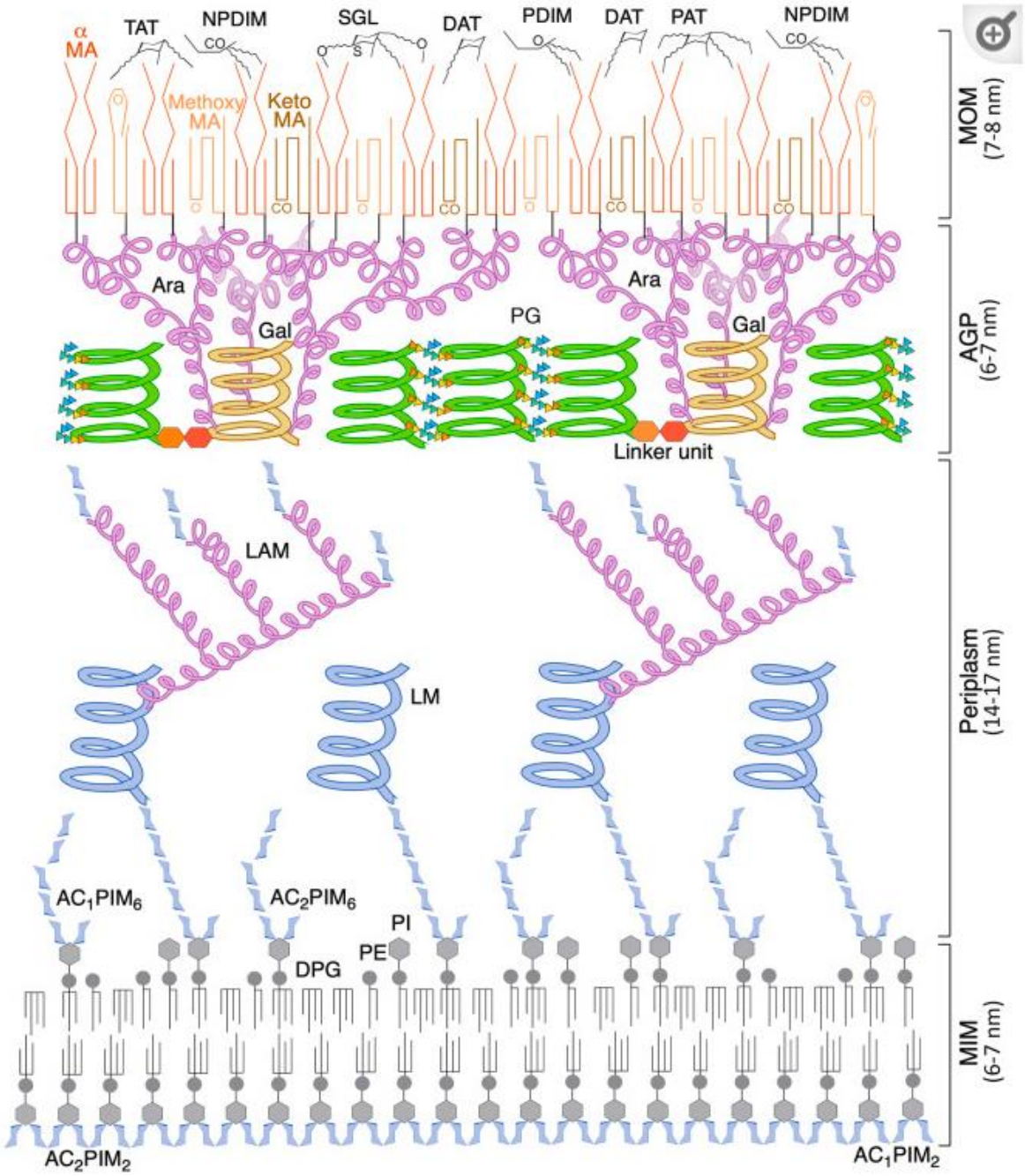


Figure 1.5: Structure of the mycobacterial cell envelope – taken from Batt, Minnikin and Besra, (2020). MA = Mycolic acids, DAT/TAT/PAT = di/tri/penta-acyl trehalose, NPDIM = phthiodiolone dimycoserates, SGL = sulfolipids, LAM= lipoarabinomannan, LM = lipomannan, $AC_{1/2}PIM_{2/6}$ = mono/diacyl phosphatidylinositol di/hexamannosides, PE = phosphatidylethanolamine, PI = phosphatidylinositol, DPG = diphosphatidylglycerol.

The periplasmic space between the two membranes contains sugar polymers, including lipid bound lipomannan (LM) and LAM, and the modified peptidoglycan and arabinogalactan polymers. LM has additional α(1→6) linked mannose units building onto the $Ac_2PIM_{2/3/4}$, forming a core mannan chain of 21-34 residues, with additional α(1→2) linked mannose residues (Hunter and Brennan, 1990; Batt, Minnikin and Besra, 2020). Arabinofuranose sugars can be added onto LM, leading to LAM formation, which occurs at specific branchpoints from the mannan core. Then additional arabinofuranose monomers are added using α(1→5) linkages and α(1→3) branchpoints on the arabinofuranose polymerised chain (Chatterjee et al., 1991; Batt, Minnikin and Besra, 2020). Finally, a terminal β(1→2) arabinofuranose is added, sometimes followed by a mannose cap (Chatterjee et al., 1992). The processes responsible for controlling the ratio between LM and LAM are currently unknown. It is also an ongoing debate whether some of the LM and LAM are anchored in the outer membrane, rather than the inner membrane (Batt, Minnikin and Besra, 2020).

The arabinogalactan layer within the periplasm has been predicted to be composed of helical polymers of peptidoglycan and galactan, with branched arabinofuranose chains connecting the galactan to the mycolic acid outer membrane (Minnikin et al., 2015). The peptidoglycan polymers are composed of alternating *N*-acetylglucosamine (GlcNAc) with *N*-acetylmuramic acid/*N*-glycolylmuramic acid (MurNAc/MurNGlyc) (Maitra et al., 2019; Minnikin et al., 2015). The peptide stems for crosslinking of peptidoglycan are L-alanyl-γ-D-isoglutamyl-*meso*-diaminopimelate-D-alanyl-D-alanine, crosslinking between the penultimate D-Ala and *meso*-diaminopimelate (*m*DAP) (Wietzerbin et al., 1974). The key differences present in mycobacteria are the presence of MurNGlyc, which increases the resistance of mycobacteria to lysozyme,

an increase in crosslinking to 70-80% from the 40-50% in *E. coli*, and the formation of *m*DAP to *m*DAP crosslinking in two thirds of the links present (Wietzerbin et al., 1974; Raymond et al., 2005; Maitra et al., 2019). The galactan core of arabinogalactan is linked via an α-*L*-rhamnopyranose (1→3) α-D-GlycNAc-1-phosphate onto a MurNGlyc on the outside of peptidoglycan (McNeil, Daffe and Brennan, 1990). The galactan core is formed of alternating β(1→5) and β(1→6) galactan units, with arabinofuranose connected via the 5th carbon of a β(1→6) galactan unit (Daffe, Brennan and McNeil, 1990). Similar to LAM, the arabinofuranose chains are α(1→5) linkages with α(1→3) branchpoints (Shi et al., 2006). The main difference is the terminal structure in arabinogalactan is a hexa-arabinoside link ([β-Araf-(1→2)-α-Araf]$_2$-3,5,-α-Araf(1→5)-α-Araf) covalently binding mycolic acids, to between two and four of these arabinofuranose units (McNeil, Daffe and Brennan, 1991; McNeil et al., 1994).

The inner leaflet of the outer membrane is composed exclusively of these covalently bound mycolic acids, which are lipid molecules with 70-90 carbons, considerably longer than typical phospholipids (Minnikin et al., 2015; Lee, Brennan and Besra, 1996). The inner leaflet is composed of α-mycolates (dicyclopropylmycolates) and mycolates retaining one cyclopropane ring and the other replaced with a methoxy or keto group (Lee, Brennan and Besra, 1996; Minnikin et al., 2015). The outer leaflet of the mycolic acid membrane contains a large assortment of free lipid moieties, including phthiocerol dimycocerosate (PDIMs), phenolic glycolipids (PGLs), trehalose monomycolates (TMM), trehalose dimycolate (TDM), diacyl trehalose (DAT), penta-acyl trehalose (PAT) and sulfolipid (SL) (Minnikin et al., 2015; Batt, Minnikin and Besra, 2020).

As previously mentioned, SL, DAT and PAT are not present in *M. bovis* BCG but are found in the outer mycolic acid membrane in *M. tuberculosis* (O'Neill, Mortimer and Pepperell, 2015). In addition to the three lipids already mentioned, *M. smegmatis* is also missing PDIMs and PGLs from the outer membrane, suggesting mycolic acids are the major component of its outer membrane (O'Neill, Mortimer and Pepperell, 2015).

1.3.2. Mycobacterial Latency

Another mechanism of survival exhibited by *M. tuberculosis* is the latent growth state, in which metabolic activity is vastly reduced, sometimes called persister cells (Barry III et al., 2009; Pai et al., 2016). The reduced metabolic activity allows it to survive treatment with antibiotics whose mechanisms of inhibition rely on active growth or metabolism, such as isoniazid and β-lactams (Dutta and Karakousis, 2014).

This can be artificially induced in laboratory settings through the removal of oxygen and nutrient starvation of mycobacteria, hence referred to as hypoxia-induced (Dutta and Karakousis, 2014). However, whether this method of latent induction recapitulates the *in vivo* mechanisms remains to be determined (Dutta and Karakousis, 2014; Barry III et al., 2009).

Out of the four front-line drugs, both pyrazinamide and rifampicin have some activity against persister cells, however rifampicin relies on intermittent metabolic activity and pyrazinamide requires acidic environments for activity (Zhang, 2005; Mitchison, 1979). Hence, these cannot kill all persister cells. More recently approved drugs bedaquiline and nitroimidazoles appear to kill persister cells (Manjunatha, Boshoff and Barry, 2009; Koul et al., 2008), but whether they can kill under all *in vivo* conditions is unknown.

Evaluation of the activity of novel antimycobacterial compounds against persister cells should be undertaken, to determine their range of antibacterial activity (Gibson et al., 2022).

1.3.3. Mycobacterial Efflux

Mycobacteria have many different efflux pumps, from a variety of classes. In general, efflux pumps fall into five groups: resistance nodule division (RND); major facilitator superfamily (MFS); ATP-binding cassette (ABC); small multi-drug resistance (SMR) and multidrug and toxic compound extrusion (MATE), with at least four groups present in mycobacteria. Efflux pumps generally remove unwanted compounds from the cell, rather than membrane transport proteins, which move required compounds into the periplasm. The structures of most efflux pumps currently haven't been elucidated, due to the difficulty of structural determination of membrane proteins, however, recently predicted structures have been released for all *M. tuberculosis* proteins (Varadi et al., 2022), and this can allow functional annotation in some cases. Efflux pumps provide resistance by removing drugs from the cytoplasm and lowering their concentration, hence, requiring a higher drug concentration to have the same physiological effect.

The different types of efflux pumps are separated based on their structure, mechanism of export and energy use. ABC transporters undertake ATP hydrolysis, while RND, MFS and SMR rely on the membrane proton gradient and MATE rely on either proton or sodium gradients (Bhardwaj and Mohanty, 2012) and are displayed in Figure 1.6 (Laws, Jin and Rahman, 2022).

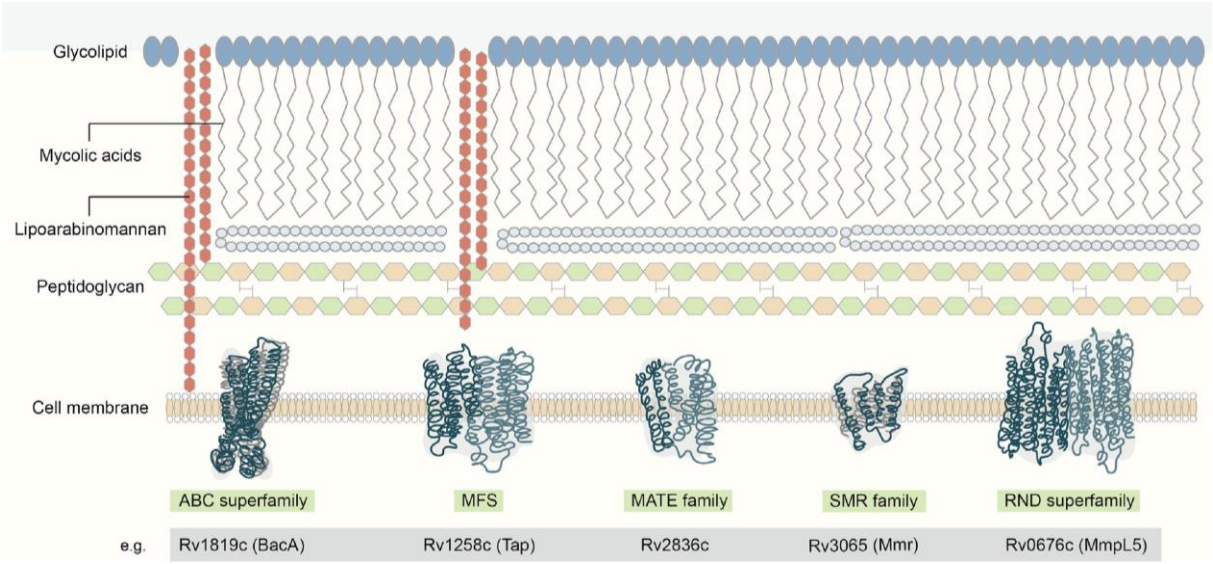


Figure 1.6: Types of efflux pumps found in mycobacteria, showing cellular location and examples. Adapted from Laws *et al.* 2022, reprinted here with permission from Elsevier, copyright 2022.

In relation to substrates of mycobacterial efflux pumps, there seems to be some overlap, with several different pumps implicated in exporting the same compounds (Pule et al., 2016; Laws, Jin and Rahman, 2022; Remm et al., 2022). For example, evidence has been provided that EfpA, Tap and Rv0194 all efflux ethidium bromide from mycobacteria (Remm et al., 2022; Laws, Jin and Rahman, 2022; Johnson et al., 2020). In addition, efflux has been implicated in the resistance to many antimycobacterial drugs, with many efflux pumps being identified as responsible for the drug efflux. However, further work needs to be undertaken to characterise how specific this efflux activity is and whether some efflux pumps have been mischaracterised during *in vitro* studies (Remm et al., 2022; Laws, Jin and Rahman, 2022).

Inhibition of efflux is one approach being explored in TB drug discovery, as it would eliminate one possible resistance mechanism, and may allow current antimycobacterial drugs to be used at lower concentrations, reducing side effects. Inhibition of efflux can either occur through specific efflux pump inhibitors or more

general efflux inhibitors (Remm et al., 2022). The former directly bind and inhibit efflux pumps, while the latter target cellular energetics processes (ATP synthesis, the electron transport chain or the proton motive force), a downstream effect being efflux inhibition (Remm et al., 2022). The proton motive force relies on the maintenance of both the electric potential ($\Delta\psi$) and the proton gradient (ΔpH) (Feng et al., 2015).

In relation to efflux inhibitors which target mycobacteria, these compounds either have more general efflux inhibition methods, or unknown mechanisms of action, with no evidence of specific efflux pump inhibitors against mycobacteria (Remm et al., 2022; Laws, Jin and Rahman, 2022; Pule et al., 2016). Compounds used within this work will be introduced in more detail, however many other efflux inhibitors have been discovered, with a few being tested for activity against mycobacteria including reserpine, piperine and phenothiazines (Remm et al., 2022; Laws, Jin and Rahman, 2022; Pule et al., 2016).

Verapamil was identified as a calcium channel inhibitor in mammalian cells (Singh, Ellrodt and Peter, 1978) (Figure 6), and its efflux pump inhibition activity has been assumed to directly translate to bacterial cells, without confirmation of the efflux pumps it inhibits (Chen et al., 2018). Several studies have shown it can potentiate the activity of antimycobacterial drugs (Chen et al., 2018; Gupta et al., 2014a), and more recently the exact mechanism of action, disruption of the ΔpH gradient and hence membrane energetics, has been elucidated (Chen et al., 2018). Hence, verapamil is a general efflux inhibitor in mycobacteria, rather than possessing the specific efflux pump inhibitory activity it has in mammalian cells (Chen et al., 2018). The continued development of verapamil as a bacterial efflux inhibitor is uncertain, as during clinical

use, high concentrations of verapamil were associated with toxicity (Andersen, Holland and Jacq, 2006).

Carbonyl cyanide *m*-chlorophenylhydrazone (CCCP, Figure 6) is a protonophore which is known to dissipate the proton motive force, affecting both components ($\Delta\psi$ and ΔpH), through movement of protons across the membrane (Remm et al., 2022; Sharma, Gupta and Pathania, 2019). A downstream effect of this, is inhibition of efflux, as both the proton gradient has been disrupted and no ATP can be synthesised (Remm et al., 2022). CCCP has not been developed further due to its toxicity to mammalian cells (Pule et al., 2016).

One class of compounds, cationic amphiphiles, have also been shown to have some uncoupling effects on the membrane potential, these include bedaquiline, SQ109 and clofazimine (Feng et al., 2015) (Figure 2 & 3). These drugs already have specific targets in mycobacteria, but this work suggested these drug molecules may have multiple mechanisms of action which lead to cell death, with efflux inhibition being another downstream effect (Feng et al., 2015). For bedaquiline specifically, it has been shown to collapse the ΔpH but not the $\Delta\psi$ (Jeon et al., 2019), suggesting it targets ATP synthesis in two ways, directly against the ATP synthase protein and through disruption of the proton gradient through uncoupling (Andries et al., 2005; Feng et al., 2015; Biuković et al., 2013).

1.3.4. Specific Resistance Mechanisms

In contrast to these intrinsic resistance mechanisms, *M. tuberculosis* can also become drug resistant through random mutations which are then selected during drug treatment.

Focussing on the front-line drugs initially. Isoniazid resistance has occurred through mutations within the target, *inhA*, but also mutations are present in *katG*, preventing compound activation, and in *ndh*, representing resistance based on a secondary target (Telenti, 1998; Banerjee et al., 1994). Pyrazinamide is a pro-drug and hence, the main source of resistance were mutations in the *pncA* gene, preventing activation of the drug (Scorpio and Zhang, 1996). In the case of ethambutol, *embB* is the main gene which is mutated in clinical isolates, representing the direct target; however, additional resistance mechanisms can cause phenotypic resistance (Li et al., 2020; Telenti, 1998). Finally, for rifampicin, the majority of the resistant mutants identified have been within the *rpoB* gene, on a protein level, these mutations prevent rifampicin binding to the drug target (Telenti, 1998; Zhang et al., 2014).

More limited clinical data exists for secondary-line drugs, due to their lower frequency of use and lower number of cases of MDR and XDR-TB. Aminoglycoside resistance is associated with mutations in the *rrs* gene, which alters the target rRNA preventing binding (Alangaden et al., 1998; Georghiou et al., 2012; Dookie et al., 2018). For kanamycin specifically, resistance can also be linked to mutations within the promoter region of *eis*, which encodes an aminoglycoside acetyltransferase (Georghiou et al., 2012; Zaunbrecher et al., 2009; Dookie et al., 2018). The majority of clinical linezolid resistance is associated with *rplC* mutations, with a minor component including *rrl* mutations, these encode parts of the 23S portion of the 50S ribosomal subunit and hence prevent linezolid binding (Zimenkov et al., 2017; Dookie et al., 2018; Wasserman et al., 2019). For fluoroquinolones, mutations within the *gyrA* and *gyrB* genes have led to resistance, the former being more common in clinical isolates; these mutations alter the target DNA gyrase, reducing or preventing fluoroquinolone binding

(Pantel et al., 2012; Telenti, 1998; Dookie et al., 2018). PAS resistance has been associated with several mutations, including mutations in *folC*, preventing PAS activation, and mutations in *thyA*, which reduces the requirement for DfrA activity (Dookie et al., 2018; Minato et al., 2015). In addition, overexpression of either DfrA or RibD have been associated with increased PAS resistance, by compensating for drug inhibition (Dookie et al., 2018; Minato et al., 2015). Ethionamide resistance has been found to occur through mutations in the *inhA* gene, encoding the protein target, and also in *ethA*, encoding the activating enzyme (Banerjee et al., 1994; DeBarber et al., 2000; Dookie et al., 2018). Resistance to bedaquiline can occur through either target alteration, caused by mutations in *atpE* encoding the target, or upregulation of efflux, with mutations in *rv0678* (*mmpR)* the regulator of the MmpL5-MmpS5 efflux pump; the latter being more common in clinical isolates (Zimenkov et al., 2017; Ndjeka and Ismail, 2020; Dookie et al., 2018). Finally, the nitroimidazoles have been in clinical use for a much shorter duration, hence, few clinical resistant strains have been identified. The only identified resistant mutants have been enzymes involved in prodrug activation, primarily Rv3547 and others upstream involved in F420 synthesis or turnover (Dookie et al., 2018; Wen et al., 2019).

For many drugs which are currently in clinical development, the generation of resistant mutants was the main method for target identification (Makarov et al., 2009; Naik et al., 2014; Shirude et al., 2013; Tahlan et al., 2012; Pethe et al., 2013). Whether these mutations occur *in vivo*, will be confirmed if they are approved for clinical use. Based on *in vitro* data, many of the drugs currently under development have very low rates of resistance compared to current front-line drugs, ideally, this will translate into a lower frequency of resistance occurrence.

In summary, a majority of resistance to antimycobacterial drugs is through mutations which directly alter the drug's target, but *M. tuberculosis* could also gain resistance through alterations to prodrug activating enzymes. In addition, some mutations can enhance the other resistant mechanisms, such as increasing efflux. D-cycloserine appears to be an exception, with no clinical resistance emergence documented (Evangelopoulos et al., 2019).

1.4. Drug Discovery & Development Approaches

1.4.1. High-throughput Screening

One common approach used within drug discovery is high-throughput screening, which involves screening large compound libraries in robust assays to identify hits which possess the required activity. The compound libraries chosen will depend on the desired output, novel chemical discovery, drug repurposing or targeted discovery. Compound library screening is financially expensive and hence is being used less frequently for antibacterial discovery, due to lower economic rates of return. In addition, when screening natural products, there is a high rate of re-discovery of compounds. When designing a high-throughput screen, there are two general approaches, either performing a drug to target or target to drug screen.

1.4.1.1. Drug to Target Approach

Drug to target screening, sometimes referred to as phenotypic screening, involves testing molecules for activity against whole cells. In the case of antibacterials, this would focus on growth inhibition or metabolic inhibition as end points. This approach guarantees that the hit can reach its target and exert the killing activity, but the target is unknown (Abrahams and Besra, 2020). This approach has been successful for the

discovery of many antimycobacterial drugs (Andries et al., 2005; Ballell et al., 2013). However, it has also led to many drugs targeting so-called promiscuous drug targets, such as MmpL3 and DprE1, which have been identified as the targets of many hits from drug to target screens against mycobacteria (Li et al., 2019; Piton, Foo and Cole, 2017). While these are valid antimycobacterial drug targets, it hinders the ability of these types of screens to identify molecules with more diverse targets.

1.4.1.2. Target to Drug Approach

The alternative approach is to start with a protein target and screen compound libraries to identify inhibitors of the protein. The type of screening has not been successfully applied to antimycobacterial drugs, despite being utilised successfully for anti-cancer drugs (Barry III, 2009; Projan, 2002; Cooper, 2013). Ideally, target selection would involve choosing an essential gene for *M. tuberculosis* or a target involved in an infection-linked phenotype e.g. virulence, persistence or signalling (Zhang, 2005; DeJesus et al., 2017). This method would allow unique targets, not currently inhibited by clinically used drugs, to be focussed upon and prevent cross-resistance. This approach has generally failed as potent protein inhibitors have not been optimised for their ability to cross the cell envelope and hence cannot reach their targets (Cooper, 2013; Benedetto Tiz, Kikelj and Zidar, 2018). More recent development such as fragment-based screening (Projan, 2002) and increased knowledge of the entry rules for bacterial cell envelopes may allow these approaches to be more successful in the future (Benedetto Tiz, Kikelj and Zidar, 2018).

1.4.2. Natural Products & Semi-synthetic Approaches

Natural product discovery has been the main source of hits with antimycobacterial activity, which were later developed into drug treatments for TB. As outlined earlier, hits from natural products were later developed into isoniazid, pyrazinamide, ethionamide, rifampicin, streptomycin and D-Cycloserine, among several others (Zhang, 2005; Margalith and Beretta, 1960). Natural products have been screened extensively, as natural products represent bioactive molecules already, and it can be easier to alter already active molecules than try and generate bioactivity synthetically (Lachance et al., 2012).

The more complex scaffolds found within natural products can then be altered to increase potency and reduce toxicity, producing semi-synthetic drug molecules (Lachance et al., 2012). Direct use of natural products is less common, however examples such as streptomycin and penicillin are exceptions (Schatz, Bugle and Waksman, 1944). Rifampicin is a clear example of a semi-synthetic drug, rifamycins were isolated from *Amycolatopsis rifamycinica* (previously named *Streptomyces mediterranei*, *Nocardia mediterranei* and *Amycolatopsis* mediterranei) (Margalith and Beretta, 1960), followed by large numbers of structural alterations to increase its potency and oral availability (Sensi, 1983; Barry III, 2011).

Natural product testing is still a common drug discovery approach, especially with improvements in our ability to identify novel biosynthetic gene clusters (Cimermancic et al., 2014) and more diverse sources of microbes being identified (Roberts, 2020; Nichols et al., 2010; Ling et al., 2015). Some of the antimycobacterial drugs currently under development have also been derived from natural products, these include

clofazimine from lichen, SPR720 based on coumarins and sanfetrinem based on β-lactams (Barry et al., 1957; Grillot et al., 2014; Di Modugno et al., 1994).

1.4.3. Drug Repurposing

Drug repurposing focusses on studying drugs which have already been tested for one clinical implication to determine if they also have activity against another target or organism. This repurposing is based on the principal that drugs which have already been tested will have a wealth of *in vivo* clinical data (absorption, distribution, metabolism, excretion, and toxicity (ADMET) etc.). This could help expedite hit to clinic development and can highlight common side effects to study. This approach has been used extensively for second-line drugs to treat TB, including fluoroquinolones and linezolid. In addition, repurposed drugs also represent one-quarter of all the new TB drugs currently in clinical trials (WHO, 2022a).

Compound libraries of known drugs will inherently be less structurally diverse, however, there is no risk of repeated re-discovery rates common with screening micro-organisms for natural products. Examples of compound libraries for drug re-purposing include the 6,798 compound Broad Institute library (Corsello et al., 2017) and the 1,520 compound Prestwick library, containing mainly FDA-approved compounds (Kanvatirth et al., 2019). One issue with this approach for antimycobacterial compound discovery is their physiochemical properties can be distinct from general ‘drug-like’ properties (Motamen and Quinn, 2020; Fullam and Young, 2021).

1.4.4. Computational Approaches

Rather than undertake the high-cost experiments associated with high-throughput screening of compounds libraries, a lower cost option is to undertake computational approaches, including virtual screening, cheminformatics, or molecular dynamic (MD) simulations. This can reduce the number of compounds to be tested and provide *in silico* evidence of compound binding.

Two main approaches are used for drug discovery projects, either ligand-based (i.e., cheminformatics) (Geppert, Vogt and Bajorath, 2010) or structure-based (i.e., virtual screening) (Kitchen et al., 2004; Lohning et al., 2017; Shaker et al., 2020) approaches. The former uses publicly available datasets containing chemical structures and associated biological activity, while the latter focusses on modelling drug-target interactions. The end goal of both is to identify compounds which might bind to a particular target or inhibit a specific organism. However, virtual screening against a specific protein has a greater potential to find novel chemical structures compared to cheminformatics (Swift et al., 2016). Ligand-based approaches only utilise chemical structures, so use less computational power and have seen more recent progress with machine learning implementations (Geppert, Vogt and Bajorath, 2010). In contrast, structure-based approaches require modelling of both the chemical and their interactions with a rigid protein, requiring higher computational power, and have not yet benefitted from machine learning (Kingdon and Alderwick, 2021; Li et al., 2018). The only exception is machine learning applications to re-score previously generated docked poses, for which several programmes have been developed, as this targets the least computationally expensive part of molecular docking (Kingdon and Alderwick, 2021; Ballester, 2019; Li et al., 2018).

Molecular docking is the main structure-based approach which will be used within this work. Various docking programmes exist and they all use different algorithms to try and fit a compound into the binding site of the protein (Kitchen et al., 2004). They generate several potential conformations, or poses, which are then scored, and the top scoring poses represent the main output from the programme (Kitchen et al., 2004). These programmes focus on the compounds' flexibility, while treating the protein as completely rigid (Carlson and McCammon, 2000; Klebe, 2000); this approach saves computational power, but also decreases the accuracy (Mobley and Dill, 2009). A large range of docking programmes have been applied to *M. tuberculosis* drug discovery (Kingdon and Alderwick, 2021). However, while the virtual screening campaigns appear robust, many studies only performed *in silico* work and hence the efficacy of these approaches are difficult to quantify when no *in vitro* data on activity is supplied (Kingdon and Alderwick, 2021).

MD simulations are a more computationally intensive approach to model the motions of atoms over short nanosecond timeframes (McCammon, Gel and Karplus, 1977; Phillips et al., 2005; Hospital et al., 2015). They can be used to study protein movement or protein-drug interactions in more detail, compared to the rigid structures used in molecular docking. An initial input structure is required for all simulations, which specifies the position and velocities of all the atoms, both of the protein and surrounding water molecules. The simulation has pre-determine force fields which are used to calculate the forces acting on each atom. Based on the input structure, the atom locations and velocities are used to solve the Newtonian equations of motion generating a trajectory and the atoms are moved to this new position. Given the high computational power required, only a small timestep of two femtoseconds (fs) is solved

in a single step. This process continually loops, generating new sets of atom positions, until a pre-specified number of timesteps has elapsed (Hospital et al., 2015). For a short ten nanosecond simulation, five million timesteps need to be calculated (Kingdon and Alderwick, 2021). Several programmes exist to undertake these MD simulations, with NAMD (Phillips et al., 2005) and GROMACS (Abraham et al., 2015) being utilised the most. If MD simulations have been applied to study *M. tuberculosis* protein interactions with drugs, this has rarely been paired with *in vitro* compound testing, so the utility of this approach cannot be evaluated (Kingdon and Alderwick, 2021). The structural confirmations generated by performing MD simulations can also be used for ensemble docking, which docks the same molecules against multiple protein confirmations, highlighting the molecules which are predicted to bind the protein consistently (Gioia et al., 2017; Carlson and McCammon, 2000; Lin et al., 2003).

Computational approaches represent a growing field of drug discovery, including their use to discover novel antimycobacterial drugs, however, the lack of *in vitro* testing and hence method validation has prevented verification of the efficacy of this approach.

1.4.5. Hit to Lead Optimisation

Once hits have been identified, either from high-throughput screening, drug repurposing, computational approaches or other methods, there is normally further development before pre-clinical testing. The optimisation of a hit compound will involve the chemical synthesis of analogues, to accomplish one or more of several aims. This can include increased potency, reduced toxicity, increased target specificity and improved ADMET properties. If possible, several distinct chemical hits will go through this process, to provide assurance one can reach pre-clinical or clinical trials for the

desired implication. However, in academic settings, generally one compound series will be focussed upon, due to resource limitations.

1.4.5. Thesis Outlook

This thesis is split across two main drug discovery projects, both with the end goal of developing drug compounds for the treatment of TB or other antimicrobial resistant pathogens. Within this work, *M. smegmatis* and *M. bovis BCG* were used as model organisms due to safety regulations, however, it is hoped work on these model systems can be directly translated to *M. tuberculosis.*

Chapter two took a target to drug approach, focussing on an essential *M. tuberculosis* protein and trying to develop assays to test for protein inhibition and binding. This was followed by computational and structural approaches to try and find new drug compounds which inhibit this protein. Alongside this, drug compounds were tested for whole-cell inhibition.

Chapter three was based on a drug to target approach; a previous high throughput screening effort had been undertaken against *M. smegmatis* and *M. bovis BCG* focussing on drug repurposing. One promising hit from this screen was taken forward for mode of action determination, to allow further drug development. In addition, a small medicinal chemistry investigation was undertaken, in an effort to develop a more active analogue.

Overall, this thesis contains a series of drug discovery and development projects to target *M. tuberculosis* and has identified at least one compound which would benefit from continued development and testing.

2. Targeting AroB, an Essential TB Protein

2.1. Introduction

2.1.1. Shikimate acid pathway

This project aimed to find novel chemical compounds which targeted the mycobacterial shikimate metabolic pathway, which is essential for the *de novo* biosynthesis of aromatic amino acids and nucleic acid precursors in *M. tuberculosis* (Parish and Stoker, 2002; Nunes et al., 2020; Galina et al., 2022). More specifically, the project focussed upon the AroB enzyme, 3-dehydroquinate synthetase (DHQS). The shikimate acid biosynthetic pathway is not present in animals, and hence, off-target inhibition during potential treatment is unlikely, as there are no mammalian homologs of AroB (Parish and Stoker, 2002; Nunes et al., 2020).

The shikimate acid pathway is outlined in Figure 2.1 (Nunes et al., 2020) and is composed of seven enzymes catalysing the conversion of phosphoenolpyruvate and D-erythrose 4-phosphate to chorismate. This pathway is essential for the production of aromatic amino acids and precursors of tetrahydrofolate, ubiquinone and mycobactin (Nunes et al., 2020; Parish and Stoker, 2002). In mycobacteria, these genes encode seven separate proteins, however, in fungi and some intracellular parasites, the AROM complex is encoded and performs equivalent functions to AroB, AroD, AroE, AroK and AroA (Patel and Giles, 1979; Derrer, Macheroux and Kappes, 2013). AroG catalyses the first committing step in mycobacteria and can be regulated by combinations of the aromatic amino acids (Webby et al., 2010), providing a feedback loop. Crystal structures have been solved for all seven of the *M. tuberculosis* shikimate acid pathway enzymes.

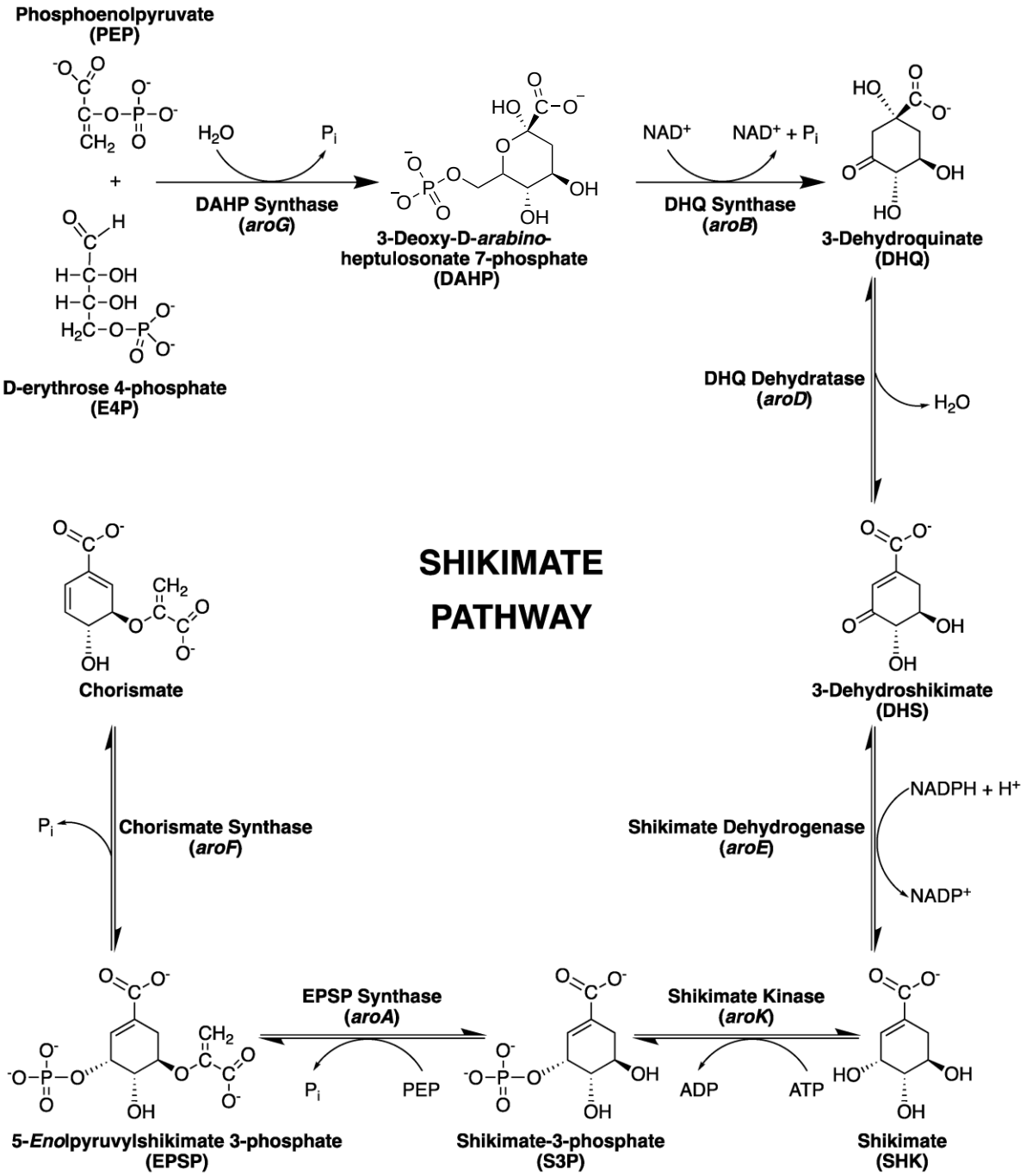


Figure 2.1: Diagram of the shikimate acid pathway, with the *M. tuberculosis* enzymes highlighted. P_i = inorganic phosphate. Figure taken from Nunes et al. (2020).

The essentiality of this pathway has been explored in several publications. Transposon mutagenesis studies have highlighted that a majority of genes are essential (DeJesus et al., 2017; Minato et al., 2019), the only exception was *aroE*, which was defined as

non-essential by DeJesus et al. (2017) but essential by Minato et al. (2019). A more recent CRISPR-interference approach was used to evaluate both the essentiality and predict the vulnerability following inhibition, and found that all seven genes to be essential (Bosch et al., 2021). The vulnerability scores were *aroG* = -13.4, *aroB* = -9.2, *aroD* = 5.9, *aroE* = -9.0, *aroK* = -10.2, *aroA* = -9.0 and *aroF* = -11.4. For comparison, known TB drugs targets, *rpoB*, *inhA* and *atpE* had vulnerability scores of -9.6, -9.9 and -8.7, respectively (Bosch et al., 2021). The deletion of the *aroK* gene from mycobacteria was not possible, even in the presence of media supplementation (Parish and Stoker, 2002). The use of CRISPR interference to knock-down the levels of the AroG protein also highlighted that media supplementation was not able to return the strain to wild type growth (Galina et al., 2022). Overall, this highlights the shikimate acid pathway and its constitutive enzymes as vulnerable targets.

Due to this vulnerability, many different attempts have been undertaken to target different enzymes within this pathway and identify novel inhibitors (Nunes et al., 2020). The range of approaches undertaken include modelling catalytic intermediates (Reichau et al., 2011), virtual screening (Nirmal, Rao and Hopper, 2015; Alhaji Isa, Singh Majumdhar and Haider, 2018; Petersen et al., 2015) and screening compounds in activity assays (Zhu et al., 2018; Simithy et al., 2018). Currently, none of these attempts have resulted in a drug, with these targets, undergoing pre-clinical or clinical evaluation.

2.1.2. AroB

AroB is the second enzyme in the shikimate acid pathway, acting as a dehydroquinate synthase enzyme (Dutra De Mendonça et al., 2007; Ducati, Basso and Santos, 2007), converting 3-Deoxy-D-*arabino*-heptulosonic acid 7-phosphate (DAHP) into 3-

dehydroquinate. While it is not the committing step to the shikimate acid pathway, it would cause a bottleneck when inhibited. This enzyme catalyses a complex set of reactions, as displayed in Figure 2.2 (Carpenter et al., 1998). Initially, the DAHP undergoes an oxidation, forming a ketone (step 1), this is followed by the β-elimination of the phosphate group (step 2). The ketone formed in step 1 is reduced back to the hydroxyl group. Then, a ring opening reaction occurs (step 4), following by an aldol condensation (step 5) to form the 3-dehydroquinate product. The enzyme is involved in both direct catalytic activity and stabilisation of reactive intermediates. Resistance through mutations in catalytic residues may be less likely to occur, due to the complex mechanism; but mutations causing conformational changes are equally likely to occur.

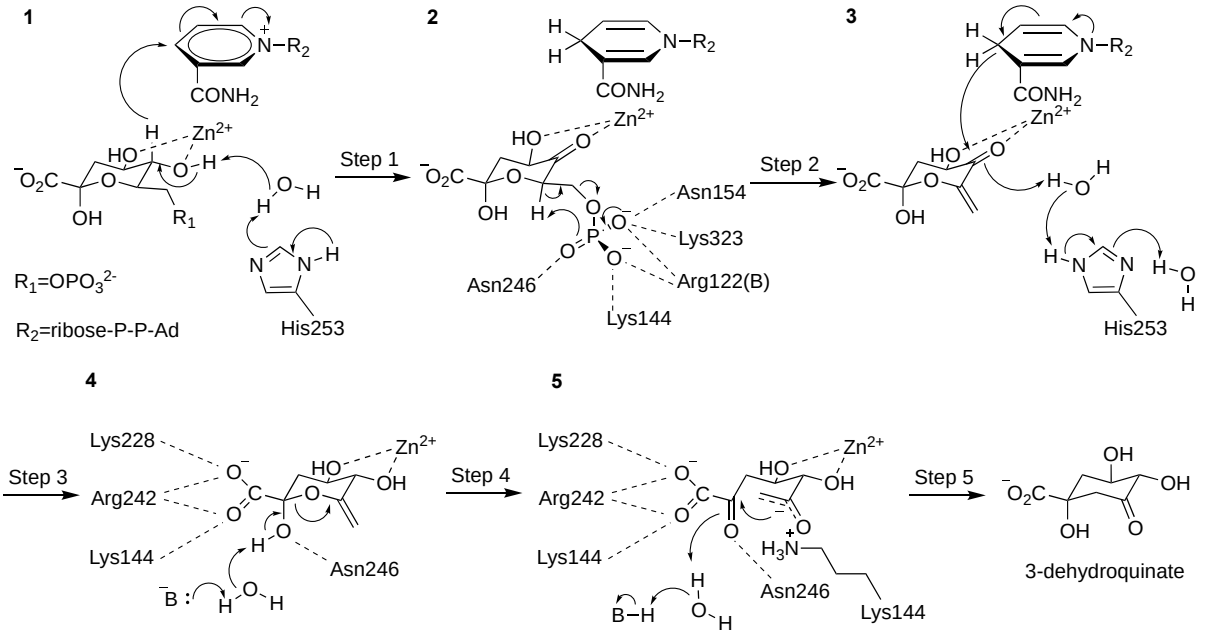


Figure 2.2: MtAroB enzymatic mechanism converting DAHP into 3-dehydroquinate. Remade, but adapted from Carpenter et al. (1998), replacing residue numbers with *M. tuberculosis* labelling. Ad = adenosine, P = phosphate, B = general base.

Two crystal structures of MtAroB have been solved and are currently present in the protein data bank (PDB), an apo crystal structure (3QBE) and an NAD^+-bound structure (3QBD). However, no publication corresponds to these structures. Both

structures were very similar, with an RMSD of 0.65 Å, suggesting the bound co-factor, nicotinamide adenine dinucleotide (NAD), may not cause large structural changes. Comparing the sequence of the AroB homologous protein across a range of species, there is a clear split between Gram-negative and Gram-positive species (Figure 2.3A,

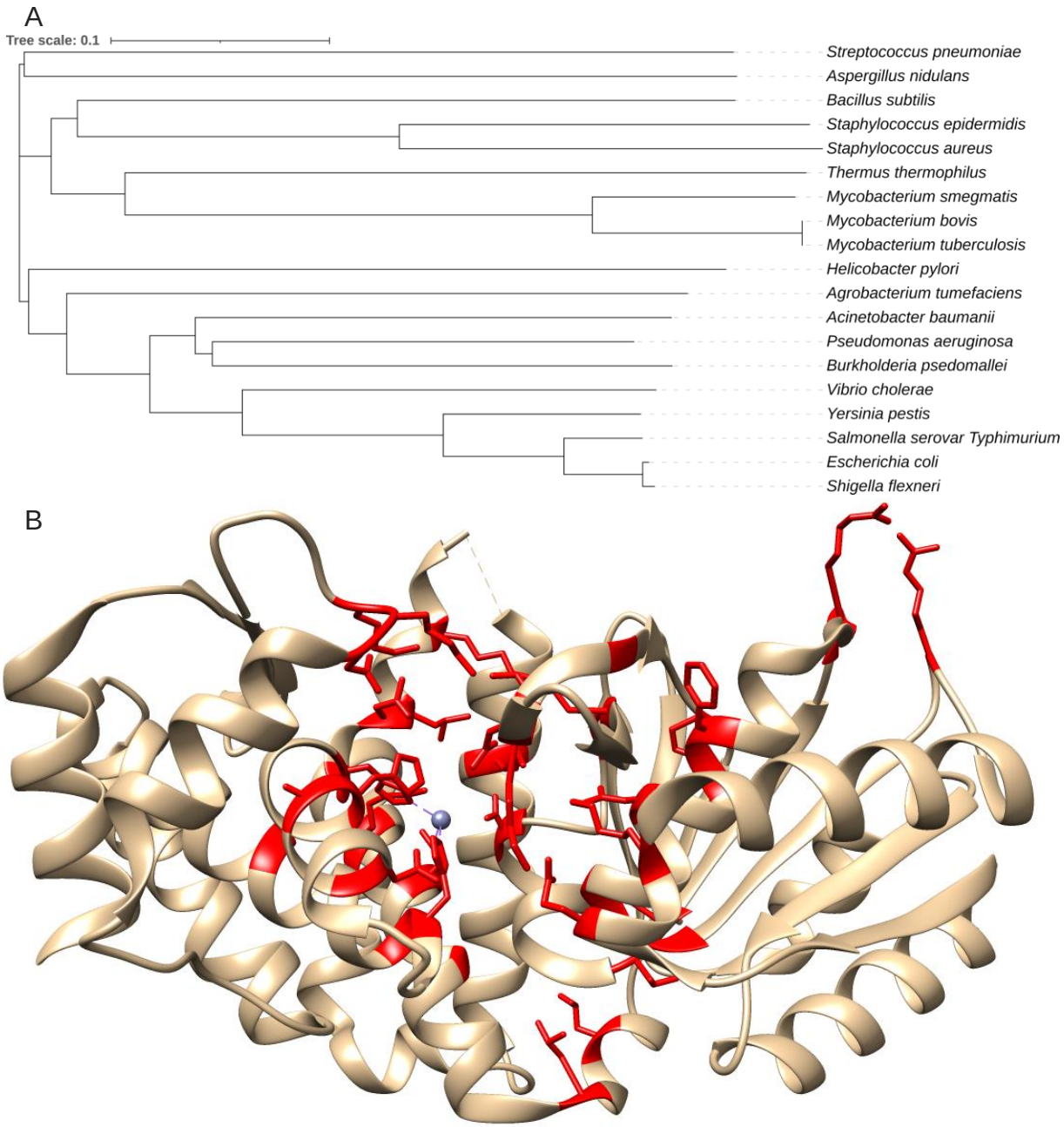


Figure 2.3: Conservation of the AroB protein across bacterial species. (A) A dendrogram showing the similarity of protein sequences across species. Produced in iTOL. (B) Conserved residues (red) are shown on the MtAroB crystal structure, PDB=3QBE.

produced using iTOL (Letunic and Bork, 2016)). This likely represents evolutionary divergence over time. There is still a high-level sequence similarity, especially between closely related species. Focussing on the conserved residues which remained the same across all species investigated, they were clustered in the protein active site, with low conservation in the periphery of the protein. The conserved residues are displayed on the MtAroB crystal structure (PDB=3QBE, Figure 2.3B). The main exception to the active site residue clustering is the conservation of the Arg97 and Arg122 residues, which if the protein were a dimer, would point into the active site of the other monomer. The high degree of conservation suggests that these residues are unlikely to mutate and produce resistant mutants if targeted by a compound.

Currently, this enzyme is not targeted by any current or experimental TB drug. Carbaphosphonate is a substrate analogue which has been shown to reversibly bind AroB and inhibits its activity, however, it is currently only used for research purposes and has not been developed into a drug molecule due to poor pharmacological properties. Further development of carbaphosphonate as a drug candidate is unlikely due to its inability to penetrate bacterial membranes and low yielding synthetic route (Tian, Montchamp and Frost, 1996). However, carbaphosphonate does show an antagonist effect on AroB activity and this suggests that alternative drug molecules would be able to inhibit this enzyme.

The crystal structure of MtAroB has been used in molecular docking experiments to suggest potential inhibitors, without further *in vitro* and *in vivo* confirmation being undertaken (Alhaji Isa, Singh Majumdhar and Haider, 2018; Sivaranjani et al., 2019). Hence these compounds are unlikely to be developed further. In addition, IMB-T130 is a recently discovered drug which binds to the *M. tuberculosis* AroB (Zhu et al., 2018);

however, this drug has also been shown to bind *M. tuberculosis* aminoacyl-tRNA synthetase (Zhu et al., 2015). These pleotropic effects may hider its further development but provide further evidence that drug development against this target is a worthy endeavour. These studies, including a recent review (Nunes et al., 2020), highlight AroB as a promising target and suggest it should be the focus of further drug development.

This chapter has been split into a section on the development of tools to study compound binding to, and inhibition of, MtAroB and a section on drug discovery attempts to target MtAroB. Overall, a wide range of biophysical methods and some computational approaches were utilised within this chapter. During the development of assays, two known binding compounds DAHP and NAD were used, alongside a known non-binding compound, vanoxerine (see Chapter 3 for more information).

2.2. Results

2.2.1. Tools to study AroB

As the *M. tuberculosis* AroB (MtAroB) protein was identified as a viable target for drug discovery, several strategies to study drug binding and inhibition were devised. This was undertaken to allow novel compound binding to be tested and ideally allow drug development to target this essential protein.

The majority of these approaches relied on obtaining the purified MtAroB protein, for both activity assay development and binding interaction studies. Hence, the *M. tuberculosis* AroB gene, was cloned into the pET28a expression vector, from *M. tuberculosis* genomic DNA (Appendix 1). For this cloning, the pET28a vector encoded a 6-His tag onto the N-terminus of the protein, allowing nickel-column purification to be undertaken.

2.2.1.1. Expression/Purification of MtAroB

After the successful HiFi cloning of the MtAroB gene into the pET28a vector, this plasmid was transformed into the *E. coli* BL21 (DE3) expression strain, to allow protein expression trials to be undertaken. Four colonies were chosen to analyse for protein expression, prior to performing a large-scale expression. This trial run showed a clear band at around 39 kDa for all four strains and hence one was taken forward for large scale expression and purification. A one-litre culture was grown to mid-log, before ITPG was added to induce protein expression and this was allowed to continue overnight. The cells were harvested, lysed by sonication and the clarified lysate loaded onto a nickel-NTA column. The purification process is highlighted on the SDS-PAGE gel (Figure 2.4). The band at 39 kDa corresponding to MtAroB is present across all

fractions, suggesting some protein was lost in the insoluble, flow-through and wash fractions. However, the majority of the MtAroB protein was eluted using 67 mM imidazole. As only 4x the column volume was used at each elution step, not all the protein was eluted with the initial 67 mM imidazole fraction. This gel also highlighted that some contaminating proteins were also eluted at 67 mM imidazole and hence further purification was undertaken on this fraction.

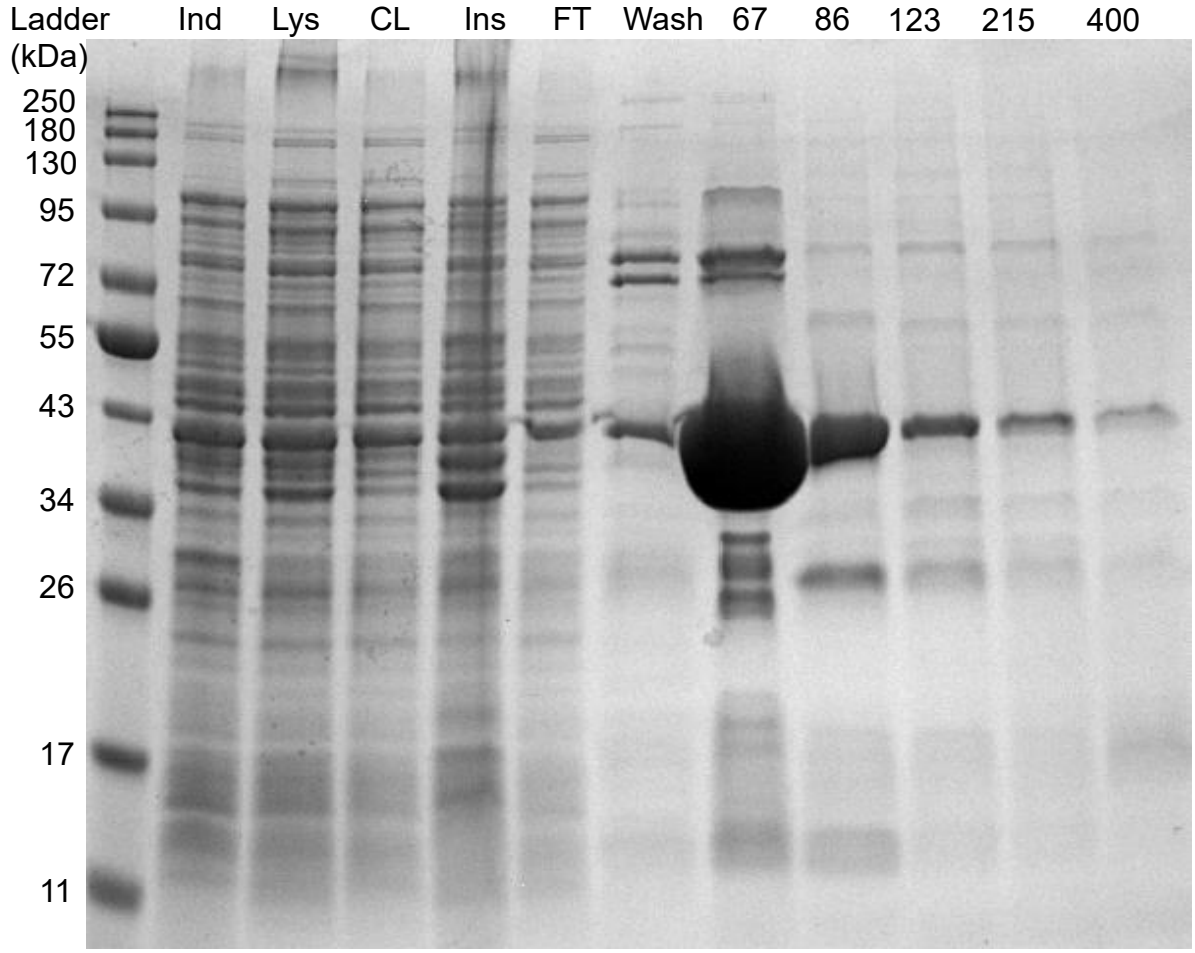


Figure 2.4: SDS-PAGE gel showing the initial purification of MtAroB (39 kDa) using a nickel column. The induced cells (Ind) were lysed (Lys) and then centrifuged, leaving the clarified lysate (CL) and insoluble pellet (Ins). The clarified lysate was loaded onto the Nickel His-column in Buffer A, flow-through (FT) and wash (Wash) fractions were monitored. Then the protein was eluted by increasing the fraction of Buffer B. Values 67 to 400 represent the millimolar amount of imidazole in each elution step.

As the contaminating proteins had clear difference in size, at ~28 and ~72 kDa compared to the 39 kDa MtAroB, size exclusion chromatography was selected. The protein was dialysed to remove imidazole and concentrated prior to loading onto the column. The fractions which contained protein were run on an SDS-PAGE gel to assess which fractions contained MtAroB (Figure 2.5). The two fractions which contained the purest MtAroB protein, D11 and D12, were pooled and concentrated for crystallisation trials. The more impure fractions D10, E1 and E2 were pooled and concentrated for activity assay trials. Both sets of pooled protein were flash frozen for use in later procedures.

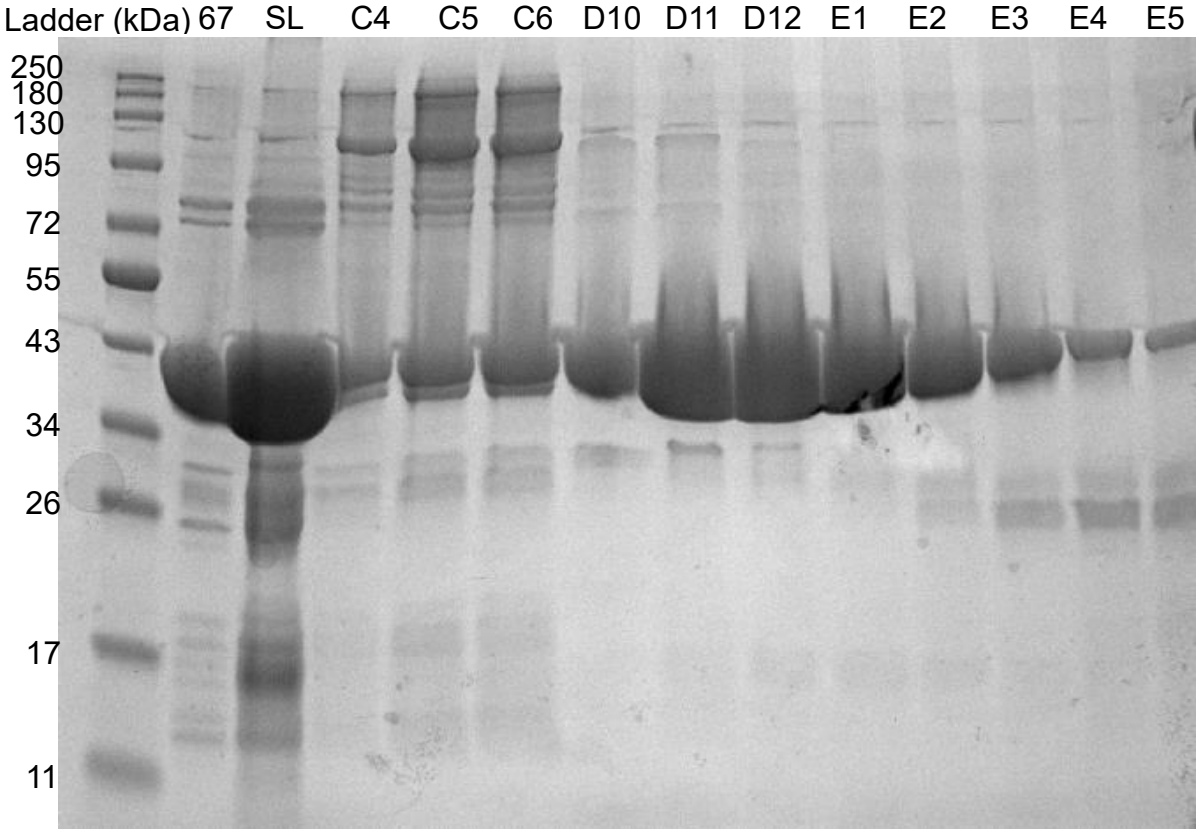


Figure 2.5: SDS-PAGE gel showing the final purification of MtAroB (39 kDa) using a size-exclusion column. The fraction from the nickel column containing MtAroB (67), was concentrated (SL) in Buffer C and then loaded onto the pre-equilibrated Superdex 200 size exclusion column. The eluted fractions (C4 to E5) which contained protein were analysed by SDS-PAGE.

2.2.1.2. MtAroB activity assay

Following the successful purification of the MtAroB protein, an activity assay was developed, allowing quantification of the rate of reaction, and inhibition of the enzyme to be assessed. Several publications had previously described AroB activity assays (Dutra De Mendonça et al., 2007, 2011; Neetu et al., 2020; Zhu et al., 2018). These either focussed on detection of the phosphate ion produced during the reaction, or converted the product, 3-dehydroquinate, into another molecule which could be detected. The phosphate detection was either an endpoint, through addition of malachite green, or continuous detection using 6-mercapto-7-methylguanosine (MESG) (Zhu et al., 2018; Dutra De Mendonça et al., 2007). For this work, the continuous phosphate detection approach was used, as it allowed kinetics to be determined for the enzyme, while using commercially available components. The reaction process is outlined in Figure 2.6 and relies on the conversion of MESG into 6-

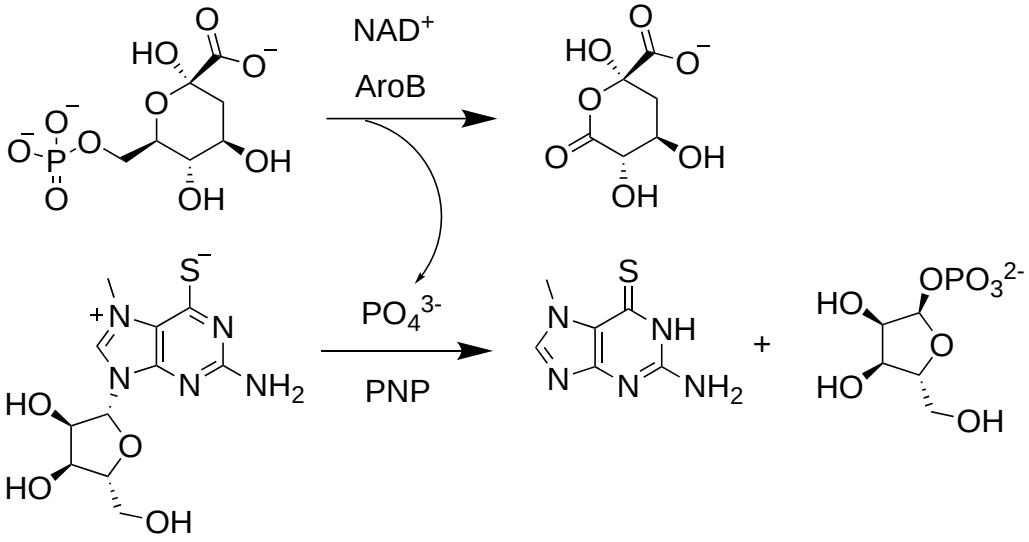


Figure 2.6: MtAroB activity assay reaction scheme. NAD^+ = nicotinamide adenine dinucleotide, PNP = purine nucleoside phosphorylase.

mercapto-7-methylguanine (Webb, 1992) and the different absorbances of these two molecules.

The monitoring of MtAroB activity is dependent on the rapid conversion of MESG into 6-mercapto-7-methylguanine, hence, a trial run was undertaken to assess the amount of PNP required to convert differing amounts of phosphate (Figure 2.7A). In this assay, a large excess of phosphate was added, to monitor the rate of conversion. For 1 U/mL PNP, a non-linear conversion was present when comparing 100 to 500 µM, however, for both 2.5 and 5 U/mL PNP, there was a linear rate of conversion and hence these two concentrations of enzyme could be used in future assays. The addition of 500 µM phosphate was used as a positive control.

The other assay component concentrations were based on previous assays (Dutra De Mendonça et al., 2007). The rate of 6-mercapto-7-methylguanine production was monitored at varying DAHP concentrations to allow enzymatic parameters to be determined (Figure 2.7B). Plotting the enzyme activity against the substrate concentration indicated that the enzyme had non-Michaelis-Menten kinetics (Figure 2.7C). A more sigmoidal curve was present, suggesting cooperativity between two monomers. Further assays were set up to evaluate the effects of varying both the enzyme concentration and co-factor (NAD) on the activity of MtAroB, at 100 µM DAHP (Figure 2.7D,E). This suggested increasing concentrations MtAroB from 0.01 until 1 µg/mL caused a linear increase activity, but above this enzyme concentration other factors limited the rate. For NAD, altering the concentration had no effect on the rate, even when tested at two different enzyme concentrations, suggesting NAD was not a limiting factor at the concentrations tested.

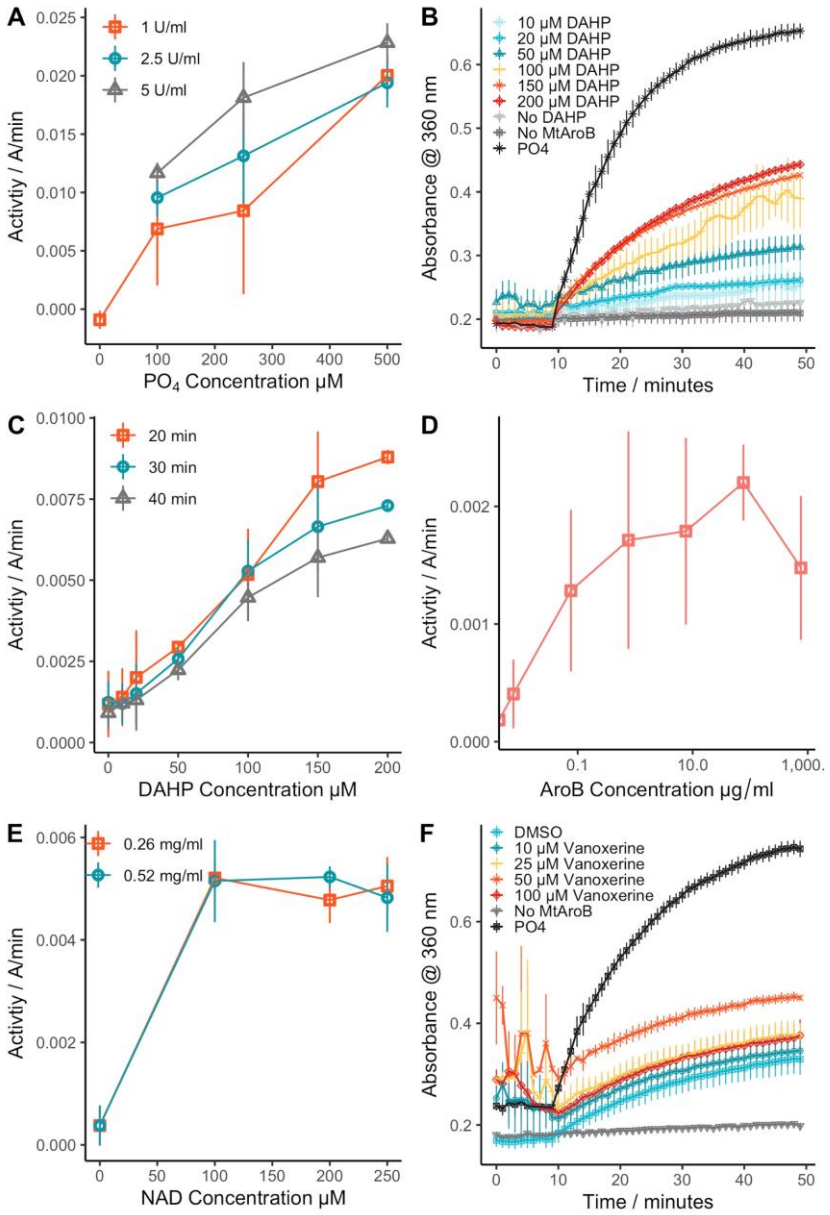


Figure 2.7: The development and testing of the MtAroB activity assay. Component concentrations based on Dutra De Mendonça et al., (2007). **(A) Testing the impact of varying PO_4 and PNP concentrations on MESG turnover.** Legend indicates amounts of PNP, this assay used PO_4, PNP and MESG only. **(B) Standard MtAroB assay, varying DAHP.** Substrate was added at 10-minutes to initiate turnover. **(C) Plot of activity vs substrate concentration.** Legend indicates time window size selected to determine the rate of reaction. Rates calculated from part (B). **(D) Plot of activity vs enzyme concentration.** MtAroB concentration was varied at 100 µM DAHP. **(E) Plot of activity vs NAD concentration.** Legend indicates MtAroB concentration. **(F) 'Inhibition' assay testing varying vanoxerine concentration on enzyme activity.** Vanoxerine was pre-incubated with MtAroB for two-hours prior to addition of substrate, 10-minutes into monitoring. N=3 for all assay runs. PO_4 (500 µM) is used instead of DAHP and MtAroB addition, as a control.

Finally, to study the effect of compound inhibition on the enzyme, vanoxerine was trialled, as it was initially suggested to target the MtAroB protein (Kanvatirth et al., 2019). A range of concentrations were pre-incubated with MtAroB for two-hours, followed by addition of DAHP to initiate the reaction. However, this compound had no impact on the activity of MtAroB and MESG was converted into 6-mercapto-7-methylguanine at a similar rate to the DMSO control (Figure 2.7F). Overall, this assay has verified that the purified MtAroB protein is active and suggests it could be used to study drug inhibition.

2.2.1.3. Fluorimetry on MtAroB

The MtAroB protein has three tryptophan residues in the wild-type protein and hence, the intrinsic tryptophan fluorescence of the protein could be used to monitor binding of compounds. Two of the tryptophan residues were also within loop regions of the protein, allowing them greater flexibility to shift in response to protein conformational changes. To assess the ability of this approach to confirm protein-drug binding interactions, two different assay set-ups were trialled, a low-throughput cuvette-based fluorimetry approach and a more high-throughput plate reader-based approach (Figure 2.8).

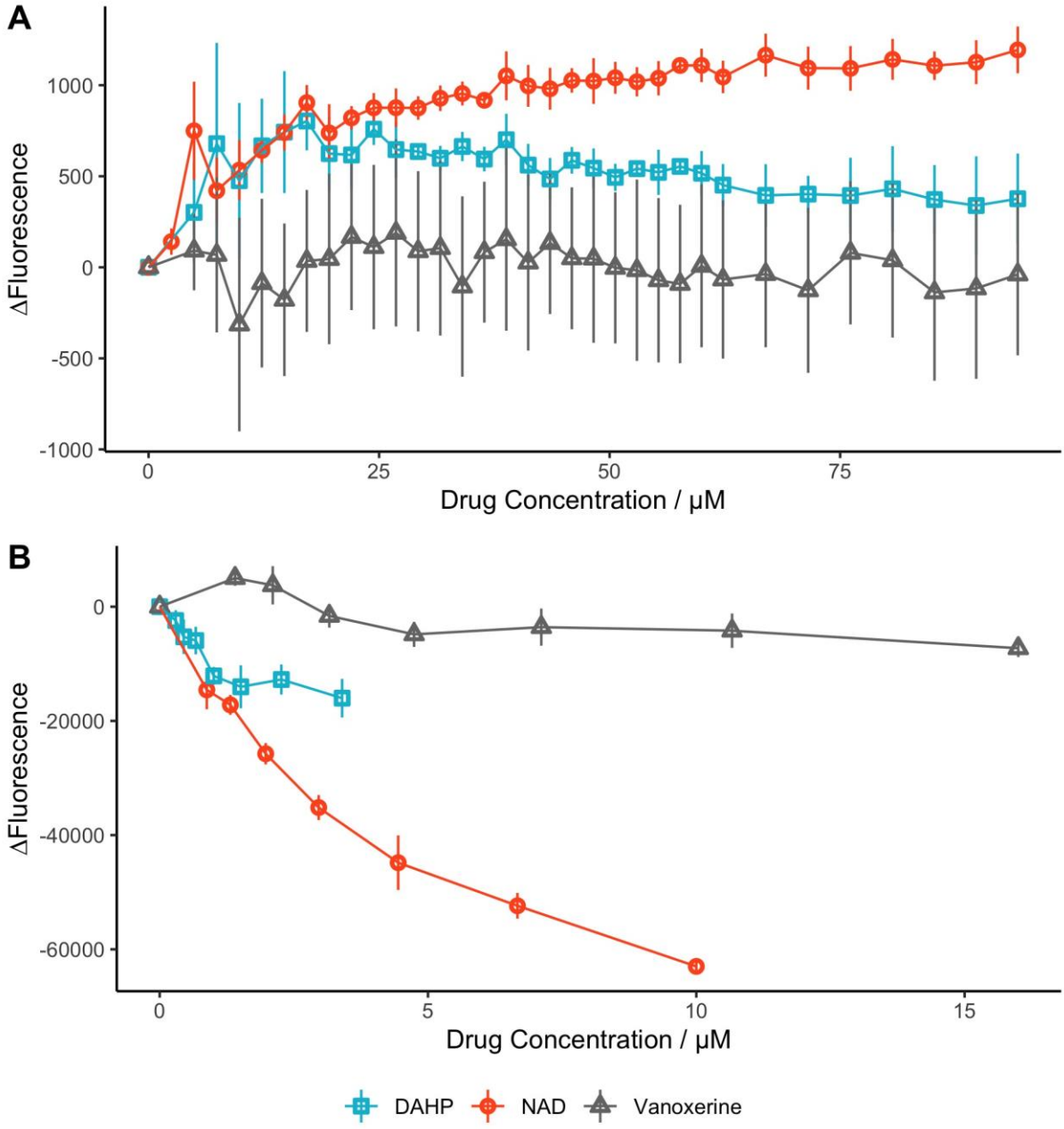


Figure 2.8: Fluorimetry using the tryptophan fluorescence of purified MtAroB protein against increasing compound concentration. (A) Cuvette based fluorimetry. MtAroB protein (35 µg/mL) was added to Buffer C, in a 1 cm quartz cuvette. The tryptophan fluorescence was measured as a baseline (25 ˚C), before compounds of interest were added (1 µL per minute, 1 mM). The fluorescence changes of the solvents (buffer or 10% DMSO) were subtracted. N=2. **(B) Plate reader based fluorimetry.** MtAroB protein (39 µg/mL) in Buffer C was added to a 96-well plate containing varying concentrations of compound (0.3 to 16 µM), differences are due to solubility differences and limitations on the highest allowable DMSO concentration (2%). Incubated for 2-hours and then fluorescence measured. Fluorescence changes in no protein controls were subtracted from each difference. N=3. DAHP (substrate) = 3-deoxy-D-arabinoheptulosonate 7-phosphate, NAD (co-factor) = nicotinamide adenine dinucleotide, Vanoxerine (non-binding). Part (A) adapted from Kingdon et al. (2022).

For the cuvette-based approach, this relied on manual addition of 1 µL of compound every minute and monitoring the tryptophan fluorescence. Rapid changes in the tryptophan fluorescence occurred following addition of either the substrate (DAHP) or the co-factor (NAD), peaking at around 12 µM compound (Figure 2.8A). This could imply saturation of compound binding and hence limited further changes were observed. Overall, NAD may have caused a larger change in fluorescence as this larger molecule could induce a larger shift in protein conformation upon binding, compared to DAHP. NAD can also cause the peak maxima to shift as the concentration increases, which may have led to an exaggerated fluorescence difference, when only comparing fluorescence emission at 340 nm across the experiment. Vanoxerine did not induce a large change in fluorescence, suggesting this assay can discriminate between binding and non-binding compounds. As this approach was very low throughput, it would not allow the testing of large numbers of molecules, in a reasonable timeframe, and hence an alternative assay set-up was explored.

The use of fixed drug concentrations rather than continuous addition, and reliance on pre-incubation of the protein and drug before reading the fluorescence, allowed higher throughput. This also allowed the assay to be undertaken in 96-well plates. The change in fluorescence was thus comparing a DMSO-only control to compound treated samples. The background fluorescence of each drug in buffer on its own was also accounted for during comparison. For this set-up, different concentrations were tested for each compound (DAHP, NAD, vanoxerine), due to differing maximum solubility and DMSO concentration limits within the assay. This assay agreed with the previous approach, showing the largest shift in fluorescence in the presence of NAD, a small shift in fluorescence when DAHP was present, and a limited fluorescence change for

vanoxerine. Hence, this higher throughput approach could be used for monitoring drug-protein interactions and was used to screen compounds later on.

2.2.1.4. Differential scanning fluorimetry (DSF) to assess compound binding

A complementary approach to using tryptophan fluorescence to study compound binding, is to use the SYPRO Orange dye to study protein melting temperature in the presence or absence of compound. The dye binds and fluoresces in hydrophobic environments, such as the residues exposed by protein unfolding. If the binding of a compound stabilises a protein, then this may cause its melting temperature to increase and hence the induction of dye fluorescence will be at a higher temperature.

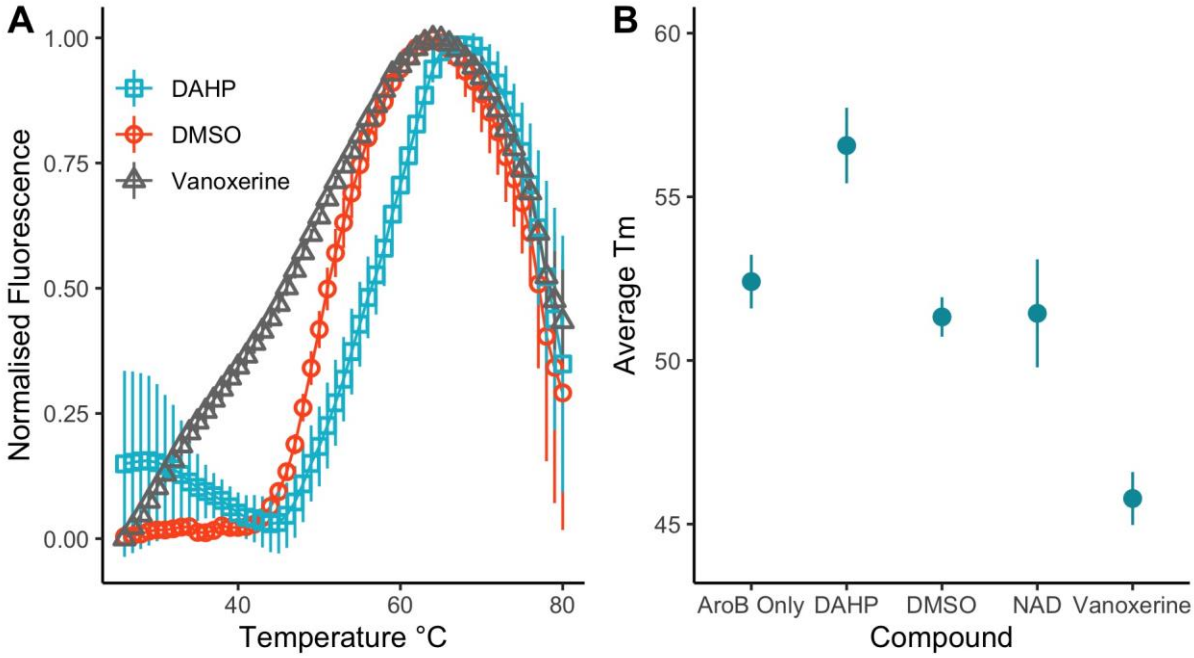


Figure 2.9: Differential scanning fluorimetry of MtAroB with DMSO, DAHP, NAD and vanoxerine. (A) Normalised Fluorescence melting temperature curve. (B) Average melting temperatures in the presence of compounds. MtAroB was incubated with compounds for 30-minutes prior to SYPRO orange addition and immediately added into the qPCR machine. The Tm is the temperature corresponding to 0.5 normalised fluorescence. Tm = melting temperature. N=4

The melting temperature curves of MtAroB in the presence of either DMSO, DAHP or vanoxerine are shown in Figure 2.9A. The average melting temperature (Tm) in the presence of DMSO was 51.3 ˚C, with the presence of DAHP causing a shift to a higher temperature and vanoxerine causing a shift to a lower temperature. However, the SYPRO orange dye had elevated fluorescence in the presence of vanoxerine, even at lower temperature, which could suggest the lipophilic compound is inducing this fluorescence in the absence of protein unfolding. Vanoxerine was previously found to induce fluorescence of 1,6-diphenyl-1,3,5-hexatriene, another compound which fluoresces within hydrophobic environments (Appendix 2); hence, it is unlikely vanoxerine is disrupting the protein structure and more likely is interfering with the assay.

Focussing on all the control compounds tested (Figure 2.9B), both DMSO and NAD caused a limited shift in Tm relative to the MtAroB protein in buffer. Then as previously indicated, DAHP stabilised the protein and increased the Tm from 52.4 to 56.5 ˚C. The lack of stabilisation by NAD could be due to its binding site on the surface of the protein, compared to DAHP's binding site in the centre of the protein. Overall, this data validates the use of DSF to assess compound binding, however, it may be limited to detecting compounds which bind in the substrate binding site, in preference to the NAD binding site.

2.2.1.5. Protein crystallography and crystal structure

Although two crystal structures of the *M. tuberculosis* AroB protein have previously been solved, the ability to confirm drug-protein interactions via crystallography would be of great benefit to the project. Hence, crystallography was attempted on the purified

MtAroB protein. If any potential binding compounds were found, similar conditions may allow co-crystallisation or soaking of the original crystals with novel compounds.

The crystallisation conditions used for the previously solved crystals were tested (0.8 M sodium formate, 20% polyethylene glycol (PEG) 2,000 MME, 0.1 M Tris pH 7.5), however, they used a hanging drop method compared to the sitting drop method used herein. No crystals formed under these sitting drop conditions, which may be due to the alternate tray set-up. As this could not be used, an unbiassed screening approach was undertaken.

A JCSG-plus screen was set-up with the MtAroB protein, to screen for other potential crystallisation conditions. This identified several conditions which induced crystal formation, from the 96 tested. Half of the conditions (nine wells) in which crystals formed contained PEG 3,350 (20% w/v), with the remaining conditions being more varied. The conditions were either unbuffered or buffered between pH 6.5-7.5. There was limited consensus amongst salts. The MIDAS-plus screen was also trialled, however, this only led to small crystals forming in a few wells. Hence, the JCSG-plus conditions were taken forward for further examination.

Two conditions were selected to send crystals for X-ray diffraction, 0.2 M magnesium chloride hexahydrate, 0.1 M sodium HEPES, pH 7.5, 30% (v/v) PEG 400 and 0.1 potassium thiocyanate, 30% (w/v) PEG 2,000 MME. Both crystals produced X-ray diffraction corresponding to the MtAroB protein, however, the former condition produced a lower resolution structure at 2.6 Å. The crystal structure was solved from the X-ray diffraction data via molecular replacement using the 3QBE crystal structure of MtAroB, followed by refinement to improve the fit with the experimental data (Figure 2.10, Appendix 3 - Table A2.1).

Renderings of the MtAroB crystal structure are displayed, showing the front and top view of the protein, with the protein's active site zinc ion shown at the centre (Figure 2.10A,B). The electrostatic charges present within the protein are displayed on the

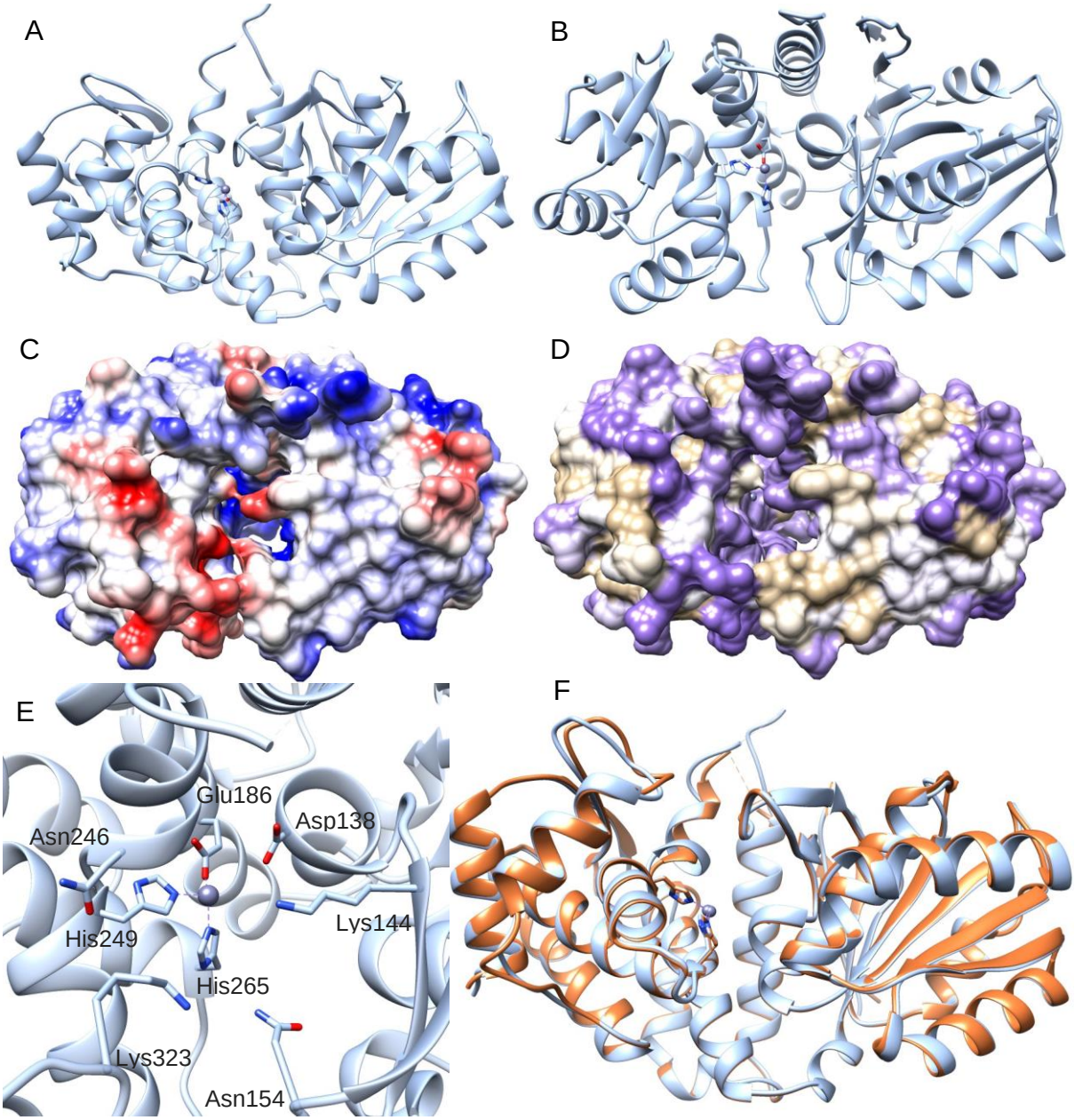


Figure 2.10: Structure of MtAroB crystallised within this work. (A) Front view of MtAroB protein, with active site in the centre. (B) Top view of MtAroB protein. (C) Surface highlighting positively charge (red) and negatively charged (blue) residues. (D) Surface view highlighting hydrophobic (tan) and hydrophilic (purple) residues. (E) Details of MtAroB active site, highlighting residues involved in enzymatic activity. (F) Comparison of MtAroB (light blue) with known crystal structure (3QBE, orange).

surface suggesting the active site surrounding the zinc ion and the NAD binding site is negatively charged, while residues at the top of the active site are positively charged (Figure 2.10C). The majority of the surface exposed residues are hydrophilic, including those present in and around the active site (Figure 2.10D), which allows the hydrophilic substrate to bind effectively. Focussing on the active site residues, this crystal structure shows the same zinc coordination as the previously solved structures (Figure 2.10E). This also highlights the positively charged residues at the top of the active site are Lys144 and Lys323.

Finally, the crystal structure solved within this work was compared with the previously solved structure. A structural comparison of the ribbon structure is shown in Figure 2.10F, highlighting a majority of the core region is structurally similar, with some deviations in the loop regions. The RMSD was 0.581 Å across all 352 α-carbon atoms and 0.315 Å across 342 pruned atom pairs. The crystal structure was also similar to the 3QBD structure, with an RMSD of 0.554 Å across 344 pairs of α-carbon atoms. The apo-structure also has space in the active site and does not appear to undergo large structural changes upon binding, hence, this may allow soaking of compounds into protein crystals to assess binding.

2.2.1.6. MD simulations of AroB protein

To gain a greater understanding of the MtAroB protein, molecular dynamic (MD) simulations were performed, which can highlight both the flexibility of proteins and generate a range of conformations for down-stream analysis. Both previously solved MtAroB crystal structures were very similar, with an RMSD of 0.65 Å, suggesting the bound co-factor NAD may not cause large structural changes. The apo-protein crystal

structure (3QBE) was chosen for MD simulations, as it was a more complete structure, with an extra seven amino acids and the catalytic Zn^{2+} ion was present in the active site.

To analyse the flexibility of the MtAroB protein, an initial run of fifty nanoseconds of classical MD (cMD) simulation was undertaken. The root-mean-square-deviation (RMSD) of the α-carbon atoms can be compared across the MD trajectory to assess the progress of the simulation. For the cMD simulation, there was an initial shift in the protein conformation of one angstrom (Figure 2.11). This then stabilised to fluctuate around 1.5 Å for the remainder of the 50 ns. This suggested the protein had entered a local energy minimum, close to the input crystal structure.

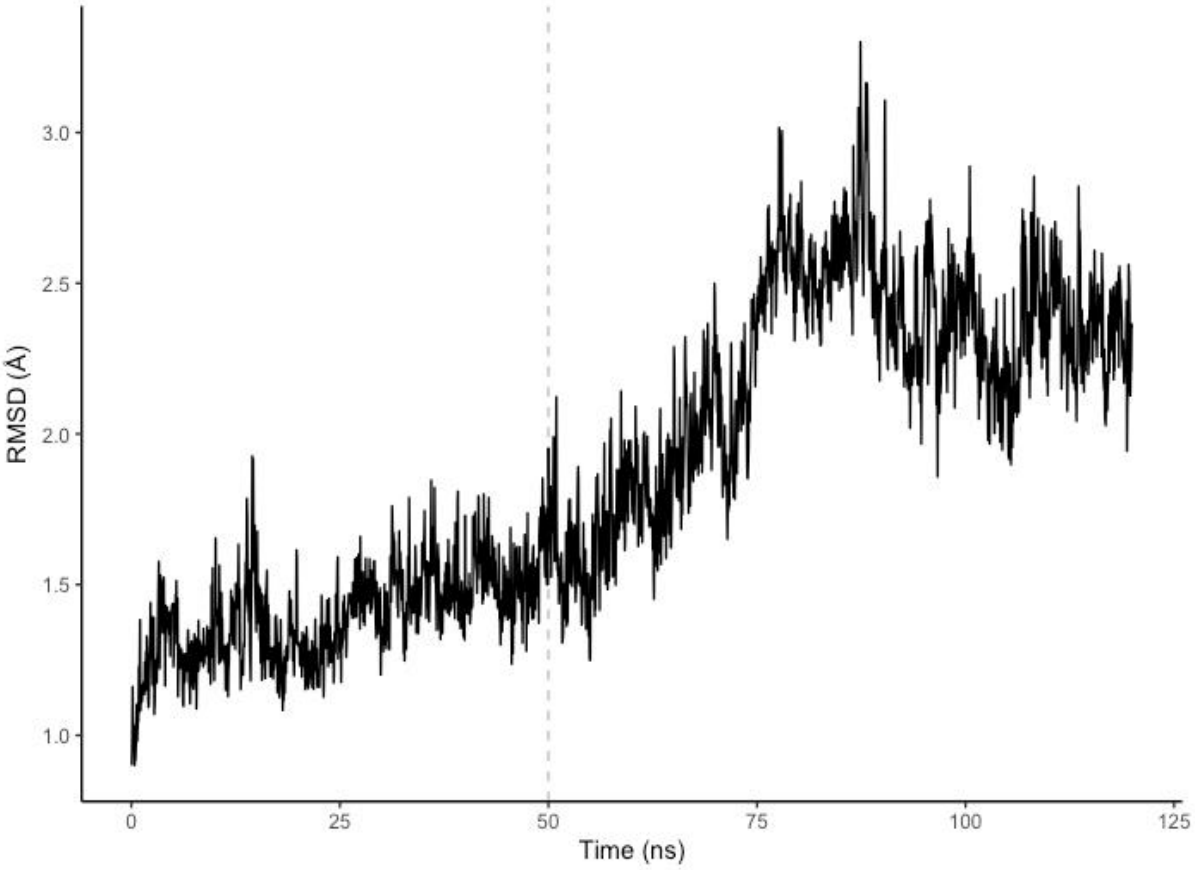


Figure 2.11: RMSD of MtAroB α-carbons across 120-nanosecond of MD simulation. The first 50-nanoseconds were cMD and the latter 70-nanoseconds were aMD, split by the dashed line.

To evaluate whether the energy minima was local or global, a seventy-nanosecond accelerated MD (aMD) simulation was performed (Figure 2.11). Specifically, the dihedral potential was boosted, using parameters calculated from the cMD trajectory. This had a clear effect on the RMSD, increasing the fluctuation from ~1.5 Å to between 2.5 and 3.0 Å, relative to the input structure. Hence, the aMD simulation allowed greater conformational space to be explored by the protein. The protein continued to fluctuate around 2.4 Å away from the input structure, for the final 20 ns of the simulation, suggesting another energy minima was reached.

While the global RMSD change over time gives an indication of the total space being explored by the protein, it does not indicate which residues are contributing towards these values. Therefore, the root-mean-square-fluctuation (RSMF) can be calculated as an equivalent of RMSD on a per atom basis. This measures the fluctuation of the α-carbon of each of the protein's residues over the timeframe of the simulation. This is used to identify flexible regions of the protein which may be important for compounds or co-factor binding.

The RMSF values for all residues can be projected onto the MtAroB crystal structure to allow the flexible regions to be identified, Figure 2.12. The RMSF values indicated that the main flexible loop regions were: 145-159, 235-241, 259-264 and 322-330. These regions all form part of the edge of the MtAroB active site and contain or are adjacent to catalytically important residues, including: Lys144, Asn154, Asn246, His249, and Lys323 (Zhu et al., 2018). Lys323 is especially flexible, with RSMFs of 6.8 and 11.0 Å for cMD and aMD respectively. The other residues displayed a range of RMSF values between 0.8 to 2.7 Å during cMD, and between 1.9 to 3.7 Å during AMD.

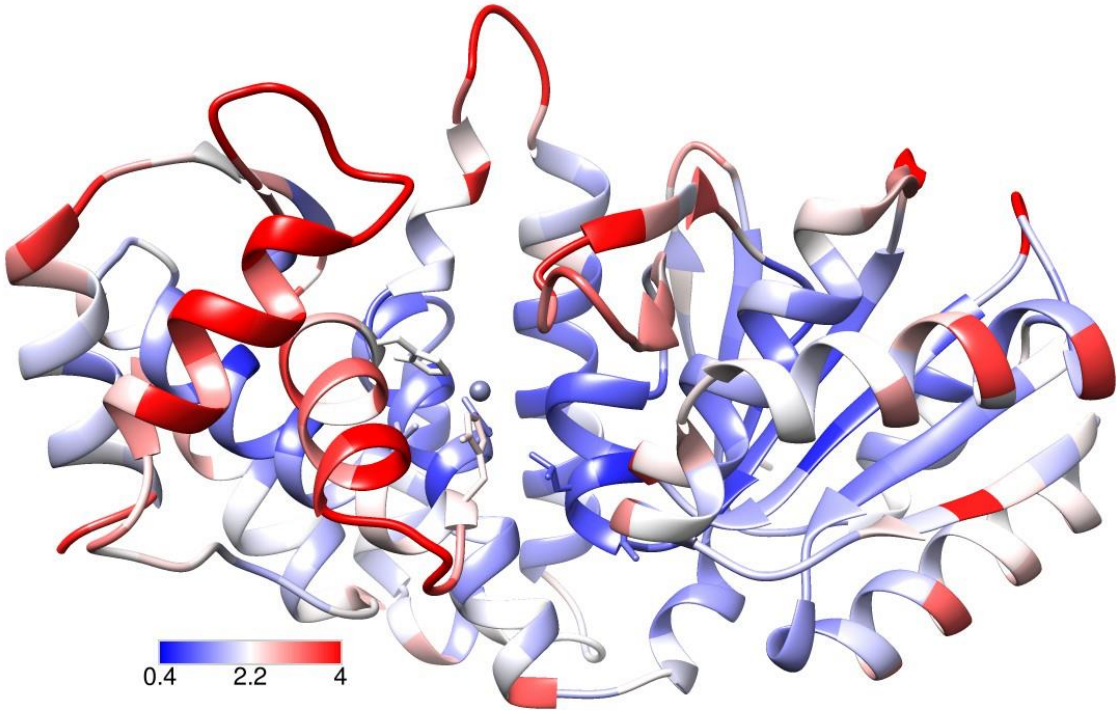


Figure 2.12: RMSF of each backbone α-carbon atom, following MD simulation for 120 ns, projected onto each residue of MtAroB protein. Used PDB=3QBE. Colour scale is between 0.4 to 4 Å. All RMSF values > 4 Å are shown in the same colour. The active site zinc is shown at the centre.

As the MtAroB protein has a catalytic zinc ion coordinated in the protein active site, this ion and its binding residues were investigated over the course of the simulation. For comparison, the coordination present in the MtAroB crystal structure is shown, Figure 2.13A. It indicates coordination through three monodentate residues, two histidine residues and one glutamine. During the cMD simulation, the coordination of the zinc changed almost immediately, Figure 2.13B. Two of the three coordinating residues remain consistent, but with a switch from His265 to Asp138. The distance between the displayed coordination and the ideal metal coordination geometry can also be compared. The crystal structure's coordination geometry has RMSD values of 0.186, 0.206 and 0.239 Å away from the ideal octahedral, tetrahedral, and trigonal bipyramidal coordination geometries. Whereas the cMD simulated structure has RMSD values of 0.033, 0.601 and 0.033 Å away from the ideal octahedral, tetrahedral,

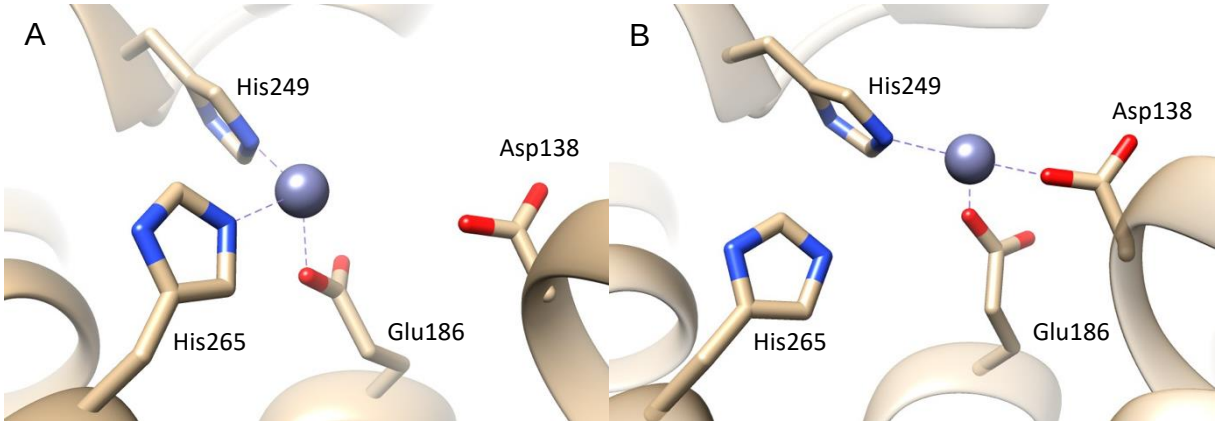


Figure 2.13: Coordination of the active site zinc ion in MtAroB. (A) Coordination of zinc from the crystal structure PDB=3QBE. (B) Coordination of zinc ion in an averaged structure representing the cMD simulation.

and trigonal bipyramidal coordination geometries. This indicates a simulated switch from limited metal geometry preference to a strong preference for octahedral or trigonal bipyramidal coordination. This could be enforced by the MD simulation forcefields, rather than suggesting this altered zinc binding coordination occurs *in vitro*.

2.2.1.7. Clustering of MD MtAroB simulations

As the MD simulation contained 60,000 timesteps (trajectory frame), each containing a slightly different protein conformation, it is unreasonable to examine every timestep. Initially during processing, only every fifth timestep was kept, leaving 12,000 protein conformations. One analysis approach is to examine the conformational space covered, by clustering the protein's conformations based on similarity. A representative or average structure for each cluster can then be used for further analysis or to form an ensemble of protein conformations for docking.

The clustering is normally based on the RMSD values between conformations. A user-specified cut-off value or computational algorithm will dictate which conformations cluster together. A number of programmes exist, two examples include, Chimera's ensemble clustering, which applies an algorithm to an RMSD matrix (Kelley, Gardner

and Sutcliffe, 1996; Pettersen et al., 2004) and GROMACS g_cluster, which requires a user specified cut-off value (Abraham et al., 2015). The former approach suffers from using a hierarchical based algorithm, which favours homogeneous cluster sizes; while the latter approach provides more control over the clusters produced; but could miss 'true' clusters by using an arbitrary cut-off value (Shao et al., 2007).

For this work, the g_cluster method was chosen, as it provided the greatest flexibility for cluster size determination. Several clustering methods can be implemented within g_cluster, however, the gromos algorithm (Daura et al., 1999) has been utilised in several studies (Bhutani et al., 2015; Motta et al., 2018; Motta and Bonati, 2017; Kappel, Miao and Mccammon, 2017; Brigo et al., 2005) and was recently adapted into a stand-alone binary programme, BitClust (González-Alemán et al., 2020). Hence, it was used within this work. The gromos algorithm is a bottom-up algorithm, which clusters trajectory frames based on RMSD similarity, grouping the maximum number of structures within a RMSD cut-off value.

The two MD trajectories performed on the MtAroB protein, cMD and aMD were both individually clustered, as well as the total MD trajectory. A range of different cut-off values were tested for each trajectory, to balance the total number of clusters, number of clusters with one member, and number of clusters which represent a majority of the overall trajectory. For the cMD trajectory, a cut-off of 1.0 Å was chosen, leading to the top five clusters representing 70% of the total trajectory. Both the aMD and the total MD trajectories had greater variability, hence the less stringent cut-off value of 1.35 Å was chosen. For the aMD trajectory, the top eight clusters represented 70% of the variation, while for the total MD trajectory, the top ten clusters represented 90% of total variation. To compare within each set of clusters, the most and least similar clusters

were compared for RMSD differences, for cMD this was 0.43 and 1.13 Å, for aMD this was 1.04 and 2.06 Å and for the total MD this was 0.68 and 2.27 Å. The top five clusters from each individual MD type and the top ten clusters over the MD trajectory were taken forward for further analysis.

From the selected clusters, average structures were generated, to allow comparisons of the RMSD and perform principal component analysis (PCA). Using Bio3d, the RMSD differences between each structure's 'core' region were compared, producing a dendrogram highlighting structures similarities, Figure 2.14A. The average structures from the cMD simulation clustered together, alongside the first structure from the total MD simulation. The top five aMD structures group in a pairwise manner to structures two to six from the total MD simulation and appear to be nearly identical in this 'core' protein region (Figure 2.14A). The remaining structures from the total MD simulation appear to represent deviations from other structures rather than completely new conformations.

PCA was also performed on the twenty average structure. PCA tries to reduce the complexity of protein structural differences by calculating principal components axes that represent maximal differences between protein structures. Then each protein conformation is assigned an eigenvalue per axes, based on its similarity to either extreme. The PCA is displayed in Figure 2.14B-E, only fifteen points are visible, as clusters a1-a5 overlap with t2-t6. The top three PCA axes were used to differentiation the clusters (Figure 2.14B-D). They account for approximately 83% of the total variability between the twenty structures (Figure 2.14E). Principal component (PC) one appears to be mirror the dendrogram (Figure 2.14A,B), suggesting it is splitting by RMSD.

Overall, this data provides information on the diversity present in the identified clusters and whether similar clusters have been found. This indicated there is an overlap between the clusters from aMD clusters and overall full MD clustering, which is not surprising as the cut-off values used were identical. Due to this overlap, the average structures based on clustering of the total MD simulation will be used in preference to the clusters based on the aMD simulation. It also highlighted that some structural diversity was lost during clustering of the total MD compared to cMD clustering. This is indicated by the separate grouping of clusters c2 and c3 from any t-clusters (Figure 2.14A). Cluster c2 is also separated from the other cMD clusters by PC2. Hence, all ten clusters from the total MD simulation and cluster c2 will be used for dynamic docking against MtAroB, section 2.2.2.2.

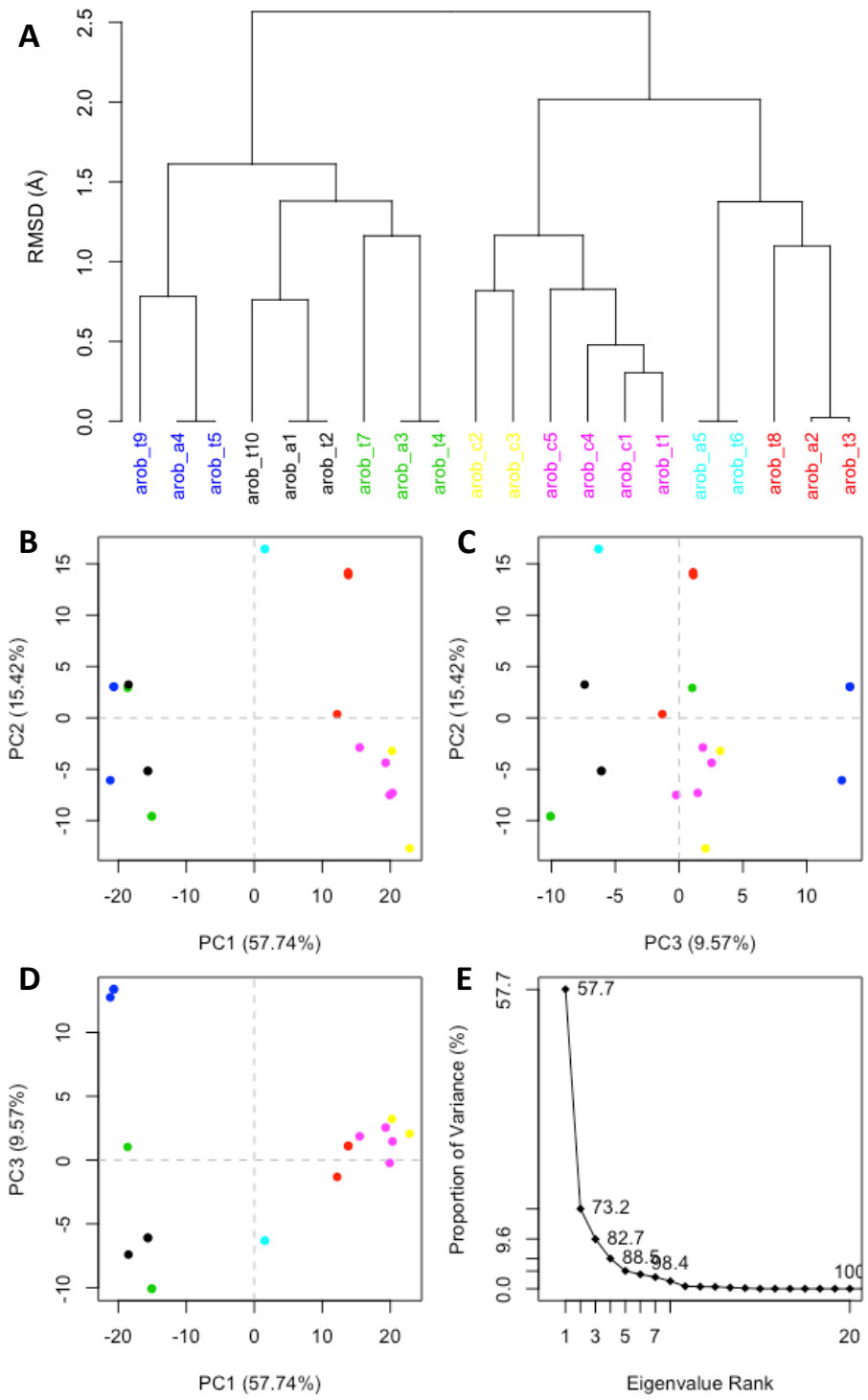


Figure 2.14: Comparison of the twenty MtAroB trajectory clusters by RMSD and principal component analysis. (A) RMSD cluster dendrogram generated by g_cluster gromos. All labels are arob_?#, where ? is either a=aMD, c=cMD or t=total MD, and # is the cluster number. **(B-E) Principal component analysis, displaying pairwise comparisons of the top three principal component axes (B,C,D) and overall proportion of variance explained by increasing principal component axes (E).** Groups of clusters were coloured by RMSD similarity, highlighting the most similar conformations across the dendrogram and PCA.

2.2.1.8. Principal component analysis (PCA) on MD simulation trajectories

Rather than clustering the trajectory and then performing PCA on the averaged structured, the PCA can be performed on the MD trajectory itself. Representative structures can then be generated, corresponding to different points along each PC axis, for downstream analysis. Use of PCA to evaluate MD trajectories may be superior to clustering analysis (Rajan, Freddolino and Schulten, 2010), but will be compared to the above clustering within this work.

First, all trajectory frames from the total MD simulation were superimposed based on the protein atom coordinates of the input crystal structure, excluding hydrogen atoms. This superimposition prevents rotational and translational movements from affecting the downstream analysis. Then PCA was performed on all the non-hydrogen protein atoms and the top three PC axes distributions are displayed, Figure 2.15A-D. As this approach assessed all protein conformations found during the MD simulation, there was greater variability compared to the PCA following clustering (Figure 2.15D). The top three PC axes accounted for only 42.7% of the total variance, compared to 82.7% in the clustering approach. PC1 appears to represent the continuous divergence of the protein's structure from the initial crystal structure (Figure 2.15A). Whereas PC2 and PC3 are not dependent on the timeframe within the trajectory and do not appear to directly represent a particular physical change. In all cases, the latter half of the trajectory (the red points) appears to have a greater variability for all three PCs.

For downstream use, representative structures were required corresponding to each of the top four PC axes. As each consecutive PC axis represented less variability, less structures were generated. Structures were generated to represent the two extreme eigenvalues for each PC axis, and intermediate transitionary structures were also

generated. Four structures total were generated for PC1, three for PC2 and two for PC3 and PC4. Hence, eleven structures were taken forward.

To allow comparison between the structures generated from cluster analysis and PCA, an RMSD dendrogram was produced (Figure 2.15E). The original MtAroB crystal structure was included for comparison. The PCA generate structures were more similar than the clustering derived structure. This result was expected, as the PCA structures represent deviation from a common average and hence will be more similar overall. The PCA common average structure is indicated by arob_pc1_1 and arob_pc2_1, which are the same. The original crystal structure was most similar to the arob_c2 and arob_t1 average structures, suggesting only a small deviation.

While the PCA generated structures displayed smaller RMSD variations compared to the clustering generated structures, all structures will be taken forward for dynamic docking, except arob_pc2_1 as it was identical to arob_pc1_1. Ensemble docking to both sets of structures will take into account the former having specific regions of variation away from a common structure, compared to the latter's higher variability.

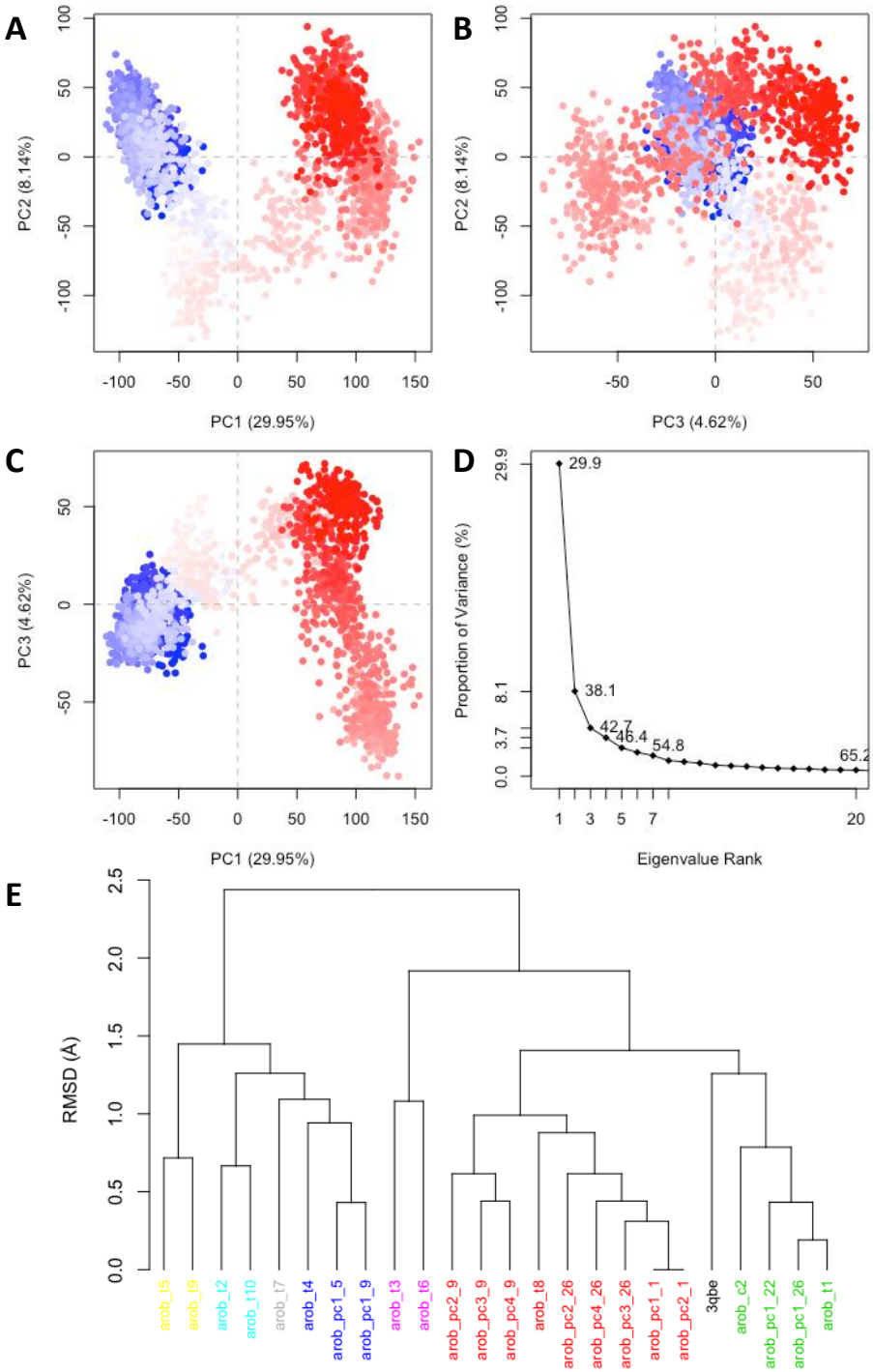


Figure 2.15: MtAroB total trajectory evaluation by principal component analysis and final splitting into clusters. (A-C) Pairwise comparisons of PC axes are displayed, sorting trajectory frames by eigenvalues. Blue to red colouration represents the start to end of the MD trajectory. **(D) Overall proportion of variance explained by increasing principal component axes. (E) RMSD cluster dendrogram.** Displays similarities between the MtAroB conformations generated by either clustering or PCA. The original protein crystal structure 3QBE is included for reference.

2.2.1.9. CRISPR-interference of AroB in *M. smegmatis*

As a contrasting approach to the computational studies of MtAroB, an *in vivo* study was undertaken to reduce the levels of AroB within *M. smegmatis*. A clustered regularly interspaced short palindromic repeats interference (CRISPRi) approach was selected, as it allowed anhydrotetracycline (ATc) dependent reductions in the level of transcription. This strategy relied on a two-plasmid system, pRH2502, containing a mutated *cas9* gene and pRH2521, which could be edited to specify the guide RNA sequences required to target each gene, developed by (Singh et al., 2016). This would allow compound testing for AroB target engagement *in vivo*. If the level of the AroB protein was reduced, in theory, a lower concentration of drug would be able to kill the cell. Hence, this would provide another tool for confirming AroB was the true target of any identified drug compound.

For the *aroB* gene, three different guide RNAs were tested in *M. smegmatis*. The guide RNAs were selected as twenty-nucleotide sequences following the 'CCX' motif within the first third of the gene. This would give the greatest possibility that a stalled Cas9 protein would block transcription. In addition, a BLAST search was performed on every twenty-nucleotide sequence to determine its similarity to other sequences within the *M. smegmatis* genome, to reduce off-target effects. The three selected guide RNA sequences only had 100% matches with 13 or 14-nucleotide length sequences within the genome or matches containing gaps of length 15 or 16-nucleotides. This suggests off-target binding and inhibition would be unlikely to occur during downstream experimentation. Each twenty-nucleotide sequence was synthesised and cloned into the pRH2521 plasmid and correct sequence insertion confirmed by sequencing.

Following transformation of the two-plasmid system into *M. smegmatis*, colonies were selected for each guide RNA and tested for growth. If the selected guide RNA was successful in knocking-down the translation of the essential AroB gene, we would expect a reduction or elimination in growth. This reduction in growth would be dependent on addition of ATc. The start and endpoints of the growth curves are shown in Table 2.1. The only *aroB* targeting guide RNA which showed a difference upon ATc addition was *arob+37*, however, this only occurred in one of the two tested colonies. The unedited control plasmid 21-02 also had a small reduction in growth during ATc addition, which is unexpected. As this growth curve was undertaken in a 96-well plate, the small well volume may have impacted the growth of strains or monitoring of the OD_{600}.

Table 2.1: *M. smegmatis* CRISPRi strains targeting AroB growth curve start and endpoints, in the presence or absence of ATc. Timepoints at 0 and 24-hours. N=3. Strains _1,_2 and _3 are different colonies transformed with the same guide RNAs.

Strain	**Growth Curve start and endpoints / OD_{600}**			
M. smegmatis	No ATc		+ ATc	
	Start	Endpoint	Start	Endpoint
21-02_1	0.02 ± 0.014	0.357 ± 0.079	0.02 ± 0.023	0.194 ± 0.067
21-02_2	0.032 ± 0.001	0.389 ± 0.063	0.018 ± 0.009	0.37 ± 0.239
21_02_3	0.029 ± 0.004	0.35 ± 0.22	0.027 ± 0.029	0.202 ± 0.213
aroB+37_1	0.04 ± 0.01	0.26 ± 0.025	0.031 ± 0.003	0.443 ± 0.251
aroB+37_2	0.022 ± 0.023	0.414 ± 0.154	0.029 ± 0.016	0.279 ± 0.055
aroB+137_1	0.016 ± 0.022	0.263 ± 0.09	0.024 ± 0.021	0.684 ± 0.628
aroB+137_2	0.006 ± 0.017	0.569 ± 0.191	0.013 ± 0.03	0.514 ± 0.077
aroB+137_3	0.027 ± 0.017	0.637 ± 0.378	0.031 ± 0.024	0.742 ± 0.111
aroB+269_1	0.038 ± 0.076	0.192 ± 0.336	0.021 ± 0.04	0.913 ± 0.176
aroB+269_2	0.026 ± 0.02	0.578 ± 0.184	0.033 ± 0.019	0.7 ± 0.281
aroB+269_3	0.03 ± 0.026	0.675 ± 0.211	0.022 ± 0.021	1.136 ± 0.404

This set of experiments was also undertaken within *M. bovis* BCG, using alternate guide RNAs for the AroB gene, however, no difference in the growth was observed in the presence of ATc. As there were also no differences in the growth of *M. smegmatis*, following induction of the CRISPRi system, this suggested two potential explanations. Either the guide RNAs selected were not effectively binding the target gene, or the level of the AroB protein is not affected by short-term transcriptional down-regulation. Unfortunately, time did not permit analysis of mRNA levels within the cells, to determine if these guide RNAs were having an impact on transcription.

2.2.1.10. Generating mutants of MtAroB

To investigate the important catalytic residues used by the MtAroB protein, site directed mutagenesis was undertaken. The targeted residues were selected, based on previously reported catalytically essential residues or the MD simulations performed. The six selected residues are displayed on the MtAroB crystal structure, Figure 2.16, and were Arg97, Arg122, Asp138, His249, His265 and Lys323. All residues were mutated to encode alanine, which would remove any catalytic side chains without introducing large or charged groups, more likely to interfere with the protein's structure. Alterations of the His249 and Lys323 residues into alanine was based on previous studies, which showed loss of activity following mutation and could be used as a control (Zhu et al., 2018). Residues Asp138 and His265 were chosen following the MD simulations prediction of two alternative zinc coordination geometries, with each residue being the unique component of each conformation. Finally, residues Arg97 and Arg122 are predicted to be at the dimer interface of the protein and hence may allow evaluation of the sigmoidal activity curve displayed in Figure 2.7C. Residue

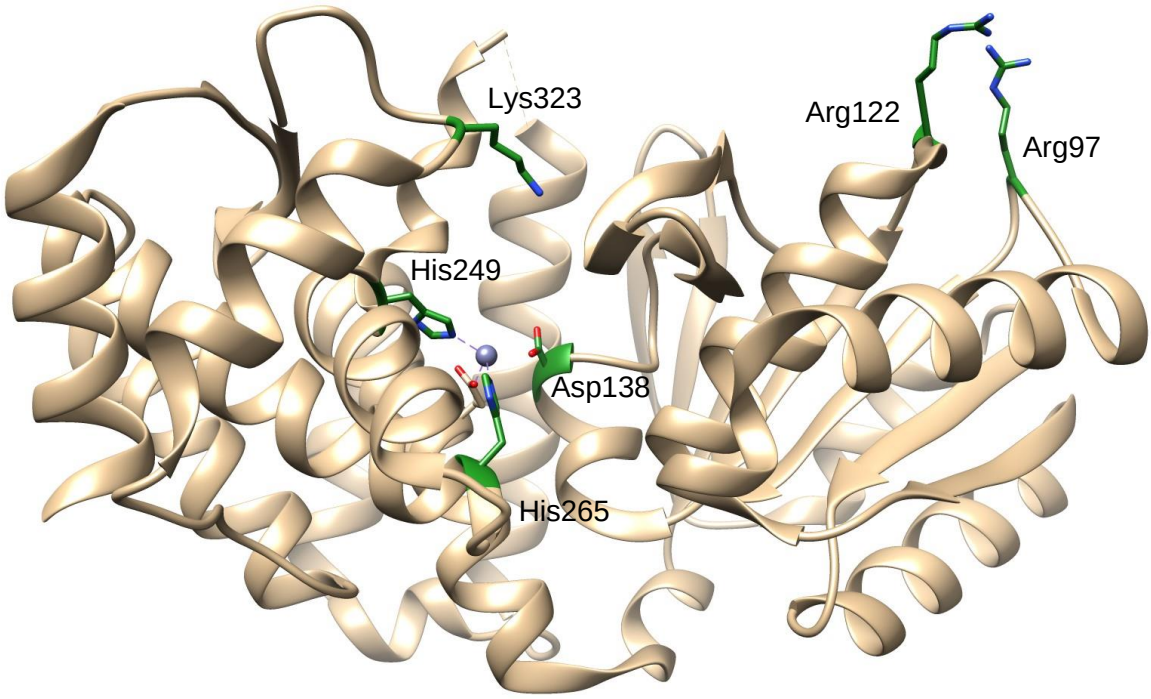


Figure 2.16: MtAroB structure with residues selected for mutation highlighted. PDB=3QBE. Six residues coloured in green and labelled.

Arg122 is equivalent to the *A. nidulans* AroB residue Arg130, which was shown to form part of the active site in the other dimer (Carpenter et al., 1998).

Site directed mutagenesis was performed on the pET28a-MtAroB plasmid to mutate each codon to the closest alanine codon sequence, with the majority changed to GCC, as the most frequently used mycobacterial alanine codon (Nakamura, Gojobori and Ikemura, 2000). All mutations were confirmed by sequencing the *aroB* gene and the vectors then transformed into *E. coli* BL21 (DE3) cells for protein expression.

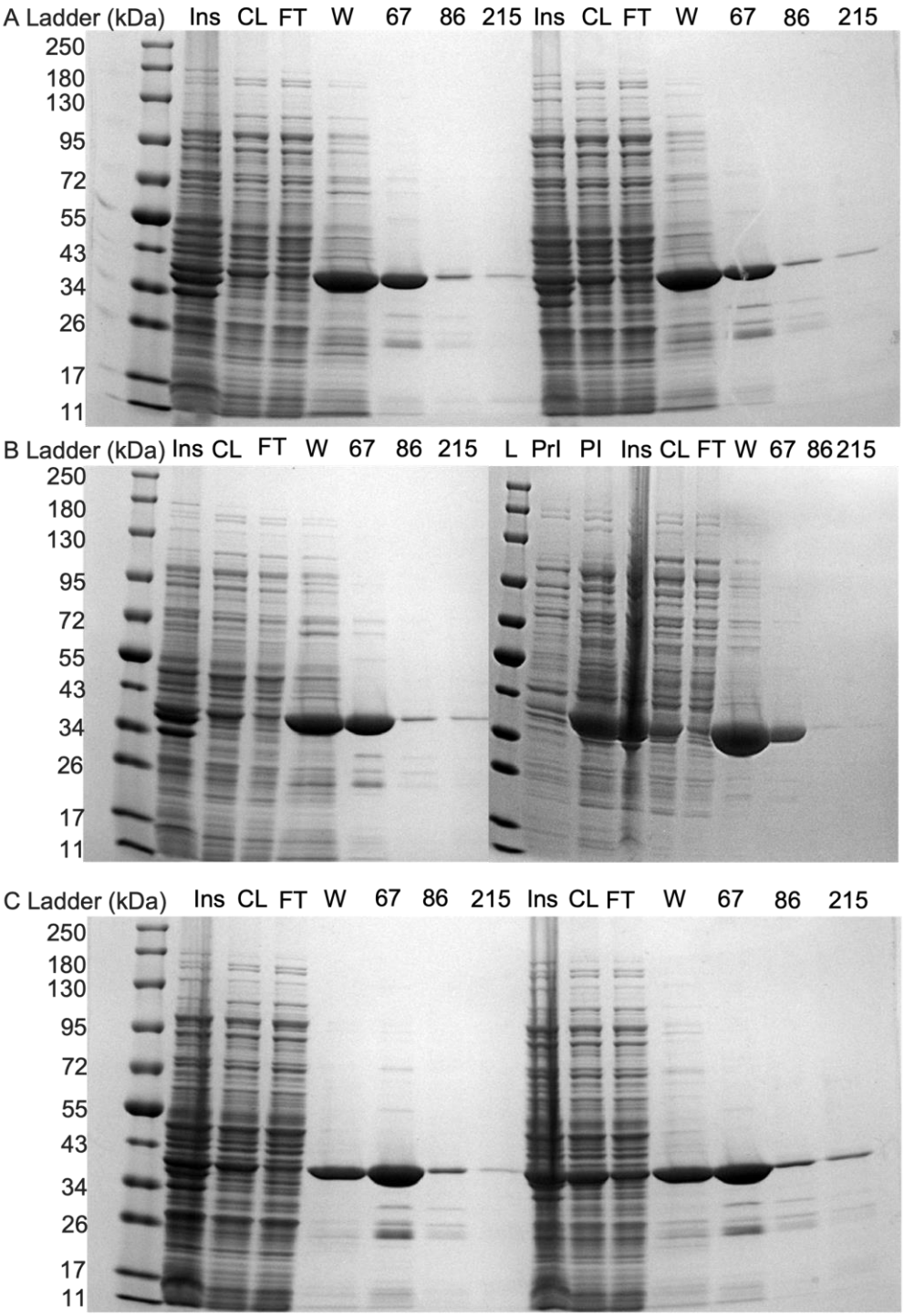


Figure 2.17: SDS-PAGE gels showing the purification of mutant versions of MtAroB, using nickel resin. In all cases, the induced cells (PI) were lysed and centrifuged, leaving the clarified lysate (CL) and insoluble (Ins) fractions. The clarified lysate was loaded onto a nickel resin, monitoring the flow-through (FT) and washed with Buffer A (W). The protein was eluted using increasing amount of Buffer B, with the millimolar concentrations of imidazole displayed (67 to 215). (A) Point mutants at amino acids 97, followed by 122. (B) Point mutants at amino acid 138, followed by 265. (C) Point mutations at amino acid 249, followed by 323. L=Ladder, PrI = pre-induced.

The large-scale expression and purification of the mutants of MtAroB was undertaken (Figure 2.17). All six proteins were purified using the same approach, which mirrored that used for the wild-type MtAroB protein, cell lysis in a Tris-HCl buffer followed by lysate clarification. The cell lysate was then added to gravity flow columns containing nickel-NTA resin. A sub-optimal amount of nickel NTA resin was used, as it allowed the mutated MtAroB proteins to oversaturate the resin's binding sites, causing a majority of other proteins to be removed in the wash step (Figure 2.17). While this caused a loss of some MtAroB protein in the wash step, it provided much purer protein when eluted at 67 mM imidazole and prevented the need for further purification before use in activity assays. The gel shown in Figure 2.17D for expression of the MtAroB-265 mutant is slightly different, as it required re-cloning and was expressed on a large scale at a later date. The successful production of all six mutated proteins allowed for rapid downstream characterisation of their activity.

2.2.1.11. Activity of MtAroB mutants

Initially, all six mutants were compared to the wild type MtAroB protein for their level of activity and highlighted the majority of mutations reduced the activity (Figure 2.18A). The activity assay was performed with 100 µM DAHP, so substrate concentration did not impact activity or prevent direct comparisons. The only mutant which did not show a drop-in activity was the Arg97 mutant. To further quantify the activity levels, the rate of reaction was calculated for each mutant across the first 10 minutes following enzyme addition (Figure 2.18B). This indicated that the His265 mutant had no activity and hence was excluded from further analysis. The Arg122, Asp138 and His249 mutants had vastly reduced activity, from 0.015 A/min of the wild type to between 0.001-0.002

A/min for the mutants. The Lys323 mutant had moderately reduced activity, about half of the wild type, at 0.007 A/min.

To assess whether the mutants retained the sigmoidal activity vs substrate concentration displayed for the wild type MtAroB protein; the activity assay was repeated for each mutant protein, while varying the DAHP concentration (Figure 2.18C). The sigmoidal activity curve is not as clear in this repeat; however, it does not show Michaelis-Menten kinetics for either the wild type or Arg97 mutant. All the other four mutants had much lower rates of reaction, as previously mentioned and hence their data is plotted in subplots (Figure 2.18D,E), to allow the kinetics curves to be visible. Both the Arg122 and His249 mutants appear to display Michaelis-Menten kinetics, which could imply these mutations prevent cooperativity between the two monomers. The Asp138 mutant appears to retain the sigmoidal activity curve, whilst the Lys323 mutant does not have a clear shape and may require additional substrate concentrations to be tested. Overall, this verifies that most of the purified MtAroB mutants are functional and suggests that the mutagenesis is the cause of their loss in activity. However, the mutations many cause the protein to misfold during translation and hence the misfolded protein would be inactive or have greatly reduced activity.

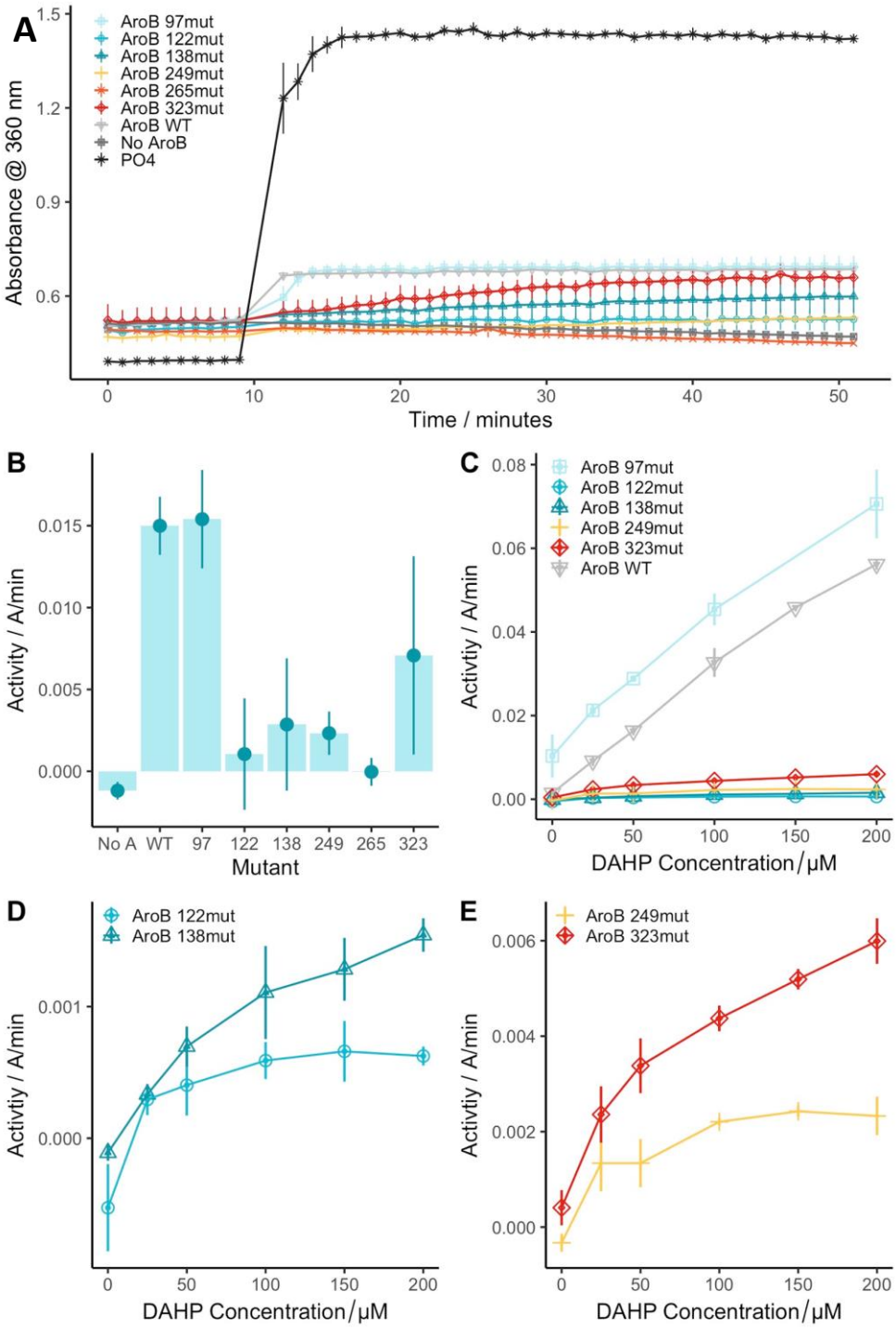


Figure 2.18: Activity of MtAroB mutant proteins. (A) Activity assay comparing MtAroB mutants at 100 µM DAHP. Each well contained NAD, MESG, DAHP and PNP in buffer; the MtAroB proteins and PO_4 were added at 9-minutes. **(B) Bar graph displaying mutants' rates vs wild type, at 100 µM DAHP.** Rates were calculated from 10 minutes following enzyme addition. No A = No AroB. Mutant 265 was excluded from later panels due to lack of activity. **(C) Plot of enzymes' activity vs substrate concentration. (D) Subset plot of mutants 122 and 138. (E) Subset plot of mutants 249 and 323.** N=3 for all assays.

2.2.1.12. CD spectra of mutant MtAroB proteins

As there was large decrease in activity in the majority of the mutant MtAroB proteins, it was investigated whether these proteins were folded correctly. To this end, CD spectroscopy was used, as it gives an indication of the α-helix, β-sheet, loop, and unfolded regions of proteins as an overall global spectrum. Hence this would indicate if the protein had unfolded during overexpression or purification.

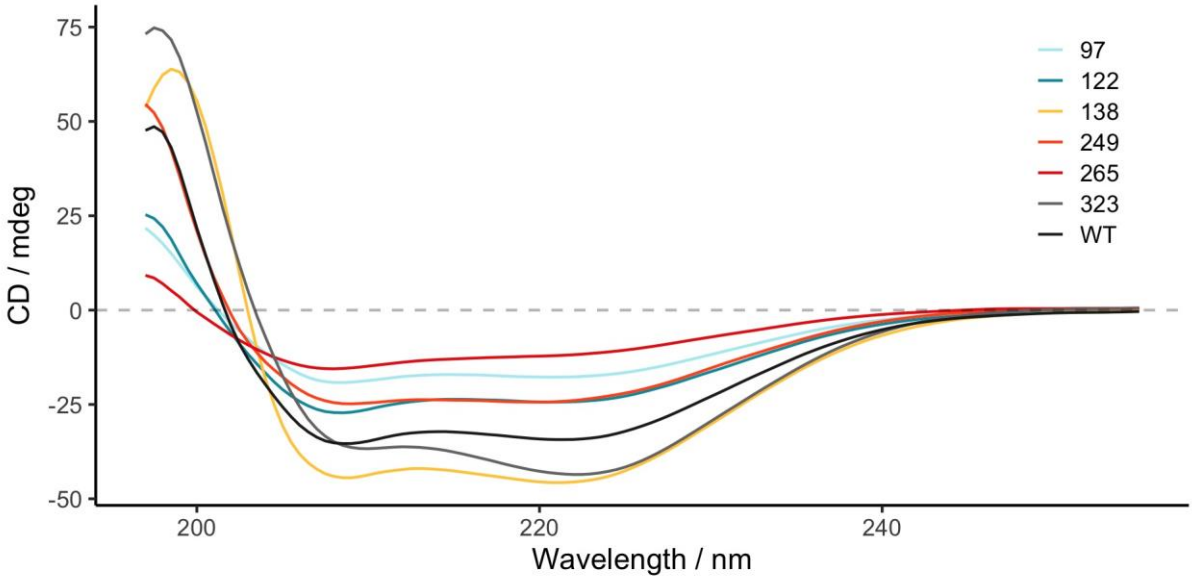


Figure 2.19: CD spectra of MtAroB wild-type and mutants in the near-UV. MtAroB wild type and mutants were transferred into 20 mM $NaPO_4$ pH 7.4 buffer and diluted to 0.021 mg/mL. The CD spectra were acquired at 50 nm/min at 0.5 nm intervals, and 10 accumulations were performed per spectra. A baseline reading and the CD of the buffer were subtracted from each reading. The baseline was corrected to zero and minor smoothing was applied using the Savitzky-Golay method. All CD data points corresponding to a HT value >600 were removed.

The CD spectrum of all six mutants was compared to the wild-type MtAroB protein (Figure 2.19). This indicated that most of the mutants are folded in a similar manner to the wild-type protein and hence the point mutations have not impacted protein folding. This is indicated by the double minima at approximately 209 and 221 nm and is present, even if the magnitude of the signal differs between mutants. The only exception is the mutant 265, which has a much weaker signal and hence the double

minima was less clear. However, a random coil has a positive CD value from approximately 210 nm and above (Corrêa and Ramos, 2009), hence the MtAroB-265 mutant is likely to be at least partially folded. Overall, this suggests that the loss of activity is due to the specific point mutations and not the inability of the protein to fold.

2.2.1.13. MtAroB-GFP fusion protein

In an effort to increase the number of protein-drug binding interactions studies which could be undertaken on MtAroB. The production of an MtAroB with green fluorescent protein (GFP) fusion protein was performed. Restriction free cloning was used to merge the *gfp* gene from another plasmid with the *aroB* gene present in the pET28a-MtAroB plasmid. Given the N-terminal His-tag had already successfully been used for protein purification, the *gfp* gene was added onto the C-terminal end of the *aroB* gene. This would also prevent the GFP from interfering with the correct folding of the MtAroB protein, given its translation would occur later. To confirm cloning had taken place, initially colony PCR was performed to monitor an increase in band size of the gene insert within the pET28a vector. This was followed by sequencing of the vector to confirm insertion. DNA gels related to the cloning of *arob-gfp* are shown in Appendix 1.

The successfully produced pET28a-MtAroB-GFP vector was cloned into the *E. coli* BL21 (DE3) expression strain and trialled for the expression of the 67 kDa protein. Following success in a small-scale trial, a larger scale expression and purification experiment was undertaken and the SDS-PAGE gel highlighting the process is shown in Figure 2.20. As the purification of the protein could be monitored in real time, due to its fluorescent nature, a pre-packed nickel-NTA column was used for purification. In comparison to the mutant MtAroB proteins, the column was not oversaturated and hence a minority of protein was lost at the wash step. Unfortunately, the elution at 67 mM imidazole contained a similarly sized contaminating protein, which would be challenging to separate from the MtAroB-GFP protein. Luckily, the elution at 86 mM

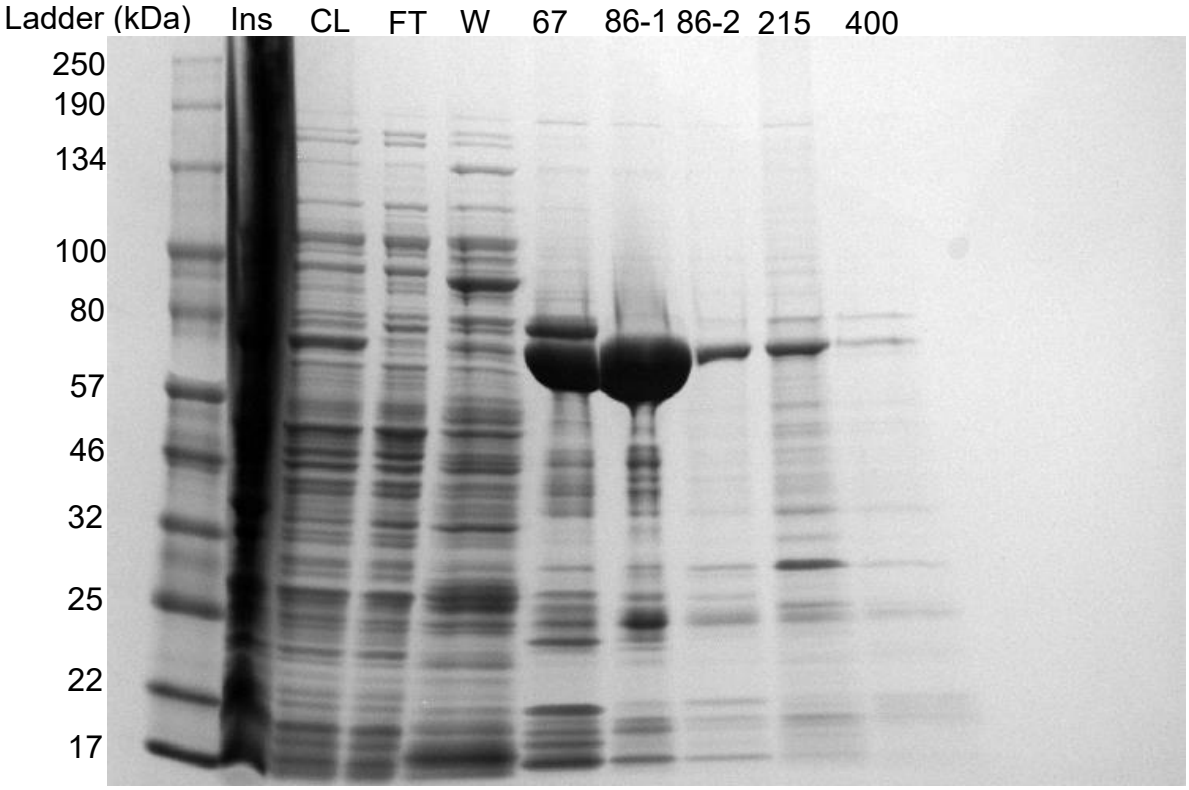


Figure 2.20: SDS-PAGE gel showing the purification of MtAroB-GFP (67.4 kDa) using nickel resin. The induced cells were lysed and centrifuged to gain clarified lysate (CL) and an insoluble fraction (Ins). The clarified lysate was loaded onto nickel resin and the flow-through (FT) monitored, followed by washing (W) with Buffer A. The protein was eluted with increasing concentrations of Buffer B, the millimolar concentrations of imidazole are displayed (67 to 400).

did not contain this contaminating protein and could be used. The 86 mM elution was also split into two fractions, as the point at which the GFP fluorescence was not seen in the column output was separated into a new collection tube. Despite having several smaller proteins as impurities, the MtAroB-GFP fusion protein was the major protein in the 86-1 fraction and hence was used for downstream analysis without further purification.

2.2.1.14. Microscale thermophoresis (MST)

Following the successful purification of the fusion MtAroB-GFP protein, it was investigated whether a microscale thermophoresis (MST) binding assay could be used as an analogous approach to assess drug-protein interactions. In this case, the substrate DAHP, co-factor NAD and non-binder vanoxerine were used to assess whether MST could distinguish between binding and non-binding compounds (Figure 2.21). All three compounds were pre-incubated with the MtAroB-GFP protein for 30 minutes, at sixteen different concentrations, before starting the assay. For each concentration, the fluorescence is measured before heating the sample with a laser and then continually measured for 20-seconds during laser heating. The normalised fluorescence (Fnorm) can then be calculated, by comparing the fluorescence of a one second window during laser heating to the pre-heated fluorescence. If the compound caused a difference in the response of the protein to laser heating, such as a slower rate of diffusion due to increased mass upon binding, this would translate into a concentration-dependent shift in the Fnorm. Due to time constraints, only one repeat of this testing was undertaken. As indicated, shifts in the Fnorm were found for both DAHP and NAD and binding curves could be plotted for each compound (Figure 2.21).

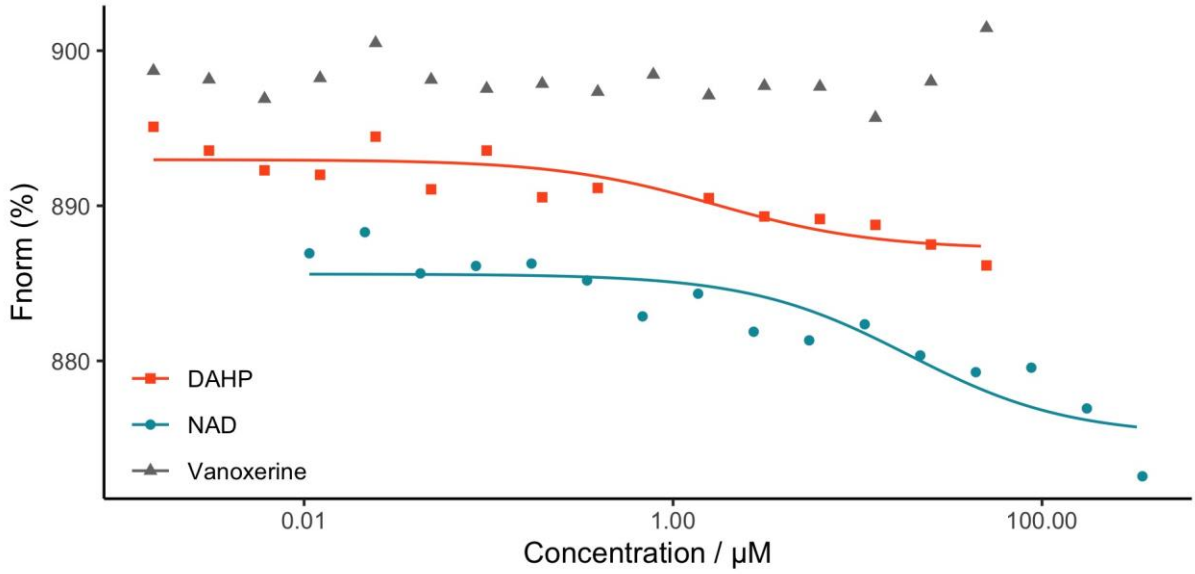


Figure 2.21: MST response of MtAroB-GFP in the presence of DAHP, NAD or Vanoxerine. MtAroB-GFP was pre-incubated with compound for 30-minutes prior to MST analysis. Dose response data was chosen at 10s, 20s and 10s for DAHP, NAD and vanoxerine, respectively. Kd binding curves were fitted to the dose response curves of MtAroB-GFP, a binding curve failed to fit to the vanoxerine data. Fnorm is the fluorescent ratio before and after heating. N=1

These allowed Kd calculations for binding affinity, with a Kd of 16.9 µM for DAHP and a Kd of 190 µM for NAD. A more accurate prediction of the Kd could have been achieved by increasing the protein concentration from 160 nM to closer in concentration to the predicted binding affinity values. The addition of vanoxerine to MtAroB-GFP did not cause a concentration-dependent shift and hence a binding curve could not be fitted to the data. Overall, this suggests MST can successfully distinguish between binding and non-binding compounds, however, further validation is required if this approach is to be used.

2.2.2. Finding drugs to target AroB

2.2.2.1. XCHEM

XCHEM drug screening, a drug discovery approach offered by Diamond Light Source, was selected as it would allow direct drug-protein interactions to be analysed and provide a more robust drug discovery platform against this novel target. XCHEM is a fragment screening approach using protein crystallography and X-ray diffraction to assess the binding of compounds. In ideal conditions, up to 800 compounds can soaked into protein crystals, one compound per crystal, followed by X-ray diffraction to determine if the compound bound in the active site.

The MtAroB protein was selected for this process, as the active site of the protein crystal remained empty, except for the catalytic zinc ion and the resolution obtained was 2.27 Å, based on crystals grown in a sitting-drop vapour diffusion crystal tray. The XCHEM pipeline had more stringent requirements for protein crystal growth compared to the current laboratory approaches. This included use of the SwissCi 3-drop crystal tray, reduction of the reservoir volume to <50 µL and a drop size maximum of 300 nL. Initially, the conditions that had previously been used in the vapour diffusion crystal trays were trialled, as they had led to crystals with good enough diffraction (<2.5 Å). However, for these known conditions, only tiny crystals were observed in A10 (0.2 M potassium formate, 20% (w/v) PEG 3,350) and G2 (0.02 M magnesium chloride hexahydrate, 0.1 M HEPES, pH 7.5, 22% (w/v) poly(acrylic acid sodium salt) 5100). Hence, a new trial was set up using JCSG-plus screen. This led to more crystal formation than the previously used tested conditions.

While these single crystal drops were informative, the crystallisation conditions needed to consistently produce crystals across multiple trays. Four crystallisation conditions

were re-tested based on the initial hits, B8 (0.2 M magnesium chloride hexahydrate, 0.1 M Tris, pH 7, 10% (w/v) PEG 8,000), E11 (0.16 M calcium acetate hydrate, 0.08 M sodium cacodylate, pH6.5, 14.4% (w/v) PEG 8,000, 20% (w/v) glycerol), G6 (0.2 M sodium malonate dibasic monohydrate, 20% (w/v) PEG 3,350), and G8 (0.15 M DL-malic acid, 20% (w/v) PEG 3,350). For G8 testing, only L-malic acid could be sourced and hence no crystals formed. In the repeat of E11, only very small crystals formed and hence the condition was not developed further. Condition B8 gave lots of crystals, however, two different morphologies were present with variable size and hence, development was not continued due to risk of salt crystal formation. Finally, G6 gave reproducible crystals in 22-30% of drops and was optimised further.

First, a commercial additive screen was trialled, using G6 as the base condition and adding a small quantity of other reagents with the aim of improving the crystals formed. From the ninety-six conditions tested, only the addition of 15.6 mM calcium acetate hydrate allowed formation of crystals. Other additives were also independently trialled, including 5% isopropanol, 5% (w/v) PEG 8,000 and 5% (w/v) PEG 400. The addition of 5% (w/v) of either PEG 400 or isopropanol led to more consistent formation of crystals. In the case of isopropanol, this increased the number of crystals with drops to 90% of the wells tested. Alongside additive screens, the conditions of G6 were also altered to test around this crystallographic hit. The sodium malonate concentration was tested in 0.125 M increments from 0.15 to 0.275 M in a matrix against the %PEG (w/v) 3,350 in 2% increments from 14 to 30 %. This matrix test highlighted that protein crystals formed in 24% or greater PEG 3,350 regardless of salt concentration, at least above 0.15 M sodium malonate. However, the best crystals formed in 28% or 30%

PEG 3,350. The best condition, which was selected for protein crystal growth for XCHEM, was 28% (w/v) PEG 3,350 with 0.175 M sodium malonate dibasic hydrate. Following this optimisation of the crystal reproducibility, these conditions were sent to Diamond Light source to allow growth of the protein crystals. The planned process is listed in Figure 2.22, alongside the actual process which occurred.

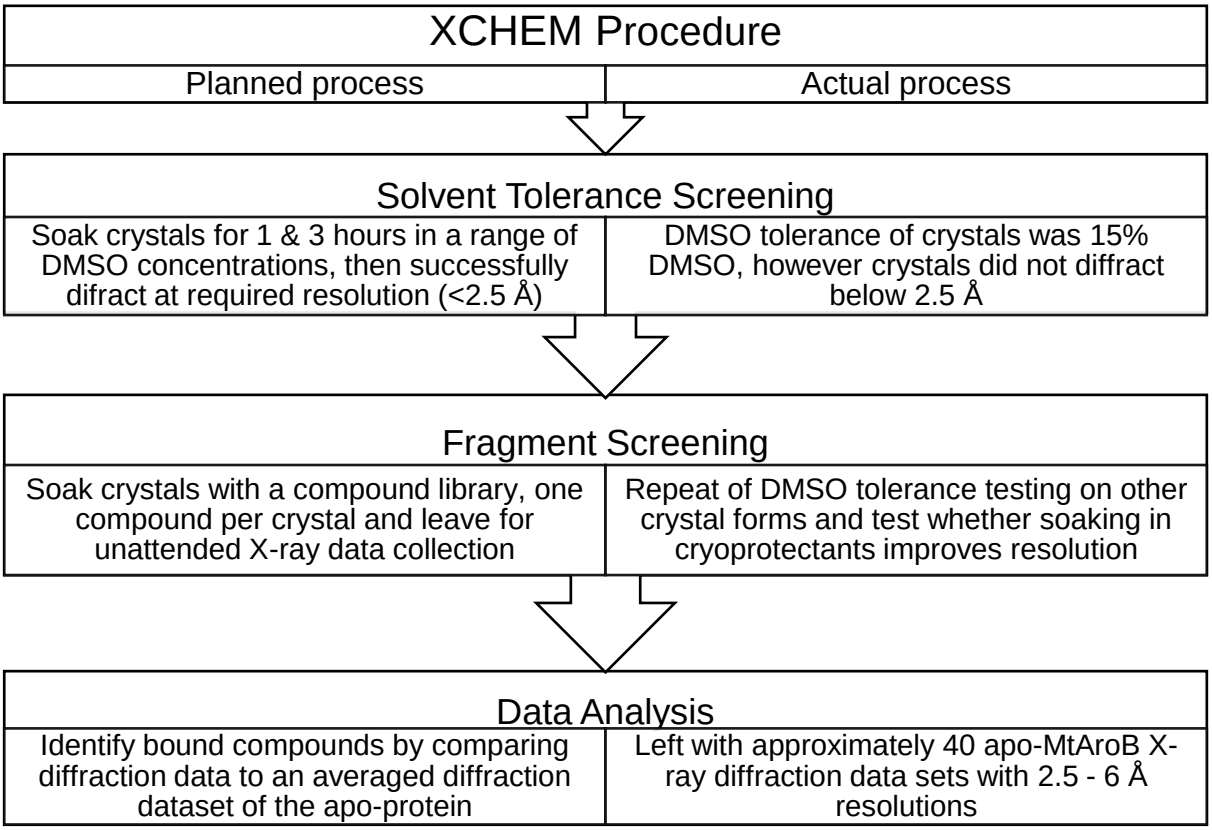


Figure 2.22: Comparison of the planned vs actual XCHEM process for MtAroB crystallographic fragment screening.

The main issue with this screening approach was the inability to optimise for diffraction quality at the same time as optimising for crystal formation reproducibility. While the crystals based on G6 and the surrounding conditions were not good enough for diffraction and compound screening, other crystallisation conditions may provide better resolution alongside good reproducibility. Any of A10, B8, E11, G2 or G8 from the

JCSG-plus screening set, could be optimised in the future to provide stronger crystallography diffraction.

2.2.2.2. Docking of the Prestwick library

Following the unsuccessful approach used for XCHEM, a more computational approach was favoured. The general scheme of work is outlined in Figure 2.23, to perform ensemble docking of the Prestwick library against an ensemble of MtAroB protein conformations. This work directly builds on the MD simulations of the MtAroB protein undertaken previously and allows the proteins flexibility to be accounted for during the docking procedure. This work started from the set of ensemble conformations generated by clustering and principal component analysis of the MD simulation trajectory. The Prestwick library was selected, as corresponding *in vivo* activity levels have already been experimentally determined (Kanvatirth et al., 2019). At the start of computational work, the aim was to rank the compounds by their

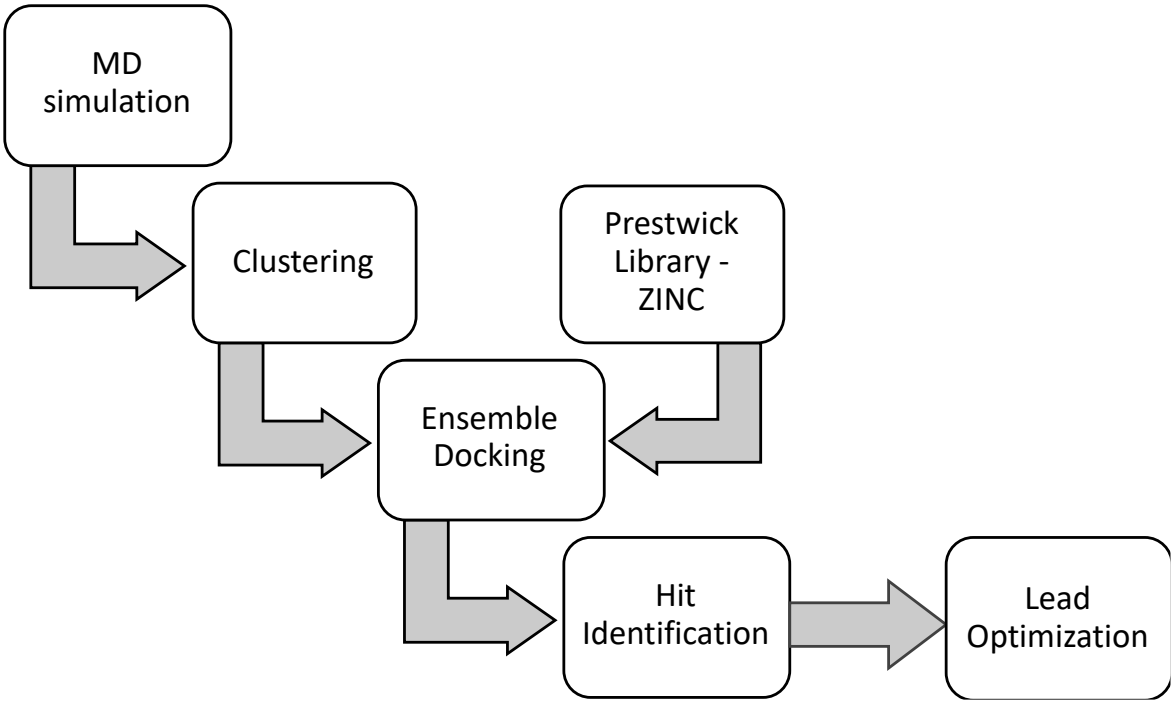


Figure 2.23: Scheme for computational drug discovery virtual screening

weighted average docking. AutoDOCK Vina was used to virtually screen the Prestwick library for binding against the twenty-two protein conformations. An unbiased docking approach was used, with a 66.0 by 47.1 by 41.6 Å cuboid surrounding the total protein to define the search area. Scores for up to eight poses of each compound were generated against all twenty-two structures. Weighted averages were performed separately for structures derived from clusters vs PCA. The spread of the docking scores was analysed, for clustering derived structures, a range between -3.2 and -13.9 kcal/mol was found. For PCA generated structures, a range of scores between -3.3 and -13.9 kcal/mol was found. While the maximum and minimum docking scores were similar, the overall score distributions indicated that the PCA derived structures had more favourable docking scores. The increased docking scores for PCA structures should not affect downstream analysis, as all scores are judged relative to each other. Hence, the compound rank is more important than the docking score.

In addition to the Prestwick library, several compounds which are known to bind to AroB were also included in the docking analysis. These included DAHP, NAD^+ and a known inhibitor of AroB, carbaphosphonate (Derrer, Macheroux and Kappes, 2013). The docking of these compounds would indicate the overall accuracy of the approach. However, they were not ideal controls, as NAD^+ binds to an alternate region of the protein, while DAHP and carbaphosphonate are smaller than most of the Prestwick library compounds, and hence this leads to less favourable docking scores. However, no other compounds have proven binding site locations on MtAroB.

To evaluate the docking of carbaphosphonate, DAHP and NAD against MtAroB, several parameters were selected (Table 2.2); including the best and worst docking scores, the number of predicted docking poses in the known binding site, and for NAD,

number of predictions with the correct orientation. The latter two measurements were determined by visual inspection of the docking poses, and average scores across the eleven conformations from g_cluster or PCA were calculated. Comparing between the g_cluster derived conformations and the PCA-derived conformations, the latter produced the higher docking scores, while the former had a higher chance of generating docked poses within the known binding site (Table 2.2). This could allow a combination of clusters to provide the optimum scoring and pose prediction properties required.

Table 2.2: Evaluation of docked control compounds against both g_cluster and PCA derived conformations of MtAroB. For each compound, eight docking poses were generated for each MtAroB conformation, resulting in 176 docking predictions. The average best and worst docking scores across each set of eleven conformers was calculated. The location and orientation in the protein's active site was visually inspected and defined. CRB = Carbaphosphonate, DAHP = 7-phospho-2-dehydro-3-deoxy-D-arabino-heptonate, NAD = nicotinamide adenine dinucleotide

Structure	Compound	Best Score	Worst Score	Active Site molecules	Correct Orientation
g-cluster	DAHP	-5.9 ± 0.4	-5.4 ± 0.3	4.7 ± 1.6	N/A
	NAD	-9.3 ± 0.6	-8.8 ± 0.5	2.1 ± 1.1	0.5 ± 0.8
	CRB	-6.5 ± 0.3	-6.0 ± 0.3	3.9 ± 1.5	N/A
PCA-derived	DAHP	-6.1 ± 0.3	-5.7 ± 0.2	1.9 ± 1.2	N/A±
	NAD	-9.4 ± 0.5	-8.9 ± 0.56	1.4 ± 1.1	0.4 ± 0.7
	CRB	-6.8 ± 0.2	-6.2 ± 0.2	1.5 ± 1.2	N/A±

To further probe the binding of these control compounds, the docked poses were compared to the crystallographic binding locations on AroB proteins. For NAD, this was compared to the MtAroB structure (3QBD), for carbaphosphonate, this was compared to the *A. nidulans* AroB (1NR5). No crystal structure exists of AroB with DAHP bound and hence this control could not be compared. First, each crystal

structure containing the bound compound was overlaid onto the MtAroB structure which had been used for docking. Then each docked pose was visually inspected for similarity to the crystal structure. From the 176 docked poses for each compound, the best docked poses are displayed in Figure 2.24. For NAD, the orientation of the molecule and the nicotinamide moiety being in the correct active site location were the important factors (Figure 2.24A). However, no docked doses displayed the observed ribose or adenine binding site locations of the NAD. For carbaphosphonate, the active site location was the most important factor, and then the correct orientation relative to the zinc ion was used to select the best docked pose (Figure 2.24B). For comparison, the worst docked poses were ~20 Å away from the active site, due to the unbiased docking approach undertaken, and hence were not displayed. Given this ~1-2%

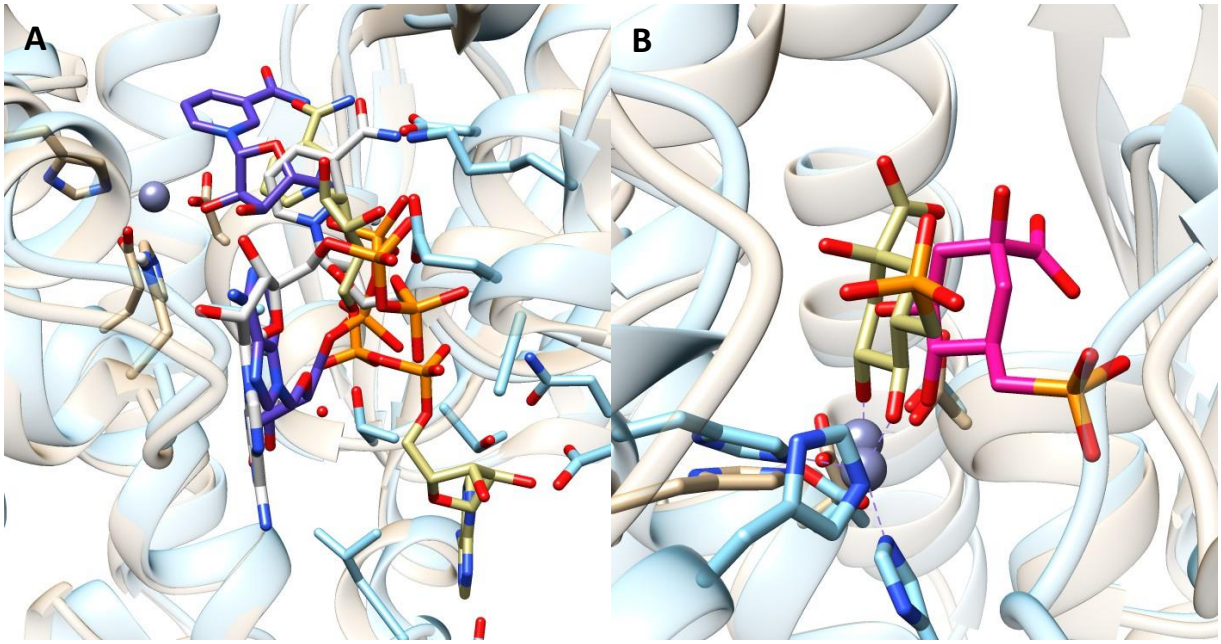


Figure 2.24: Best docked poses of NAD and carbaphosphonate compared to the crystal structure binding poses. (A) Top 2 NAD docked poses (purple and light grey) against MtAroB (3QBE, light blue) compared to NAD (khaki) bound in MtAroB (3QBD, light khaki) crystal structure. (B) Best carbaphosphonate (pink) docked pose against MtAroB (3QBE, light blue), compared to carbaphosphonate (khaki) bound in *Aspergillus nidulans* AroB (1NR5, light khaki) crystal structure.

success rate for predicting a similar pose to the crystallographic binding pose, this does not provide confidence in this approach.

To assess the docking process, all the docking scores for each molecule were compared to the molecular properties predicted for each structure by ChemMine (Backman, Cao and Girke, 2011). This is highlighted in the correlogram (Figure 2.25), showing the significant correlations between docking scores and molecular properties. As the docking scores are negative values; a negative correlation suggests that an increase in that property of the molecule correlates with a better docking score. The

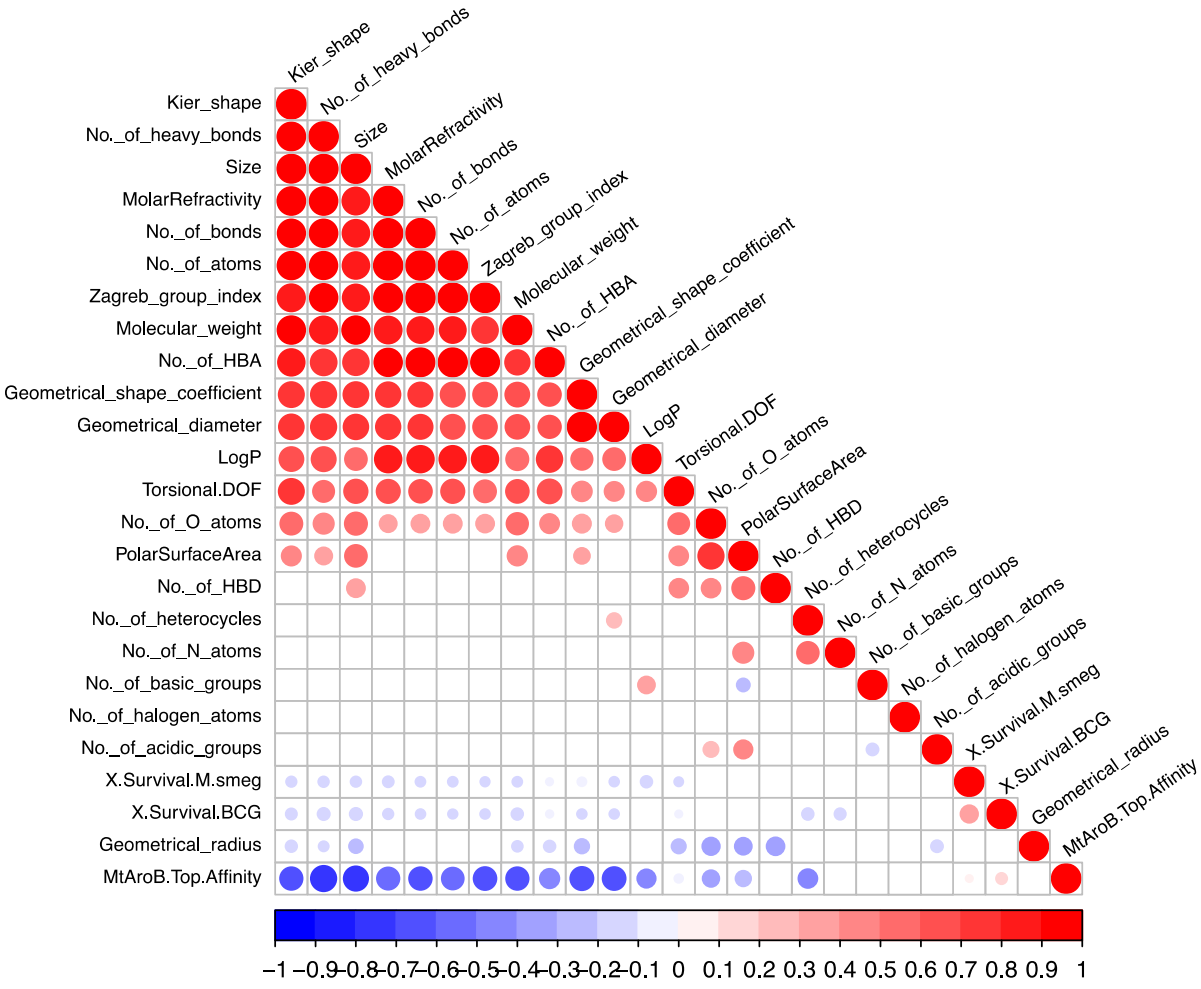


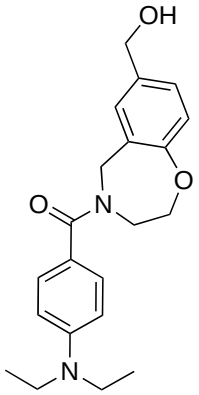
Figure 2.25: Correlogram showing the correlations between molecular properties, whole cell efficacy against mycobacteria and docking scores against MtAroB. DOF = degrees of freedom, HBA = hydrogen bond acceptors, HBD = hydrogen bond donors.

top three set of correlations with the docking scores (MtAroB top affinity) were the number of heavy bonds, size, and the geometric shape coefficient, being -0.77, -0.7 and -0.64. Although many other parameters related to the size of the molecule also negatively correlated with the docking scores. The %survival following drug treatment of *M. smegmatis* or *M. bovis* BCG did not strongly correlate with any other scores, but did positively correlate with each other, +0.34 (Kanvatirth et al., 2019). No functional groups present on the compounds appeared to correlate with a better docking score. Based on the strong correlation with molecule size and shape, and the lack of strong predictions of the correct docking poses, this dataset was not used for further testing. The small size of the compound library, alongside its large variation in compound sizes, may have contributed towards this issue. However, molecular docking has still been successfully used against *M. tuberculosis* proteins (Kingdon and Alderwick, 2021), and hence a collaboration was formed with Dr Jóhannes Reynisson (University of Keele) and Dr Daniel Moscoh (University of Ghana) to undertake computational work against the MtAroB protein.

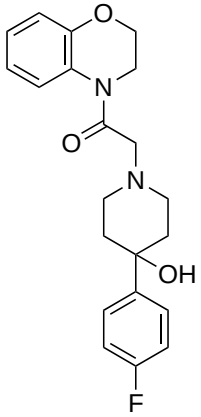
2.2.2.3. Virtual screening against MtAroB

This work was undertaken by Dr Daniel Moscoh (University of Ghana). The Hit2Lead ChemBridge library was selected, as it contained commercially available compounds, and was screened for compounds with drug-like properties. This identified 9,991 compounds which were screened with a low search efficiency against the binding pocket of the MtAroB protein (3QBE) using GOLD (Jones et al., 1997; Verdonk et al.,

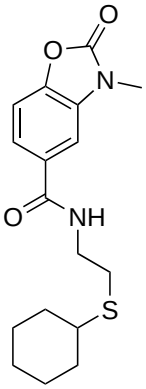
11654105



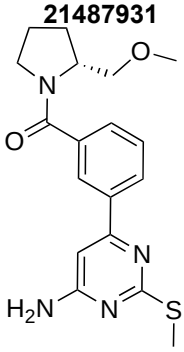
18077207



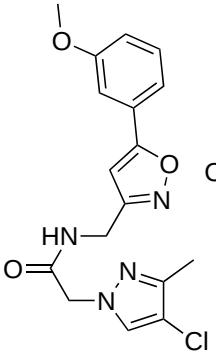
20530397



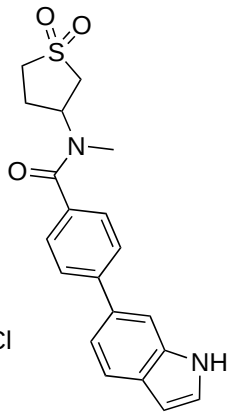
21487931



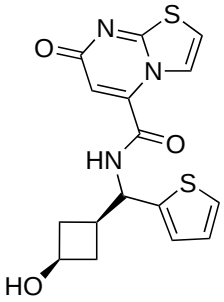
25761029



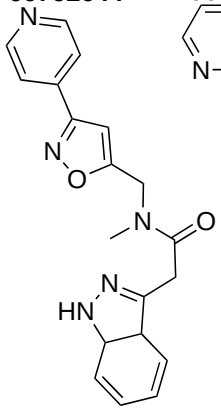
26694214



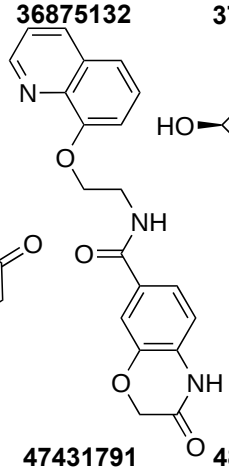
27313805



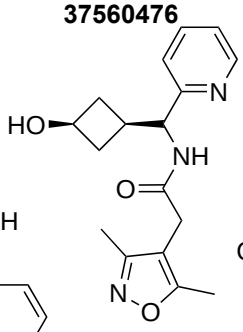
33782544



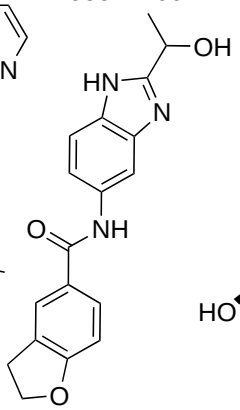
36875132



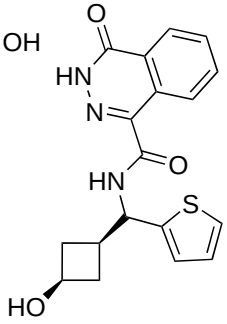
37560476



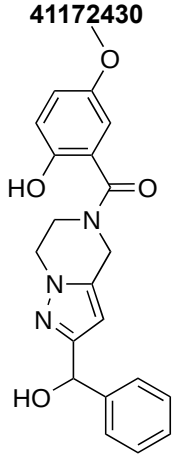
38571466



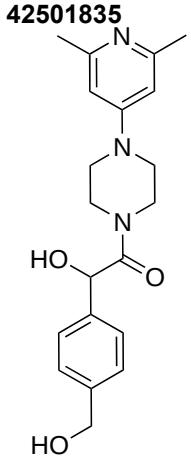
39181163



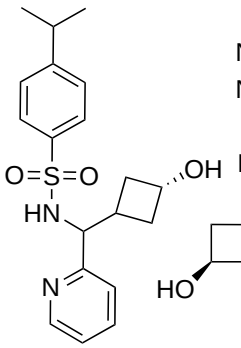
41172430



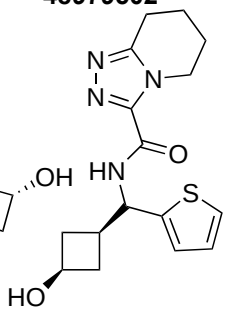
42501835



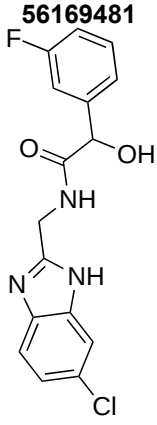
47431791



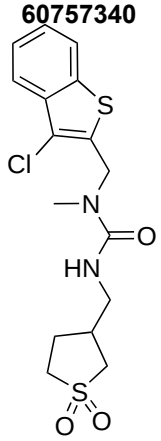
48979502



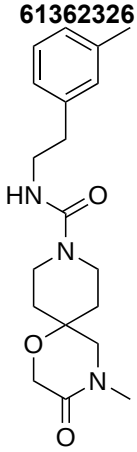
56169481



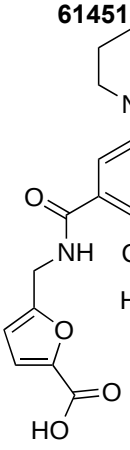
60757340



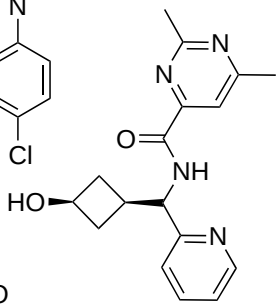
61362326



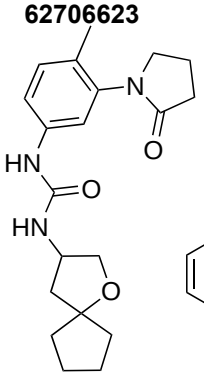
61451847



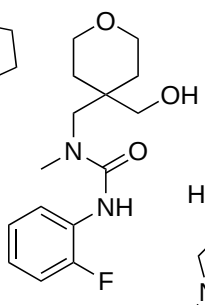
61486468



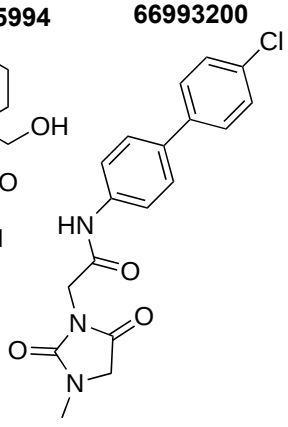
62706623



66325994



66993200



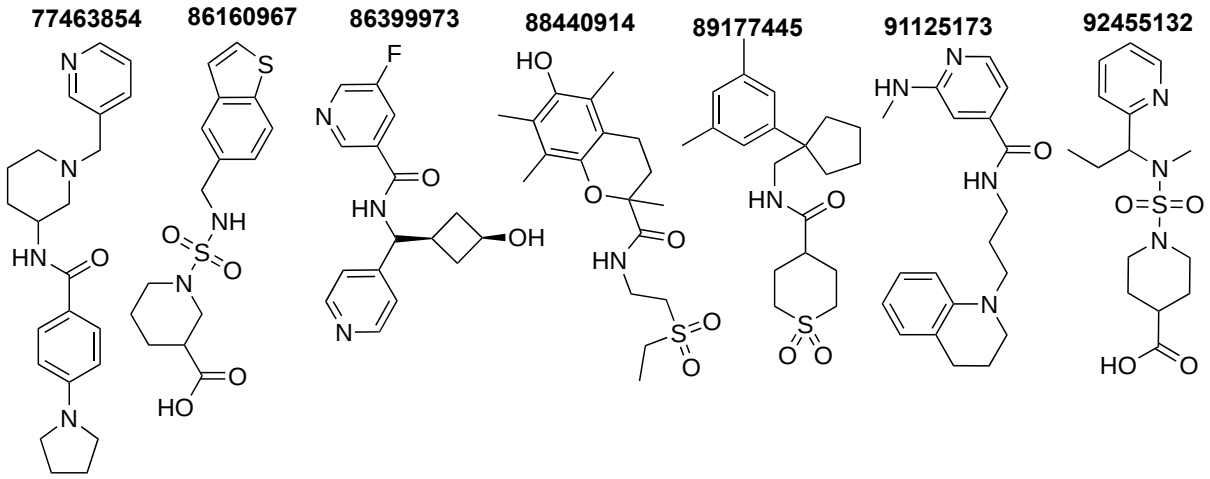


Figure 2.26: Top 31 molecules from virtual screening effort against MtAroB. Identifying numbers are from the ChemBridge database.

2003). The docked molecules, with at least one intermolecular hydrogen bond and scores greater than pre-defined cut-offs (ChemScore (15.3), GoldScore (45.2), Chem PLP (45.5), and Astex statistical potential (20.4)), were then screened at a higher efficacy (2,796 molecules). More stringent cut-off values (ChemScore (>24.1), GoldScore (>53.3), ChemPLP (>70.2), Astex statistical potential (>61.0)) were used to select molecules of interest, with 439 candidates being selected for visual inspection. Consensus of predicted conformations, the plausibility of the ligand's conformation (not strained, no lipophilic moieties pointing into water) and known undesirable moieties linked to cell toxicity or chemical reactivity were all used to screen molecules. This method has been previously used to identify active compounds (Bhusal et al., 2017; Huang et al., 2017; Leung et al., 2021), and hence was repeated herein. This led to thirty-one compounds being selected for experimental testing, with their structures shown in Figure 2.26. The associated docking scores are displayed in Appendix 4.

2.2.3. Testing hits from virtual screening

2.2.3.1. Whole cell inhibition data – against *M. smegmatis* and *M. bovis* BCG

Following commercial acquisition of these 'hit' compounds, they were tested for whole cell activity against both *M. smegmatis* and *M. bovis* BCG. This was performed at two different concentrations, to allow any concentration-dependent effects to be identified. The percentage survival was calculated in comparison to DMSO and rifampicin treated controls, and is displayed for *M. smegmatis* (Figure 2.27A) and *M. bovis* BCG (Figure 2.27B). For activity against *M. smegmatis*, most compounds had a greater than 75% survival at both tested concentrations. The best compound was 77463854, with a percentage survival of 55% (or 45% inhibition), when tested at 100 µM. When selecting compounds for follow-up MIC testing, the 100 µM concentration needed to show greater growth inhibition than the 20 µM concentration. For *M. bovis* BCG inhibitory activity, no compound reduced survival below 85% and hence it is unlikely these thirty-one compounds have any activity. The *M. smegmatis* follow-up testing (Figure 2.27C), showed a lack of inhibitory activity at all concentrations of the eight selected compounds. This highlighted that none of the tested compounds have activity against mycobacteria at 200 µM or lower.

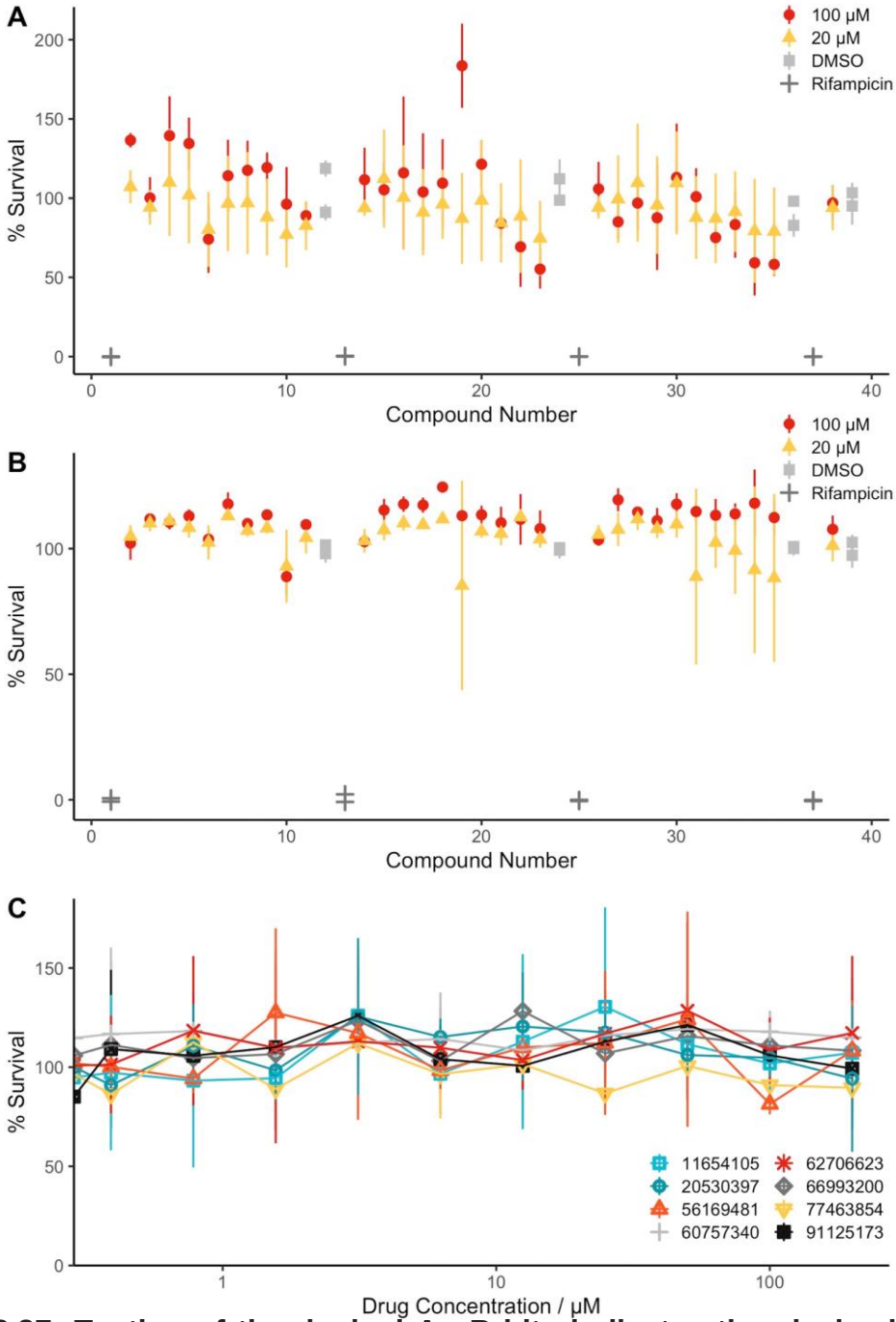


Figure 2.27: Testing of the docked AroB hits indicates they lack whole-cell activity against mycobacteria. (A) Testing compounds at 20 and 100 µM against *M. smegmatis*. %Survival values calculated from DMSO and rifampicin controls (also shown), following 24-hours of incubation, based on resazurin turnover. **(B) Testing compounds at 20 and 100 µM against *M. bovis* BCG.** %Survival values calculated from DMSO and rifampicin controls (also shown), following 7-days of incubation, based on resazurin turnover. **(C) %Survival curves for top eight compounds tested against *M. smegmatis*.** %Survival calculated in comparison to DMSO and rifampicin controls, after 24 hours incubation, based on resazurin turnover. N=3 for all assays.

2.2.3.2. AroB protein inhibition assay

The lack of whole cell inhibition could be due to lack of penetration through the mycobacterial cell envelope to reach the intracellular target. Hence, inhibition of the purified MtAroB protein was assessed. This involved pre-incubation of the protein with drug compound for one-hour, before addition of DAHP to initiate the enzymatic reaction. The change in absorbance (∆absorbance) across the first ten-minutes following DAHP addition was assessed and compared to the wild type MtAroB protein (Figure 2.28A). The majority of compounds had a limited effect on the activity at the 100 µm tested, compound 11654105 appeared to cause the greatest inhibition, at a change of only 0.026. However, the top eight compounds were repeated to confirm any inhibitory effects in a separate assay, but this showed that no compounds inhibited the MtAroB enzyme (Figure 2.28B). Hence, the previous activity of 11654105 is likely to be a procedural error. The lack of inhibition suggests that no compounds bind more strongly than either NAD or DAHP, preventing inhibition of the activity.

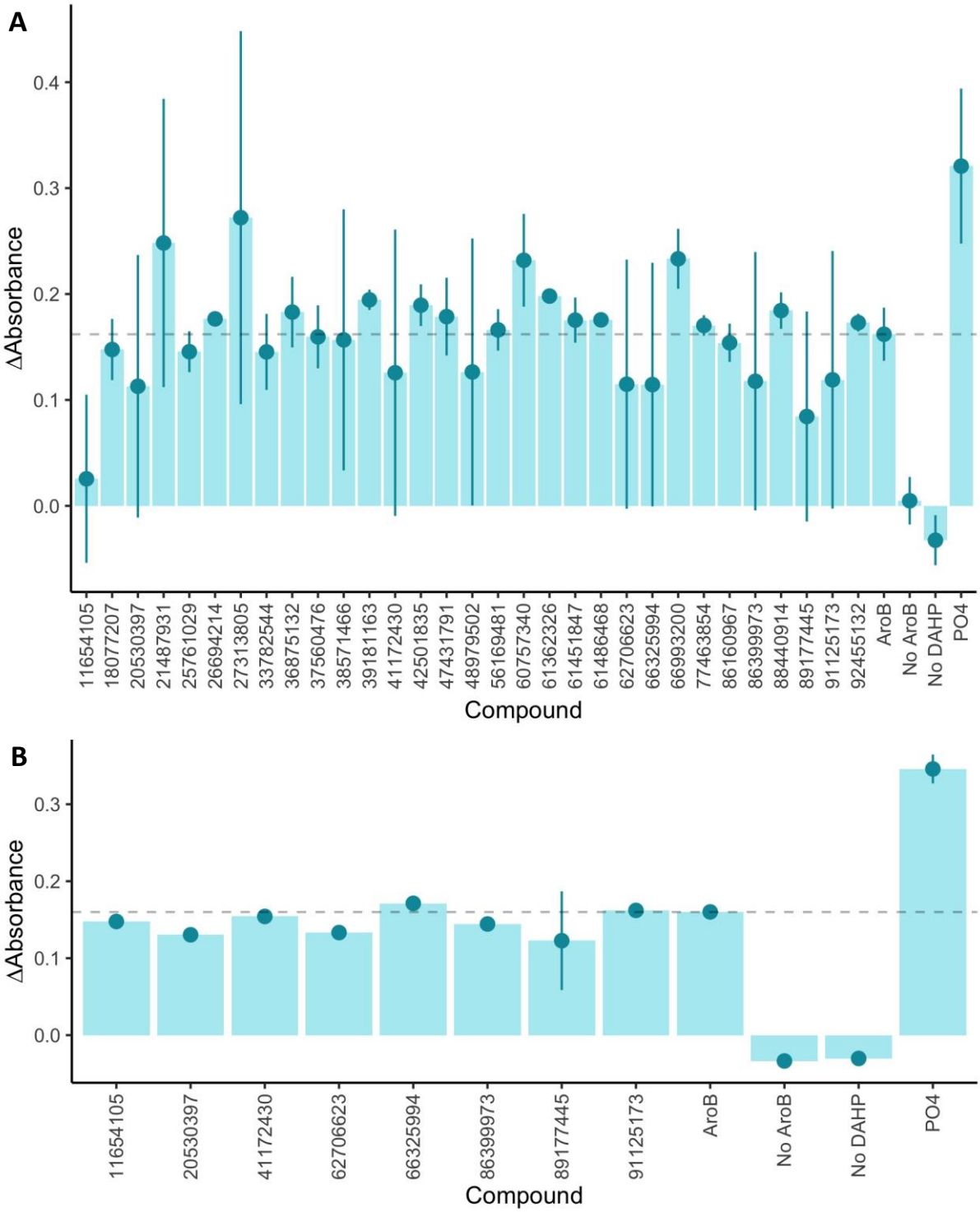


Figure 2.28: MtAroB inhibition assay to assess putative hit compounds. **(A) All hit compounds test. (B) Best performing hits repeated.** MtAroB was incubated with compound for 1 hour, the absorbance was monitored for 10-minutes, then DAHP was added to initiate the reaction. The change in absorbance at 360 nm (ΔAbsorbance), was assessed 10-minutes after DAHP addition (A) or the rate determine across 3 minutes (B). Dashed line indicates the MtAroB protein in DMSO, to allow comparison relative to each drug compound. N=3.

While these assays would be useful for compound activity confirmation, the molecular docking process does not predict for inhibition of the protein or whole cell activity, only that the molecule is predicted to bind to the protein. Hence, alternative biophysical assays were undertaken to assess the compound-MtAroB interactions.

2.2.3.3. MST initial binding test

As an initial approach to monitor the binding of the 'hit' compounds, MST was undertaken to compare the normalised fluorescence in the absence and large excess of compound, as evidence of protein binding (Figure 2.29). All compounds had previously been tested in buffer alone, to check for interference with the fluorescent output. This assay was carried out in-quadruplicate per compound and the average normalised fluorescence calculated. Most compounds showed a limited shift compared to the MtAroB-GFP protein. The presence of DMSO caused a shift and hence, many compounds which displayed a reduction in the normalised fluorescence are likely to not bind, as the shift was due to DMSO. As previously reported, NAD caused a large shift in the fluorescence, whilst DAHP did not have an impact. Compounds 26694214 and 77463854 both caused an increased difference in the normalised fluorescence, similar to NAD. Due to the low-throughput nature of this approach and the limited time remaining on the project, alternative biophysical approaches were trialled to confirm binding of these two-compounds and assess the remaining compounds.

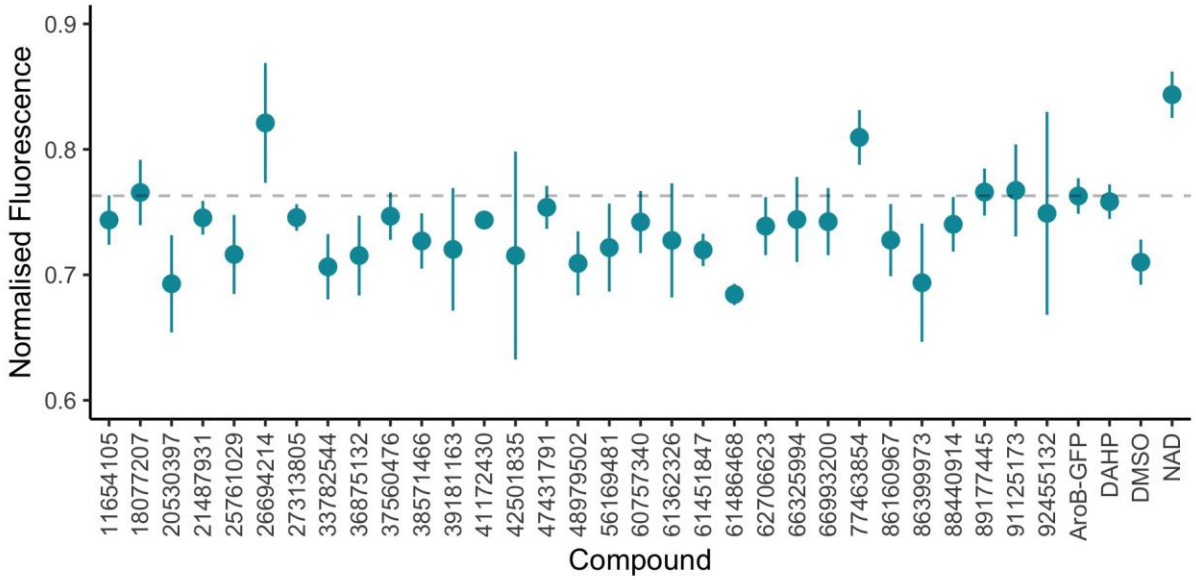


Figure 2.29: MST binding check analysing of MtAroB-GFP with hit compounds. MtAroB-GFP (40 nM) was incubated with compound (500 µM) for 30-minutes, prior to running MST binding analysis. Nano-Blue at 20% excitation and medium power were used. Normalised fluorescence is calculated by comparing the fluorescence at -1 to 0s, prior to laser heating, to fluorescence at 14-15 seconds of laser heating. N=4, except AroB-GFP N=48.

2.2.3.4. DSF for compound binding

A more high-throughput screening approach was DSF, which allowed binding to be monitored in a 96-well format in a qPCR machine, this allowed the 'hits' to be tested in-quadruplicate across two assay runs. The melting temperature of the MtAroB protein in the presence of compound was calculated and compared to the protein in DMSO (Figure 2.30A). Compound 66993200 was excluded, as it caused a two-phase transition state, preventing the melting temperature from being accurately determined. Several compounds were run in a separate assay plate and were exposed to the dye for 4-hours prior to running the assay, and hence showed a large decrease in melting temperature. Compounds 11654105, 20530397, 27313805, 38571466, 42501835, 56169481, 62706623, and 89177445 are displayed in Figure 2.30B, due to these

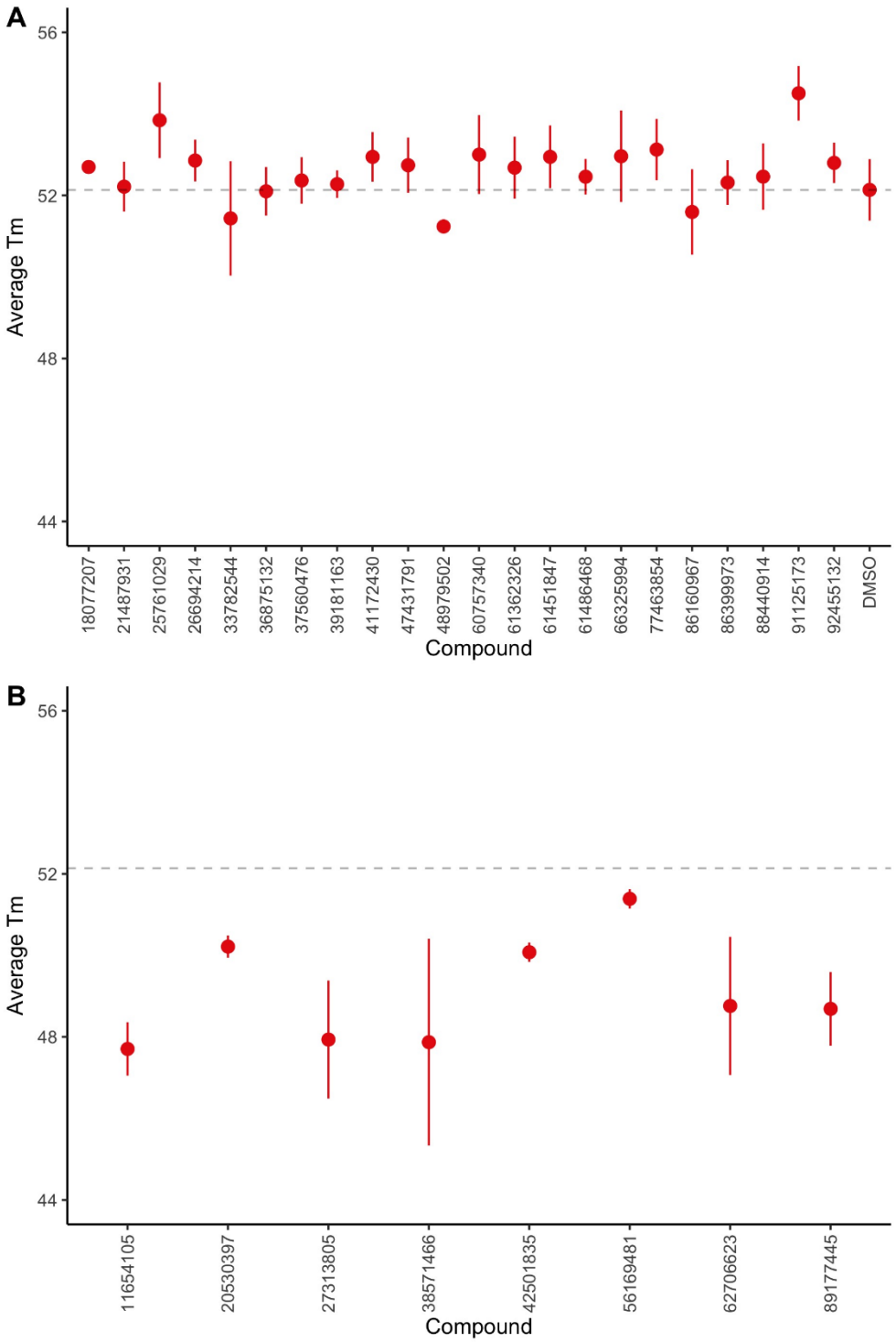


Figure 2.30: Differential scanning fluorimetry to assess compound binding and stabilisation of MtAroB. Compounds were incubated with MtAroB for 30-minutes prior to exposure to SYPRO orange dye and immediately added (A) or left for 4-hours at room temperature before addition (B) to the qPCR machine. The average Tm was calculated from the mid-point of the protein melting curve. Dashed line = 52.135 ˚C, the Tm of MtAroB+DMSO. N=4, except N=3 for 21487931, 61362326, 18077207, 25761029, 77463854, 86160967.

different conditions. Hence, the decrease in Tm compared to the DMSO control, is likely due to exposure to the dye and not destabilisation of the protein by the tested compounds. Unfortunately, time did not permit the repeat of these samples and this data should not be used to justify further investigation. For the remaining compounds, both 25761029 and 91125173 led to increase in the melting temperature, from 52.1 to 53.8 and 54.5 ˚C, respectively. This difference is smaller than the 4.1 ˚C difference between DMSO and DAHP binding MtAroB but could still indicate binding. The two compounds highlighted by MST only showed 0.72 and 0.99 ˚C differences, for 26694214 and 77463854 respectively, which were not significant differences. Due to these contrasting results, a further biophysical approach was trialled to confirm or refute putative binding.

2.2.3.5. MtAroB fluorimetry binding

The previously mentioned plate-reader tryptophan fluorescence assay was used to provide an alternative higher-throughput approach to provide further quantification on the MtAroB binding interactions with the ‘hit’ compounds. To allow the largest comparison, the tryptophan fluorescence in the absence of compound, was compared to 8 µM compound and the change in fluorescence calculated (Figure 2.31A). The compounds in only buffer were also measured for fluorescence, and 25761029, 36875132 and 47431791 had large shifts in fluorescence in the absence of protein. Hence, they cannot be evaluated using this approach. In this assay, the known binding compounds DAHP and NAD had large shifts in fluorescence, alongside chlorogenic acid, which was shown to bind the *Providencia alcalifaciens* AroB protein homologue

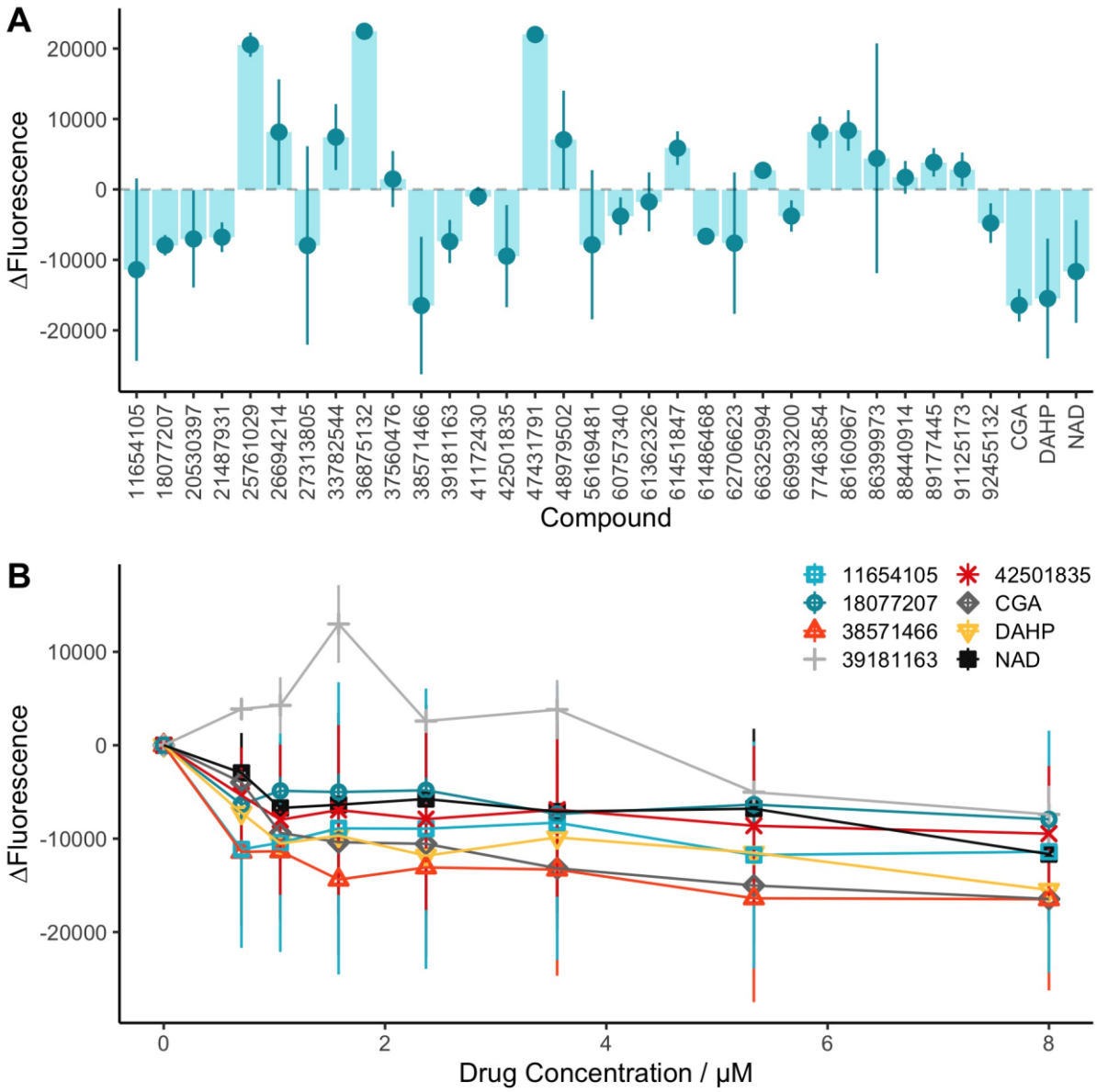


Figure 2.31: Tryptophan fluorescence binding analysis of AroB hit compounds. (A) Change in Fluorescence following incubation with compounds. MtAroB (1 μM) was incubated with 8 μM of each compound for 24-hour prior to measuring the tryptophan fluorescence. **(B) Tryptophan fluorescence change along a concentration gradient for the top 5 compounds + controls.** Concentration gradient of 2:3 serial dilution. MtAroB (1 μM) was incubated for 24-hours prior to measuring the tryptophan fluorescence. N=3 for both assays. Background compound fluorescence was removed.

(Neetu et al., 2020). Concentrating on the compounds which caused the largest fluorescence shifts, five were selected to compare with the known binding compounds (Figure 2.31B). This highlights compound 39181163 is unlikely to bind, given the lack

of a consistent concentration-dependent fluorescent shift. A majority of compounds had very large error bars, which prevented the true shift in fluorescence being determined or compared with the control compounds. Only 11654105 had very small error bars, but it did not cause a concentration dependent reduction in the fluorescence. Overall, this and the other biophysical approaches undertaken, provide little evidence supporting the binding of any of the thirty-one compounds to MtAroB. If they do bind, this is with an affinity too low to be useful for downstream drug development.

2.3. Discussion

This project has resulted in the development of numerous tools to allow drug discovery against the essential MtAroB protein. This includes a combination of biochemical, biophysical, and computational approaches, to gain more information about the protein and provide assays to assess binding or inhibition. In addition, some protein crystallography work provided a starting point for co-crystallisation of the protein with potential hit compounds. The loss of activity of the Arg122 mutant provides strong evidence the MtAroB protein acts as a dimer, which has already been proven for other homologues. Several attempts were undertaken to identify compounds which could act as MtAroB inhibitors; however, only molecular docking produced some potential binding compounds. These compounds did not have inhibitory effects on the MtAroB protein and did not have detectable binding interactions. Unfortunately, the attempts to find novel drug compounds were unsuccessful, however, the developed toolkit will allow for rapid confirmation of other putative inhibitors.

The MtAroB protein has been expressed in three previous studies (Dutra De Mendonça et al., 2007; Skinner et al., 1998; Zhu et al., 2018), with subsequent purification occurring in two studies (Dutra De Mendonça et al., 2007; Zhu et al., 2018). Another group published the MtAroB crystal structures on the PDB, with no associated paper. For induction of expression, varying levels of isopropyl-β-D-thiogalactopyranoside (IPTG) were used, ranging from none to 0.8 mM, compared to 1 mM used herein. The purification method used herein was adapted from Zhu et al. (2018), as it only required nickel column chromatography, compared to Dutra De Medonça et al. (2007), which required three columns to purify MtAroB. A direct

comparison of the final purification is not possible, due to varying approaches and information presented.

Previous studies which purified the MtAroB protein did not undertake protein crystallography, as crystal structures were already present on the PDB (3QBE and 3QBD). The structure derived within this work was only RMSD ~0.5 Å away from the PDB entries and hence suggests similar protein crystals can form under varying conditions. The structure was expected to be similar as the same crystallographic space group was present. The structure also highlights a potential difficulty of targeting the MtAroB protein, the active site is mostly composed of hydrophilic, charged residues. This would likely require a hydrophilic inhibitor to strongly bind, which is in direct contrast to the hydrophobic properties required to penetrate the mycobacterial cell envelope (Maitra et al., 2019; Dulberger, Rubin and Boutte, 2020).

In contrast to limited crystallographic studies, the activity of the MtAroB protein has been analysed several times (Dutra De Mendonça et al., 2007, 2011; Zhu et al., 2018). One study showed that MtAroB was homomeric and does not require additional proteins to perform its activity (Dutra De Mendonça et al., 2007), which was also confirmed herein. The ability of MtAroB to act as a dimer has been suggested, and for other AroB homologues, this has been proved (Carpenter et al., 1998). Work presented within this chapter has provided evidence that the *M. tuberculosis* protein does act as a dimer *in vitro*. The Arg122 residue is equivalent to the *A. nidulans* Arg130 residue, involved in the catalysis, and its mutation led to rapid loss in activity and potential loss of cooperativity between the two monomers. Previous evidence for the sigmoidal binding curve includes positive cooperativity found between the binding sites of a MtAroB dimer, reducing the equilibrium dissociation constant for binding from 167 to

0.3 µM, if one DAHP molecule is already bound (Dutra De Mendonça et al., 2011). Two of the mutant proteins generated within this work, His249 and Lys323, had previously been produced, and a similar loss of activity was found (Zhu et al., 2018). Direct comparison is not possible, due to the end-point approach used versus the continuous assay approach used herein. The other mutants which led to loss of activity were Asp138 and His249, confirming their essentiality to protein activity. The CD spectra for the MtAroB wild type and mutants is also similar to a previous spectra (Zhu et al., 2018), highlighting correct folding of the protein and that any loss of activity is due to the mutagenesis and not incorrect folding.

The majority of the inhibition studies performed on the AroB protein have been based around biochemical assay inhibition (Liu et al., 2008; Chandran and Frost, 2001; Arrow Therapeutics, 2001; Zhu et al., 2018). Only two studies used a biophysical method to evaluate drug binding, opting for surface plasmon resonance (Neetu et al., 2020; Zhu et al., 2018). Hence, the current work has filled this gap, by providing examples of orthogonal biophysical assays, alongside supporting data, which could confirm binding and validate biochemical assay hits. For higher throughput uses, both the tryptophan fluorescence and DSF assays could be scaled and allow screening of many compounds. The former assay may identify a greater number of hit compounds, as both NAD and DAHP had a strong signal, while in the later, only DAHP caused protein stabilisation. MST could then be utilised for more detailed binding analysis and binding constant determination. The only assay which could provide evidence of chlorogenic acid binding to the MtAroB protein was tryptophan fluorescence, as chlorogenic acid interfered with the biochemical assay, DSF and MST. This compound was not

investigated further, due to time limitations, and its lack of inhibition of mycobacteria at 1 mM, the highest tested concentration.

In work undertaken by Alhaji Isa, Singh Majumdhar and Haider, (2018), they performed a 50-ns MD simulation of MtAroB containing the active site zinc ion and found an RMSD of 1.0-1.5 Å away from the input structure, based on PBD=3QBE. This output is very similar to the initial 50 ns cMD simulation performed within this work and suggests the crystal structure represents a local energy minimum. Their study had larger RMSF values for all residues but had similar peaks in RMSF focussed on residues within flexible loop regions such as 259-264 and 322-330. However, they also saw additional regions of flexibility centred around residue 200 and 300. This suggests similar results were achieved despite using different approaches, NAMD vs AMBER. No other MD simulations had been undertaken on the MtAroB protein, preventing a more comprehensive comparison.

The virtual screening of the Prestwick library resulted in the largest molecules being selected in preference to any other compounds docked within the study and a strong correlation was found between size and docking score. The highest scoring molecules found included dihydroergotamine, itraconazole, bromocriptine, telmisartan and irinotecan, which have been identified as the best scoring molecules in several other molecular docking studies against unrelated proteins (Arulanandam, Ragothaman and Kaveriyappan, 2021; Cava, Bertoli and Castiglioni, 2021; Gul et al., 2021; Saha et al., 2022; Zimmermann et al., 2019). This suggests they do not have specificity for binding MtAroB, but rather interfere with virtual screening, due to their size relative to the rest of the screened library.

The virtual screening approach used by Dr Daniel Moscoh has previously identified several active compounds when used against other proteins (Bhusal et al., 2017; Huang et al., 2017; Leung et al., 2021). Unfortunately, against the MtAroB protein, this did not identify any molecules with activity or binding interactions. This could suggest the pre-screening for drug-like molecules eliminated more potent binding molecules, for instance, the phosphonate group on the known carbaphosphonate inhibitor would likely be removed due to the negative charges and associated poor bioavailability (Heidel and Dowd, 2019). The virtual screening was also undertaken against the MtAroB monomer, and hence may generate false positives, as the additional interactions at the dimer interface were not modelled. Alternatively, the relatively small compound library used for screening, approximately 10,000 compounds compared to the >500,000 compounds used in several other screens against other *M. tuberculosis* proteins (Kingdon and Alderwick, 2021), could have limited diversity of potential compound hits. However, this virtual screening effort represented the largest library of compounds docked against MtAroB, compared to 1,490 (Prestwick library, herein), 1,082 (Sivaranjani et al., 2019) and 400 compounds (Alhaji Isa, Singh Majumdhar and Haider, 2018). Excluding the Prestwick library, all three sets of docked compounds had undergone pre-screening to select from larger databases, either for drug-like properties herein, conformational fit relative to the protein's active site (Alhaji Isa, Singh Majumdhar and Haider, 2018), or comparison to carbaphosphonate and other known binding compounds (Sivaranjani et al., 2019).

These hits can also be compared to those found by the other virtual screening approaches. For Alhaji Isa, Singh Majumdhar and Haider, (2018), eleven out of the eighteen best docked molecules had >480 g/mol molecular weight, with 500 g/mol

being the upper limit set for the screen, suggesting a similar size-related bias. The top three hits were PubChem 72341, ZINC633887 and ZINC8983432, with molecular weights of 475.6, 450.0 and 493.7 g/mol, respectively (Figure 2.32). None showed a strong similarity to the hits found herein. For Sivaranjani et al. (2019), only the top two molecules were listed and were not similar to the 31 hits described herein. Both hits had unique central moieties, lead one had a bicyclo[4.3.0]nonane ring, while lead two had a fused isoxazole-bicyclo[3.1.1]heptane ring system (Figure 2.31). Finally, docking of IMB-T130 (Figure 2.31), a compound proven to inhibit MtAroB, has also been undertaken against the protein (Zhu et al., 2018). A docking pose was suggested; however, the docking was undertaken in the absence of the active site zinc ion, and hence predicted hydrophobic interactions between IMB-T130 and the His249 and Asn246 residues. This would place the pyridine ring directly next to the zinc ion and is unlikely to represent the true binding conformation of the molecule.

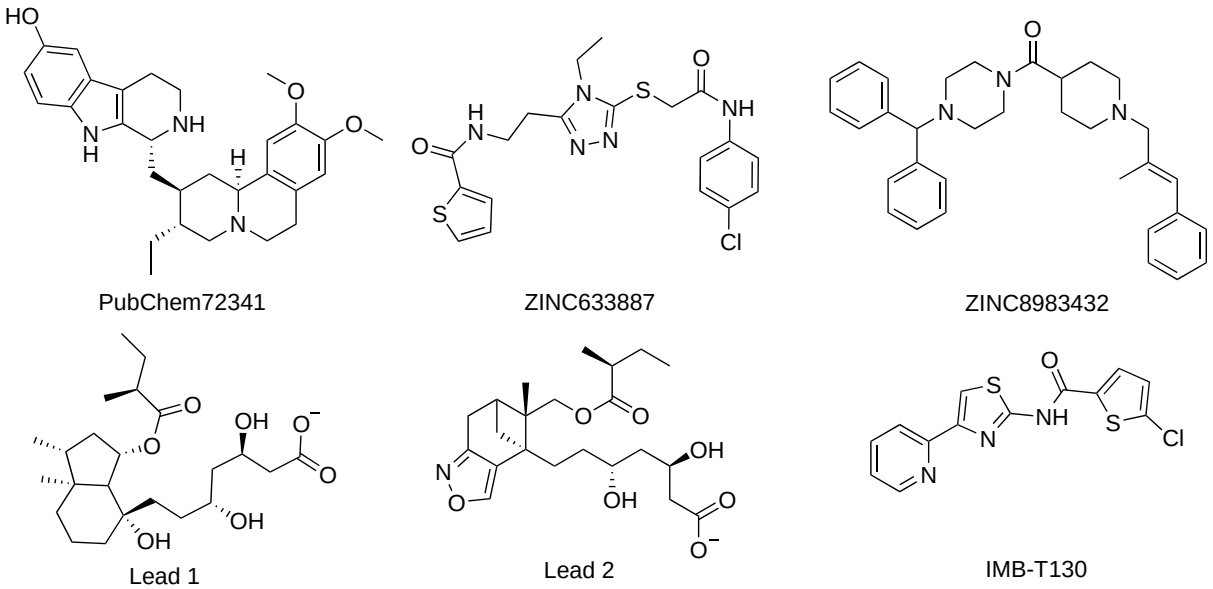


Figure 2.32: Structures of proposed MtAroB inhibitor, alongside tested inhibitor IMB-T130. The upper three compounds are from Alhaji Isa, Singh Majumdhar and Haider, (2018). Leads 1 and 2 are from Sivaranjani et al. (2019). IMB-T130 is from Zhu et al. (2018).

Work within this chapter has resulted in the purification of the MtAroB protein, the development of a biochemical assay, alongside several biophysical assays and the crystallisation of the protein. This provides the tools to perform a screening cascade against the MtAroB protein, providing several options for orthogonal confirmation of hit compounds. Future screening approaches could also utilise the computational predictions of MtAroB conformers, to provide more information about drug-protein interactions.

3. Mode of Action Determination of Vanoxerine Against Mycobacteria

Parts of this chapter were adapted from a pre-print/publication on the vanoxerine mechanism of action, of which AK was the lead author (Kingdon et al., 2022, 2023).

3.1. Introduction

Vanoxerine (also known as GBR12909, Figure 3.1) is a synthetic drug compound, with activity as a dopamine reuptake inhibitor. A recent study screened the Prestwick library, which contains approximately 1,500 drugs, of which the majority have approval for a large range of clinical implications. Their activity was determined against *M. smegmatis* and *M. bovis* BCG (Kanvatirth et al., 2019). During this screen, vanoxerine was one of the identified hits and further confirmation of its MIC_{99} was undertaken against *M. smegmatis, M. bovis* BCG and *M. tuberculosis* H37Rv (Kanvatirth et al., 2019). Vanoxerine had previously been found to have activity against *M. tuberculosis* H37Rv during an earlier screening of the Prestwick library, with an MIC_{99} of 6.5 µg/mL, but was ranked as medium level potency and not progressed further (Ananthan et al., 2009).

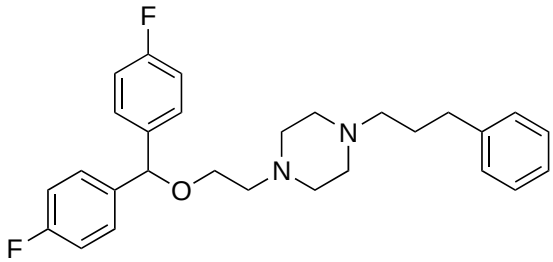


Figure 3.1: Structure of vanoxerine (GBR12909).

The initial discovery of vanoxerine was based on work studying the effects of diphenhydramine and orphenadrine for their impact on the uptake of noradrenaline and serotonin (Van Der Zee and Hespe, 1973). This provided the diphenylmethoxy group of vanoxerine, likely as one determinant of its central nervous system bioactivity.

Later work involved addition of halogens onto the phenyl rings, leading to increased potency (Van Der Zee and Hespe, 1978). Finally, the replacement of the terminal amine with a piperazine ring linked to a phenylpropane group, led to specific activity against dopamine reuptake, rather than broad spectrum inhibition (Van Der Zee et al., 1980).

Following these *in vitro* studies on activity, the *in vivo* effects of vanoxerine were also explored, culminating in a clinical trial focussing on treatment of cocaine dependency. This passed the phase I clinical trial, being well tolerated in healthy volunteers (Lewis et al., 1999; Schmitt et al., 2008), however, no further clinical research has been undertaken for this application. This appears to be due to lack of resources within this clinical area, rather than issues with vanoxerine itself.

Vanoxerine was also investigated for use as an antiarrhythmic drug, as it impacts the hERG potassium and calcium channels of the heart (Lacerda et al., 2010). It was found to have no adverse effects on healthy volunteers in a phase I clinical trial and a phase II clinical trial showed its ability to treat atrial fibrillation (Lacerda et al., 2010; Laguna Pharmaceuticals, Inc., 2015; Cakulev et al., 2011; Obejero-Paz et al., 2015). However, a phase III clinical trial was stopped early, after only 41 patients admitted, due to adverse effects on the heart in the treatment group, specifically ventricular proarrhythmia in three individuals, with one going on to develop torsades de pointes (Piccini et al., 2016). All three patients had structural heart disease, a condition present in two-thirds of the patients enrolled in the trial, hence, its early termination (Piccini et al., 2016).

Despite this outcome, vanoxerine has been well-tolerated in healthy volunteers and thus could be repurposed for use against mycobacteria (Søgaard et al., 1990; Preti,

2000; Lacerda et al., 2010; Laguna Pharmaceuticals, Inc., 2015). Further trials are required to study its effects on other patient groups and confirm its safety in the absence of structural heart disease (Piccini et al., 2016; Geng, Lin and Nguyen, 2020). As the human targets of vanoxerine are already known, future developments could focus on reducing activity on dopamine reuptake, while retaining its antimycobacterial activity. Potential side effects would be easier to monitor at each stage of drug development.

Although, the antimycobacterial properties of vanoxerine were previously discovered (Kanvatirth et al., 2019; Ananthan et al., 2009), the mechanism of action against mycobacteria was not validated. In the previous study, AroB was suggested as the mycobacterial target of vanoxerine, based on *M. smegmatis* resistant mutants grown in the presence of drug, all containing mutations within the *aroB* gene (Kanvatirth et al., 2019). A follow-up experiment undertaking constitutive overexpression of the protein led to a shift in the MIC of vanoxerine, compared to an empty vector control (Kanvatirth et al., 2019). However, this did not provide direct evidence of an *in vitro* interaction. As shown in Chapter 2, the purified Mt-AroB protein did not show any interactions with vanoxerine. Within this chapter, work was undertaken to investigate if vanoxerine acted against AroB *in vitro* and explore other potential mechanisms of action. In addition, several structural analogues of vanoxerine were synthesised and tested for efficacy against mycobacteria. Finally, vanoxerine had additional antibacterial effects against Gram-positive species, so work was undertaken to explore its impact on these species.

3.2. Results

3.2.1. MtAroB overexpression did not affect vanoxerine resistance

AroB was implicated as the target of vanoxerine (Kanvatirth et al., 2019), hence, the *M. tuberculosis aroB* gene was re-cloned into pVV16 and also cloned into pTIC6a, to allow both constitutive and inducible overexpression. This cloning is outlined in Appendix 1. These plasmids were then transformed in *M. smegmatis*, to allow the effects of AroB over-expression to be observed. As displayed in Figure 3.2, no shift in the percentage survival curves occurred when comparing the overexpression strain to its associated empty-vector control. The only shift which occurred, was in the pTIC6a vector strains, which required the addition of 200 ng/mL ATc to induce protein

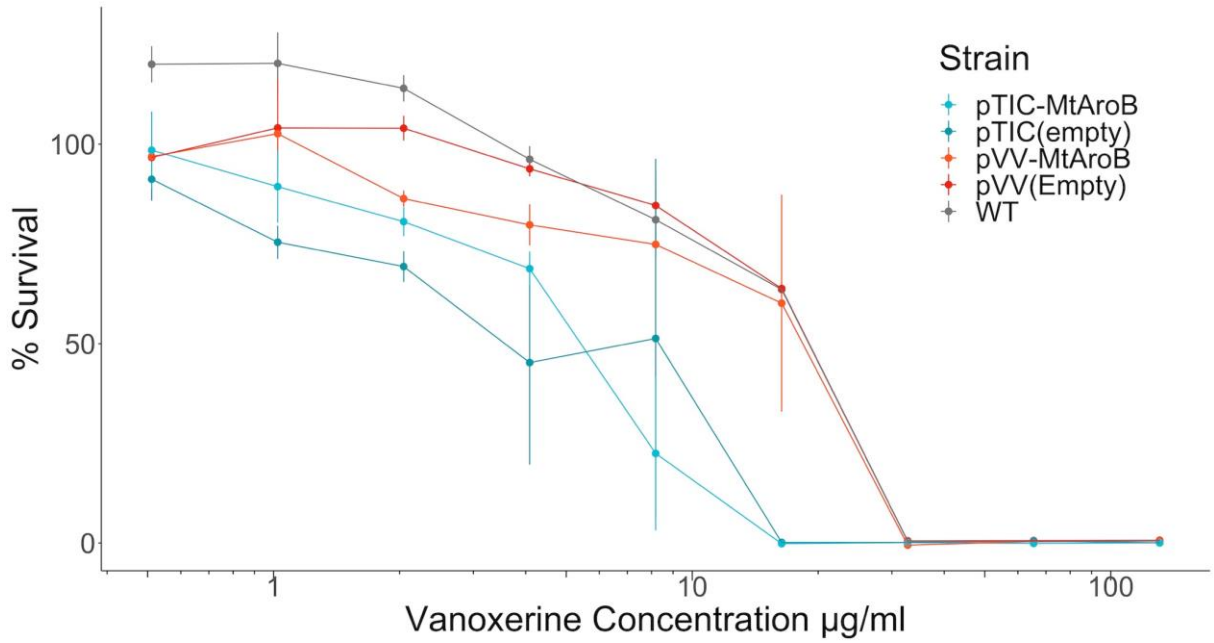


Figure 3.2: Percentage survival curves of *M. smegmatis* overexpressing MtAroB, showing no shifts in MIC_{99} compared to empty vector controls. Cultures were grown from OD_{600} 0.05 in the presence of a vanoxerine serial dilution, for 21-hours, before resazurin was added for 3-hours to quantify survival. The %survival is calculated relative to rifampicin and DMSO only controls. N=3. Taken from Kingdon et al. (2022).

expression and hence their MIC_{99}s were shifted from 32.7 µg/mL to 16.4 µg/mL (Figure 3.2).

The lack of shift in percentage survival curves is in direct contrast to the previously reported results, which showed a shift of just over two-fold. However, as shown in Chapter 2, vanoxerine did not interact with purified MtAroB, suggesting a shift was unlikely to occur.

3.2.2. *aroB* mutations are unlikely to cause resistance

As vanoxerine did not appear to be affected by AroB over-expression, the original spontaneous resistant mutants, found in the previous study, were investigated in more detail (Kanvatirth et al., 2019). The four 'resistant mutants' present in the *M. smegmatis aroB* gene following vanoxerine treatment would have no effect on the *M. tuberculosis*

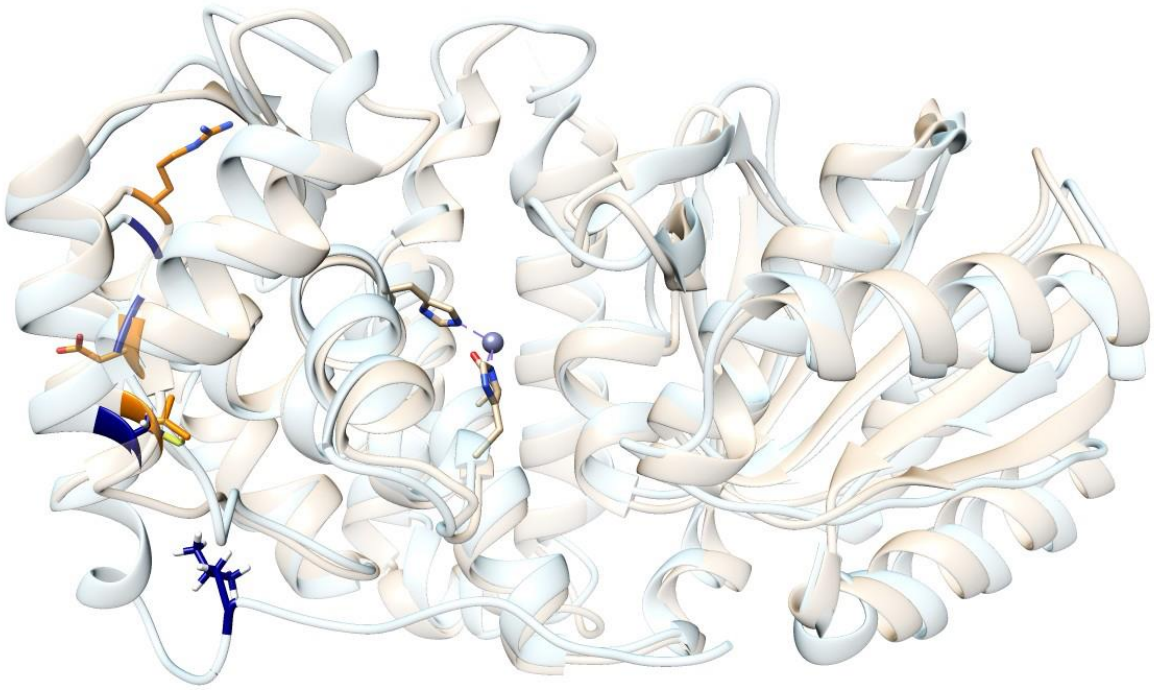


Figure 3.3. Overlay of MtAroB (PDBE=3QBE, khaki) and MsAroB (ITASSER MODEL, blue) structures, highlighting the resistant mutant residues in MsAroB (navy) and equivalent MtAroB residues (orange). The active site zinc and coordinating residues are also shown.

AroB protein. One mutation, conferring a L363P amino acid substitution, is in a terminal unstructured region not present in the *M. tuberculosis* protein. The remaining three mutations convert the AroB *M. smegmatis* amino acid residues into the equivalent residues already present in the *M. tuberculosis* AroB protein (Figure 3.3, PDB = 3BQE). The overlay structure depicted also indicates all four mutations alter protein residues far from the AroB active site. In addition, these residues are not widely conserved across homologous AroB proteins (Figure 2.3B).

Alongside this *in silico* investigation, the laboratory strain of *M. smegmatis* used within the previous and current work, was sent for whole-genome sequencing (WGS), as both sets of work were conducted in the Alderwick group. The genomic sequence was then compared to a reference *M. smegmatis* mc^2155 genome (GCA_000283295.1) for all mutations. The full list of SNPs and Indels are provided in Appendix 5. In Table 3.1, the mutations in the *aroB* gene, found in the lab strain from WGS, are compared to 'resistant mutants' published in the previous study (Kanvatirth et al., 2019). As displayed, all three missense mutations are identical, and the frameshift mutation caused the same amino acid substitution. Given these *aroB* mutations are present as background in the laboratory strain of *M. smegmatis*, which vanoxerine can inhibit (Table 3.1), it is highly unlikely AroB represents a true target of vanoxerine. Given the only potential mycobacterial target of vanoxerine was disproven, the mechanism of action remained unknown.

Table 3.1: Comparison of *aroB* mutations in the *M. smegmatis* lab strain and 'resistant mutants' to vanoxerine found in *M. smegmatis.*

aroB mutations present in lab strain			*aroB* mutations reported following vanoxerine treatment (Kanvatirth *et al.* 2019)		
Mutation type	**Position**	**Amino acid substitution**	**Mutation type**	**Position**	**Amino acid substitution**
Missense	Ggg to Agg (844)	G282R	Missense	Ggg to Agg	G282R
Missense	gGc to gAc (851)	G284D	Missense	gGc to gAc	G284D
Frameshift	T to GTG (1066)	C356V (and early stop codon)	Frameshift	Tgc to GTtgc	C356V
Missense	cTa to cCa (1088)	L363P	Missense	cTa to cCa	L363P

3.2.3. Minimum Inhibitory Concentrations (MICs)

As there was a discrepancy between the previously published data and current findings, the MIC data was repeated to confirm whole-cell activity. In addition, the spectrum of activity of vanoxerine was evaluated, by performing MICs against clinically relevant Gram-positive (*Enterococcus faecium* and *Staphylococcus aureus*) and Gram-negative (*Acinetobacter baumannii, Klebsiella pneumoniae* and *Pseudomonas aeruginosa*) species, alongside *C. glutamicum* and *B. subtilis*. The MIC_{99} was found by calculating a percentage survival value for every drug concentration tested, normalised relative to DMSO and known antibiotic controls (rifampicin for *C. glutamicum*, *K. pneumoniae*, mycobacteria and *S. aureus*; apramycin for *A. baumannii*; kanamycin for *P. aeruginosa;* and Biocleanse for *E. faecium*). Plots of this data are displayed in Figure 3.4. The MIC_{99} is the lowest drug concentration which caused one percent or lower survival (Table 3.2). Although the liquid MIC_{99} found for *M. bovis* BCG was higher than *M. tuberculosis*, the solid agar MIC_{99} was comparable, at 15.2 µg/mL.

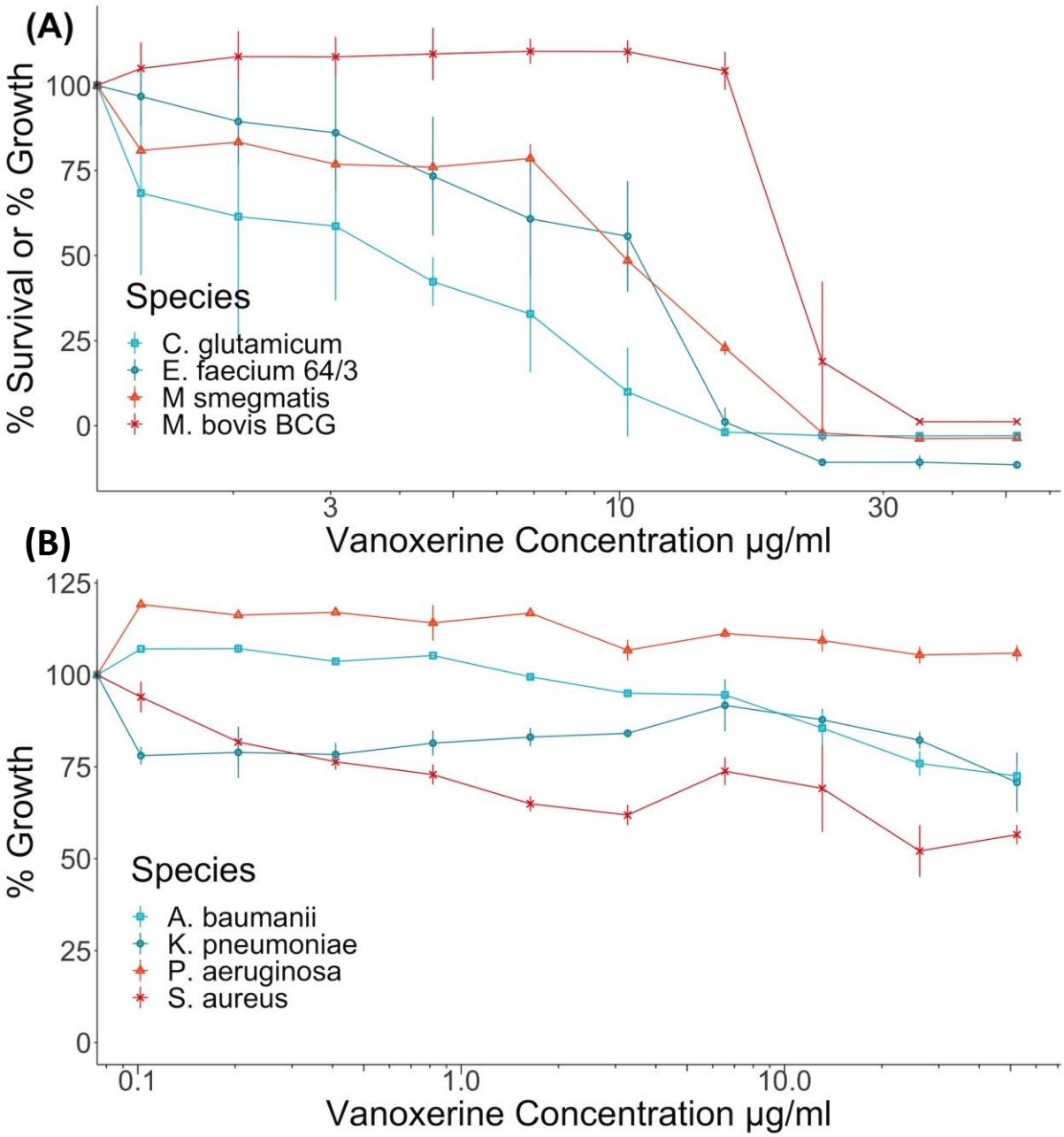


Figure 3.4: Vanoxerine treated cells %Survival or %Growth. (A) Species vanoxerine could inhibit. (B) Species vanoxerine had limited activity against. Bacterial cultures were diluted from mid-log to OD_{600} 0.05 and added to a serial dilution (2:3, or 1:2) of vanoxerine and incubated for 21 (*M. smegmatis*), 23 (*C. glutamicum*), 24 (*A. baumannii, E. faecium, K. pneumoniae, P. aeruginosa* and *S. aureus*) or 144 (*M. bovis* BCG) hours. For *C. glutamicum*, *M. smegmatis* and *M. bovis* BCG, resazurin was added and the plate was re-incubated for 1, 3 or 24 hours, respectively. The resorufin fluorescence was measured. For the remaining species, the OD_{600} was measured. The %survival or growth was calculated relative to DMSO only and antibiotic controls. Taken from Kingdon et al. (2022).

Table 3.2: Minimum inhibitory concentrations (MIC_{99}) of vanoxerine against representative species. Parts of this table were published in Kingdon et al. (2023).

Species	MIC_{99} (µg/mL)
M. smegmatis (Moynihan lab strain)	23
M. smegmatis (Alderwick lab strain)	35
M. bovis BCG	26
M. tuberculosis H37Rv	14 (Kanvatirth et al., 2019)
B. subtilis	52
C. glutamicum	15.5
E. faecium 64/3	23
E. faecium E745	23
S. aureus	>52
A. baumannii	>52
K. pneumoniae	>52
P. aeruginosa	>52

The selectivity of vanoxerine for mycobacteria and Gram-positive species was clear, with low MIC_{99} values for *M. tuberculosis* and *C. glutamicum* of 14 and 15.5 µg/mL, compared to greater than 52 µg/mL for *A. baumannii* and *P. aeruginosa*. No antibacterial activity was exhibited against the Gram-negative species tested (Table 3.2). This included experiments performing ethylenediaminetetraacetic acid (EDTA) permeabilisation of the outer membrane (Figure 3.5). For both *A. baumannii* and *K. pneumoniae*, there was a limited impact of EDTA-permeabilisation on their inhibition by vanoxerine. However, EDTA-permeabilised *P. aeruginosa* was reduced to 52% growth at 52 µg/mL vanoxerine, compared to unaffected growth in the absence of pre-treatment. Overall, this suggests a Gram-negative target is less likely, but cannot be ruled out, due to the shift in *P. aeruginosa* growth. The mode-of-action may be more effective against Gram-positive species and mycobacteria. Amongst Gram-positive species, there appears to be some specificity, as *C. glutamicum* and *E. faecium* were inhibited more strongly, *B. subtilis* was only inhibited at the highest tested

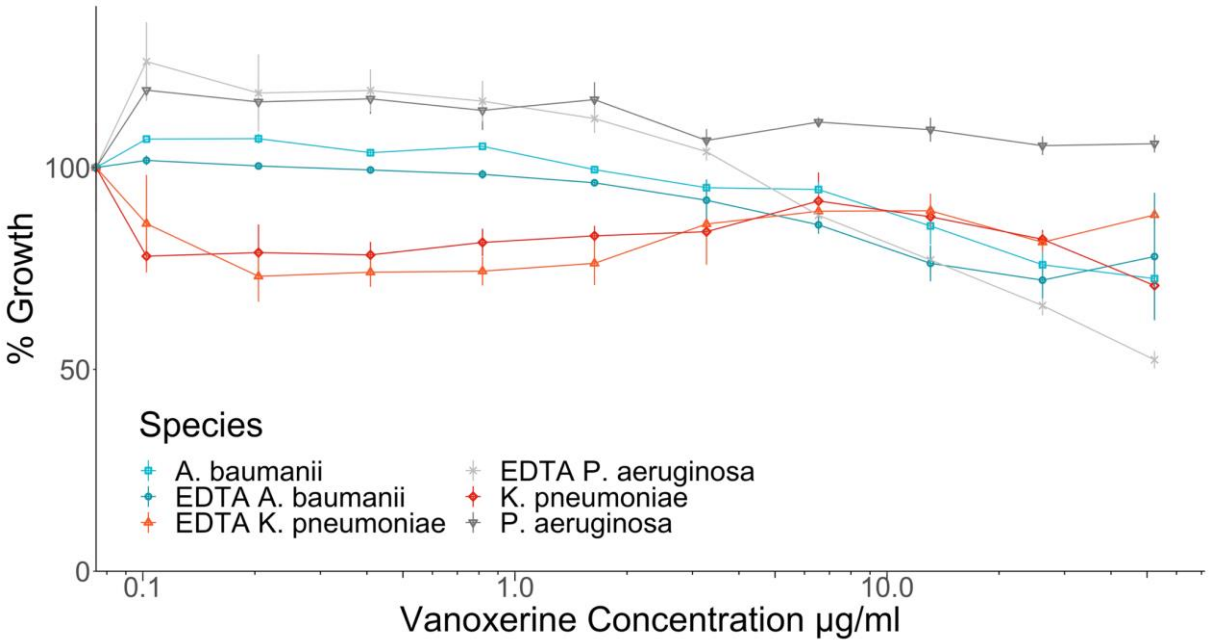


Figure 3.5: Vanoxerine percentage growth curves of *A. baumannii*, *K. pneumoniae* and *P. aeruginosa*, either untreated or following EDTA-mediated permeabilisation. Cells were incubated at room temperature in 3 mM EDTA, 50 mM Tris-HCl pH 7.8 for 30 minutes. Following washing in PBS, cells were resuspended in LB broth and added to a vanoxerine 1:2 serial dilution. The plates were incubated for 24-hours, before the OD_{600} was measured and percentage growth was calculated relative to DMSO and antibiotic controls. N=3. Non-EDTA treated conditions are included for reference.

concentration and no effect was found against *S. aureus*. Until the mechanism of action of vanoxerine is determined, the exact reasoning for these differences remain unknown. The antibiotic resistance of *E. faecium* did not have an impact on the MIC_{99}, both *E. faecium* strains tested were clinical isolates, with 64/3 being rifampicin and fusidic acid resistant, while E745 is also vancomycin resistant. However, these resistance mechanisms did not impact vanoxerine susceptibility.

3.2.4. Monitoring killing of mycobacteria

MICs provide an endpoint output as a proxy for growth inhibition and highlight whether a compound has activity within a 24-hour or seven-day (*M. bovis* BCG) timeframe.

However, this provides no information on the speed at which a compound can impact growth. In an effort to monitor the activity of vanoxerine in an ongoing manner, several assays were performed.

One approach undertaken was monitoring the production and fluorescence of the GFP protein, as a proxy for growth. Fluorescence monitoring was chosen in preference to absorbance, as the OD_{600} can be difficult to monitor using a plate reader, due to the clumping of mycobacterial cells. Initially, *M. smegmatis* and *M. bovis* BCG were transformed with the pSMT3-eGFP plasmid to induce continuous production of GFP, this plasmid was produced by Dr Sarah M. Batt, derived from the original pSMT3 vector (Herrmann et al., 1996). The *M. smegmatis* + GFP strain was monitored for fluorescence production in the presence of DMSO (1%) or vanoxerine ranging from 0.5x to 5x MIC (13 to 130 µg/mL), Figure 3.6A. Across the 16-hour timeframe, *M. smegmatis* produced GFP in conditions containing up to 1x MIC vanoxerine, although lower amounts of GFP were produced in its presence, with ~15,000 RFU in DMSO, ~10,000 in 0.5x MIC and ~5,000 in 1x MIC. The presence of vanoxerine also appeared to delay the production of GFP, in DMSO, a deviation in fluorescence can be observed 5-6 hours into the assay, whereas a deviation is delayed until 10-11 hours into the assay in the presence of 1x MIC vanoxerine.

Due to the reduced well volume size of the 96-well plates and the risk of the plate drying out over the assay timeframe, the *M. bovis* BCG growth curves were performed in 12-well plates. At each timepoint, every 24-hours, a sample was then transferred to a 384-well plate, for reading. A similar decrease in overall GFP production and delay in fluorescence increase was observed following vanoxerine treatment of *M. bovis* BCG (Figure 3.6B). GFP production, above the baseline, could be observed at 96-

hours in the absence of vanoxerine, but was delayed until 120-hours in 0.3x MIC vanoxerine and was not observable at 144-hours in 0.6x MIC vanoxerine.

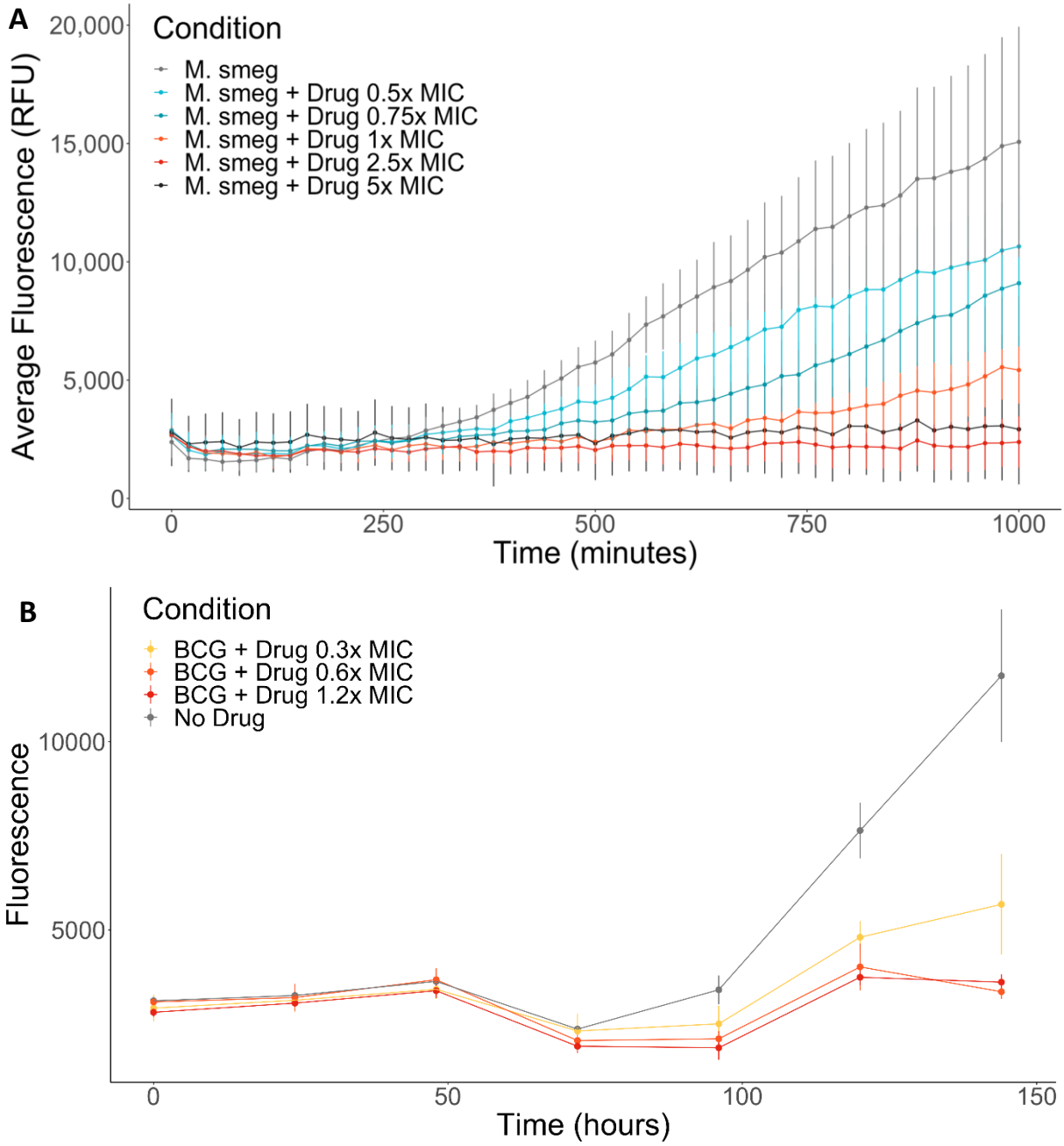


Figure 3.6: Growth curves of mycobacteria expressing GFP, grown in the presence of vanoxerine, showing growth inhibition (A) *M. smegmatis* + GFP growth. (B) *M bovis* BCG + GFP growth. Mid-log *M. smegmatis* or *M bovis* BCG + pSMT3-GFP was diluted to OD_{600} 0.05 and added into a 96- or 12-well plate, with or without vanoxerine. For *M. smegmatis* the GFP fluorescence was monitored directly in a plate reader. For *M. bovis* BCG, every 24-hours, a sample (50 µL) was taken, and the fluorescence measured. Background fluorescence was removed, to calculate the RFU = Relative Fluorescence Units. MIC = 26 µg/mL. N= 3.

While monitoring GFP production can be used as a proxy for growth, the stability of GFP prevented killing being monitored, as the protein was not degraded. This led to a baseline fluorescence due to GFP, even in the presumed absence of growth. Hence, an alternative assay was trialled.

The RealTime Glo™ MT Cell Viability Assay kit was used to monitor viability of *M. smegmatis* during vanoxerine treatment, based on a luminescence output. In this assay, viable cells can reduce the assay kit's starting material, converting it into a substrate of the NanoLuc® luciferase enzyme (Figure 3.7A). If the cell has been killed, then it can no longer reduce the assay substrate. The NanoLuc® luciferase enzyme can then turnover the substrate to produce light, as a proxy for viability. *M. smegmatis* was grown in the presence of the assay starting material and either DMSO, rifampicin or vanoxerine (Figure 3.7B). This indicated within 2-3 hours, *M. smegmatis* was no longer viable, following 2x MIC vanoxerine treatment, as limited luminescence was produced after this timepoint. Both 1x MIC rifampicin and vanoxerine appeared to cause a loss of viability after 6-hours of treatment. Whereas total loss of viability at 0.5x MIC vanoxerine did not occur in the 10-hours assay window. The untreated *M. smegmatis* had a large increase in luminescence across the same timeframe, as the cells could have divided up to 3 times across this timeframe. Overall, this approach suggested vanoxerine may reduce cellular viability within 6-hours, at 1x MIC.

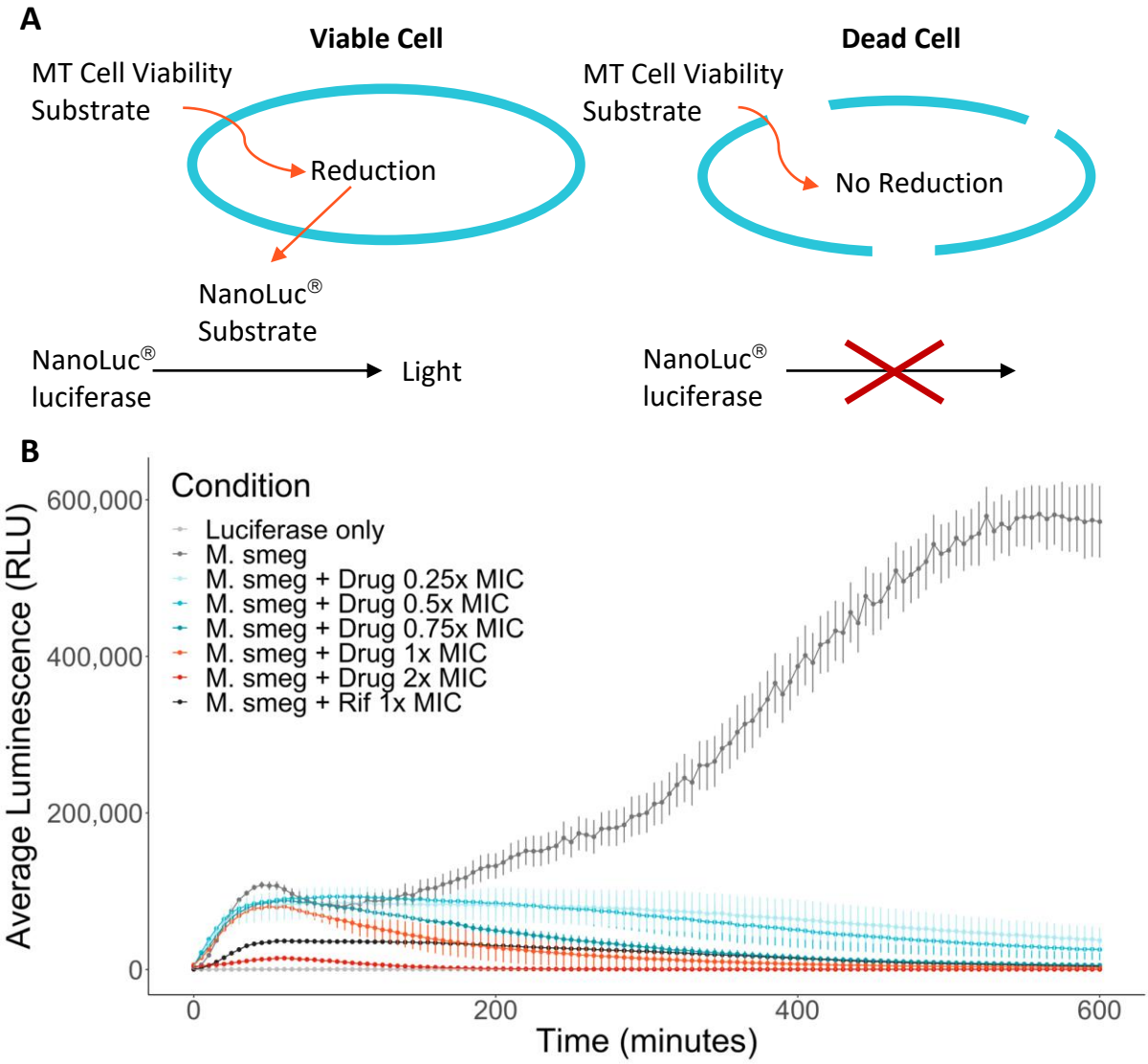


Figure 3.7: RealTime Glo™ MT Cell viability assay. (A) Diagram of the RealTime Glo™ assay on viable vs dead cells. (B) Impact of vanoxerine on the viability of *M. smegmatis*, assessed using RealTime Glo™. *M. smegmatis* was grown until mid-log, before being diluted to OD_{600} 0.1 and combined with pre-warmed 7H9 containing RealTime Glo enzyme/substrate. The diluted culture was added to a pre-warmed 96-well plate, containing drug compounds, and the luminescence monitored. Rif = Rifampicin. RLU = Relative Luminescent Units. Drug MIC = 26 µg/mL. N=3

3.2.5. Monitoring ATP levels in response to vanoxerine treatment

To allow monitoring of the ATP levels of mycobacteria in response to drug treatment, a luciferase-based system was developed. Mycobacteria would express the luciferase protein, followed by external addition of the D-luciferin substrate, and produce light relative to the internal ATP levels. The design of the FFLucRT gene sequence was taken from (Andreu et al., 2010, 2013), encoding a firefly luciferase protein, with a red-shifted light output. The pMV306-FFLucRT plasmid was cloned by Twist Biosciences, with the *hsp60* promoter region used for constitutive expression. This plasmid was then transformed into *M. smegmatis*, to allow continuous monitoring of ATP levels.

An initial assay run was undertaken monitoring ATP level across 16-hours, with drug treatment and D-luciferin addition occurring concurrently (Figure 3.8A). The DMSO treated control showed an initial luminescence of approximately 8,700 relative luminescence units (RLUs), which dropped to a minimum of 1,400 RLUs after 2-hours, followed by a steady increase to 20,000 RLUs after 16-hours. Both ethambutol and rifampicin were included as control drugs, to monitor a 'generic' drug response. These drugs both had a higher initial luminescence of 10,000 RLUs, followed by a more rapid decrease, reaching approximately 1,000 RLUs after 2-hours and continuing to decrease to 300 RLUs after 16-hours. For vanoxerine, a concentration dependent spike in luminescence was observed; addition of 52 µg/mL led to an initial luminescence of 79,000 RLUs, while 7 µg/mL led to a 24,000 RLUs spike. The luminescence values also rapidly decreased, reaching 2,700 RLUs and 1,800 RLUs after 2-hours for 52 and 7 µg/mL vanoxerine, respectively. All vanoxerine values near or above the MIC_{99} (26 µg/mL) continued to cause a decrease in luminescence, while all values below 16 µg/mL eventually led to an increase in luminescence, as not all the cell population was killed.

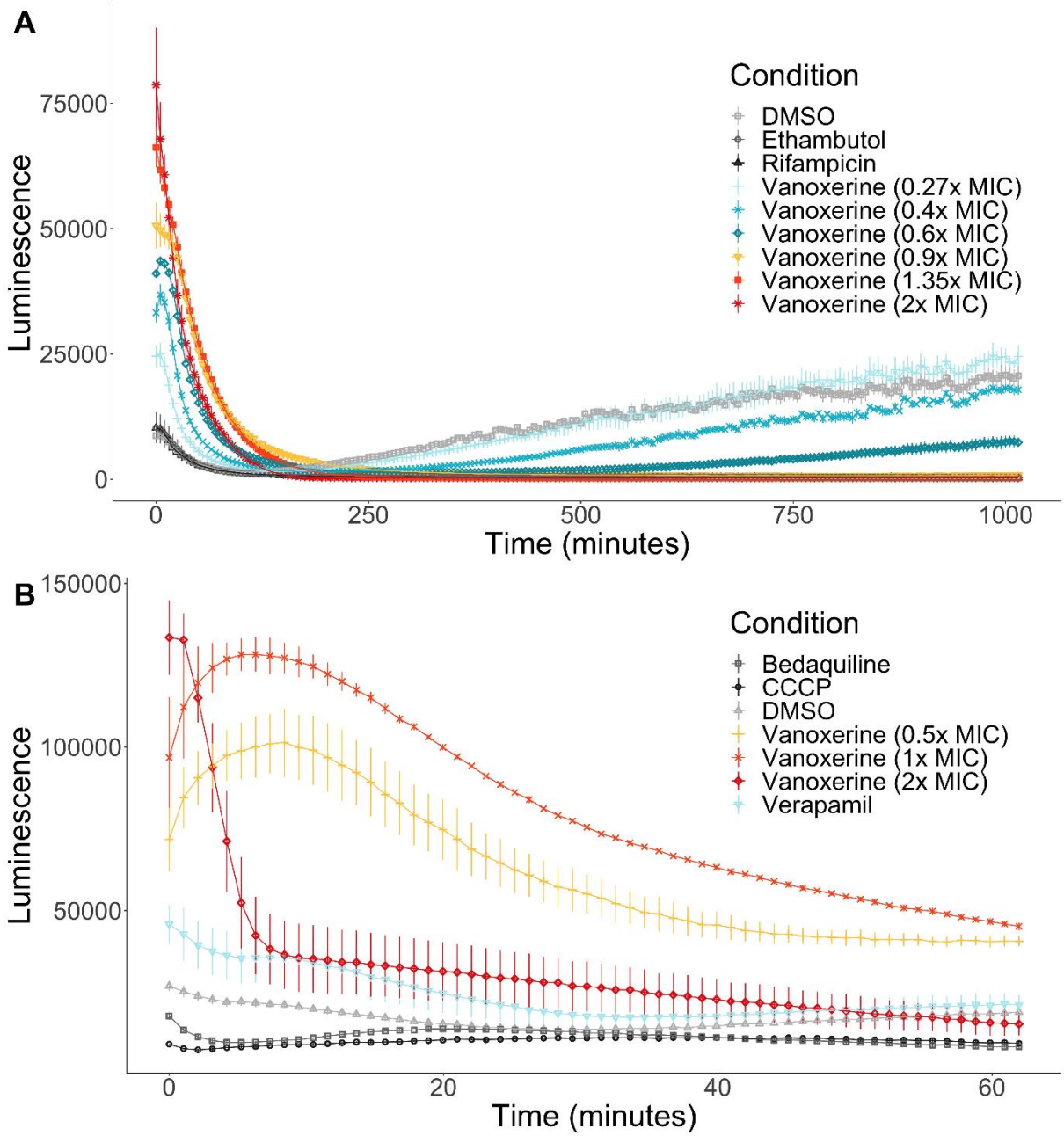


Figure 3.8: ATP levels spiked in a concentration dependent manner following vanoxerine treatment. (A) 16-hour growth curve of *M. smegmatis* FFLucRT over-expressor. (B) 1-hour monitoring of the *M. smegmatis* FFLucRT over-expressor. Cells were diluted to OD_{600} 0.1 in 7H9 containing 0.15 mM D-luciferin. The diluted cells were immediately added a 96-well plate containing drug compounds. The luminescence was monitored for 16- or 1-hour, at 5- or 1-minute intervals. N=3. DMSO = 1%, ethambutol = 100 µg/mL, rifampicin = 10 µg/mL, bedaquiline = 0.5 µg/mL, CCCP = 25 µM, verapamil = 50 µg/mL.

As details of the initial luminescence spike were missing from the growth curve style assay (Figure 3.8A), a smaller scale experiment was set-up to allow faster monitoring of the luminescence levels (Figure 3.8B). Several control compounds were used, including bedaquiline, carbonyl cyanide *m*-chlorophenyl hydrazone (CCCP) and verapamil. These were used to cover a wider range of mechanisms not highlighted by ethambutol or rifampicin. For DMSO, an initial luminescence of 27,000 RLUs was found, reducing to a minimum of 13,000 RLUs at 28-minutes, and returning to 19,000 after 60-minutes. Both bedaquiline and CCCP had lower initial luminescence at 18,000 and 9,000 RLUs, which fluctuated around 10,000 RLUs for the 60 minutes. In contrast, verapamil had a higher initial fluorescence at 46,000 RLUs, dropping to a minimum of 17,400 RLUs at 34-minutes and increasing to 21,000 RLUs after 60-minutes. Vanoxerine again displayed a concentration dependent initial luminescence spike, reaching 133,000 RLUs at 52 µg/mL and 72,000 RLUs at 13 µg/mL. The highest vanoxerine concentration caused a rapid loss in luminescence across the first 8-minutes, followed by a slower decrease to 15,000 RLUs after 60-minutes. The other vanoxerine treatment conditions had peaks in luminescence within the first 8-minutes, followed by slow decreases to 45,000 and 40,000 RLUs for 26 and 13 µg/mL vanoxerine, respectively.

3.2.6. Resistance to vanoxerine could not be developed in mycobacteria

One approach undertaken to discover protein targets of compounds, is the generation of spontaneous resistant mutants. (Abrahams and Besra, 2020). For this work, spontaneous resistant mutant generation was attempted in *M. bovis* BCG, however, no colonies grew, even at 2x MIC_{99} of vanoxerine (30 µg/mL). In an attempt to increase

the likelihood of resistance development, a Δ*recG* mutant strain of *M. bovis* BCG was used, with an increased mutation rate (Ley et al., 2019; Batt et al., 2015). However, this strain also failed to acquire spontaneous resistant mutants. Overall, this suggested the rate of resistance is lower than 10^8. Resistant development was not attempted in *M. smegmatis*, as this had already been performed in the previous study and only led to false leads (Kanvatirth et al., 2019). The low rate of resistance development is promising for future use; however, additional work was undertaken with the aim of identifying a potential target.

3.2.7. Homologues of human targets of vanoxerine

As the human targets of vanoxerine have already been characterised, one route of exploration was searching for mycobacterial homologues of these known protein targets. Homologues were found using the Phyre2 webserver, the original purpose being predictions of protein structures, however, the BackPhyre functionality allows input proteins to be compared to all protein structures from a particular organism (Kelley et al., 2015). If no input protein structure was available, then BackGene was utilised, which predicts the protein structure of the input gene sequence, before undertaking protein-protein comparisons (Kelley et al., 2015).

The human dopamine transporter SLC6A3 had no crystal structure, so BackGene was used to predict putative *M. tuberculosis* protein homologues (Table 3.3). This included many high confidence hits, with amino acid coverage over a majority of the input protein sequence. To reduce the number of homologues for downstream testing, several criteria were decided: presence of an *M. smegmatis* homologue; gene essentiality in *M. tuberculosis* and global root-mean-square-deviation (RMSD)

between the dopamine transporter and *M. tuberculosis* homologue. Only seven of the twelve predictions had *M. smegmatis* homologues and of these, two had RMSD values deemed too high, at 14.331 and 28.13 Å. Gene essentiality was not useful as a deciding factor, as almost none of the proteins were essential. Finally, visual inspection of the predicted homologues was undertaken, by overlaying the two Alpha-Fold structures and looking at the binding site cavity. The binding site was determined by comparison to the location of cocaine binding to the Drosophila dopamine transporter (PDB=4XP4), as vanoxerine has been reported to bind ~50 times more strongly than cocaine (Izenwasser, Werling and Cox, 1990). Only two protein structures had predicted binding cavities that were visually similar to the dopamine transporter. These were Rv0924c (MntH), a predicted divalent metal cation transporter, and Rv1999c, a putative amino acid/polyamine antiporter.

A similar process was undertaken for the hERG potassium ion channel, as vanoxerine blocks this channel (Lacerda et al., 2010). The crystal structure of the potassium channel has been solved (Wang and MacKinnon, 2017), so this was used for predictions (PDB=5VA2). As shown in Table 3.3, this led to only one strong prediction which had 79% coverage of the input protein, compared to 23% or lower coverage for the remaining predictions. This was Rv2434c, a putative mechanosensitive channel with sites for cyclic nucleotide binding.

Table 3.3: *M. tuberculosis* predicted structural homologues of vanoxerine's human targets. The protein structures/predictions were from *M. tuberculosis* CDC1551, giving MT codes as the initial gene outputs. These were compared to the Rv and MSMEG numbers for homologues. Gene essentially was based on (DeJesus et al., 2017; Minato et al., 2019). Global RMSD was found using Chimera to compare the AlphaFold prediction of each protein pair.

Rv Number	Phyre Confidence Score	Coverage	MT Code	*M. smegmatis* Homologue?	Essential in *M. tuberculosis?*	Global RMSD from Input
		Dopamine Transporter SLC6A3 – 620 amino acid length				
Rv3454	99.3	582	3561	No	No	11.06 Å across 339 pairs
Rv2127 – AnsP1	99.0	562	0361	No	No	9.09 Å across 422 pairs
Rv3253c	99.0	560	3551	MSMEG_1838	No	9.04 Å across 436 pairs
Rv1979c	98.6	533	2031	MSMEG_1508	No	9.44 Å across 435 pairs
Rv1704c - CycA	98.6	567	1744	MSMEG_3587	No	14.31 Å across 452 pairs
Rv0346c – AnsP2	98.4	533	2186	No	No	7.78 Å across 427 pairs
Rv0924c - MntH	98.4	497	0951	MSMEG_5589	No	7.26 Å across 379 pairs
Rv2320c - RocE	98.2	549	2383	MSMEG_1412	No	8.60 Å across 424 pairs
Rv1999c	98.2	551	2055	MSMEG_0812	No	10.52 Å across 421 pairs
Rv2690c	97.8	565	2764	MSMEG_2772	Sometimes	28.13 Å across 403 pairs
Rv0917	97.6	263	0942	No	No	27.24 Å across 457 pairs
Rv0522	97.1	513	0544	No	No	8.24 Å across 412 pairs
		hERG Potassium Channel – 533 amino acid length				
Rv2434c	100.0	423	2508	MSMEG_0028	No	
Rv0998	99.8	118	1027	MSMEG_5458	No	
Rv2565	99.7	121	2641	No	No	
Rv0104	99.6	116	0113	No	No	
Rv1364c	99.5	116	1410	No	No	

These three genes were cloned into the pMV306 vector by Twist Biosciences, with the *hsp60* promoter used for constitutive over-expression. In addition, Rv1607, a predicted calcium channel was also cloned, as vanoxerine was shown to block cardiac calcium channels (Lacerda et al., 2010). BackPhyre could not be used to predict structural homologues of the $Ca_V3.2$ channel, due to protein size limitations of the webserver. The cloned vectors were transformed into *M. smegmatis*, to study the effects of constitutive overexpression on the resistance to vanoxerine treatment.

As shown in Figure 3.9, there was a limited shift in the MIC_{99} of vanoxerine, following overexpression of the putative structural homologues within *M. smegmatis*. While overexpression of either Rv0924c or Rv2434c caused a shift in the MIC_{99} from 23 to 35 µg/mL, this was only a 1.5-fold change. For a shift in MIC_{99} to be significant, this

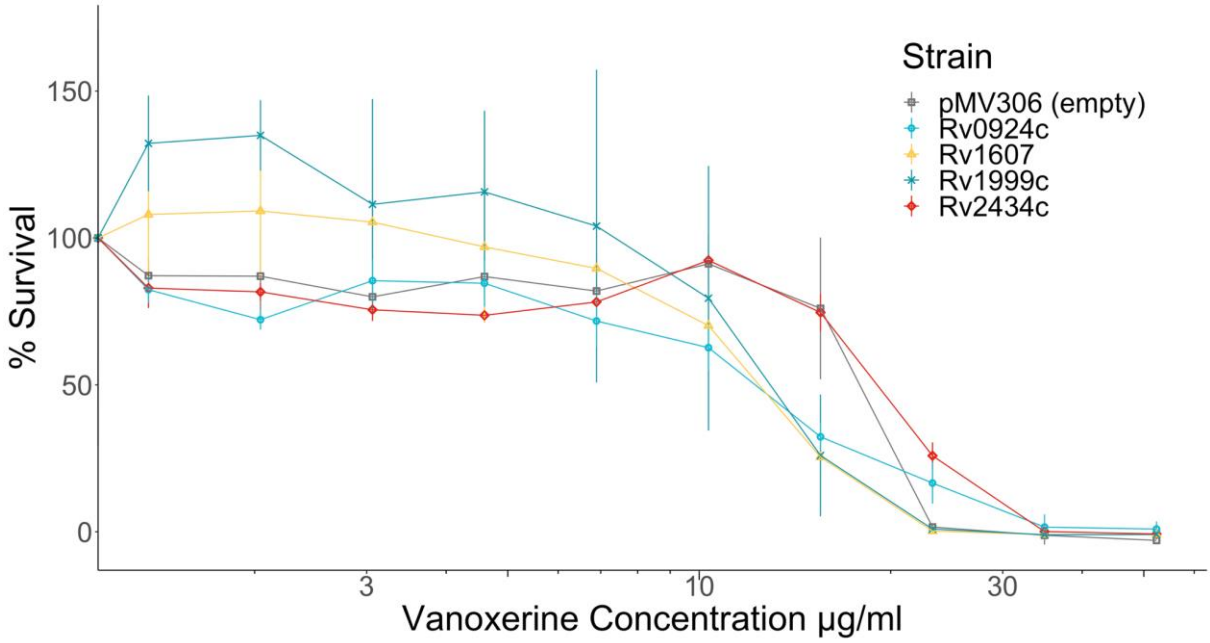


Figure 3.9: Overexpression of the predicted structural homologues of human targets of vanoxerine had limited effect on the survival of *M. smegmatis*. *M. smegmatis* containing either empty pMV306 vector or pMV306 vectors for protein overexpression were diluted to OD_{600} 0.05. The diluted cells were added to a 96-well plate containing a 2:3 serial dilution of vanoxerine and incubated for 21 hours. Resazurin was added and the plate re-incubated for 3 hours, before the resorufin fluorescence was monitored, to determine the %survival. N=3

would generally need to be a 4-fold, as changes in the MIC_{99} of 2-fold can occur through slight changes in MIC determination experimental set-up.

Due to the lack of a significant shift in the *M. smegmatis* MIC or in the percentage survival curves, these vectors were not assessed in *M. bovis* BCG. In addition, the lack of increased resistance suggested these were not the mycobacterial targets of vanoxerine. Hence, further exploratory work was undertaken.

3.2.8. Propidium iodide uptake in mycobacteria is increased by vanoxerine

As discussed in the introduction, many antimycobacterial drugs target proteins in the cell envelope, leading to disruption of membrane components (Andries et al., 2005; Pethe et al., 2013; Zumla, Nahid and Cole, 2013). To study this on a global level, a Gram-negative membrane permeability assay that used propidium iodide (PI), was adapted for studying mycobacteria and the impact of vanoxerine on cell membrane permeability. PI intercalates DNA and fluoresces more strongly but is not cell membrane permeable (Hassan et al., 2017; Zhao et al., 2010). In Gram-negative species, it provides a signal indicating whether both membranes have been disrupted, however, the exact response of mycobacteria is unknown in a plate-reader assay.

To adapt this assay for use in mycobacteria and *C. glutamicum*, a set of experiments were performed to optimise the amount of PI required and the number of cells, based on OD_{600}. Initially, *M. smegmatis* was used, varying both the OD_{600} used, 0.5 or 1.0, and varying the PI concentration in the assay, 3 or 30 µM (Figure 3.10A). The highest concentration of vanoxerine tested, 52 µg/mL, had no impact on the fluorescence of PI in the absence of cells. The PI dye on its own showed a small decrease in

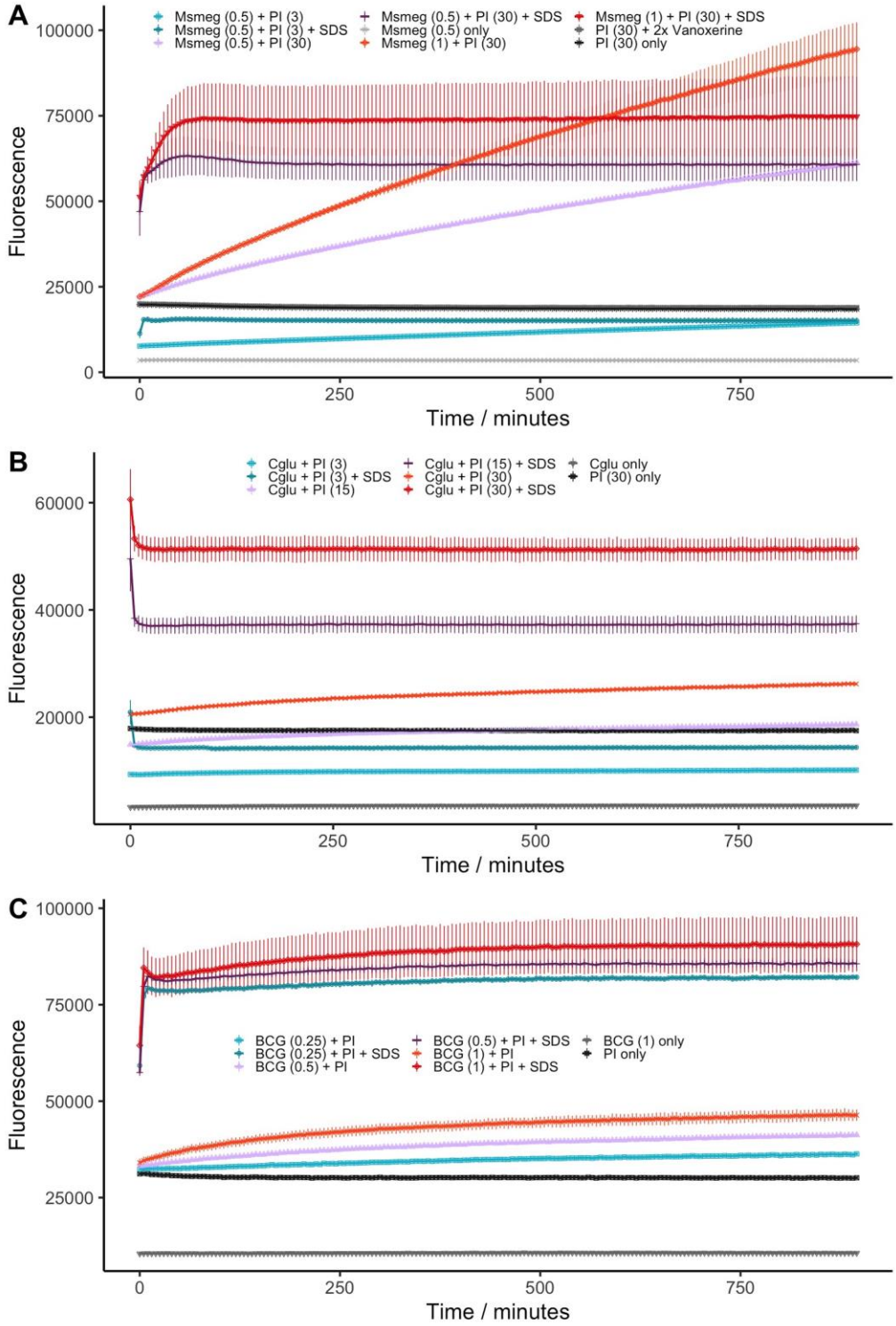


Figure 3.10: Development of propidium iodide assay in (A) *M. smegmatis*, (B) *C. glutamicum* and (C) *M. bovis* BCG. Cells were diluted from mid-log to OD_{600} 0.25, 0.5 or 1.0 in PBS and PI (3, 15 or 30 µM) was added. The diluted cells were immediately added to a 96-well plate containing either DMSO (1%) or SDS (0.05%). The PI fluorescence was immediately read every 5-minutes for 15-hours. If not specified, OD_{600} 0.5 and PI = 15 µM. Msmeg = *M. smegmatis*, Cglu= *C. glutamicum*, BCG = *M. bovis* BCG, PI = propidium iodide. N=3.

fluorescence from ~20,000 to ~19,000 RFUs across the 15-hours. This assay compared the PI fluorescence in the absence of membrane permeabilisation (DMSO-only), to SDS-permeabilised cells, to define the assay window. Comparing 3 to 30 µM PI, the assay window increased from between ~8,000 to ~15,000 using 3 µM, to between ~23,000 to ~60,000 RFUs using 30 µM. Increasing the OD_{600} from 0.5 to 1.0 had a much smaller effect on the assay window but caused the rate of PI influx to increase in the absence of membrane permeabilisation. Hence, an OD_{600} of 0.5 was set as a preliminary value.

In *C. glutamicum*, 15 µM PI was tested in addition to 3 and 30 µM, as the dye concentration had a larger impact on the fluorescence differences (Figure 3.10B). The assay windows for 3, 15 and 30 µM PI were ~31,000, ~22,000 and ~5,000 RFUs, respectively. Comparing the PI fluorescence increase in the absence of membrane permeabilisation, these were ~5,600, ~3,800 and ~800 for 3, 15 and 30 µM PI. The gain in assay window size when using 30 µM PI rather than 15 µM was smaller than the gain of background PI fluorescence, 1.41x vs 1.47x. Hence, 15 µM PI was used as the standard concentration in future assays.

Finally, *M. bovis* BCG was tested using 15 µM PI, at varying OD_{600} values (Figure 3.10C). This indicated that OD_{600} had a limited effect on the assay window. The rate of PI influx, in the absence of membrane permeabilisation was also smaller than *M. smegmatis*. Hence, it was decided to use OD_{600} of 0.5 for *M. smegmatis* and *C. glutamicum*, but an OD_{600} of 1.0 for *M. bovis* BCG. This initial optimization then allowed vanoxerine to be tested in this assay.

The treatment of *M. smegmatis* was undertaken and led to an increase in the amount of PI fluorescence (Figure 3.11A). In the presence of vanoxerine, both the rate of

increase and total fluorescence were greater than the DMSO-only control. The increase in PI fluorescence was concentration dependent, as 52 µg/mL (2x MIC_{99}) vanoxerine led to ~100,000 RFUs after 15-hours, compared to ~89,000 RFUs for 13 µg/mL vanoxerine and 61,000 RFUs for the DMSO-only control (Figure 3.11A).

Given the large effect on the *M. smegmatis* membrane, the effect of vanoxerine on PI influx within *C. glutamicum* was undertaken. For *C. glutamicum*, Figure 3.11B, there was a clear difference in both the rate of fluorescence increase and total fluorescence, relative to the DMSO-only control. The final fluorescence values were ~52,000 RFUs following 52 µg/mL vanoxerine treatment, compared to ~42,000 RFUs for 13 µg/mL vanoxerine and ~19,000 RFUs for the DMSO-only control.

In contrast to the clear difference present in *C. glutamicum*, *M. bovis* BCG showed a much smaller difference in PI fluorescence following vanoxerine treatment (Figure 3.11C). In this assay, the DMSO-only control had an endpoint fluorescence of ~47,000 RFUs, compared to ~50,500 RFUs following 13 µg/mL vanoxerine treatment and ~83,000 RFUs following 52 µg/mL vanoxerine. Only the highest concentration of vanoxerine tested showed a clear effect on *M. bovis* BCG. Overall, this highlights that vanoxerine has an impact on the mycobacterial and corynebacterial membranes, which may allow propidium iodide to enter viable cells. Alternatively, this could suggest that vanoxerine is rapidly killing cells and hence allowing propidium iodide to enter non-viable cells.

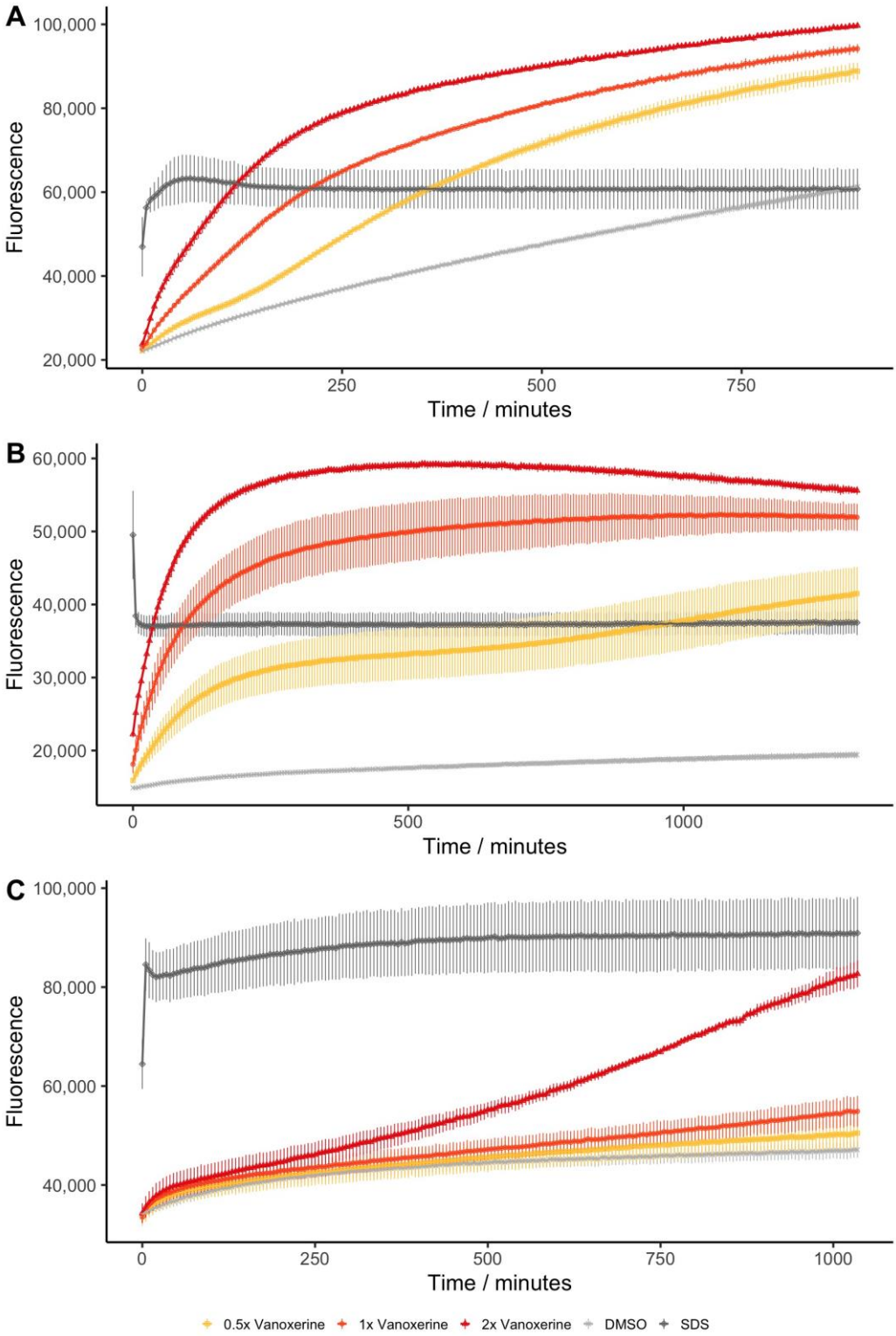


Figure 3.11: Vanoxerine treatment increased the propidium iodide fluorescence of *M. smegmatis* and *C. glutamicum* at 0.5x MIC_{99} and *M. bovis* BCG at 2x MIC_{99}. (A) *M. smegmatis*. (B) *C. glutamicum.* (C) *M. bovis* BCG. Mid-log cells were diluted to OD_{600} 0.5, combined with 15 µM PI and immediately added to a 96-well plate containing DMSO, vanoxerine or SDS. Fluorescence was measured every 5-minutes for 15 to 22-hours. N=3

3.2.9. Ethidium bromide accumulation is increased, and efflux inhibited in mycobacteria

As propidium iodide influx suggested that the membrane was affected by vanoxerine, ethidium bromide accumulation and efflux was used to monitor this impact in more detail. It provides information on both the membrane integrity and cellular energetics, required for active efflux. The accumulation and efflux of ethidium bromide has been well characterised in mycobacteria, for monitoring the impact of drugs on efflux and membrane permeability (Rodrigues, Aínsa and Viveiros, 2021). Fluorescence of ethidium bromide following DNA intercalation is used to indicate it is within the cell.

To prevent toxicity due to ethidium bromide, the MIC_{99} was determined, for both *M. smegmatis* and *M. bovis* BCG, to be 6.25 µg/mL. In each assay, the maximum concentration of ethidium bromide used was 0.625 µg/mL, or $1/10^{th}$ the MIC_{99}. Glucose was added to some of the assay conditions, to provide an energy source and enable the efflux of more ethidium bromide.

Across the 60-minute assay, vanoxerine treatment led to a significant increase in ethidium bromide accumulation inside both *M. smegmatis* and *M. bovis* BCG (Figure 3.12A,C). Sub-MIC values of 0.125x MIC_{99} vanoxerine (3.27 µg/mL) caused more ethidium bromide accumulation than the DMSO controls in both mycobacterial species. The increased accumulation of ethidium bromide by vanoxerine was concentration dependent, as 2x MIC_{99} (52 µg/mL) vanoxerine caused 2.6x more fluorescence than DMSO and 1.2x more fluorescence than 0.5x MIC_{99} (13 µg/mL) in *M. smegmatis* (Figure 3.12A**).** This difference was smaller in *M. bovis* BCG, with 2x MIC_{99} (52 µg/mL) vanoxerine causing 1.3x more fluorescence than DMSO and 1.1x more fluorescence than 0.5x MIC_{99} (13 µg/mL) (Figure 3.12C)**.** Explanations for the increased ethidium

bromide accumulation include: efflux inhibition, membrane disruption/lysis, or impacting cellular energetics, hence, further work was undertaken.

As a follow-up, the inhibition of ethidium bromide efflux was directly studied. Mycobacterial cells were allowed to accumulate ethidium bromide in the presence of verapamil, a non-toxic efflux inhibitor. The verapamil MIC_{99} against both *M. smegmatis* and *M. bovis* BCG was greater than 100 µg/mL. Once the ethidium bromide had accumulated, the verapamil was removed before use in the assay. Loss of ethidium bromide was monitored as loss of fluorescence. In the absence of an efflux inhibitor, a decrease in fluorescence of approximately 65% could be observed in *M. smegmatis* (Figure 3.12B). In the presence of known efflux inhibitor verapamil (50 µg/mL), the decrease in fluorescence was reduced to approximately 32%, indicating efflux inhibition and retention of ethidium bromide. In the presence of 1x or 2x MIC_{99} of vanoxerine, the observed drop in fluorescence was even smaller, at 25% and 13%, respectively (Figure 3.12B). Similar rates of efflux to the DMSO control occurred at 0.125x MIC (3.27 µg/mL) vanoxerine, leading to a 63% decrease in fluorescence. For *M. bovis* BCG, the changes in fluorescence were smaller (Figure 3.12D), due to lower amounts of ethidium bromide accumulating in the cell initially. This includes normal drops in fluorescence of approximately 30%, compared to only an 11% drop in the presence of 2x MIC_{99} vanoxerine or 18% following addition of verapamil (Figure 3.12D). Overall, this provide strong evidence that vanoxerine is inhibiting mycobacterial efflux.

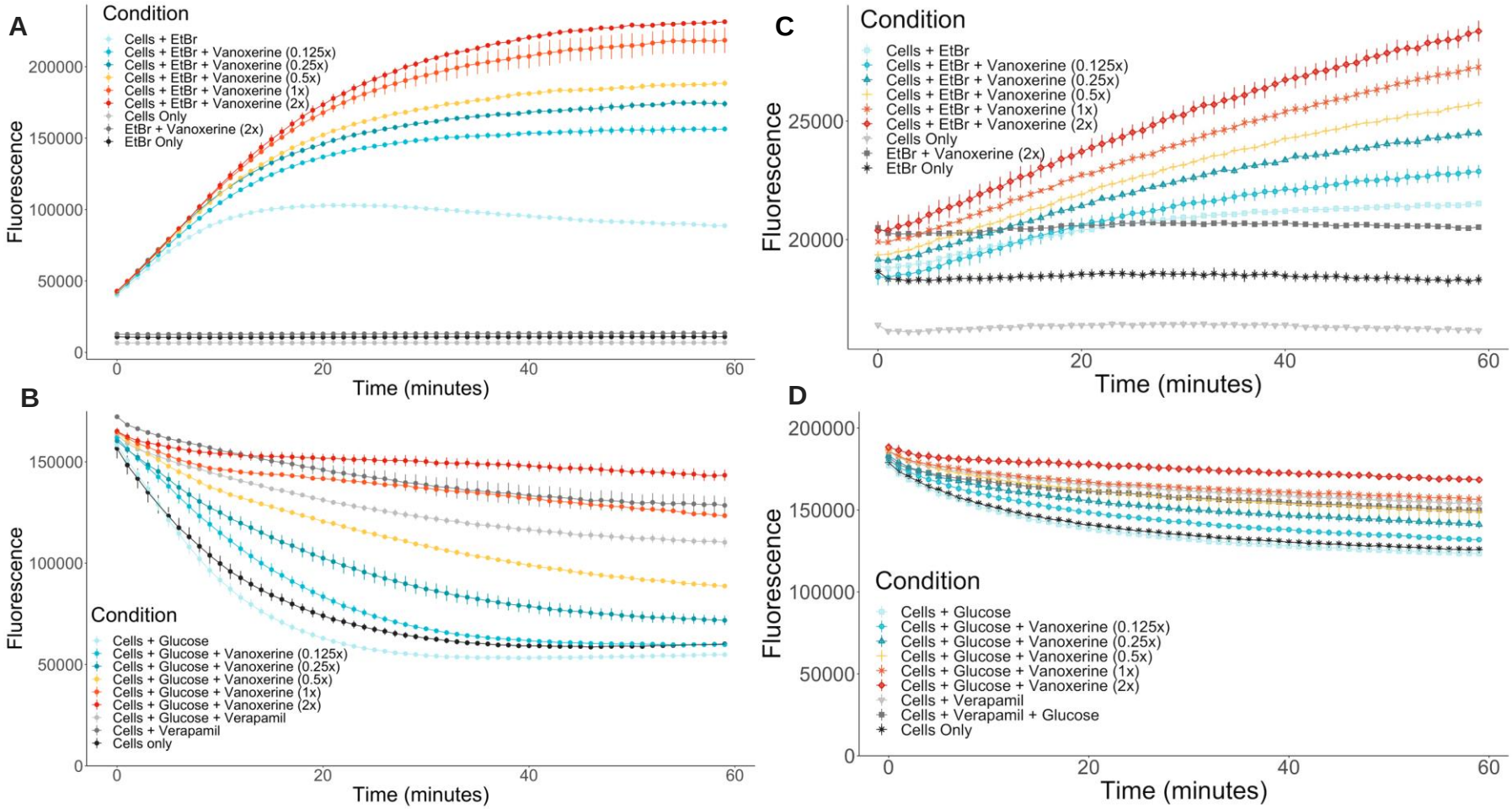


Figure 3.12: Vanoxerine treatment leads to increased accumulation of ethidium bromide and prevents its efflux from mycobacteria. For efflux, mycobacteria (0.8) were allowed to accumulate ethidium bromide (0.625 µg/mL) for 2-hours. For accumulation, cells (0.8) were combined with ethidium bromide (0.625 µg/mL) immediately before the assay start point. In both cases the cells were resuspended in PBS + glucose (0.4%) and added to a 96-well plate containing compounds. The fluorescence was measured every minute for 60-minutes. (A) *M. smegmatis* accumulation. N=3. (B) *M. smegmatis* efflux. N=3. (C) *M. bovis* BCG accumulation. N=3. (D) *M. bovis* BCG efflux. MIC = 26 µg/mL. Taken from Kingdon et al. (2022). EtBr = ethidium bromide

3.2.10. Disruption of the electric potential by vanoxerine

Vanoxerine was able to inhibit efflux of ethidium bromide, to further quantify the impact on the membrane, the voltage sensitive dye $DiOC_2(3)$ was used to monitor the electric potential ($\Delta\psi$) of the membrane, as $\Delta\psi$ disruption would prevent the majority of efflux (Remm et al., 2022). $DiOC_2(3)$ partitions across phospholipid membranes proportionally to the $\Delta\psi$ present (Chen et al., 2018; Chawla et al., 2012; Hudson, Siegele and Lockless, 2020; Li et al., 2019; Novo et al., 1999), fluorescing red inside cells and green in solution. It was investigated whether vanoxerine disrupts the $\Delta\psi$ of the membrane using $DiOC_2(3)$ membrane partitioning.

One approach to study this effect is looking at $DiOC_2(3)$ partitioning and whether concurrent drug treatment has an impact on this process (Figure 3.13A). The increase in red/green fluorescence over time indicates that more dye is entering the cell, suggesting there is a voltage difference across the membrane. This occurs in DMSO, kanamycin and bedaquiline treated cells, as these compounds do not affect the membrane $\Delta\psi$ and hence reach a red/green fluorescent ratio of 1.55 (Figure3.13A). CCCP is a protonophore which is known to disrupt both the $\Delta\psi$ and proton gradient (ΔpH) of the membrane (Chen et al., 2018) and hence prevented dye partitioning, leading to a ratio of 0.99. Vanoxerine treatment reduced the red/green fluorescent ratio of $DiOC_2(3)$ in a concentration dependent manner, with 52 µg/mL vanoxerine reaching a ratio of 1.08, while 13 µg/mL vanoxerine reached a ratio of 1.36 (Figure 3.13A). These lower ratios suggest vanoxerine is reducing the voltage difference across the membrane, impacting dye partitioning.

The alternative approach trialled, was allowing the dye to equilibrate across the membrane proportional to the $\Delta\psi$, by pre-incubating *M. bovis* BCG with the dye for two

hours. This indicated that the red/green fluorescence ratio fluctuated around 1.75 in the absence of compound, reducing to 1.60 across the 60-minute assay (Figure 3.13B). Vanoxerine was able to disrupt the dye partitioning compared to the DMSO-only control, with 52 µg/mL vanoxerine reducing the ratio to 1.09 after 50-minutes, suggesting disruption of the $\Delta\psi$. This effect was concentration dependent and occurred even at sub-MIC_{99} amounts of vanoxerine, 13 µg/mL (0.5x MIC_{99}) led to a reduced ratio of 1.30. The known protonophore CCCP caused the lowest red/green fluorescent ratio in this assay, of 0.95. The rate of dye disruption was slower in the presence of vanoxerine compared to CCCP. This assay was specific for the $\Delta\psi$ disruption, rather than more general proton motive force (PMF) disruption. This was confirmed by bedaquiline, which disrupts the ΔpH of the PMF, but not the $\Delta\psi$ component and hence had a similar response to DMSO, of 1.63 (Feng et al., 2015). There was also no impact of kanamycin on the dye partitioning compared to the DMSO only control, with a fluorescent ratio of 1.63 after the 50-minute assay. Hence, the mechanism of disruption if unlikely to be a general bacterial response to drug inhibition. A further control, such as the QcrB inhibitor telacebec (Pethe et al., 2013), would have determined if disruption of the electron transport chain also dissipated the $\Delta\psi$.

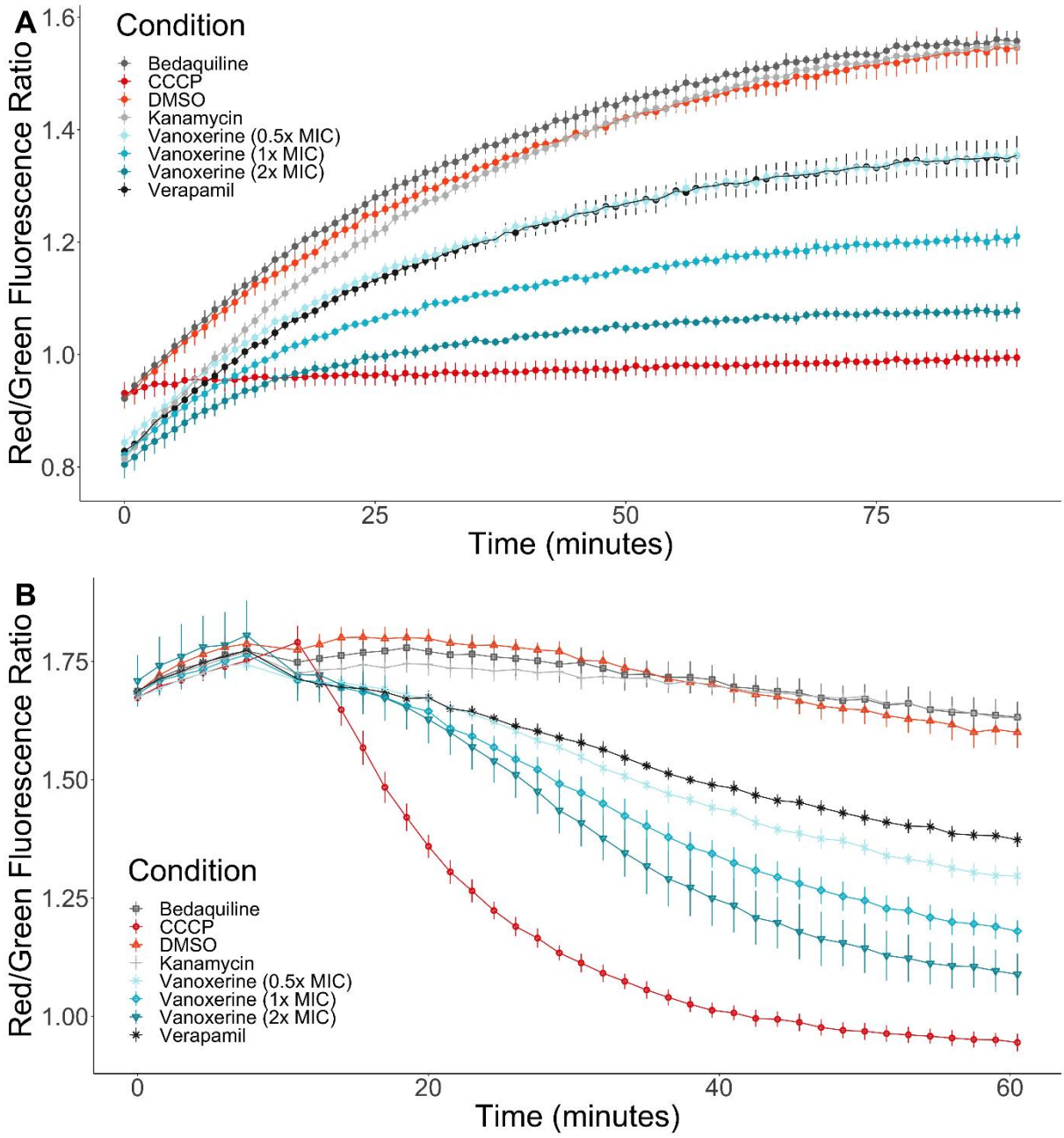


Figure 3.13: Vanoxerine disrupts the partitioning of the $DiOC_2(3)$ dye, suggesting membrane electric potential dissipation. $DiOC_2(3)$ dye (30 µM) was added to cells and the mixture either immediately added to drug compounds (A) or incubated for 2-hours prior to addition (B). The fluorescence was measured every 90-seconds for 90 minutes. Bedaquiline = 0.5 µg/mL, CCCP = 25 µM, DMSO = 1%., Kanamycin = 500 µg/mL, verapamil = 50 µg/mL. N=3. Part (B) taken from Kingdon et al. (2022)

3.2.11. Vanoxerine does not potentiate the activity of other antimycobacterial drugs

Vanoxerine inhibited mycobacterial efflux, hence, it was hypothesised that any antimycobacterial drugs which are known to be removed from the cell via efflux, would have increased efficacy if used alongside vanoxerine. Resistance to the more recent antimycobacterial drugs including bedaquiline, clofazimine and FNDR-20081 have been shown to occur via mutations in Rv0678. This is the transcriptional repressor of the *mmpL5-mmpS5* operon. Rv0678 mutants cause up-regulation of the MmpL5 efflux pump, suggesting all three compounds are pumped out of the cells by this protein (Hartkoorn, Uplekar and Cole, 2014; Andries et al., 2014; Remm et al., 2022; Kaur et al., 2021). Hence, checkerboard MICs were set up against *M. bovis* BCG, to test for the interactions of vanoxerine with bedaquiline, clofazimine and FNDR-20081. Alongside this, a rifampicin vs vanoxerine checkerboard was set up to test for synergy with this front-line drug. In the presence of a sub-MIC amount of vanoxerine (10.3 µg/mL), the MIC_{99} of rifampicin, clofazimine and FNDR-20081 were reduced by 2x (0.05 to 0.025 µg/mL, 4.8 to 2.4 µg/mL, and 24.5 to 12.3 µg/mL, respectively, Figure 3.14). The FIC values were calculated as 0.676 for rifampicin and 0.896 for clofazimine and FNDR-20081, with vanoxerine. As these FIC values were over 0.5, they indicate no interactions were occurring; hence, further work needs to be undertaken to determine if the observed MIC_{99} reductions are due to the presence of the vanoxerine or due to experimental set-up. In contrast, an FIC value of 1.13 was calculated for bedaquiline, also suggesting no interaction, but there was also no difference to the bedaquiline MIC_{99} in the presence of 10.3 µg/mL vanoxerine (Figure 3.14).

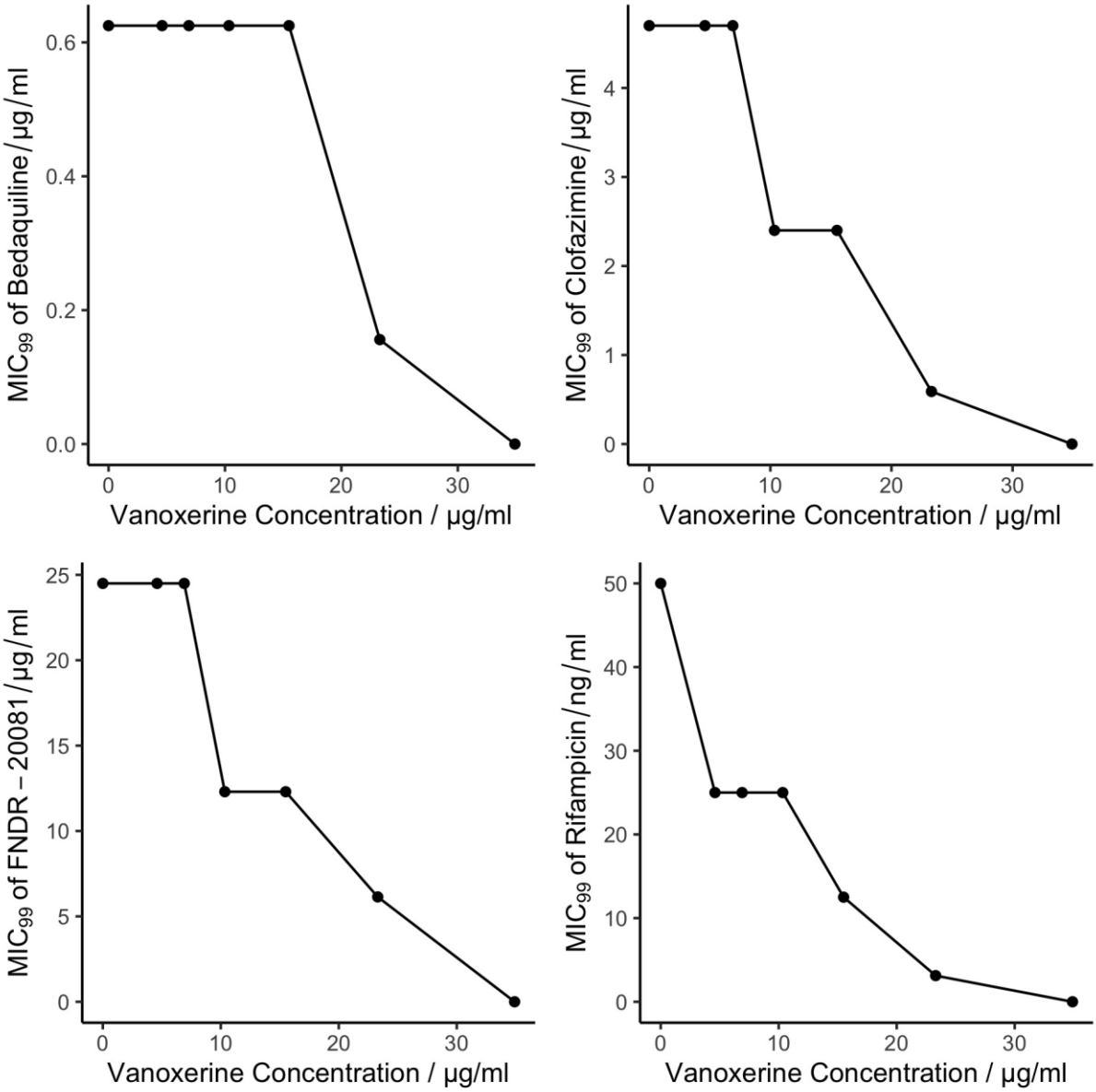


Figure 3.14: Vanoxerine does not potentiate the effects of other antimycobacterial drugs. (A) Bedaquiline. (B) Clofazimine. (C) FNDR-20081. (D) Rifampicin. The checkerboard MICs tested seven vanoxerine concentrations against eleven of the other drugs, with a final DMSO concentration of 2%. The mid-log cultures were diluted to OD_{600} 0.05, before addition to the checkerboard plates. Plates were incubated for 6-days before resazurin turnover was used to assess survival. The determined MIC_{99} of each drug is plotted against the corresponding vanoxerine concentration. N=3. Figure adapted from Kingdon et al. (2022).

3.2.12. RNA-Sequencing following treatment of *M. bovis BCG* with vanoxerine

Given the ability of vanoxerine to inhibit efflux and disrupt of the membrane electric potential at sub-inhibitory concentrations (Figure 3.12, Figure 3.13), this suggested other pleotropic effects may be the cause of cell death. Hence, detailed transcriptomic analysis of *M. bovis* BCG was undertaken, using RNA-sequencing, following 8-hours of drug treatment. Two different drug concentrations were investigated, 15 and 30 µg/mL vanoxerine, to identify any transcriptomic differences that were concentration dependent. At both vanoxerine concentrations, clear transcriptomic differences were found compared to the no drug control samples (containing 1% DMSO). There was a clear separation between pairwise comparisons of both the no drug vs 15 µg/mL vanoxerine and no drug vs 30 µg/mL vanoxerine samples (Figure 3.15A,B). 93% and 96% of the variance between each pair of eight samples was due to the treatment conditions. At 15 µg/mL (0.5x MIC_{99}) vanoxerine, 322 gene transcripts were significantly dysregulated compared to the no drug control (fold change = 2 or more, P-value < 0.05) (Figure 3.15C). This number increased to over 800 genes which were transcriptionally dysregulated following 30 µg/mL vanoxerine, relative to the no drug control (Figure 3.15D). If the significantly dysregulated genes following each vanoxerine treatment condition were compared, there were 304 genes in common. For the 15 µg/mL vanoxerine condition, only 17 significantly dysregulated genes were unique, whilst 510 gene transcripts were unique to the 30 µg/mL vanoxerine condition. The list of 304 genes could be reduced to 31 gene transcripts that were dysregulated in a concentration dependent manner, when selecting genes which were significantly dysregulated at 30 µg/mL vanoxerine relative to 15 µg/mL vanoxerine baseline (Table 3.4).

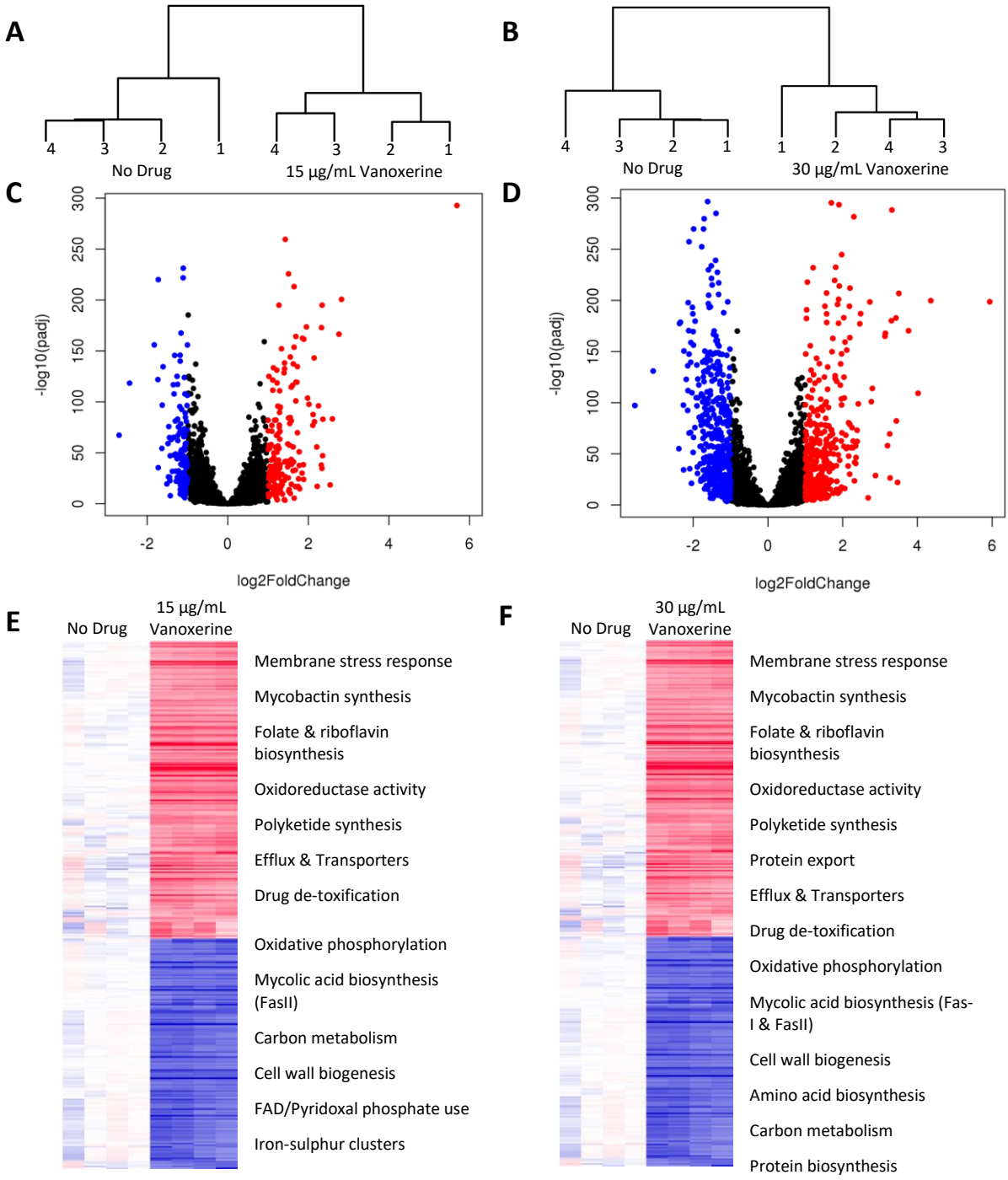


Figure 3.15: Vanoxerine induces many transcriptional changes in *M. bovis* BCG, following 8-hours of drug treatment. (A&B) Dendrograms of no-drug vs vanoxerine sample differences (A) 15 ug/mL. (B) 30 ug/mL. (C&D) Volcano plots showing significantly dysregulated genes following vanoxerine treatment. Highlighted points have a fold-change > 2 and a p-adjusted value <0.05; red = up-regulated, blue = down-regulated. N=4 (C) 15 µg/mL. (D) 30 µg/mL. (E&F) Clustered comparisons of transcriptional differences between the DMSO-only and vanoxerine treated samples. Biological functions of the dysregulated genes are listed. (E) 15 µg/mL. (F) 30 µg/mL. Figure adapted from Kingdon et al (2022).

The significantly dysregulated genes at both 15 and 30 µg/mL vanoxerine were functionally annotated and clustered using the DAVID server (Sherman et al., 2022; Huang, Sherman and Lempicki, 2009), to identify biological processes or pathways that were up- or down-regulated in response to vanoxerine (Figure 3.15E,F). In relation to the up-regulated transcripts, these clusters included: membrane stress responses; mycobactin synthesis; folate and riboflavin biosynthesis; oxidoreductase activity; polyketide synthesis; efflux; transporter proteins and drug de-toxification, across both drug concentrations. At 30 µg/mL vanoxerine, protein export pathways were also upregulated. The upregulation of genes involved in membrane stress, protein export, efflux and other transport proteins provides further evidence that vanoxerine's mechanism of action inhibits these processes.

Conversely, the down-regulated pathways included: oxidative phosphorylation; mycolic acid biosynthesis (FasII); cell wall biogenesis; amino acid biosynthesis; carbon metabolism and protein biosynthesis. At 15 µg/mL, both flavin adenine dinucleotide/pyridoxal phosphate utilisation and iron-sulphur cluster genes were down-regulated. At 30 µg/mL vanoxerine, Fas-I lipid synthesis protein, amino acid biosynthesis and protein biosynthesis were also downregulated. The down-regulated genes suggest many cellular functions are being reduced following the impact on growth.

Only 31 genes were significantly dysregulated in a concentration dependent manner, hence, these were investigated in more detail (Table 3.4). Amongst the significantly up-regulated genes, there was little consensus of function, with a majority being of unknown function. The *mmpL5-mmpS5* gene pair that encode the MmpL5 efflux pump and MmpS5 accessory protein were significantly up-regulated, which may be due to

vanoxerine's impact on efflux at higher concentrations. A majority of significantly down-regulated transcripts encoded the mycolic acid biosynthetic proteins. Explanations for this result could include the high energetic costs associated with mycolic acid production, indirect inhibition of MmpL3, or vanoxerine directly impacting this pathway.

Table 3.4 Significantly dysregulated genes comparing treatment of *M. bovis* BCG following treatment of 15 and 30 µg/mL of vanoxerine. Adapted from Kingdon et al. (2022).

ID	ID in TB	Functional Annotation	Log_2 Fold Change	P-adjusted
acpM	*acpM*	Mycolic acid biosynthesis	-1.71	4.13E-24
kasA	*kasA*	Mycolic acid biosynthesis	-1.64	4.24E-43
fabD	*fabD*	Mycolic acid biosynthesis	-1.58	6.23E-54
kasB	*kasB*	Mycolic acid biosynthesis	-1.38	6.23E-68
BCG_2265	*Unknown*	Unknown	-1.12	3.46E-11
ahpE	*ahpE*	Peroxidase	-1.06	4.20E-12
cysK2	*cysK2*	Cysteine synthesis	1.01	1.15E-28
lat	*lat*	Lysine - glutamate conversion	1.05	6.53E-28
PPE47	*Rv3021c*	Unknown	1.06	1.01E-13
esxR	*esxR*	Secreted protein	1.06	1.09E-05
PPE46	*Rv3018c*	Unknown	1.07	1.89E-44
BCG_0231	*Rv0194*	Multidrug efflux ATP-binding/permease protein	1.103	4.80E-96
BCG_0728c	*Rv0679c*	Unknown	1.15	5.48E-98
BCG_3926	*Rv3863*	Unknown	1.18	3.14E-39
IS1606'	*Rv0850*	Transposase	1.20	6.15E-06
BCG_1993c	*Unknown*	Unknown (DUF402)	1.22	4.71E-59
mmpL5	*mmpL5*	Efflux	1.25	5.07E-87
lpqS	*lpqS*	Lipoprotein of unknown function	1.26	1.46E-22

echA5	*echA5*	Fatty acid oxidation	1.27	2.22E-53
PPE32	*PPE32*	Unknown	1.33	4.02E-28
BCG_0369c	*eccE3 (Rv0292)*	ESX-3 secretion system protein EccE	1.33	4.13E-120
PPE33a	*PPE33a*	Unknown	1.35	2.60E-11
BCG_0842c	*Rv0789c*	Unknown	1.39	6.68E-89
mmpS5	*mmpS5*	Efflux	1.44	1.95E-25
BCG_1466c	*Rv1405*	Putative methyltransferase	1.46	3.67E-14
hsp	*hsp*	Stress response	1.54	4.00E-158
BCG_0368c	*Rv0329c*	Putative methyltransferase	1.54	2.22E-31
BCG_3766c	*Rv3706*	Unknown	1.83	1.61E-22
BCG_0365	*Rv0325*	Putative methyltransferase	1.85	1.96E-44
BCG_0367	*Rv0328*	Possible transcriptional regulator	2.09	1.04E-105
cyp135A1	*cyp135A1*	Cytochrome P450	2.42	7.71E-73

To follow-up on the RNA-sequencing data outlined, several genes were identified from the transcriptome which were significantly dysregulated in response to vanoxerine treatment. These are outlined in Table 3.5 and were selected as they are involved in specific pathways, such as membrane stress (*clgR* and *whiB3*) or drug efflux (*mmpL5*). In addition, some were selected due to being essential genes that were dysregulated (*ribC, narG*). Several approaches were undertaken to determine if the encoded proteins had an impact on survival to vanoxerine.

Table 3.5 Genes of interest from the RNA-sequencing. Values are comparing no-drug to 30 µg/mL vanoxerine conditions.

ID	Functional Annotation	Log_2 Fold Change	P-adjusted
bcg_0727 (rv0678)	Mmpl5 transcriptional regulator	2.36	3.75E-47
bcg_3184c (rv3160c)	Putative oxidase	5.96	<2.23E-308
clgR	Membrane stress response regulator	2.19	7.14E-31
mmpL5	Efflux pump	3.94	<2.23E-308
mmpS5	MmpL5 accessory protein	4.02	6.44E-110
narG	Nitrate reductase	1.07	1.08E-106
ribC	Riboflavin synthase	1.01	3.33E-17
whiB3	Stress response regulator	1.17	8.88E-06

3.2.13. Testing *M. bovis* BCG Danish transposon mutants

To study the effect of some of the genes highlighted by the RNA-sequencing of *M. bovis* BCG (Table 3.5), some transposon mutants were selected from a BCG Danish strain collection (Borgers et al., 2020). This collection only contained transposon mutant strains for non-essential genes and required approximately two-months to recover the *M. bovis* BCG strains from frozen stocks, hence only mutants in *mmpL5*, *narG* and *whiB3* were selected. These experiments assumed that removing known upregulated proteins would make the strains more susceptible to killing by vanoxerine. The percentage survival curves for *M. bovis* BCG Danish and the mutant strains are displayed in Figure 3.16. This showed a limited shift in MIC, remaining between 23 and 35 µg/mL vanoxerine, suggesting these proteins are not direct targets of inhibition. This could also suggest that although transcription of *mmpL5* is upregulated, it is not directly increasing vanoxerine influx or efflux from the cell.

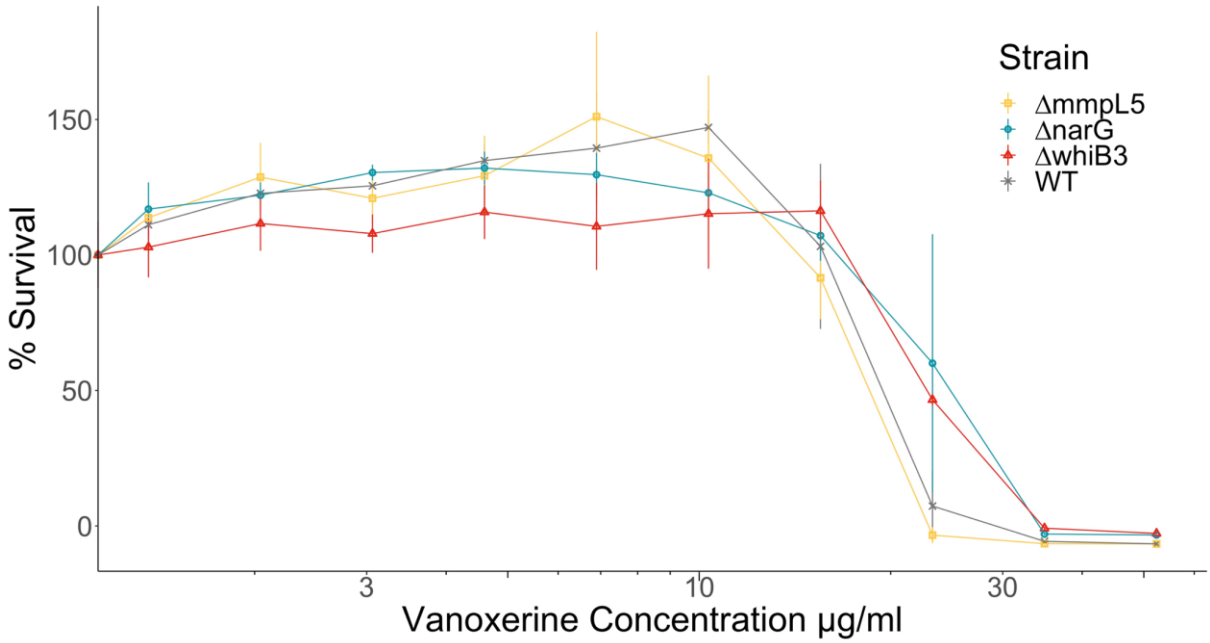


Figure 3.16: Limited shift in MIC occurred in BCG Danish mutants compared to the wild-type strain. *M. bovis* BCG was diluted to OD_{600} and added to a 2:3 vanoxerine serial dilution. Plates were incubated for 6-days, resazurin was added, and the plates re-incubated for 24-hours. %Survival was calculated based on resorufin fluorescence. WT= wild type. N=3

3.2.14. Testing over-expressor strains for vanoxerine resistance

As there were restrictions placed on the availability of the BCG Danish mutant strains, but many more genes showed significant dysregulation in their transcription during vanoxerine treatment, additional genes were selected for over-expression studies. These were *clgR, mmpR5* (*bcg0727*)*, narK2, ribC* and *whiB3*. These five genes were cloned into the pMV306 vector by Twist Biosciences, with a *hsp60* promoter for constitutive expression. Genes *mmpR5* and *narK2* were chosen to replace *mmpL5* and *narG*, due to the cost of synthesising these larger genes. NarK2 is a nitrate/nitrite transporter, that was shown to increase nitrate reduction and is downstream in the same pathway as NarG (Sohaskey and Wayne, 2003). MmpR5 is the regulator of the *mmpL5-mmpS5* operon, equivalent to Rv0678, and is involved in down-regulating

MmpL5 (Andries et al., 2014). Following the cloning of these genes, all vectors were then transformed into both *M. smegmatis* and *M. bovis* BCG.

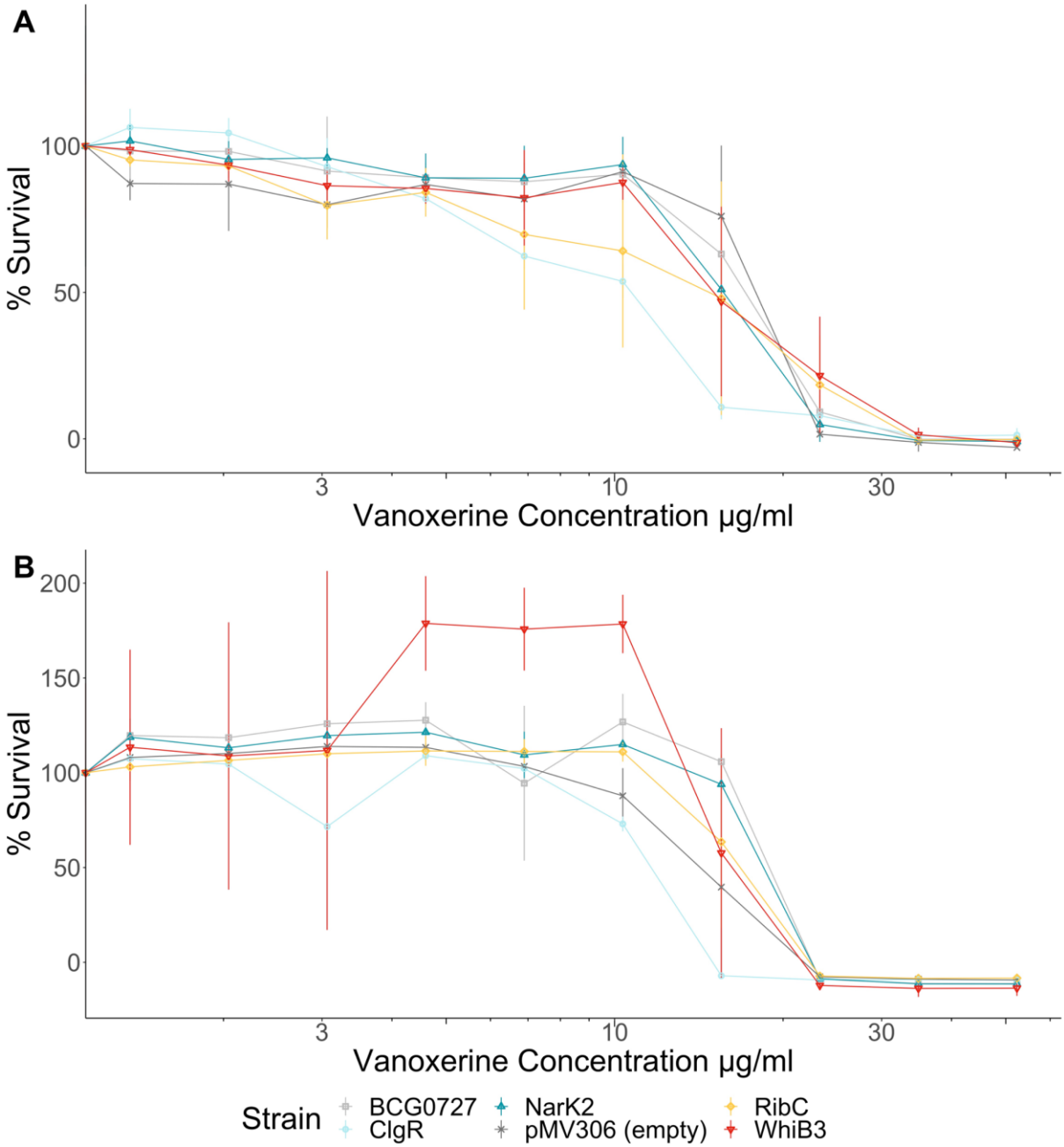


Figure 3.17: Overexpression of *bcg0727, clgR, narK2, ribC* and *whiB3* had a limited impact on the vanoxerine MIC. (A) *M. smegmatis*. (B) *M. bovis* BCG. Cells were diluted to OD_{600} 0.05 and added to a 2:3 vanoxerine serial dilution. Plates were incubated for 21-hours (*M. smegmatis*) or 6-days (BCG), before resazurin was added and plates re-incubated for 3-hours (*M. smegmatis*) or 24-hours (BCG). The resorufin fluorescence was measure and %survival was calculated. N=3.

The percentage survival curves of *M. smegmatis* comparing the empty pMV306 vector to the over-expression vectors are displayed in Figure 3.17A. The overexpression of *clgR, ribC* and *whiB3* shifted the MIC_{99} from 23 to 35 µg/mL, however, this was not a large enough shift to assume target engagement. Despite *clgR* overexpression shifting the MIC_{99} higher than the empty vector, it also showed much lower survival at sub-MIC of vanoxerine. Overall, these are small shifts in the percentage survival curve are unlikely to represent direct targets.

As the RNA-sequencing was undertaken in *M. bovis* BCG, the overexpression of these proteins was also performed in *M. bovis* BCG, to provide a closer genetic background. As shown in Figure 3.17B, there was limited shift in the MIC_{99} for the majority of the over-expressor strains. The exception was *clgR* overexpression, which led to a reduction in the MIC_{99} from 23 to 15 µg/mL, however, this was not a significant shift. This approach did not yield any more target identification.

3.2.15. Testing CRISPRi strains for vanoxerine susceptibility

The BCG transposon mutant library could only assess non-essential genes and was limited in terms of availability. Hence, a CRISPRi strategy was undertaken, to knock-down selected genes, as mentioned in Chapter 2. The system was ATc inducible and for every selected gene, three different guide RNAs were tested. The genes selected were *bcg3184c* (*rv3160c*), *clgR, narG, ribC* and *whiB3* (Table 3.5). As the *aroB* CRISPRi strategy did not show promising results, several control targets were also selected, being *mmpL3, pknB* and *inhA*.

Initially, the impact of CRISPRi on the growth of *M. bovis* BCG was studied by performing growth curves. Due to time constraints, only one repeat per guide RNA

could be undertaken for most strains, however, the control unedited pRH2521+pRH2502 strain was measured in triplicate and the *mmpL3*+10 strain was measured in duplicate. The growth curves of the control targets are displayed in Figure 3.18, with error bars shown if multiple replicates were measured.

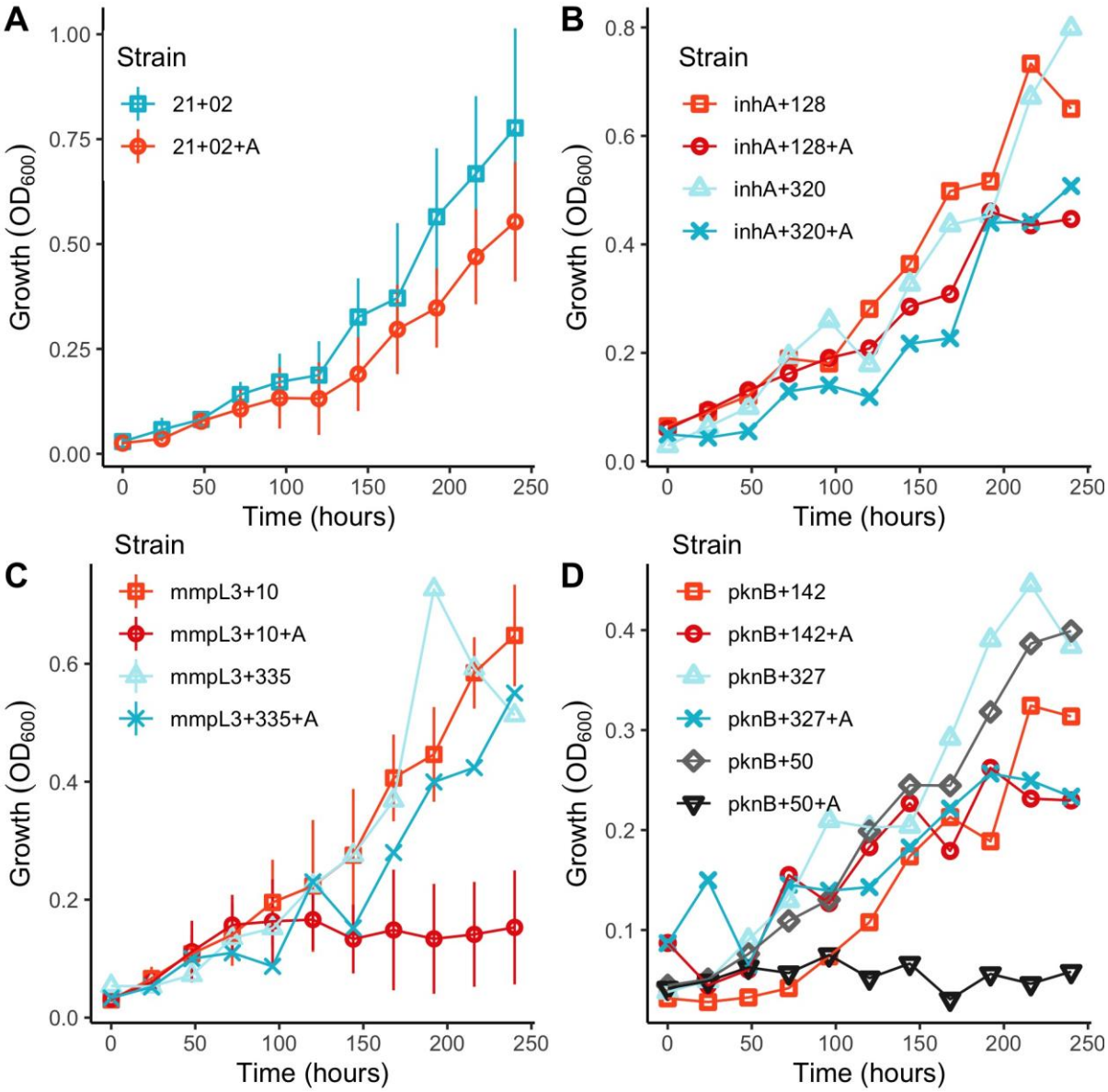


Figure 3.18: Growth curves of *M. bovis* BCG CRISPRi strains, showing that only *mmpL3*+10 and *pknB*+50 strains are affected by addition of ATc. (A) control 21-02 strain. N=3 (B) *inhA* knockdown strains. N=1 (C) *mmpL3* knockdown strains. N=1/2 (D) *pknB* knockdown strains. N=1. Mid-log cells were diluted to 0.05 and incubated with or without the addition of ATc for 10-days. Every 24-hours a sample was taken to measure the OD_{600} and every 48-hours ATc (200 ng/mL) was added.

As shown, only knockdown strains *mmpL3*+10 and *pknB*+50 were affected by the addition of ATc and displayed limited or no growth across the time course. Strains *inhA*+128, *pknB*+142 and *pknB*+327 all appeared to stagnate 196-hours into the growth curve if ATc was added, however, as only one repeat was undertaken, this data is inconclusive. The remainder of the control target strains were not affected by the addition of ATc, which could suggest these guide RNAs were not effectively suppressing the targeted genes.

The growth curve data for the remainder of the strains tested is summarised in Table 3.6, highlighting the start and endpoint OD_{600} values. Due to time limitations, some of the generated strains could not be tested in this growth curve assay. The majority of strains had slightly lower OD_{600} values in the presence of ATc, however, most reached mid-log values, indicating a normal level of growth across the ten-day assay period. This is expected, as none of the targeted genes have been classified as essential (DeJesus et al., 2017).

Table 3.6 *M. bovis* BCG CRISPRi strains growth curve start and endpoints, in the presence or absence of ATc. Timepoints at 0 and 240-hours. N=1 (except N=3 for 21-02)

Strain	Growth Curve start and endpoints / OD_{600}			
	No ATc		+ ATc	
	Start	Endpoint	Start	Endpoint
21-02	0.029 ± 0.009	0.78 ± 0.24	0.025 ± 0.003	0.55 ± 0.14
***bcg_3184c* +118**	0.046	0.61	0.042	0.46
***bcg_3184c* + 29**	0.040	0.89	0.035	0.63
***clgR* + 104**	0.036	0.55	0.060	0.43
***narG* + 196**	0.035	0.54	0.065	0.53
***narG* + 289**	0.029	0.59	0.031	1.11
***narG* + 7**	0.059	0.42	0.025	0.55
***ribC* + 10**	0.056	0.63	0.051	0.57
***ribC* + 165**	0.021	0.45	0.027	0.48
***ribC* + 80**	0.023	0.35	0.023	0.27
***whiB3* + 102**	0.072	0.86	0.062	0.78
***whiB3* + 30**	0.037	0.73	0.058	0.76

The strains which could be tested for a shift in vanoxerine MIC_{99} are listed in Table 3.7. Due to limited time, some of the strains which were produced could not be tested. For every strain, the MIC_{99} was determined in the absence of ATc first, without inducing gene knock-down and then repeated whilst inducing gene knock-down through ATc addition every 48-hours. In total, fifteen strains were tested from a possible nineteen strains (Table 3.7).

Table 3.7. Vanoxerine MICs of *M. bovis* BCG CRISPRi strains, in the presence or absence of ATc. N=3

Strain + position of guide RNA	**Vanoxerine MIC_{99} / µg/mL**	
	No ATc	+ ATc
Control 21-02 strain	23	23
***bcg_3184c* +118**	35	23
***bcg_3184c* +196**	23	23
***bcg_3184c* + 29**	35	23
***clgR* + 104**	23	23
***mmpL3* + 10**	23	15.5
***mmpL3* + 335**	23	23
***narG* + 196**	23	35
***narG* + 289**	23	23
***narG* + 7**	35	35
***ribC* + 10**	35	23
***ribC* + 165**	23	23
***ribC* + 80**	35	23
***whiB3* + 102**	23	23
***whiB3* + 30**	23	35

The testable hypothesis was that any gene knock-down which was targeted by vanoxerine would have a lower MIC_{99}, as there would be a smaller amount of 'target' protein for vanoxerine to inhibit. Hence, only strains which had a reduction in the MIC_{99} to vanoxerine following ATc supplementation were investigated further. The strains which showed differences were *bcg3184c*+118, *bcg3184c*+29, *mmpL3*+10, *ribC*+10 and *ribC*+80. The percentage survival curves for these strains, alongside the control 21-02 strain are shown in Figure 3.19.

For the 21-02 control strain, Figure 3.19A, there was no difference in the MIC_{99} and a limited difference in the percentage survival curve. For the majority of other strains

displayed, the change in the percentage survival curve was minor. There were only small decreases in percentage survival upon ATc addition for *bcg3184c*+118, *bcg3184c*+29, *ribC*+10 and *ribC*+80 (Figure 3.19B,C,E,F). While strain *mmpL3*+10 showed a larger difference, based on the average percentage survival, this is not a significant change (Figure 3.19D). The small shift in the *mmpL3*+10 strain MIC_{99} may be due to the inhibition of growth induced by addition of ATc (Figure 3.18C). Despite the MIC_{99} values shifting upon ATc addition, putative knock-down of these genes did not appear to affect vanoxerine susceptibility.

The decrease in mRNA transcript levels expected from this CRISPRi strategy was not confirmed due to lack of time. The next step would be confirming these CRISPRi plasmids interfered with the targeted genes. Hence, in the current format, this set of experiments did not aid target identification. The lack of an observed difference in the MIC_{99} could be due to lack of mRNA downregulation or due to these selected proteins not affecting the resistance to vanoxerine.

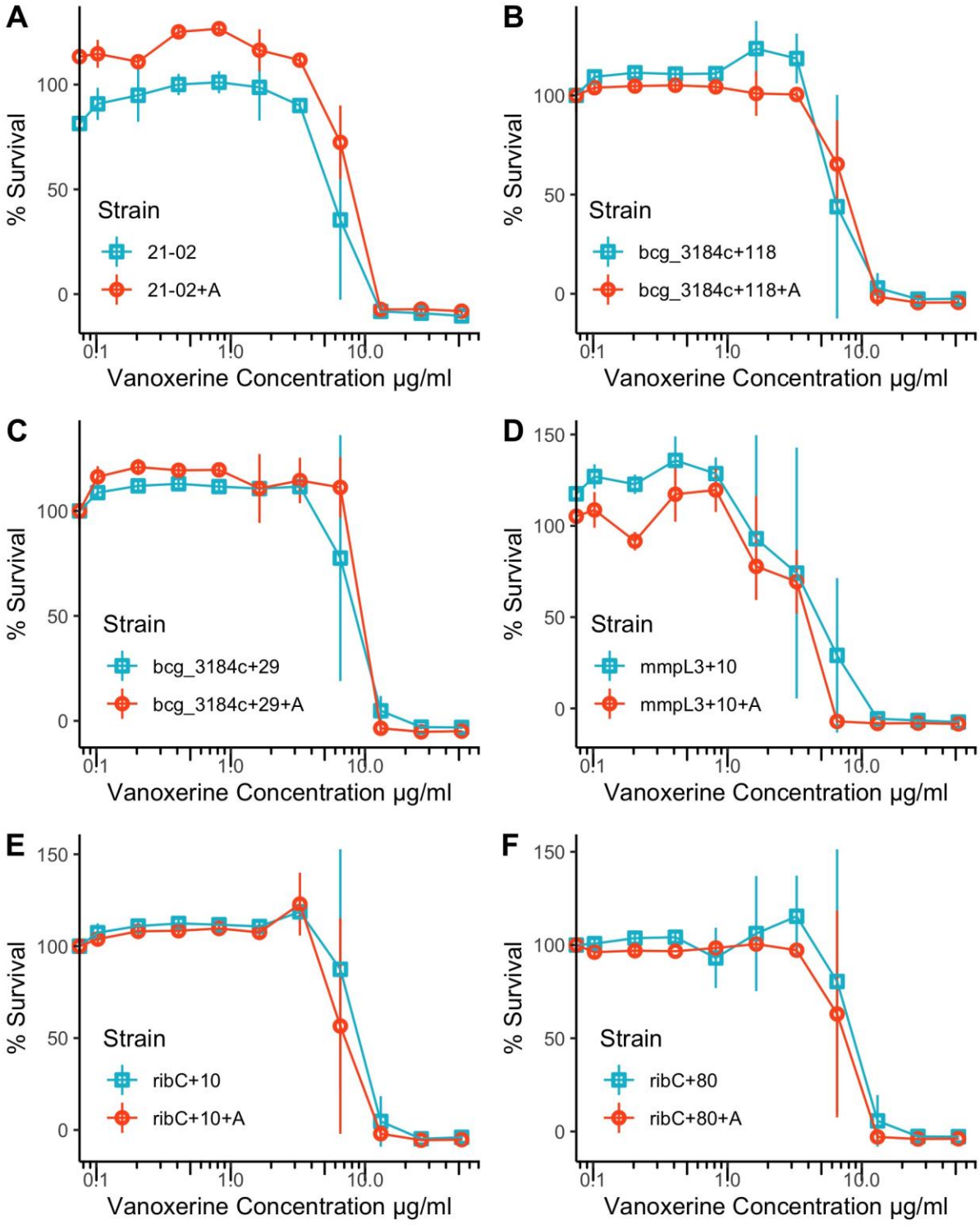


Figure 3.19: Percentage survival curves of *M. bovis* BCG CRISPRi strains following vanoxerine treatment, in the presence/absence of ATc. (A) Control 21-02 strain. (B) *bcg3184c*+118 strain. (C) *bcg3184c*+29 strain. (D) *mmpL3*+10 strain. (E) *ribC*+10 strain. (F) *ribC*+80 strain. Mid-log strains were diluted to OD_{600} 0.05 and added to a 2:3 vanoxerine serial dilution. Plates were incubated for 6-days, before resazurin addition and re-incubation for 1-day. N=3.

3.2.16. Trehalose mono-mycolate (TMM) is lost following treatment of *M. smegmatis*

As the genes selected for analysis following RNA-sequencing did not alter vanoxerine resistance, other areas were focussed upon. The mycolic acid biosynthetic pathway was investigated, as four genes were transcriptionally downregulated in a concentration dependent manner, hence the impact on all the genes in the pathway was investigated (Table 3.8). Following vanoxerine treatment, all the genes in the mycolic acid biosynthetic pathway were transcriptionally repressed, including the FAS-I and FAS-II enzymes. The only gene transcript that was not downregulated was mmpL3. However, its transcription was not significantly different to the no-drug control.

Table 3.8. Gene expression of mycolic acid biosynthesis genes, comparing no drug to 30 µg/mL vanoxerine. N=4.

Gene ID	Log_2 Fold Change	P-adjusted
accD6	-1.43	2.24E-123
acpM	-2.05	2.27E-22
cmrA (rv2509)	-0.55	2.76E-25
fabD	-1.79	6.13E-78
fabG1	-1.75	2.69E-104
fabH	-0.39	0.00083
fadD32	0.11	0.41
fas	-0.97	4.06E-51
fbpA	-1.40	2.66E-76
fbpB	-2.37	1.51E-177
fbpC	-0.55	0.00049
hadA	-1.48	2.07E-07
hadB	-1.03	3.50E-19
inhA	-1.73	1.44E-47
kasA	-2.11	1.09E-72
kasB	-2.07	1.78E-137
mmpL3	0.79	5.21E-32
pks13	-0.18	3.47E-07

Given the clear trend of mycolic acid biosynthetic gene down-regulation, it was investigated whether this translated into a loss or reduction in mycolic acids *in vitro*. Hence, lipid extraction was undertaken on *M. smegmatis* treated with vanoxerine. At the same time as drug treatment, the lipids were labelled using C^{14} acetic acid. The extracted lipids were separated using thin-layer chromatography (TLC), performed in $CH_3Cl/MeOH/H_2O$, 80:20:2, v/v/v, and visualized by exposure to an X-ray film (Figure 3.20A). The loss of trehalose mono-mycolate (TMM) was clear at 0.5x MIC_{99} vanoxerine and loss of trehalose di-mycolate (TDM) at 2.5x MIC_{99} vanoxerine. To confirm that the reduction in TMM was not due to lower growth in the presence of vanoxerine, the radioactivity was quantified as counts on the TLC plate. The number of counts was compared between the extracted lipids in the presence and absence of vanoxerine treatment (Figure 3.20B). A clear drop in TMM was apparent, accounting for 7% of the total counts in DMSO, compared to less than 1% in all the vanoxerine concentrations tested. As mycolic acids are essential for mycobacterial growth, this could indicate another mechanism of vanoxerine inhibition. Additional solvent systems were used to evaluate the impact of vanoxerine on lipids, Appendix 6.

To further investigate the impact of vanoxerine, we used *C. glutamicum* which produces mycolic acids but does not require them to survive. It has already been shown that vanoxerine could inhibit *C. glutamicum*, with an MIC_{99} of 15.5 µg/mL (Table 3.2). As this MIC_{99} is comparable to that of *M. tuberculosis*, this suggests mycolic acid biosynthesis is not the main target of vanoxerine. To assess whether mycolic acid biosynthesis inhibition was required for vanoxerine growth inhibition, a *C. glutamicum* Δpks mutant was used (Gande et al., 2004). The percentage growth following vanoxerine treatment is shown for both the wild-type and Δpks mutant (Figure 3.20C).

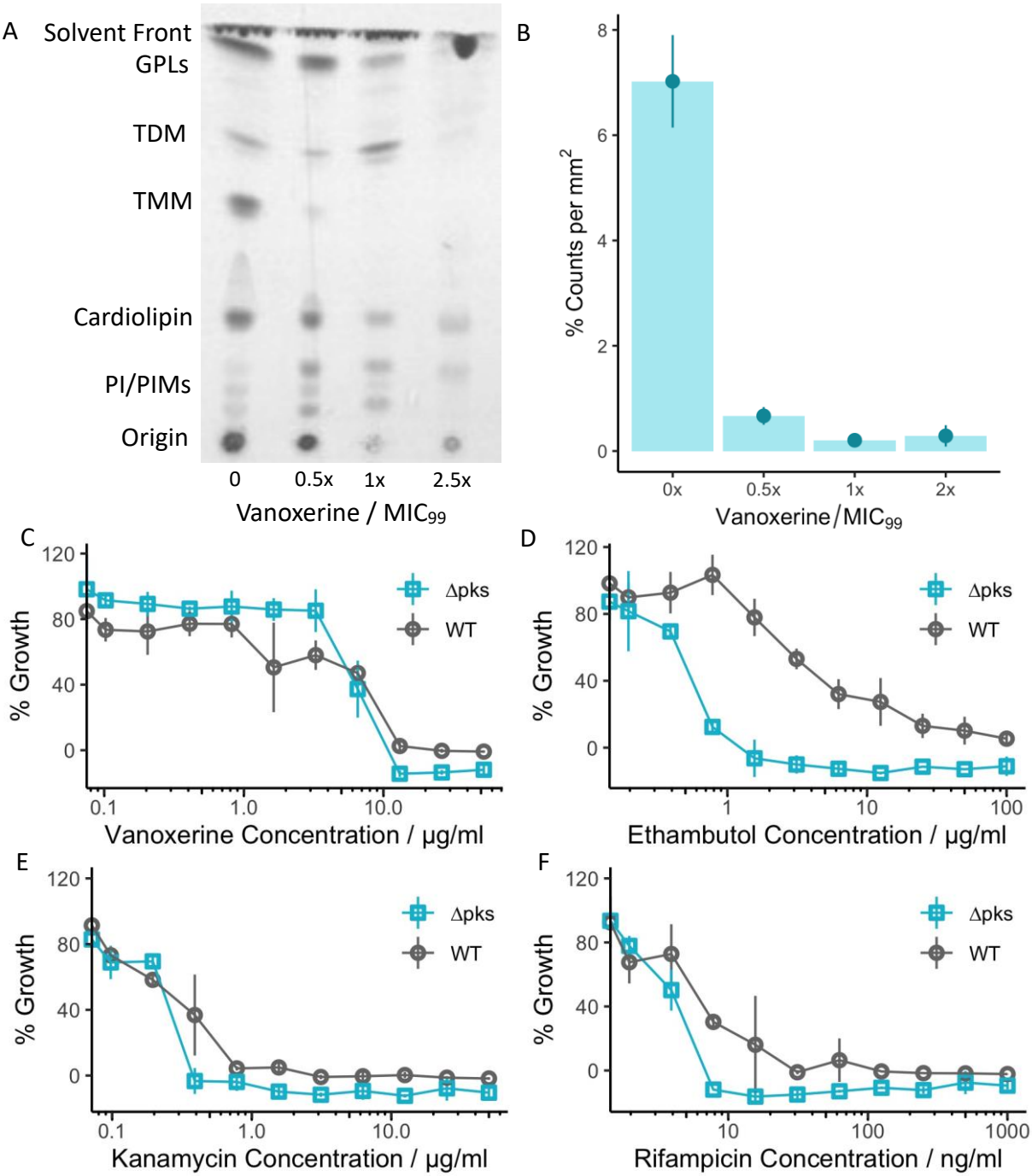


Figure 3.20: Loss of TMM occurred in *M. smegmatis* following drug treatment but does not appear to be cause of killing. (A) Thin Layer Chromatography of *M. smegmatis* lipid extractions, performed in $CH_3Cl/MeOH/H_2O$, 80:20:2, v/v/v. 10,000 counts per sample. GPL = Glycopeptidolipids, TDM = Trehalose dimycolates, TMM = Trehalose monomycolates, PI = Phosphatidylinositol, PIMs = phosphatidylmannosides. N=4 (B) Densiometric analysis of TMM following vanoxerine treatment. Counts for the TMM spot were compared to the total counts per lane, generating a %counts per mm^2. N=4. (C-F) %Survival comparing *C. glutamicum* WT vs Δpks13 mutant in (C) vanoxerine, (D) ethambutol, (E) kanamycin, (F) rifampicin. %Growth calculated by measuring OD_{600} after 48-hours incubation. WT= wild type N=3. Parts (A,B,C) adapted from Kingdon et al. (2022)

No difference in the MIC_{99} or shift in the percentage growth curve was observed, suggesting mycolic acid biosynthesis is not a main target of vanoxerine inhibition. For comparison, the wild-type and ∆pks *C. glutamicum* mutant were treated with several other antimycobacterial drugs to investigate the effects. Ethambutol, targeting the cell envelope arabinogalactan, led to a large shift in the percentage growth and MIC_{99} in the ∆pks mutant (Figure3.20D). As the cell envelope was already weaker, this additional disruption had a more potent effect on the *C. glutamicum* ∆pks mutant. In contrast, both kanamycin and rifampicin caused smaller differences in the percentage growth and MIC_{99} (Figure 3.20E,F). This is likely due to them having intracellular targets and hence they have a lower synergistic effect with the ∆pks mutant. Overall, this provides further evidence that vanoxerine does not directly inhibit cell envelope biosynthetic processes but has indirect impacts on the cell envelope.

3.2.17. Overexpression of mycolic acid biosynthesis pathway

Given the impact of vanoxerine on the *M. smegmatis* mycolic acids, but limited impact on other lipids, the mycolic acid biosynthesis pathway was investigated. This involved overexpression of the genes involved in this synthetic pathway. All over-expressor strains were created by Dr Sarah M. Batt, Dr Katherine Abrahams, and Dr Rebecca Taylor (University of Birmingham). As previously generated strains were used, overexpression was performed in the strain the over-expressor plasmid was already in, either *M. smegmatis* or *M. bovis* BCG. The pMV261 vector used the same *hsp60* promoter for constitutive overexpression as the pMV306 vector used herein.

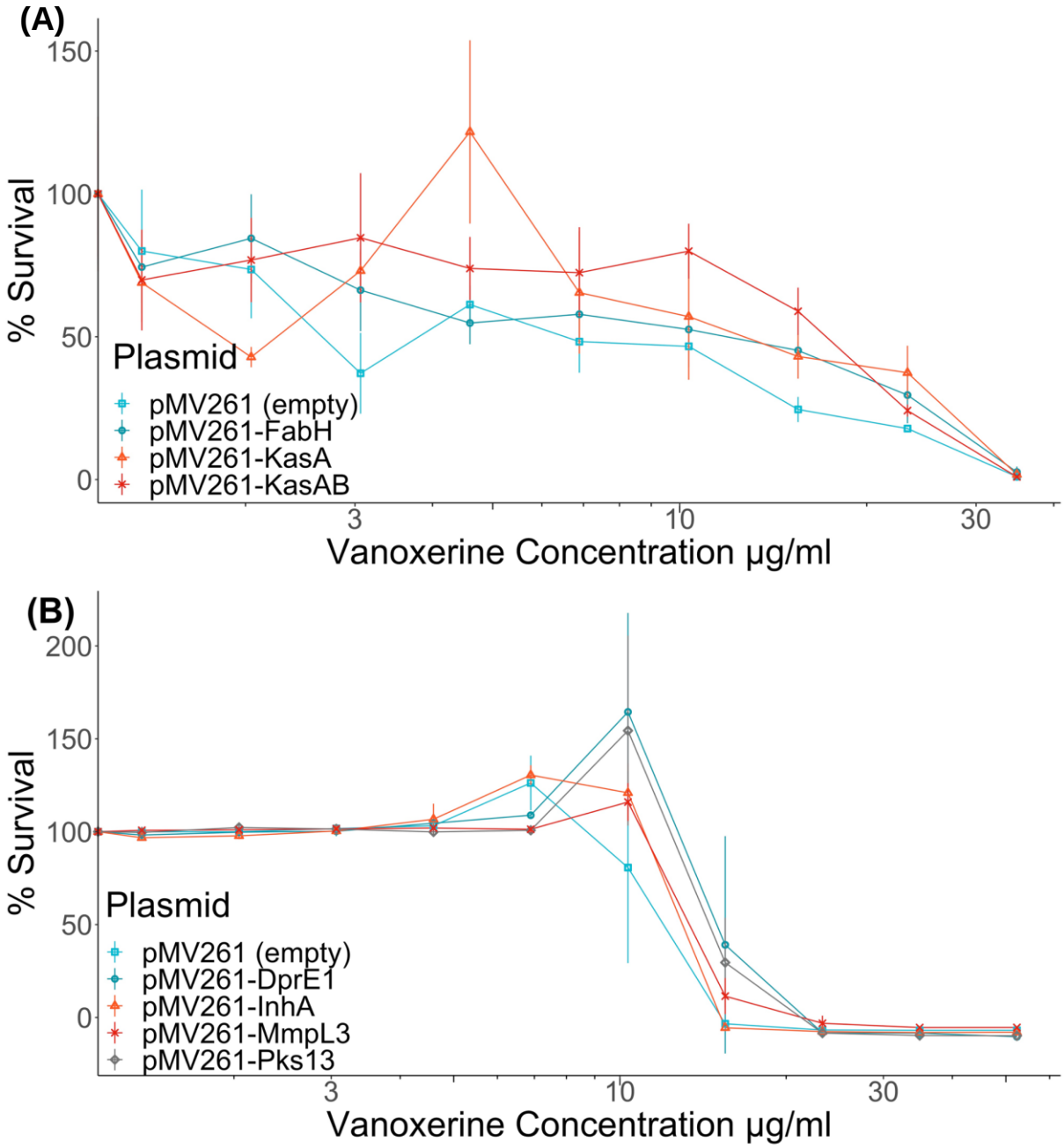


Figure 3.21: Overexpression of mycolic acid biosynthetic enzymes did not affect the resistance to vanoxerine. (A) *M. smegmatis* over-expressor strains. (B) *M. bovis* BCG over-expressor strains. Cells were diluted to OD_{600} 0.05 before addition to a 2:3 vanoxerine serial dilution. Plates were incubated for 21-hours (*M. smegmatis*) or 6-days (BCG), before resazurin was added and plates re-incubated for 3-hours (*M. smegmatis*) or 24-hours (BCG). The resorufin fluorescence was measure and %survival was calculated. N=3. Taken from Kingdon et al. (2022)

The percentage survival curves are shown in Figure 3.21. For *M. smegmatis,* there was no shift in the MIC_{99} and no impact on the percentage survival at sub-MIC_{99} of vanoxerine (Figure 3.21A). For *M. bovis* BCG over-expressor strains, there was a small difference in the MIC_{99} to vanoxerine (Figure 3.21B). There was an overlap of error bars at 15.5 µg/mL vanoxerine suggesting some replicates of each over-expressor strain were killed at this concentration, and all strains were killed at 23 µg/mL. The lack of a significant shift following MmpL3 overexpression, provides further evidence that this is not a direct target of vanoxerine.

3.2.18. Vanoxerine analogues

As the potency of vanoxerine against mycobacteria is not very high, analogues were synthesised in an effort to produce a more effective analogue. The analogues EMK022, EMK023, EMK024, EMK025 and EMK026 were synthesised by Eleni Marina Kasimati (Department of Chemistry, University of Birmingham). The design and synthesis of the EMK022-026 analogues was undertaken before the commencement of this current project. The analogues 482, 486 (resynthesis of EMK041), 488, 489 and 490 were all synthesised by Dr Holly Adcock (University of Birmingham). Analogue EMK041 was previously synthesised and showed similar efficacy to vanoxerine at 55% purity, hence it was resynthesized, and renamed to analogue 486. Analogues 490 and 488 were intermediates used in the synthesis of 482, which was chosen to allow a protein pull-down experiment to be undertaken. Analogue 489 was chosen as a study suggested it had a half-life of one month or more in rhesus monkeys (Lewis et al., 1999), hence, if the antimycobacterial activity was maintained, this would allow much lower frequency of dosing. GBR12935 was obtained commercially and was chosen to

determine the effect of the fluorine atoms on the diphenylmethoxy moiety. The compounds' structures are displayed in Figure 3.22.

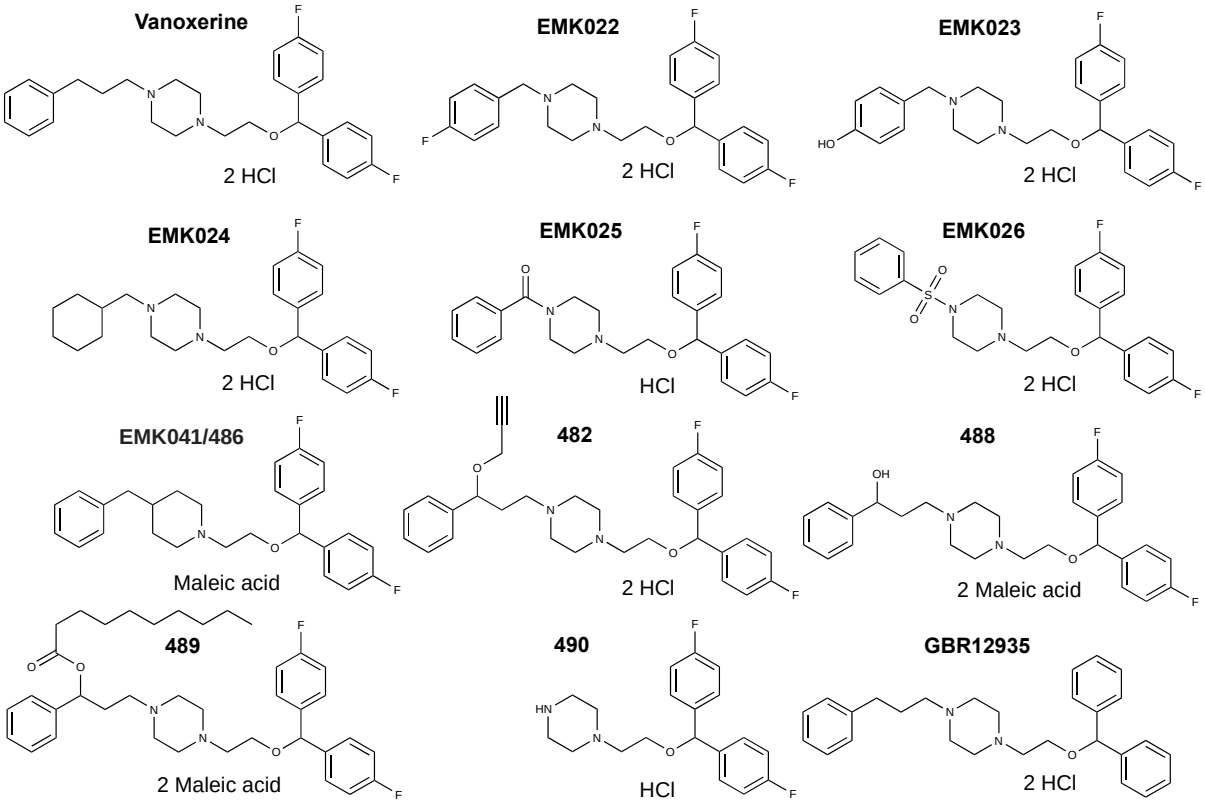


Figure 3.22: Structural analogues of vanoxerine.

3.2.19. Vanoxerine analogues – MICs

Following the synthesis of the analogues, these were then tested against a subset of the species originally tested. It was decided to focus upon *M. smegmatis, M. bovis* BCG and *E. faecium*, to gain information about the mycobacterial susceptibility and the retention of activity against Gram-positive species. The MIC_{99} values determined are displayed in Table 3.9. Maleic acid was also tested, as it was used as a salt during purification of some analogues.

Table 3.9. MIC_{99} values determined for vanoxerine analogues

Compound	MIC_{99} (μM)		
	M. smegmatis	*M. bovis* BCG	*E. faecium* E745
Vanoxerine	50	50	44
EMK022	>100	50	>100
EMK023	>100	>100	>100
EMK024	100	>100	100
EMK025	>100	>100	>100
EMK026	>100	>100	>100
482	100	100	>100
486 (EMK041)	50	25	25
488	100	50	>100
489	>100	>100	>100
490	>100	>100	>100
GBR12935	100	100	>100
Maleic acid	>100	>100	>100

The majority of analogues were less effective than vanoxerine, with many having no activity at the highest tested concentration (Table 3.9). The exception to this rule was compound 486, which was more effective against both *M. bovis* BCG and *E. faecium*. In addition, EMK022 and compound 488 were equally affective against *M. bovis* BCG. The only other compounds which displayed antibacterial activity were EMK024, compound 482 and GBR12935. Maleic acid had no activity on its own, suggesting the activity of compounds 482 and 486 was due to the compound alone. Plots of

percentage survival or growth used to determine the MIC_{99} are shown in Appendix 7, for *M. smegmatis, M. bovis* BCG and *E. faecium* E745.

3.2.20. Vanoxerine analogues – accumulation/efflux of ethidium bromide

The activity of vanoxerine as an efflux inhibitor has already been elucidated, hence, it was tested whether the compound analogues retained this activity. As a range of growth inhibition activities had been identified, if the activity correlates with efflux inhibition and electric potential disruption, this will provide further confirmation of the mechanism of inhibition.

For each compound, the rate of both ethidium bromide accumulation and efflux was assessed, across a ten-minute assay window and the final change in fluorescence summarised in Table 3.9. The first five minutes of the assay were excluded from rate determination, due to an influx of ethidium bromide across all conditions. The rate was determined for ten minutes, five minutes into the assay window. The rate of accumulation analysis (Table 3.10) highlighted compounds 482 and 488 caused very high rates of influx, at 4,500 RFUs/min. Compound 486 had a similar influx rate to vanoxerine, both at 3,000 RFUs/min. In contrast, the DMSO only control had an influx rate of 800 RFUs/min. The percentage change in fluorescence at the end of the 60-minute assay window allowed a more representative comparison between the compounds. The best performing compounds remained 482, 486 and 488, alongside vanoxerine and verapamil, leading to approximately 300% increases in fluorescence. EMK022 was the only other compound to cause a fluorescence increase of greater than 100%. Ethambutol and maleic acid were included as negative controls and caused similar levels of ethidium bromide accumulation to the DMSO-only condition.

Table 3.10. Rates of accumulation and efflux of ethidium bromide in *M. smegmatis* and the impact of vanoxerine analogues. All analogues were tested at 100 µM. N=3, (N=9 for DMSO, vanoxerine and verapamil). All values were rounded based on the standard deviation. Rate of accumulation from 5-14 minutes, rate of efflux from 0-9 minutes.

Drug	Rate of Accumulation (RFUs/min)	% Change in Fluorescence (Accumulation)	Rate of Efflux (RFUs/min)	% Change in Fluorescence (Efflux)
DMSO only	N/A	N/A	-5900 ± 800	-59 ±0.3
DMSO + Glucose	800 ± 220	33 ± 11	-6500 ± 500	-61 ± 0.2
Vanoxerine	3000 ± 130	299 ± 3	-1100 ± 500	-11 ± 0.5
GBR12935	1100 ± 40	90 ± 3	-2000 ± 100	-37 ± 0.2
EMK022	1300 ± 20	175 ± 4	-1700 ± 200	-25 ± 0.2
EMK023	1100 ± 40	75 ± 2	-2500 ± 200	-49 ± 0.3
EMK024	1000 ± 16	94 ± 2	-2200 ± 60	-43 ± 0.2
EMK025	600 ± 30	37 ± 2	-4300 ± 400	-63 ± 0.1
EMK026	700 ± 20	44 ± 1	-4000 ± 130	-59 ± 0.02
482	4500 ± 260	323 ± 7	-1200 ± 200	-13 ± 0.1
486	3000 ± 100	286 ± 1	-1400 ± 200	-11 ± 0.1
488	4500 ± 40	349 ± 1	-1100 ± 110	-11 ± 0.1
489	1000 ± 160	39 ± 2	-5600 ± 160	-59 ± 0.1
490	2700 ± 310	57 ± 6	-4500 ± 400	-57 ± 0.1
Verapamil	N/A	N/A	-1400 ± 400	-21 ± 0.4
Verapamil + Glucose	2900 ± 140	210 ± 7	-1500 ± 400	-25 ± 0.5
Ethambutol	400 ± 30	32 ± 2	N/A	N/A
Maleic acid	1000 ± 50	28 ± 1	-5400 ± 2100	-58 ± 0.9

Focussing on the effect on ethidium bromide efflux, the rate of efflux was based on the first ten-minutes of the assay, as it was not affected by additional ethidium bromide influx. In this case, the lower the rate of efflux, the more effective the analogue at inhibiting efflux. Compounds 482 and 488 had similar rates of efflux to vanoxerine, at

-1,100 RFUs/min. Compound 486 had a similar rate of efflux to verapamil, at -1,400 RFUs/min. This suggests all three analogues are efflux inhibitors. All compounds tested, except maleic acid and compound 489, appeared to reduce the rate of efflux compared to the DMSO plus glucose control. The overall percentage change in fluorescence indicated that compounds 486 and 488 were equally effective as vanoxerine, retaining 89% of the fluorescence. Compound 482 was only slightly less effective, retaining 87% of the fluorescence, which was better than the verapamil control at 75% retention. This dataset showed that GBR12935, EMK022, EMK023 and EMK024 caused some retention of ethidium bromide compared to the DMSO plus glucose control.

To allow a more thorough analysis of the best performing analogues, compounds 482, 486, and 488, the accumulation and efflux inhibition graphs are displayed in Figure 3.23. Testing was undertaken at 50 and 100 µM for these drug analogues and compared against vanoxerine and verapamil. As previously shown in Table 3.7, these analogues have a similar effect on the accumulation of ethidium bromide to vanoxerine, at 100 µM. However, a clear difference is apparent when comparing 50 µM vanoxerine to the other analogues, Figure 3.23A. All three analogues had lower efficacy, causing 260, 210 and 275% increases in fluorescence for compounds 482, 486 and 488 respectively, compared to a 338% increase in fluorescence for 50 µM vanoxerine. This trend of analogue efficacy is reversed when studying the impact on efflux rather than accumulation (Figure 3.23B). As the change in fluorescence in the presence of 50 µM of each analogue was -23.6, -18.8 and -24.2% for compounds 482, 486 and 488 respectively. This is compared to -17.5% for 50 µM vanoxerine. Testing

the analogues at 100 µM had an almost indistinguishable effect compared to 100 µM vanoxerine, as shown in Table 3.10.

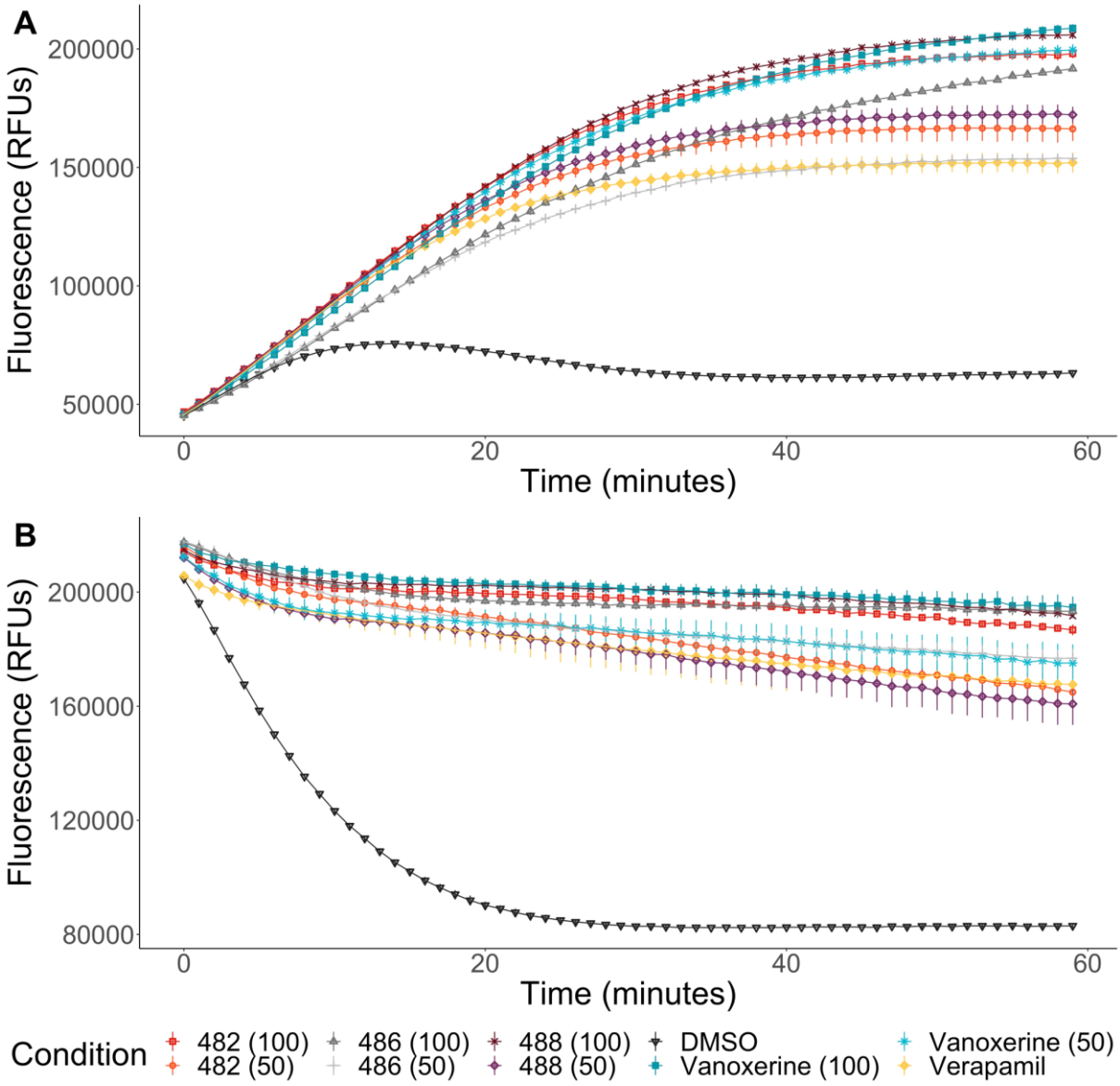


Figure 3.23: Comparison of the effect of compounds 482, 486, 488, and vanoxerine on the accumulation and efflux of ethidium bromide by *M. smegmatis*. (A) Accumulation. (B) Efflux. Compounds were tested at either 50 or 100 µM. For efflux, cells were allowed to accumulate ethidium bromide (0.625 µg/mL) for 2-hours. For accumulation, cells were combined with ethidium bromide (0.625 µg/mL) immediately before the assay start point. In both cases the cells were resuspended in PBS + glucose (0.4%) and added to a 96-well plate containing compounds. The fluorescence was measured every minute for 60-minutes. N=3. DMSO = 1%, verapamil = 50 µg/mL.

3.2.21. Vanoxerine analogues – $DiOC_2(3)$ dye disruption

As the inhibition of ethidium bromide efflux was also caused by the analogues of vanoxerine, it was tested whether this was occurring through the dissipation of the membrane electric potential. The prevention of the partitioning across the membrane of $DiO_2(3)$ of *M. bovis* BCG is shown in Figure 3.24A,B, split across the active and inactive compounds for clarity, based on growth inhibition. The ability of the vanoxerine analogues to disrupt the dye partitioning, and hence electric potential, is displayed in Figure 3.24C,D. Although each dataset is split across two graphs, each experiment was performed concurrently, and hence the control data for DMSO, CCCP and vanoxerine are displayed for clarity across both pairs of graphs. All compounds were tested at 100 µM, to compare the same concentration of drug, despite the differences in MIC_{99}.

Focussing on the initial partitioning of the $DiOC_2(3)$ dye, all the 'active' analogues led to a lower accumulation of red fluorescence compared to the DMSO-only control (Figure 3.24A). From the 'inactive' analogues, only compound 490 had this effect, while the remaining analogues did not cause a deviation from the DMSO-only control (Figure 3.24B). CCCP caused an ~11,000 RFUs reduction in red fluorescence, associated with membrane depolarisation, whereas the DMSO-only control had a ~44,000 RFUs increase in red fluorescence, representing typical dye partitioning across the membrane. Vanoxerine caused an increase of ~20,000 RFUs, suggesting some disruption to electric potential, but not complete dissipation. In the accumulation assay, only compounds 486 and 488 performed better than vanoxerine, as they lowered the red fluorescence increase to ~7,000 and ~14,000 RFUs, respectively.

Similar results were obtained for the experiments directly studying the disruption of the $DiOC_2(3)$ dye from its partitioned state. All the 'active' analogues were able to cause some dissipation of the electric potential, although EMK022 and EMK024 were considerably less effective than the remaining analogues (Figure 3.24C). From the 'inactive' analogues, compounds 490 and EMK023 were more effective at dissipating the electric potential than the DMSO-only control (Figure 3.24D). Known protonophore CCCP caused a reduction in red fluorescence of ~35,000 RFUs, compared to a reduction of only 1,500 RFUs for the DMSO-only control. Vanoxerine caused a reduction of ~23,000 RFUs in red fluorescence. In this assay, the analogues 482, 486 and 488 were all more effective than vanoxerine at electric potential dissipation, causing red fluorescence reductions of ~27,500, ~27,000 and ~30,000 RFUs, respectively. Overall, this provides an explanation for the increased efficacy of compound 486 over vanoxerine and similar activity levels for compound 488, in relation to whole-cell inhibitory activity.

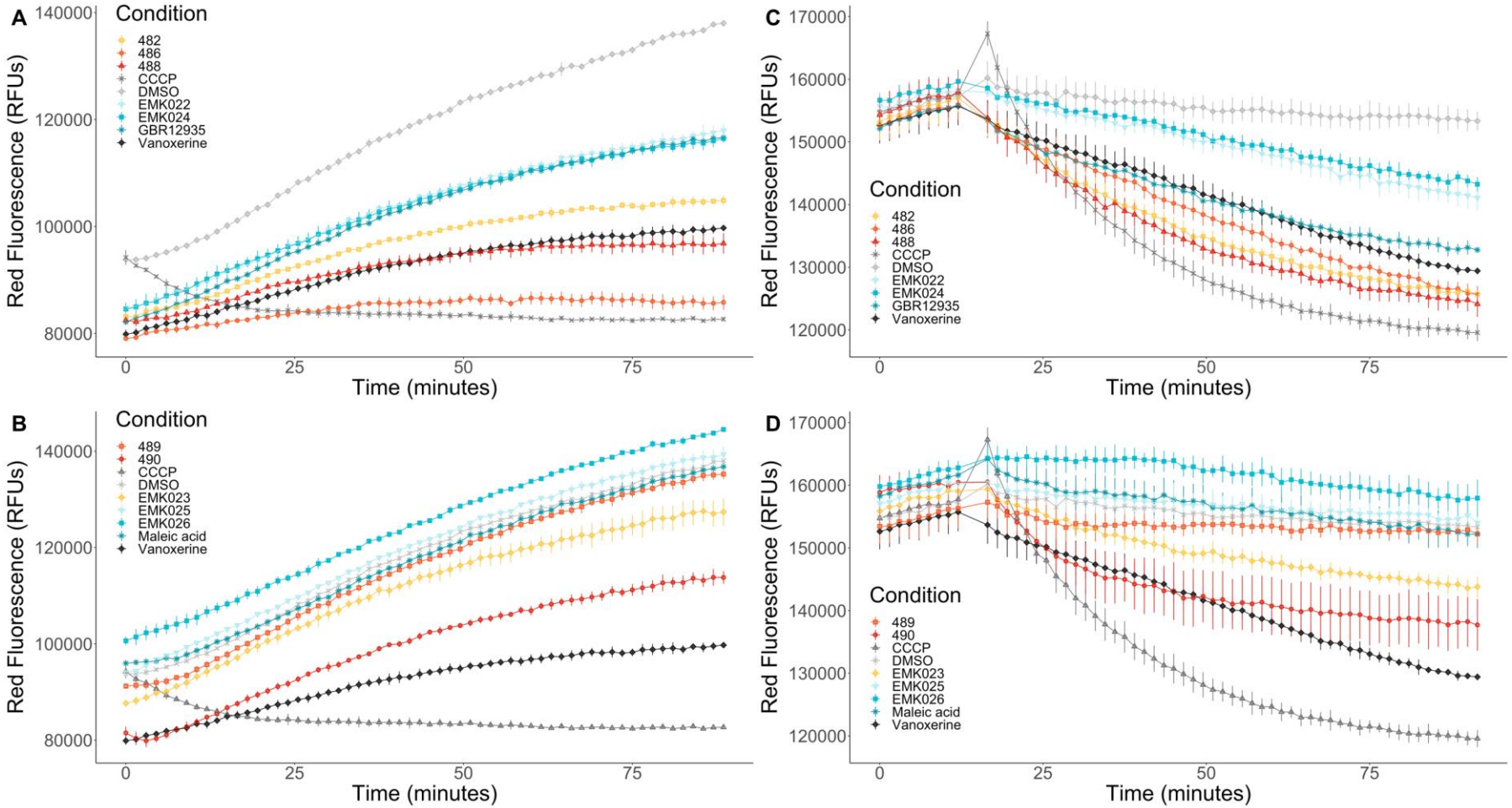


Figure 3.24: Vanoxerine analogues can disrupt the *M. bovis* BCG membrane electric potential. Immediate addition of dye and compounds (A) MIC active compound (B) MIC inactive compounds. Dye equilibration for 2-hours before compound addition (C) MIC active compounds. (D) MIC inactive compounds. All compounds were tested at 100 µM. $DiOC_2(3)$ dye (30 µM) was added to cells and the mixture either immediately added to drug compounds (A&B) or incubated for 2-hours prior to addition (C&D). The fluorescence was measured every 90-seconds for 90 minutes. The controls (CCCP, DMSO and vanoxerine are the same across A&B and C&D). CCCP = 25 µM, DMSO = 1%. N=3.

3.2.22. Vanoxerine analogue 482 – protein pull-down

As a protein target had yet to be identified for vanoxerine within mycobacteria, a protein pull-down experiment was undertaken. This involved crosslinking of vanoxerine analogue 482 to azide-agarose resin, using click chemistry to irreversibly fuse the two components together (Figure 3.25A). To avoid non-specific interactions, the modified agarose resin was incubated with bovine serum albumin (BSA) for two hours. After washing, the resin was incubated with *M. smegmatis* cell lysate for two hours. If any specific 482-protein interactions were occurring, this was predicted to displace the non-specific agaraose-482-BSA interactions. 3-[(3-cholamidopropyl)dimethylammonio]-1-propanesulfonate (CHAPS) was included in the lysis buffer to solubilise membrane proteins and improve the chance of binding to a vanoxerine protein target. Following incubation with the cell lysate, the resin was washed extensively, and fractions were analysed by running on an SDS-PAGE gel (Figure 3.25B). The same procedure was repeated with unmodified azide-agarose resin. No proteins were enriched in the presence of 482-agarose compared to the unmodified resin. However, BSA appeared to bind more strongly to the unmodified resin, requiring three more wash steps to fully elute, compared to the 482-resin. The lack of a protein binding to the 482-resin suggests either vanoxerine has no protein target, or the attachment site of 482 onto the agarose resin blocked binding to the protein.

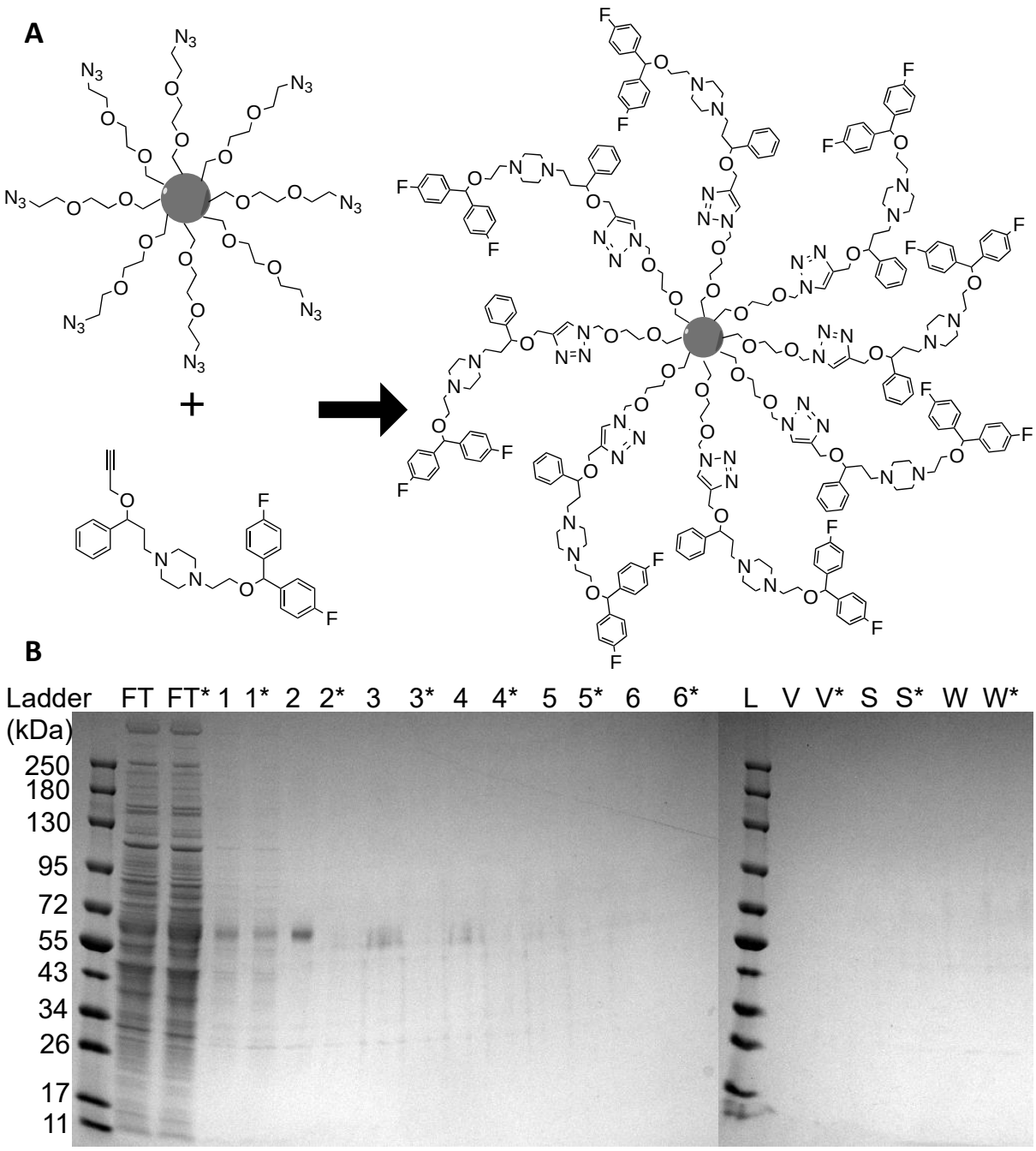


Figure 3.25: The fusion of compound 482 to agarose resin did not allow a mycobacterial protein target to be selected. (A) Creation of the 482-agarose fused resin. (B) SDS-PAGE gel showing attempted protein pull-down from *M. smegmatis* cell lysate. (A) 482 (1 mM) and azide-agarose resin (1 mM) was incubated with $CuSO_4$, THPTA and sodium ascorbate to form the 482-agarose resin. (B) Agarose resin, either azide or modified with 482 (*), was blocked with BSA (66.5 kDa) for 1 hour, before being incubated with *M. smegmatis* cell lysate (FT) for 2 hours. The resin was washed six times before eluting any remaining protein using vanoxerine (V), SDS (5%, S) and water (W).

3.2.23. Dopamine transporter inhibition study

This work was undertaken by Eurofins Discovery, performing a dopamine transporter uptake antagonist assay on the top three vanoxerine analogues, 482, 486 and 488. This assay used Chinese hamster ovary cells transfected with human recombinant dopamine transporter protein and quantified the uptake of [^{3}H] dopamine across 90-minutes, based on radioactive counts (Janowsky et al., 1986). The uptake was assessed in the absence or presence of compound, or vanoxerine (GBR12909) as a control. Due to cost, each compound was tested in triplicate at five concentrations, in half-log dilutions from 10 µM to 100 nM, the control was undertaken at pre-specified concentrations. If the compound caused less than 50% inhibition at a tested concentration, then the IC_{50} was calculated. The results from this assay are displayed in Table 3.11.

Table 3.11 Inhibitory impact of vanoxerine analogues on the dopamine transporter uptake. N=3

Compound	IC_{50} against dopamine transporter (nM)	Inhibition at 100 nM (%)
482	<100	95
486	140	35.8
488	<100	98.2
Vanoxerine	1.9-3.0	N/A

The vanoxerine analogues retained activity against the dopamine transporter. For compound 486, the IC_{50} could be calculated, and this highlighted that it was between 47-74x less effective at inhibiting the dopamine transporter compared to vanoxerine. To reach >95% inhibition, 1 µM 486 was required. Compounds 482 and 488 were more effective at inhibiting the dopamine transporter than 486 and hence inhibited at greater than 90% for all tested concentrations. Unfortunately, this prevented IC_{50}

values from being calculated, but suggested they were more similar in activity level to vanoxerine.

3.2.24. Vanoxerine targets the cell envelope in *B subtilis*

As mentioned earlier, vanoxerine was able to inhibit *B. subtilis* with an MIC_{99} of 52 µg/mL. Despite having low potency, this allowed a collaboration with Prof. Heike Brötz-Oesterhelt (University of Tübingen), to test vanoxerine against their set of *B. subtilis* bioreporter strains. The bioreporter strains covered a range of potential targets of antimicrobials and was based on gene induction in response to stress being coupled to LacZ reporters (Wex et al., 2021). This work was performed by Anne Wochele (University of Tübingen).

The reporter strains and associated responses are displayed in Table 3.12. This show no stress response induction was linked to DNA, RNA, or protein stress. Similar to the RNA-sequencing results from *M. bovis* BCG, cell envelope stress was also induced in *B. subtilis*. This was both a general stress response and linked to lipid-II interference, which is involved in peptidoglycan biosynthesis. However, the induction of *liaI* can also be caused by detergents. In contrast, the lack of *fabHb* induction suggests no interference with fatty acid biosynthesis in *B. subtilis* by vanoxerine.

Table 3.12. Responses of *B. subtilis* reporter strains due to vanoxerine treatment. N=2. - = No Induction. + = weak induction. ++ = strong induction.

Reporter Strain	Associated Stress	Response
yorB	DNA	-
ypuA	Cell envelope	++
liaI	Cell envelope (focussed on lipid-II cycle)	+
fabHb	Biosynthesis of fatty acids	-
yppS	RNA	-
yheI	Protein (ribosome staller)	-

This highlighted that vanoxerine was also targeting the cell envelope in *B. subtilis* and that is did not appear to hit other pathways within *B subtilis*. As this result matched with our proposed mechanism of action of vanoxerine, the assays performed to study both ethidium bromide efflux and electric potential were repeated in *B. subtilis* and *E. faecium*. This could provide confirmation that vanoxerine had the same mechanism of action across all the species that it targeted.

3.2.25. Vanoxerine caused accumulation of ethidium bromide in *E. faecium* and *B. subtilis*

Initially, the effect of vanoxerine on the accumulation of ethidium bromide was investigated. During experimental design, the MIC_{99} of ethidium bromide was determined for both *B. subtilis* and *E. faecium*, being 12.5 and 25 µg/mL, respectively. In addition, at high concentrations, ethidium bromide naturally enters the cell. Hence, a range of concentrations of ethidium bromide were tested, in the absence of drug treatment, to find concentrations which plateaued over the assay window. This led to ethidium bromide concentrations of 0.125 and 0.625 µg/mL being used in the *B. subtilis* and *E. faecium* assays, respectively.

B. subtilis was studied as a direct follow-up to the reporter assay strains and showed vanoxerine caused a large increase in ethidium bromide fluorescence compared to the DMSO-only control (Figure 3.26A). The DMSO-only samples showed an 80% increase in fluorescence across the 60-minute assay. Verapamil treatment caused a 126% increase in fluorescence, while the lowest vanoxerine concentration tested, 13 µg/mL, caused a 137% increase in fluorescence. The increased accumulation of ethidium bromide due to vanoxerine was concentration-dependent, with 52 µg/mL vanoxerine causing a 148% increase in fluorescence.

E. faecium was studied as a more clinically relevant Gram-positive species, for which vanoxerine remained active. *E. faecium* 64/3 accumulated ethidium bromide over time and the accumulation was elevated by vanoxerine in a concentration dependent manner (Figure 3.26B). The addition of verapamil had no impact on ethidium bromide accumulation, as a 32% increase in fluorescence occurred for both the verapamil and DMSO-only conditions. In contrast, 13 µg/mL vanoxerine caused a 48% increase and 52 µg/mL vanoxerine caused a 116% increase.

The more drug resistant *E. faecium* E745 strain was also assessed and had a net negative fluorescence across the assay window, suggesting rapid influx of ethidium bromide, followed by stabilisation (Figure 3.26C). Only 26 and 52 µg/mL vanoxerine led to accumulation of ethidium bromide, causing increases of 33 and 88% in fluorescence across the 60-minutes. Verapamil also had no impact in this case, suggesting it is not active against *E. faecium*. Overall, this data supports vanoxerine causing an accumulation of ethidium bromide within Gram-positive species.

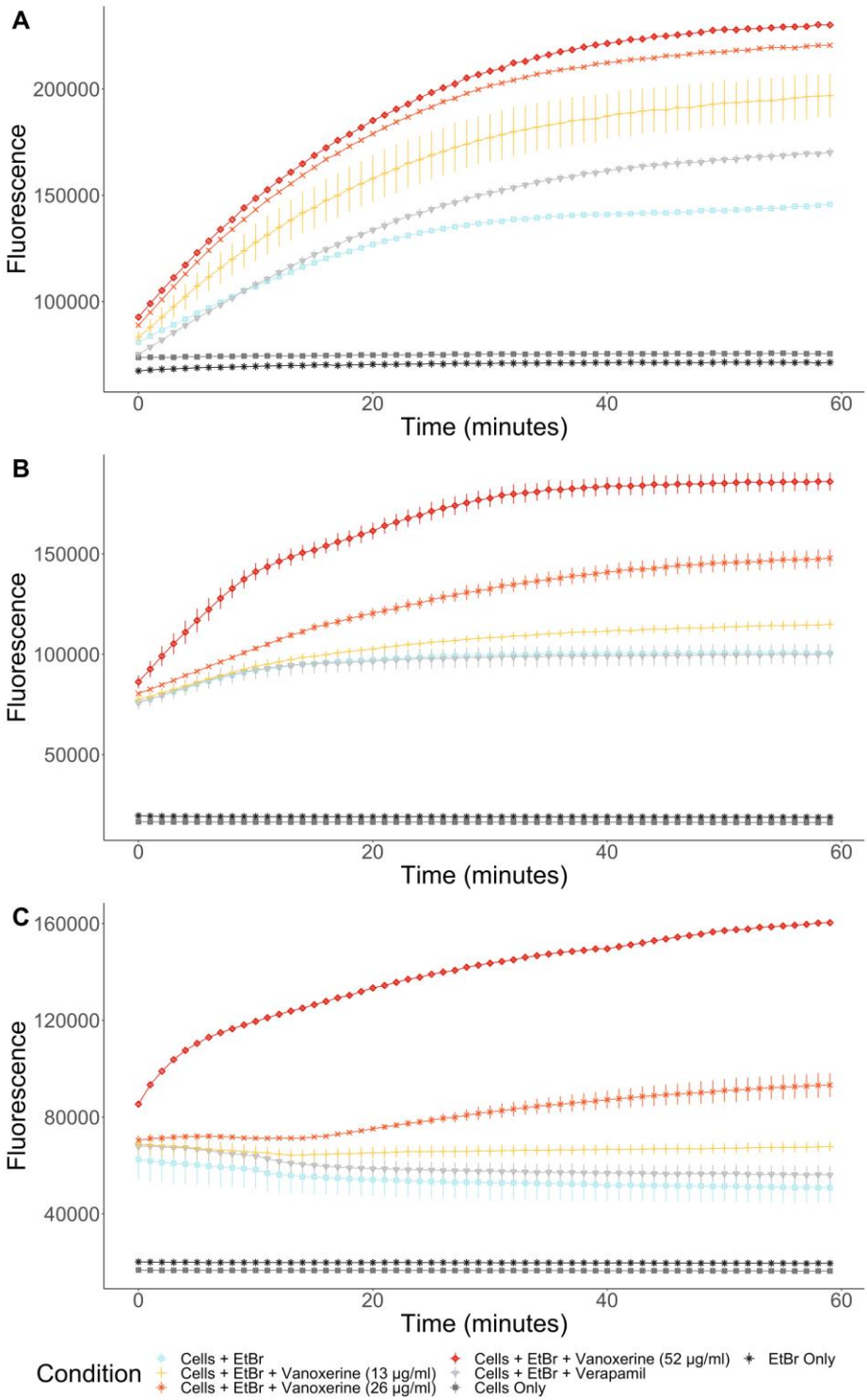


Figure 3.26: Vanoxerine caused accumulation of ethidium bromide, shown by an increase in fluorescence. (A) *B. subtilis*. (B) *E. faecium* 64/3. (C) *E. faecium* E745. Mid-log cells were washed and resuspended in PBS containing glucose (0.4%) and ethidium bromide (0.125 µg/mL for *B. subtilis*, 0.625 µg/mL for *E. faecium*), OD_{600} 0.8. The cells were immediately added to a 96-well plate containing drug compounds and fluorescence was measured every minute for 60-minutes. N=3.

3.2.26. Vanoxerine impacted *B. subtilis* efflux, but not *E. faecium* efflux

Given the accumulation of ethidium bromide following vanoxerine treatment, it was investigated whether vanoxerine had an impact on efflux directly. For both species, verapamil in the absence of glucose was used to cause ethidium bromide accumulation. Then, the loss of fluorescence could be used to monitor efflux. For *B. subtilis*, both vanoxerine and verapamil inhibited ethidium bromide efflux (Figure 3.27A). The addition of glucose caused an increase in the amount of efflux, causing a drop in fluorescence of 19% compared to 13%. Only 26 and 52 µg/mL vanoxerine caused greater retention of ethidium bromide, with fluorescence drops of 6.8 and 6.5%, respectively.

In the case of *E. faecium* 64/3, cells alone had a drop in fluorescence of 28%, with the addition of glucose causing a 42% decrease (Figure 3.28B). As shown during the accumulation experiment, verapamil had no impact on ethidium bromide efflux. Vanoxerine did not initially show a difference compared to the DMSO-only control, however, approximately 30-minutes into the assay, no further ethidium bromide was effluxed. Hence, at the end of the assay window, 13 µg/mL vanoxerine led to a drop of 39% fluorescence, while 52 µg/mL led to a drop of 32%, suggesting a small impact on efflux. This experiment was not repeated in *E. faecium* E745, given the limited effects.

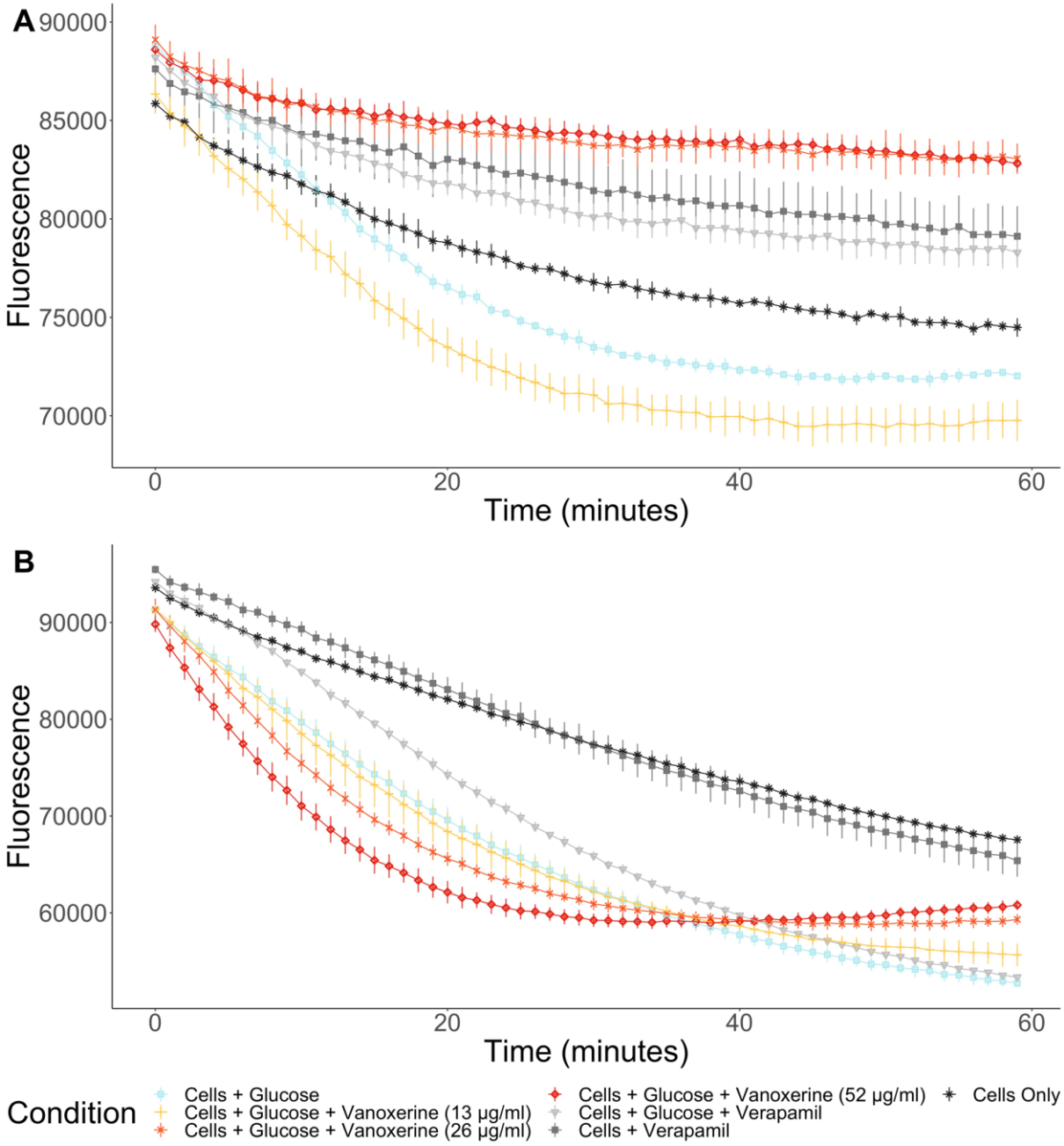


Figure 3.27: Vanoxerine prevented ethidium bromide efflux in *B. subtilis* but has limited effect on efflux in *E. faecium*. (A) *B. subtilis*. (B) *E faecium 64/3*. Mid-log cells were allowed to accumulate ethidium bromide (0.125 µg/mL for *B. subtilis*, 0.625 µg/mL for *E. faecium* 64/3) for 1 hour in PBS, OD_{600} 0.8. Cells were resuspended in fresh PBS + 0.4% glucose and immediately added to a 96-well plate containing drug compounds. The fluorescence was measured every minute for 60-minutes. N=3

3.2.27. Vanoxerine disrupted the electric potential of *E. faecium* and *B. subtilis*

Given the similar effects of vanoxerine on mycobacteria and Gram-positive species, at least for ethidium bromide accumulation, the impact of vanoxerine on the membrane electric potential was explored. This used the same $DiOC_2(3)$ voltage sensitive dye, and it was allowed to partition across the membrane relative to the electric potential. The rate of dye movement through the membrane was substantially faster in *B. subtilis* and *E. faecium* (Figure3.28), compared to *M. bovis* BCG, hence the impact of drug treatment could not be monitored concurrently with dye addition.

For *B. subtilis*, the electric potential was rapidly dissipated by addition of either CCCP or vanoxerine (Figure 3.28A). The red fluorescence, corresponding to intracellular aggregated dye, dropped from approximately 160,000 RFUs to 42,000 RFUs for CCCP and to ~40,000 RFUs for vanoxerine. All three vanoxerine treatment concentrations stabilised at the same red fluorescence, but the time required to dissipate the electric potential varied, from approximately 6-minutes for 26 µg/mL to 35-minutes for 13 µg/mL. Across the assay window, the red fluorescence dropped to ~92,000 RFUs, likely due to the lack of an energy source in the assay. Evidence for this theory is provided by the addition of glucose causing hyper-polarisation of the membrane and a peak of red fluorescence of ~202,000 RFUs.

Both strains of *E. faecium* had similar responses to vanoxerine treatment, with some dissipation of the electric potential occurring (Figure 3.28B,C). In both assays, CCCP has a limited impact on the electric potential as *Enterococcus* does not perform oxidative phosphorylation (Leblanc, 2006), hence, the exact red fluorescence associated with complete electric potential disruption is unknown. Addition of glucose

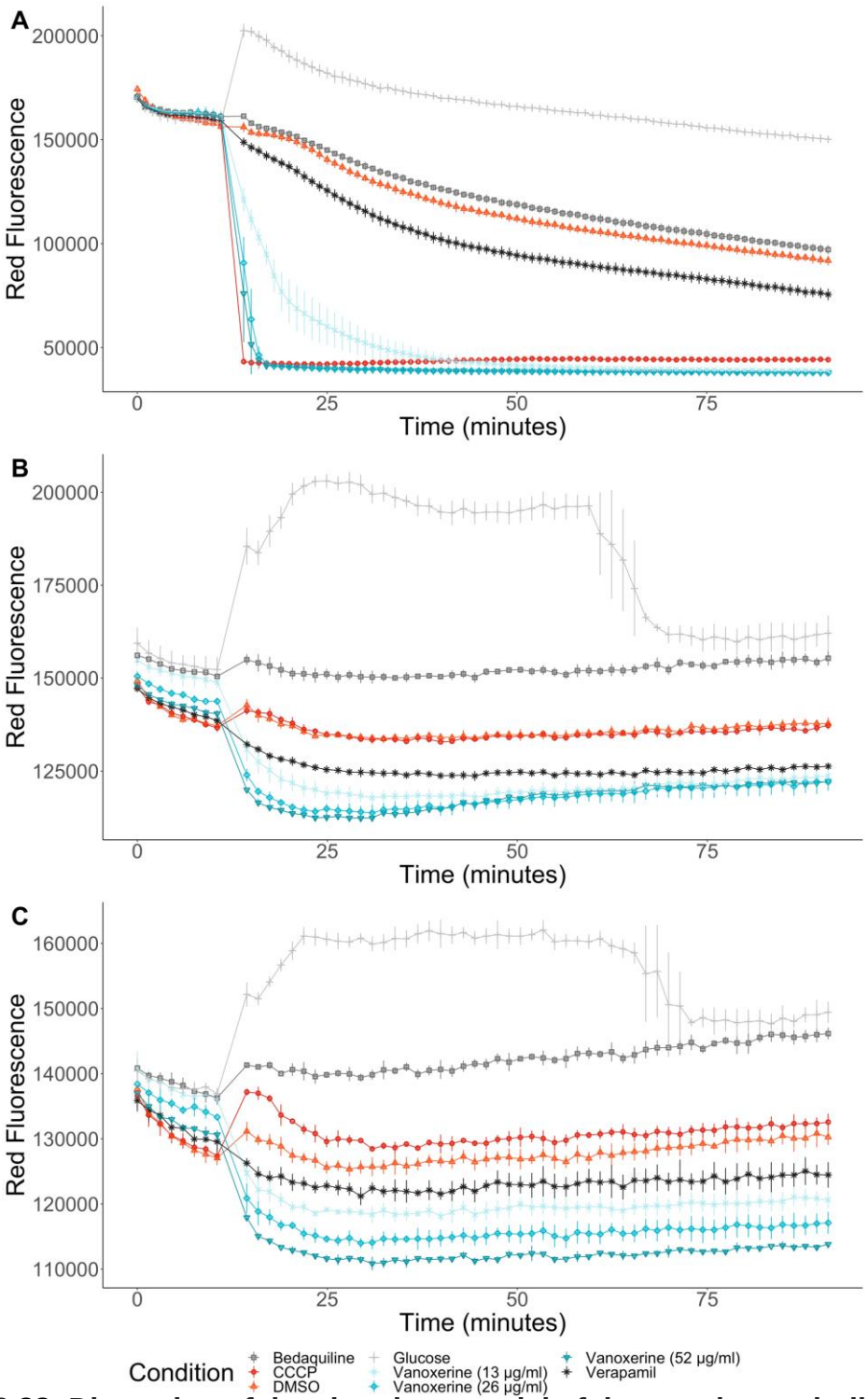


Figure 3.28: Disruption of the electric potential of the membrane, indicated by the change in red fluorescence of $DiOC_2(3)$ in (A) *B. subtilis.* (B) *E. faecium* 64/3. (C) *E. faecium* E745. Cells were incubated with 30 µM $DiOC_2(3)$ for 2-hours to allow dye partitioning. The fluorescence was measured for 10-minutes, followed by vanoxerine or drug control addition and continued measurements for 80-minutes. Bedaquiline = 0.5 µg/mL, CCCP = 25 µM, DMSO = 1%, glucose = 250 µM, verapamil = 50 µg/mL. N=3.

led to hyper-polarisation across the membrane of both strains, reading ~203,000 and ~162,000 RFUs for 64/3 and E745, respectively. Bedaquiline was included as a negative control, as it was not expected to have an impact on the *E. faecium* electric potential. For *E. faecium* 64/3, all three concentrations of vanoxerine caused a similar reduction from 140,000-150,000 RFUs to ~120,000 RFUs (Figure 3.28B). Whilst the DMSO-only condition retained red fluorescence around 135,000 to 140,000 RFUs across the 80-minute assay window. For *E. faecium* E745, the drop in red fluorescence was concentration dependent, dropping from 131,000-136,000 RFUs to ~119,000, ~114,000 and ~110,000 RFUs for 13, 26 and 52 µg/mL vanoxerine, respectively (Figure 3.28C). While the DMSO-only condition fluctuated between 127,000 to 130,000 RFUs across the 80-minute assay window. Overall, this data suggested that vanoxerine dissipates the electric potential for both mycobacteria and Gram-positive species.

3.2.28. Resistance development in *E. faecium* E745

Spontaneous resistant mutants could not be generated against vanoxerine in mycobacteria; hence an alternative approach was trialled. *E. faecium* E745 was chosen as a faster growing clinically relevant strain. This was the final experiment undertaken in an attempt to identify a protein target for vanoxerine. The experimental aim was to induce resistance, through growth in sub-MIC_{99} amounts of vanoxerine, then slowly increasing the drug concentrations alongside resistance development.

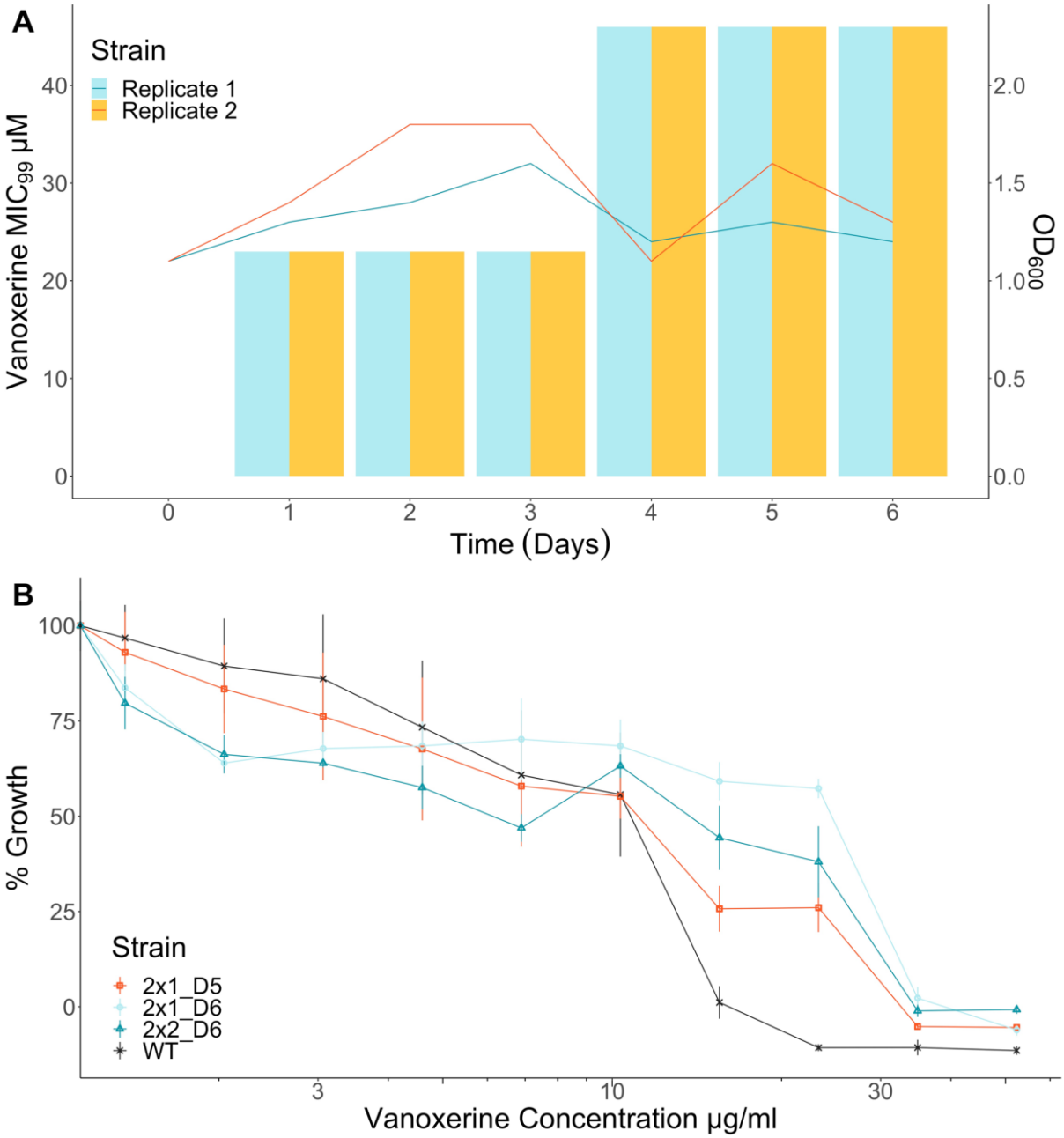


Figure 3.29: Vanoxerine resistance up to 2x MIC_{99} could be acquired following four days of sub-culture and translated into a shift in the MIC_{99}. (A) Graph of the time-course of growth in increasing concentrations of vanoxerine. Cells were initially diluted to 0.05, then added to 0.5, 1 & 2x MIC_{99} vanoxerine. Every 24-hours growth was assessed (OD_{600}) and the growing culture with the highest concentration of vanoxerine was sub-cultured (5 µL into 5 ml). **(B) Percentage growth curve of resistance strains, showing a shift in MIC_{99}.** Mid-log cells were diluted to OD_{600} 0.05 and added to a 2:3 vanoxerine serial dilution. The plates were incubated for 24-hours, before the OD_{600} was measured and %growth calculated. N=3. 2x1_D5=2x MIC_{99}, replicate 1 from day 5.

The experiment started by growing cultures of *E. faecium* E745 in 11.5, 23 and 46 µg/mL vanoxerine. The OD_{600} was monitored, alongside the level of resistance, shown in Figure 3.29A. Resistance to 1x MIC_{99}, 23 µg/mL vanoxerine, occurred within the first 24-hours. However, it took four days for *E. faecium* to develop resistance to 46 µg/mL vanoxerine, and no further resistance developed across the week-long experiment. On the first day of 2x MIC_{99} resistance development, there was an associated drop in the OD_{600}, which could suggest a growth defect. However, the OD_{600} recovered across the subsequent days, suggesting it was this was not the case. To confirm the resistance, the MIC_{99s} of the 'mutant' strains were determined against vanoxerine. In this case, one strain with 2x MIC_{99} of vanoxerine resistance from day five was selected, alongside both 2x MIC_{99} resistant strains from day six. These strains all showed a clear shift in MIC_{99} from 23 to 35 µg/mL vanoxerine and had an increased percentage growth at both 15.5 and 23 µg/mL vanoxerine (Figure 3.30B). However, this shift in MIC_{99} is not significant, only representing a 1.5-fold difference. A shift in survival still occurred and hence, these strains were sent for WGS by MicrobesNG. Alongside the mutant strains, the original *E. faecium* E745 strain and strains passaged in an equivalent amount of DMSO, increasing alongside resistance, were also sent for WGS.

The assembled genomes were compared to a reference genome for *E. faecium* E745, NCBI genome GCA_001750885.1. Several differences were found between the reference genome and the background strain, these are outlined in Appendix 8. Comparison of the *E. faecium* E745 background strains to the mutant strains did not reveal any strong candidates for potential targets (Table 3.13). Only mutations which caused mis-sense variants were investigated, while mutations in non-coding regions or synonymous variants were not evaluated further. Four genes had mutations which

met these criteria and are outlined in Table 3.13, alongside the exact mis-sense mutations identified. However, none of these genes are essential or involved in known resistance mechanisms, suggesting they are not the cause of resistance. In addition, both *E745_03041* and *E745_03042* are predicted to be on plasmids and could be involved in plasmid maintenance, rather than essential processes within *Enterococcus.*

Table 3.13. Missense mutations in *E. faecium* E745 grown in 2x MIC_{99} vanoxerine

Gene ID	Functional Annotation	Missense Mutations
EfmE745_02964	Hypothetical protein	c.5G>A p.Ser2Asn
EfmE745_02627	PIN/TRAM domain-containing protein	c.43G>A p.Ala15Thr
EfmE745_03041	Hypothetical protein	c.107A>C p.Glu36Ala c.131A>G p.His44Arg c.145T>A p.Ser49Thr c.152A>C p.Asp51Ala c.265A>G p.Asn89Asp c.283C>T p.Leu95Phe c.299_303delGTAAAinsATAAG p.Ser100Asn c.339G>A p.Met113Ile
EfmE745_03042	Plasmid recombination enzyme	c.794_799delCGGAAAinsATGAGT p.AlaGluMet265AspGluLeu c.815A>G p.Lys272Arg c.826A>G p.Lys276Glu c.840G>T p.Glu280Asp c.850G>A p.Val284Met c.863A>G p.Lys288Arg

Overall, this suggests the resistant strains have become slightly tolerant to vanoxerine, rather than developing a genetic resistance mechanism and provides further evidence that vanoxerine does not have a protein target within bacteria.

3.3. Discussion

Within this chapter, the limited spectrum of activity of vanoxerine has been highlighted, with Mycobacteriales being the main target alongside other Gram-positive species. Evidence has been provided that AroB if unlikely to be the mycobacterial target of vanoxerine, contrary to previous claims (Kanvatirth et al., 2019). In lieu of this previous target, further work was undertaken to identify the true target leading to growth inhibition. Vanoxerine was found to disrupt the membrane's electric potential, leading to downstream disruption of cellular energetics. These downstream effects were quantified through studying efflux inhibition and the disruption of transport across the membrane. This work has also provided evidence that vanoxerine does not have a protein target and over-expression of selected stress response proteins do not confer resistance. In addition, a more active analogue of vanoxerine, compound 486, was identified, which retained the same mechanism-of-action. Finally, evidence was provided that vanoxerine has the same mechanism of antibacterial action across both mycobacteria and Gram-positive species.

This work has conclusively disproven AroB as the protein target of vanoxerine. The initial evidence for this connection was found to be false, as the 'resistant' mutants were found in the lab's wild-type strain. Even if this evidence had not come to light, the position and mutations found in the *M. smegmatis aroB* gene do not affect the *M. tuberculosis* AroB homologue and so could not confer resistance (Kanvatirth et al., 2019). The residue 363 leucine to proline mutation is in a terminal unstructured region not present in the *M. tuberculosis* AroB protein. The remaining three *M. smegmatis* mutations converted the residues to the equivalent *M. tuberculosis* AroB protein residues (PDB = 3QBE). Based on this evidence, we would not expect a shift in the MIC_{99} following AroB overexpression and our data reflects this hypothesis. This is in

direct contrast to the previous results, which found a small MIC shift (Kanvatirth et al., 2019). The four resistant mutants found by Kanvatirth et al. (2019) were also found when generating resistant mutants to piperidinol derivatives by another group, and hence could represent a non-specific lab adaptation (Guy et al., 2017). In addition to the lack of *in vivo* effect of AroB overexpression, no binding interactions occurred between AroB and vanoxerine *in vitro*, see Chapter 2. Overall, the evidence provided indicates vanoxerine does not interact with AroB and is unlikely to be a target.

A standard approach for novel mode-of-action determination is the generation of spontaneous resistant mutants to a drug, followed by whole-genome sequencing, as mycobacterial drug resistance is generally acquired through point mutants or indels and not plasmids (Abrahams and Besra, 2020). As outlined, this approach was undertaken against *M. smegmatis* at high vanoxerine concentrations (Kanvatirth et al., 2019), but did not lead to target identification. Hence, this approach was repeated in *M. bovis* BCG. However, no resistant mutants to vanoxerine were isolated, despite several attempts across the course of this work, and the use of an *M. bovis* BCG Δ*recG* mutant with a higher mutation rate (Batt et al., 2015). In addition to work on mycobacteria, the induction of resistant mutants was trialled using the faster growing *E. faecium* E745. However, this did not lead to genetic differences and only development of tolerance up to 2x MIC_{99} vanoxerine. The lack of spontaneous or induced genetic resistant mutants is promising for vanoxerine, and other drugs which target the membrane electric potential. This is a positive finding, given the increasing levels of MDR tuberculosis globally (WHO, 2021), and the development of resistance to the most recently approved anti-mycobacterial drugs, bedaquiline, delamanid, and pretomanid (Zumla, Nahid and Cole, 2013). In addition, *E. faecium* E745 is a vancomycin-resistant clinical isolate, which is a WHO high priority pathogen that

urgently needs additional treatment options (WHO, 2017). The lack of *in vivo* resistance development could indicate pleotropic effects of vanoxerine on the cell, reducing resistance development or suggests there is a higher barrier to resistance due to targeting the membrane directly.

The retention of ethidium bromide by mycobacteria in the presence of vanoxerine provides strong evidence that it inhibits efflux. The formation of pores or lysis of the cell by vanoxerine are unlikely to be the mode-of-action, as this would cause a faster decrease in ethidium bromide fluorescence. The inhibition of efflux could occur via several mechanism, including disruption of membrane energetics, inhibition of ATP synthesis or direct efflux pump inhibition (Remm et al., 2022). The involvement of several different types of efflux pumps in the export of ethidium bromide from mycobacteria suggest that direct efflux pump inhibition is less likely (Remm et al., 2022; Johnson et al., 2020). Numerous papers have discussed the use of efflux inhibitors for the treatment of tuberculosis, as they could complement or enhance existing treatments (Remm et al., 2022; Pule et al., 2016; Gupta et al., 2014b; Laws, Jin and Rahman, 2022; Szumowski et al., 2013). The focus of these studies have been verapamil, CCCP or plant natural products (Chen et al., 2018; Pule et al., 2016; Gupta et al., 2014b), however, no efflux inhibitors are currently used clinically against TB (Pule et al., 2016). This is due to a variety of reasons, including the lack of safety data for plant natural products or toxicity of inhibitors on eukaryotic systems, in the case of CCCP (Pule et al., 2016). In comparison to these other inhibitors, verapamil has a better safety profile, but has been shown to cause serious adverse effects at higher drug concentrations (Pule et al., 2016). On the other hand, vanoxerine has passed phase I clinical trials without causing any adverse effects within healthy volunteers. (Obejero-Paz et al., 2015). Hence, vanoxerine represents an alternative to current

efflux inhibitors for use against tuberculosis and may be useful as an alternative tool compound in infection models.

To determine how efflux was inhibited, the voltage sensitive dye $DiOC_2(3)$ was used as an indicator of membrane electric potential ($\Delta\psi$) disruption (Chen et al., 2018; Chawla et al., 2012; Hudson, Siegele and Lockless, 2020; Li et al., 2019). Based on its fluorescence as a proxy, the disruption of the $\Delta\psi$ is likely to be a mechanism of action of vanoxerine. Disruption of the $\Delta\psi$ would cause the PMF of the cell to be dissipated, interfering with downstream energetics within mycobacteria and leading to cell death (Chen et al., 2018; Feng et al., 2015). As many efflux pumps rely on the PMF, the dissipation of the PMF would prevent active efflux and hence retention of ethidium bromide in the presence of vanoxerine (Remm et al., 2022). At physiological pH, vanoxerine is a cationic amphiphile, with a pK_a of 8.2 and a cLogP value of 5.3. Other compounds with these physiochemical properties have been shown to insert into lipid membrane and uncouple the PMF, at least in bacterial inverted membrane vesicles (Chen et al., 2018; Feng et al., 2015). Despite interfering with the membrane, these uncouplers have low mitotoxicity and have been reported to have several mechanisms of action (Chen et al., 2018; Feng et al., 2015). While the presented work does not preclude vanoxerine from having several mechanisms of action, the lack of a protein target suggests dissipation of the $\Delta\psi$ is the main mode of inhibition. The ability of drugs to interfere with cellular energetics has previously been shown to kill latent *M. tuberculosis* (Rao et al., 2008; Manjunatha, Boshoff and Barry, 2009), hence, vanoxerine should be tested for bactericidal effects in mycobacteria during latency.

The treatment of *M. tuberculosis* is always undertaken using a combination therapy of between three to six drugs, increasing treatment efficacy and reducing levels of resistance development (Nahid et al., 2016; Zumla, Nahid and Cole, 2013; Berry and

Kon, 2009). Vanoxerine dissipates the electric potential and inhibits mycobacterial efflux, hence, it was tested whether this mechanism of action showed synergy with any current or in development drugs. Based on the calculated FICs , vanoxerine showed no interactions with clofazimine, FNDR-20081 or rifampicin (Kaur et al., 2021; Gopal et al., 2013); although all showed some shifts in the MIC_{99} in the presence of sub-MIC_{99} amounts of vanoxerine. Potential drug interactions may be masked by the concurrent upregulation of the MmpL5 efflux pump, suggested to efflux clofazimine and FNDR-20081, and inhibition of mycobacterial efflux by vanoxerine (Hartkoorn, Uplekar and Cole, 2014; Andries et al., 2014; Remm et al., 2022; Kaur et al., 2021). While the MIC_{99} was shifted for these drugs, the MIC_{99} of bedaquiline was not altered in the presence of vanoxerine. This could be due to both drugs having analogous mechanisms, disrupting the PMF and hence having similar downstream effects (Andries et al., 2005; Feng et al., 2015). The lack of interactions with bedaquiline provides further evidence that the disruption of the PMF is the cause of cellular inhibition by vanoxerine.

Comparing the RNA-sequencing outputs outlined herein, to other known efflux inhibitors and uncouplers has given more perspectives. The phenothiazines have been shown to target NADH dehydrogenase II, which disrupts the electron transport chain and inhibits efflux through PMF disruption and ATP depletion (Remm et al., 2022). Transcriptomic data following phenothiazines treatment highlighted increases in *ndh*, *nuoE-G* and *icd1* transcript levels (Dutta, Mehra and Kaushal, 2010; Boshoff et al., 2004). For vanoxerine, the expression of *ndh* and *icd1* was not affected, while the transcription of *nuoE-G* were all significantly down-regulated, suggesting NADH dehydrogenase II is not a target of vanoxerine. Conversely, the transcriptomic effects of the 2-aminoimidazole class of compounds, which have been shown to dissipate the

PMF and block the electron transport chain (Jeon et al., 2019, 2017), had a high degree of similarity to vanoxerine (Table 3.13). Treatment with both 2B8 (an 2-aminoimidazole) and vanoxerine resulted in upregulation of *mprA, sigB, sigE, mmpL5, mmpL8, mmpL10, rv3160c (bcg_3184c)* and *rv3161c (bcg_3185c),* as responses to membrane stress, increasing membrane transporter/efflux and a putative dioxygenase and its regulator, respectively (Jeon et al., 2017). Both compounds also caused downregulation of mycolic acid (*fasI* and *fasII)* and peptidoglycan biosynthesis (*mur)* genes (Jeon et al., 2017). The main difference was vanoxerine did not induce transcription of the propionate detoxification genes, *prpC* and *prpD* or the *sigK* regulon (*sigK, rv0449c, mpt83, dipZ*), except for *mpt70*. Overall, the high similarity of the transcriptional responses of mycobacteria to vanoxerine and 2B8, provides further evidence that vanoxerine is impacting the PMF and cellular energetics (Jeon et al., 2019, 2017).

The micro-array RNA sequencing of *M. tuberculosis* following several drug treatments performed by (Boshoff et al., 2004) is more difficult to directly compare to the inverse rRNA selection RNA sequencing methods used herein. The magnitude of transcriptomic changes is dis-similar and prevents an unbiased comparison of the total differences between these conditions. However, a more biased approach focussed on previously highlighted gene transcripts was undertaken (Table 3.14). Genes which were upregulated across all three treatment groups included: *mmpL5-mmpS5*, *rv0678*, *rv3161c*, *mprA* and *sigB*. Only *acpM* and *ahpE* were downregulated across all three conditions, however, the verapamil transcriptomic response only represented one repeat and hence may not capture the true response. Comparing vanoxerine to CCCP, *fabD*, *kasB* and *fas* were also significantly downregulated. These comparisons also suggest that the downregulation of *nuoE-G* and *murD-G* and the upregulation of

mmpL8 and *mmpL10* may be specific to vanoxerine treatment (Table 3.14). Although, this may be due to different regulatory networks in *M. bovis* BCG compared to *M. tuberculosis*. This approach focussed on previously highlighted genes and hence may miss other important transcriptomic similarities or differences, which an unbiassed comparison might identify.

Table 3.14. Comparison of transcriptional responses of *M. tuberculosis* to CCCP, 2B8 and verapamil with the response of *M. bovis* BCG to vanoxerine. *1 repeat only. *M. tuberculosis* was treated with CCCP and verapamil for 6-hours, 2B8 for 2 and 24 hours, compared to 8-hours vanoxerine treatment of *M. bovis* BCG.

Gene ID	30 µg/mL Vanoxerine	125 µM 2B8 -2h	125 µM 2B8 -24h	50 µM CCCP	50 µg/mL Verapamil
nuoE	-1.733	-0.214	-0.635	0.371*	0.208*
nuoF	-1.715	-0.321	-0.758	-0.893	-0.25*
nuoG	-1.328	-0.575	-0.840	-0.3*	-0.05*
rv0678	2.352	1.156	3.292	2.941	1.048*
mmpL5	3.934	1.145	1.559	1.089	1.638*
mmpS5	4.012	1.513	2.373	1.851	1.352*
acpM	-2.053	-1.836	-1.385	-2.317	-1.33*
kasA	-2.117	-1.918	-1.210	0.471*	1.166*
fabD	-1.792	-1.947	-0.762	-1.697	-0.36*
kasB	-2.073	-2.077	-1.339	-2.493	-0.49*
hsp	2.606	1.964	2.706	2.367	0.637*
lpqS	0.083	0.041	1.342	-0.95*	N/A
ahpE	-2.262	-0.149	-0.716	-1.293	-0.42*
rv3160c	5.956	5.000	6.006	0.295*	0.897*
rv3161c	5.923	5.494	6.660	1.352	5.203*
clgR	2.190	0.944	1.479	0.588	0.229*
narG	1.065	-0.593	-0.153	0.105	0.333*
ribC	1.007	0.271	0.517	0.532	0.108*
whiB3	1.161	-0.044	0.616	0.36	0.374*
mmpL3	0.791	0.185	0.175	-1.267	0.14*
mprA	2.474	0.598	1.485	2.17	0.839*
sigB	2.077	0.820	1.701	1.994	1.267*
sigE	0.950	0.661	1.880	0.024	2.13*
mmpL8	1.779	0.723	0.858	-1.11	0.332*

mmpL10	1.127	0.004	0.595	-1.767	0.399*
prpC (gltA1)	-0.859	4.121	3.143	0.312	-0.28*
prpD	0.471	4.980	3.249	0.403	-0.54*
sigK	-0.402	0.700	1.119	0.321	0.237*
mpt70	1.914	5.765	5.824	-0.3*	N/A
fas	-0.966	-1.626	-0.891	-2.817	0.025*
murE	-1.258	-0.922	-0.584	0.942	0.192*
murF	-1.514	-1.083	-0.976	-0.12	-0.14*
murG	-0.509	-0.807	-0.248	0.834	0.112*
murD	-1.616	-0.747	-0.473	1.815	-0.2*

While the loss of TMM and TDM occurred following vanoxerine treatment of *M. smegmatis*, additional experimentation did not suggest that vanoxerine directly targeted mycolic acid biosynthesis. Mycolic acids are not an essential component of the *C. glutamicum* cell envelope and vanoxerine has a comparable MIC_{99} against both *C. glutamicum* and *M. tuberculosis*. Vanoxerine also had equal activity against a *C. glutamicum* wild-type and ∆pks mutant, in contrast to other antimycobacterial drugs, which were more potent against the ∆pks mutant strain. Rather than a direct inhibition of mycolic acid biosynthesis, it is more likely that the PMF disruption by vanoxerine had an indirect effect on the PMF-dependent transporter MmpL3. This protein transports TMM across the inner mycobacterial membrane (Su et al., 2019). The indirect inhibition displayed by vanoxerine is in contrast to the direct MmpL3 inhibition observed for many other antimycobacterial compounds (Li et al., 2019; Degiacomi et al., 2020). The decrease in transcription of mycolic acid biosynthesis genes could be an indirect result of MmpL3 inhibition, leading to the accumulation of TMM and other precursors in the cytoplasm. The loss of mycolates and down-regulation of the mycolic acid biosynthesis genes was also observed for the 2-aminoimidazole compounds, which also target the PMF (Jeon et al., 2017).

Numerous attempts were made within this work to identify a protein target for vanoxerine within mycobacteria, however, these efforts have suggested that vanoxerine does not have a protein target. The inability to generate resistant mutants, alongside the lack of any protein's being pulled down by the 482-azide resin, both suggest no protein target. In addition, the over-expression and knock-down experiments focussed on proteins, whose gene transcription was dysregulated during vanoxerine treatment, all highlight no shifts in the MIC_{99} occurred, suggesting none of these proteins are the target of vanoxerine. Many drugs which uncouple the PMF have secondary protein targets, however, this is not always the case (Feng et al., 2015). In addition, the front-line drug pyrazinamide currently has an debated mechanism of action, and direct inhibition of a protein target has not been suggested (Zhang et al., 2014; Peterson et al., 2015; Gopal et al., 2020). Overall, this work cannot rule out an additional protein target, however, it suggests one is unlikely.

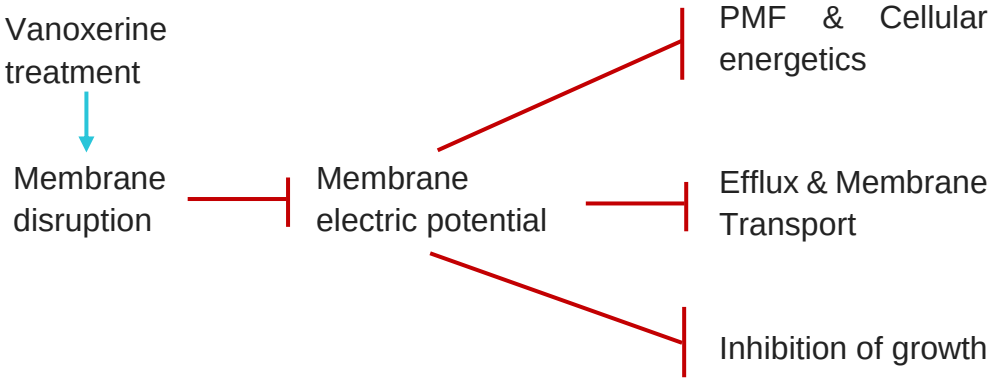


Figure 3.30: Overall summary of vanoxerine mechanism of action. PMF = proton motive force.

The mechanism of action of vanoxerine can be summarised as a disruptor of the membrane electric potential (Figure 3.30). The exact mechanism through which vanoxerine causes this disruption is unknown, although it is unlikely to be through pore formation, given the retention of ethidium bromide and propidium iodide within the cells. The downstream effects of vanoxerine treatment include inhibition of efflux,

disruption of membrane transport and inhibition of cellular growth. Further work is required to confirm this is the only mechanism of vanoxerine as an antibacterial. In addition, it should be evaluated whether vanoxerine is disrupting the membrane, or targeting the electron transport chain, both of which would lead to the described downstream effects.

Due to low potency of vanoxerine as an antimycobacterial compound, several analogues were synthesised, with the aim of finding a more active derivative. Alongside analogue synthesis, the commercially available GBR12935 was also tested (Lewis et al., 1999), to study effects of the fluoro groups on the antimycobacterial activity. The removal of the fluoro groups reduced but did not eliminate activity, suggesting the decreased lipophilicity of GBR12935, cLogP change from 5.2 to 5.0, reduced activity. Across all analogues, the general observed trend was the introduction of more polar groups onto vanoxerine led to a reduction in, or elimination of, the activity. This result fits within the general anti-tuberculosis drug landscape, as many of these drugs are more lipophilic compared to drugs for other clinical implications, due to the requirement to penetrate through the hydrophobic cell envelope (Fullam and Young, 2021; Motamen and Quinn, 2020). The most active analogue, compound 486, had a cLogP > 6 and the pK_a of the tertiary amine was increased to 9.0. Hence, a greater proportion of this compound would be cationic at physiological pH and would more easily penetrate the hydrophobic cell envelope, both likely contributing to its increased cellular activity.

The top three vanoxerine analogues were tested to evaluate their activity on the dopamine transporter, as this is a known human target. This showed that compound 486 was 47-74x less active than vanoxerine, having an IC_{50} value of 140 nM. This result is lower than a previous study, which found the IC_{50} to be 6.8 µM (Paudel et al.,

2017). However, the study's vanoxerine IC_{50} was 43 nM, a 14-22-fold increase from our result (Paudel et al., 2017). If our data is accurate, there is a 179x difference between the MIC_{99} against *M. bovis* BCG and IC_{50} against the dopamine transporter. If the data from Paudel et al. (2017) is accurate, then this difference is reduced to 3.7x. Both differences are vast reductions on the 16,666x difference in specificity currently shown by vanoxerine. Overall, this suggests compound 486 is a promising starting point for future development of a more active analogue against mycobacteria, with reduced off-target effects.

The vanoxerine analogues provide further confirmation of the proposed mechanism of action, as there are strong correlations between the MIC_{99} values and the impact on efflux and the membrane electric potential (Figure 3.31). To allow correlation of the MIC_{99} values, predictions were made for all compounds with a >100 µM MIC_{99}; labelling as either 150 µM, 200 µM or 1,000 µM, if the percentage survival curves were almost at 10%, had a down-ward trajectory, or were a flat-line around 100%, at 100 µM drug. Despite these assumptions, there were still strong positive correlations between the MIC_{99} of all species and the disruption of the membrane electric potential, 0.72, 0.71 and 0.59. There were also strong negative correlations between the MIC_{99} values and the impact on ethidium bromide efflux, -0.76, -0.72 and -0.45. The negative correlation is because an active compound will have a low MIC_{99} value but a high value for the accumulation of ethidium bromide, both indicating a high level of activity. The lower correlations for the MIC_{99} of *M. smegmatis* could be due to most compounds having some activity and so fewer were labelled as inactive or 1,000 µM. Only the *M. smegmatis* MIC_{99} showed a correlation with the cLogP of the compounds, which is surprising compared to the known propensity for more lipophilic antimycobacterial drugs (Fullam and Young, 2021; Motamen and Quinn, 2020). However, a majority of

compounds had a predicted cLogP greater than 5, suggesting they were already lipophilic enough to pass through the mycobacterial cell envelope.

The ability of vanoxerine to dissipate the membrane electric potential was also seen in *B. subtilis* and *E. faecium*. This caused inhibition of efflux in *B. subtilis*, but not in *E.*

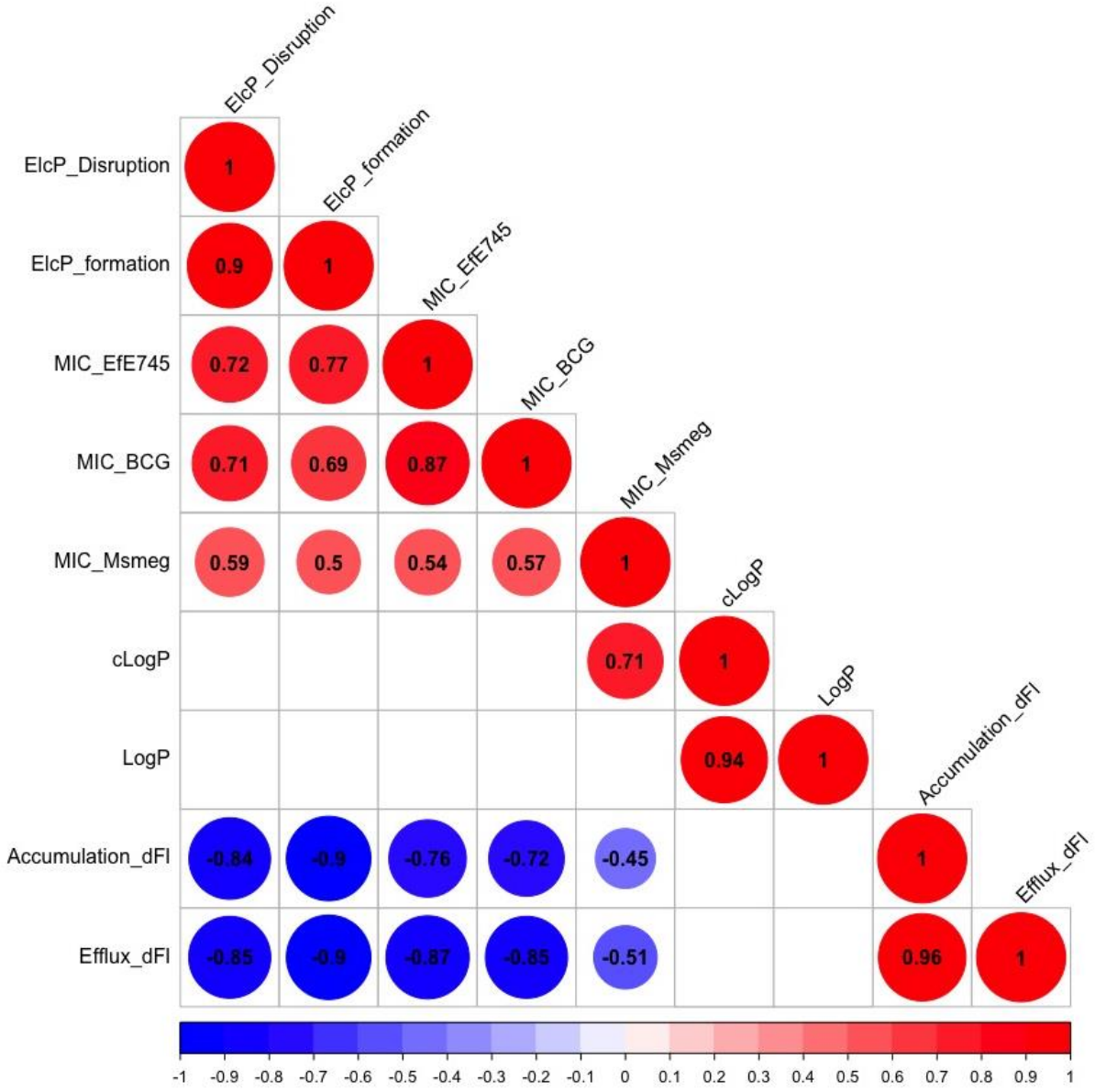


Figure 3.31: Correlogram showing the correlations between MIC_{99}, ethidium bromide influx/efflux and electric potential formation/disruption across the vanoxerine analogues. Data is taken from Tables 3.8 & 3.9, alongside raw data from Figure 3.25, cLogP and LogP were calculated within ChemDraw. Accumulation and efflux data is percentage change in fluorescence, based on *M. smegmatis* treatment. Electric potential data is based on *M. bovis* BCG treatment. ElcP = electric potential, dFI = change in fluorescence, EfE745 = *E. faecium* E745. Displaying correlations with a P-value <0.05.

faecium E745. The EbrAB efflux pump appears to be the energy-dependent exporter of ethidium bromide from *B. subtilis* (Masaoka et al., 2000) and hence would be inhibited by vanoxerine's impact on cellular energetics. As the efflux of ethidium bromide from *E. faecium* is glucose-dependent, this suggests alternative efflux pumps may be used, which are not strongly inhibited by vanoxerine's mechanism of action. The *B. subtilis* reporter strain responses also indicates lipid biosynthesis is not impacted this species, compared to mycobacteria, providing further evidence lipid biosynthesis is not directly targeted by vanoxerine. However, the induction of a lipid-II linked stress response suggests vanoxerine impacts the peptidoglycan biosynthesis in *B. subtilis*. This may explain the significant downregulation of the *mur* peptidoglycan biosynthesis genes following vanoxerine treatment of *M. bovis* BCG and hint that this process if impacted by disruption of the PMF or cellular energetics.

In conclusion, this chapter has presented evidence that vanoxerine targets the membrane electric potential and this disruption has antibacterial effects on mycobacteria and Gram-positive species. A more potent analogue of vanoxerine was identified, which retained the same mechanism of action and could represent a potential lead to future drug development. In the absence of further development, this work has identified a new antimycobacterial compound with a defined mechanism of action, allowing its use as a commercially available tool compound to compare other antimycobacterial drugs against.

4. Discussion and Future Work

This thesis has aimed to target *M. tuberculosis* and discover new compounds which could be developed into drugs. Chapter two focused on a target-to-drug approach against the AroB protein and the successful development of several tools to allow rapid investigation of putative AroB inhibitors. While the compounds tested did not have inhibitory activity, this work has developed a strong foundation for future drug discovery efforts. In contrast, chapter three performed a drug-to-target approach, taking a compound which had been identified as an anti-mycobacterial compound and determined its mode-of-action. This identified vanoxerine as a disruptor of the membrane electric potential and characterised the down-stream impact of this mechanism on the bacilli. A more active compound was identified, which also had reduced inhibitory activity on the known human target of vanoxerine, providing a future route for analogue development. Finally, the mode-of-action was also verified against Gram-positive species *B. subtilis* and *E. faecium*, potentially allowing its development against multiple pathogenic species.

In terms of follow-up work targeting the MtAroB protein falls into two main categories; incremental improvements of previous work and screening based on the developed assays. One main area which would benefit from incremental improvements would be the quality of protein crystals. If the crystal resolution was optimised from an alternative starting point, of which several were identified, the XCHEM pipeline could be repeated. The identification of known binding fragments, alongside their binding site locations, would allow a medicinal chemistry approach to develop linked fragments which hopefully retain inhibitory activity. The other area to improve would be computational screening, either through the screening of a larger compound library or the use of machine learning. The former may reduce the bias for size or prevent putative hits

from being removed due to screening for drug-like compounds only. The latter could allow faster screening of compounds by training a model to identify key qualities of inhibitors specific for MtAroB.

The developed tools could be adapted to allow screening of compounds libraries against the MtAroB protein. The outlined biochemical assay was developed to be performed in a 50 µl volume, allowing library screening within 384-well plates. The main issues were the high cost of the enzyme substrate and limited availability of known inhibitors. Alternatively, the biophysical assays, specifically tryptophan fluorescence and DSF, could be scaled to allow screening of small compound libraries. While these approaches could provide putative inhibitors of this essential *M. tuberculosis* protein, the hydrophilic nature of the active site may select for compounds which cannot penetrate the hydrophobic cell envelope. One avenue to solve this issue could be the use of pro-drug synthesis to cap any charged or polar moieties necessary to target AroB, until the compound had entered the cytoplasm.

Future directions of research to build on the vanoxerine work outlined herein can be grouped in three areas: refinement of the mechanism, synthesis of vanoxerine analogues, and experimentation for the future development of vanoxerine.

While vanoxerine was shown to disrupt the $\Delta\psi$, one component of the PMF, work could be undertaken to study the effect on the other component, the ΔpH across the membrane. The direct interactions of vanoxerine with the membrane could be studied through microscopy, to evaluate the localisation of disruption or timeframe of membrane disruption versus entry of dye molecules. Vanoxerine and the disruption of the electric potential also disrupted the mycolic acids, hence, it could be explored if vanoxerine could potentiate the effects of known mycolic acid or arabinogalactan biosynthetic inhibitors. There is also the possibility that vanoxerine targets an electron

transport chain protein, to cause membrane potential dissipation, and this could be evaluated further. Finally, while vanoxerine had no antibacterial effects against Gram-negative species, it could be explored if it still retains activity as an efflux inhibitor, as the development of non-toxic efflux inhibitors may allow potentiation of other antibiotics with lower levels of resistance.

As a more potent analogue of vanoxerine has been synthesised, this could be used as a starting point for future development. The removal of the diphenylmethoxy group may further reduce binding to the dopamine transporter, as this was the starting point from which vanoxerine was developed. The lack of a protein target and hence no known binding site may hinder more a directed medicinal chemistry approach from being undertaken.

If vanoxerine, or more likely its analogues, are going to be developed into an antibacterial drug compound, several addition experiments would be required. Most pressing would be the confirmation of assay results in *M. tuberculosis* directly, alongside a time-kill curve analysis to prove bacteriostatic vs bactericidal activity. Testing the effect of vanoxerine within both a macrophage infection model and on *M. tuberculosis* within a hypoxia-induced latent state, would provide more information on its likelihood of *in vivo* efficacy. Vanoxerine analogues could then be tested within a pre-clinical model to assess treatment efficacy. In addition, further work could be performed to assess its activity on *E. faecium*, as this WHO priority pathogen could also be the target of future development efforts. Finally, as vanoxerine could inhibit *B. subtilis*, its ability to inhibit sporulation or spore survival should be examined, as this could have applications in food preservation or *Bacillus* infections.

If this list of future experiments were to be prioritised, one of the most pressing experiments would be the evaluation of vanoxerine against a larger panel of over-

expressor strains, specifically electron transport chain proteins and efflux pumps. This would highlight whether vanoxerine has specific mycobacterial targets or if its mechanism of action is dissipation of the membrane electric potential. For the AroB project, prioritising the improvement of the protein crystal structure resolution could allow the XCHEM process to be repeated. This would ideally provide a wealth of fragment-bound AroB structures, which could then be developed into potential drug compounds, for downstream testing in the screening assays described herein.

Overall, this thesis has provided additional methods for targeting an essential *M. tuberculosis* protein and identified the mechanism of action of a novel antimycobacterial compound, which may allow repurposing to treat TB. The identification of a compound which has no observed drug resistance is especially promising, in the face of growing drug resistance and a treatment success rate of just 60% against MDR-tuberculosis. In the development of novel antimycobacterial compounds, most essential tuberculosis proteins will be targeted over time and hence, generating a comprehensive report on one essential protein will benefit this wider discovery approach. This thesis provides a strong starting point from which exploratory work could be undertaken and has provided a breadth of examples for drug discovery approaches to target *M. tuberculosis*.

5. Material and Methods

5.1. General Experimental Methods

5.1.1. Media preparation

5.1.1.1. Luria – Bertani (LB) Broth

LB broth powder (10 g, Fisher) was added to water (400 mL) and this solution was autoclaved at 121°C for 15 minutes.

5.1.1.2. Luria – Bertani (LB) Agar

LB agar powder (14.8 g, Fisher) was added to water (400 mL) and this solution was autoclaved at 121°C for 15 minutes. The agar was cooled to 50°C and poured into 90 mm Petri dishes (20 mL per Petri dish).

5.1.1.3. Terrific Broth

Terrific broth powder (47.6 g, VWR) and glycerol (8 mL, Fisher) were added to water (1 L), and this was autoclaved at 121°C for 15 minutes.

5.1.1.4. Brain-Heart Infusion (BHI) Broth

BHI broth power (18.5 g, Sigma) was added to water (500 mL) and this solution was autoclaved at 121°C for 15 minutes.

5.1.1.5. Brain-Heart Infusion (BHI) Agar

BHI broth power (14.8 g, Sigma) and Bacto Agar powder (6 g, BD) was added to water (400 mL) and this solution was autoclaved at 121°C for 15 minutes.

5.1.1.6. 7H9 Broth

Middlebrook 7H9 broth base (2.35 g, BD, Difco) and glycerol (1 mL, Fisher) were added to water (450 mL), and this was autoclaved at 121°C for 15 minutes. If *M. bovis BCG* was grown, OADC (10% v/v, BD) was aseptically added to the solution.

5.1.1.7. 7H11 Agar

Middlebrook 7H11 agar base (5.10 g, Sigma) and glycerol (1 mL, Fisher) were added to water (450 mL), and this was autoclaved at 121°C for 15 minutes. The agar was cooled to 50°C and OADC (10% v/v, BD) was aseptically added. This was mixed thoroughly prior to pouring into 90 mm Petri dishes (20 mL per Petri dish).

5.1.1.8. Tween-80 (20%)

Tween-80 (10 mL, Sigma) was added to water (40 mL) to produce a 20% Tween-80 solution, and this was filter sterilised through a 0.22 µM pore sized filter. A final concentration of 0.05% was used for mycobacterial culturing.

5.1.1.9. Transformation Buffers

5.1.1.9.1. Transformation Buffer 1 (TFB1)

Rubidium chloride (RbCl, 100 mM, Sigma), manganese chloride ($MnCl_2$, 50 mM, Sigma), potassium acetate ($KC_2H_3O_2$, 30 mM, BDH Lab Supplies), calcium chloride ($CaCl_2$, 10 mM, Sigma) and glycerol (15% v/v, Fisher) were added to water. The pH was adjusted to 5.8 through addition of hydrochloric acid (HCl, 37%, Fisher) and the solution autoclaved at 121°C for 15 minutes.

5.1.1.9.2. Transformation Buffer 2 (TFB2)

Rubidium chloride (RbCl, 10 mM, Sigma), 3-morpholinopropane-1-sulfonic acid (MOPS, 10 mM, Sigma), calcium chloride ($CaCl_2$, 75 mM, Sigma) and glycerol (15% v/v, Fisher) were added to water. The pH was adjusted to 6.8 through addition of hydrochloric acid (HCl, 37%, Fisher) and the solution autoclaved at 121°C for 15 minutes.

5.1.1.9.3. Transformation Buffer 3 (TFB3)

Glycerol (10% v/v, Fisher) and Tween-80 (0.05% v/v, Sigma) were added to water. The solution was autoclaved at 121°C for 15 minutes.

5.1.1.10. Protein Purification Buffers

5.1.1.10.1. Buffer A

Sodium chloride (NaCl, 500 mM, Fisher), Tris-hydrochloride (Tris-HCl, 50 mM, Fisher) and imidazole (30 mM, Sigma) were added to water. The pH was adjusted to 7.8 through addition of hydrochloric acid (HCl, 37%, Fisher) and the solution was filter sterilised through a 0.22 µM pore sized filter.

5.1.1.10.2. Buffer B

Sodium chloride (NaCl, 500 mM, Fisher), Tris-hydrochloride (Tris-HCl, 50 mM, Fisher) and imidazole (400 mM, Sigma) were added to water. The pH was adjusted to 7.8 through addition of hydrochloric acid (HCl, 37%, Fisher) and the solution was filter sterilised through a 0.22 µM pore sized filter.

5.1.1.10.3. Buffer C

Sodium chloride (NaCl, 200 mM, Fisher) and Tris-hydrochloride (Tris-HCl, 50 mM, Fisher) were added to water. The pH was adjusted to 7.8 through addition of hydrochloric acid (HCl, 37%, Fisher) and the solution was filter sterilised through a 0.22 µM pore sized filter.

5.1.1.10.4. Buffer D

Sodium chloride (NaCl, 150 mM, Fisher), Tris-hydrochloride (Tris-HCl, 20 mM, Fisher) and glycerol (5% v/v, Fisher) were added to water. The pH was adjusted to 7.8 through addition of hydrochloric acid (HCl, 37%, Fisher) and the solution was filter sterilised through a 0.22 µM pore sized filter.

5.1.1.10.5. Buffer E

Sodium chloride (NaCl, 150 mM, Fisher), Tris-hydrochloride (Tris-HCl, 50 mM, Fisher) and CHAPS (0.5%, Sigma) were added to water. The pH was adjusted to 7.8 through

addition of hydrochloric acid (HCl, 37%, Fisher), a proteinase inhibitor was added, and the solution was filter sterilised through a 0.22 µM pore sized filter.

5.1.1.11. SDS-Blue

Sodium dodecyl sulphate (SDS, 4% w/v, Sigma), glycerol (20% v/v, Fisher), bromophenol blue (0.2% w/v, Sigma) and Tris-hydrochloride (Tris-HCl, 100 mM, Fisher) were added to water. The pH was adjusted to 6.8 through addition of hydrochloric acid (HCl, 37%, Fisher) and aliquots were frozen at -20°C. When required, an aliquot was thawed and β-mercaptoethanol (200 mM, PanReac AppliChem) was added prior to use.

5.1.1.12. Assay Buffers

5.1.1.12.1. Activity Assay Buffer 1 (AAB1)

Tris-hydrochloride (Tris-HCl, 1 M, Fisher) was added to water and the pH was adjusted to 7.8 through addition of hydrochloric acid (HCl, 37%, Fisher) to produce a 20x stock of AAB1.

5.1.1.12.2. MST Buffer

Sodium chloride (NaCl, 150 mM, Fisher), Tris-hydrochloride (Tris-HCl, 50 mM, Fisher), glycerol (5% v/v, Fisher) and Tween-80 (0.05%) were added to water. The pH was adjusted to 7.8 through addition of hydrochloric acid (HCl, 37%, Fisher) and the solution was filter sterilised through a 0.22 µM pore sized filter.

5.1.2. Bacterial Strains and Growth Conditions

5.1.2.1. Bacterial Strains

All bacterial strains used within this report are listed in Table 5.1

Table 5.1: List of strains used

Microorganism	Strain	Plasmids/Mutations	Antibiotic Resistance	Reference
Escherichia coli	XL10			Lab strain
Escherichia coli	BL21 (DE3)			New England Biolabs, (Cat C2527I)
Escherichia coli	BL21 (DE3)	pET28a-MtAroB	Kanamycin (50 µg/mL)	This thesis
Escherichia coli	BL21 (DE3)	pET28a-MtAroB-97mut	Kanamycin (50 µg/mL)	This thesis
Escherichia coli	BL21 (DE3)	pET28a-MtAroB-122mut	Kanamycin (50 µg/mL)	This thesis
Escherichia coli	BL21 (DE3)	pET28a-MtAroB-138mut	Kanamycin (50 µg/mL)	This thesis
Escherichia coli	BL21 (DE3)	pET28a-MtAroB-249mut	Kanamycin (50 µg/mL)	This thesis
Escherichia coli	BL21 (DE3)	pET28a-MtAroB-265mut	Kanamycin (50 µg/mL)	This thesis
Escherichia coli	BL21 (DE3)	pET28a-MtAroB-323mut	Kanamycin (50 µg/mL)	This thesis
Escherichia coli	BL21 (DE3)	pET28a-MtAroB-GFP	Kanamycin (50 µg/mL)	This thesis
Mycobacterium smegmatis	mc^2155			Lab strain
Mycobacterium smegmatis	mc^2155	pTIC6a (empty)	Kanamycin (50 µg/mL)	This thesis
Mycobacterium smegmatis	mc^2155	pVV16 (empty)	Kanamycin (50 µg/mL), Hygromycin (50 µg/mL)	This thesis
Mycobacterium smegmatis	mc^2155	pTIC6a-MtAroB	Kanamycin (50 µg/mL)	This thesis
Mycobacterium smegmatis	mc^2155	pVV16-MtAroB	Kanamycin (50 µg/mL), Hygromycin (50 µg/mL)	This thesis
Mycobacterium smegmatis	mc^2155	pSMT3-GFP	Hygromycin (50 µg/mL)	Lab strain
Mycobacterium smegmatis	mc^2155	pRH2102 + pRH2521	Kanamycin (50 µg/mL), Hygromycin (50 µg/mL)	This thesis
Mycobacterium smegmatis	mc^2155	pRH2102 + pRH2521-arob+37	Kanamycin (50 µg/mL), Hygromycin (50 µg/mL)	This thesis
Mycobacterium smegmatis	mc^2155	pRH2102 + pRH2521-arob+137	Kanamycin (50 µg/mL), Hygromycin (50 µg/mL)	This thesis
Mycobacterium smegmatis	mc^2155	pRH2102 + pRH2521-arob+269	Kanamycin (50 µg/mL), Hygromycin (50 µg/mL)	This thesis
Mycobacterium smegmatis	mc^2155	pMV306 (empty)	Kanamycin (50 µg/mL)	This thesis
Mycobacterium smegmatis	mc^2155	pMV306-FFLucRT	Kanamycin (50 µg/mL)	This thesis
Mycobacterium smegmatis	mc^2155	pMV306-Rv0924c	Kanamycin (50 µg/mL)	This thesis
Mycobacterium smegmatis	mc^2155	pMV306-Rv1607	Kanamycin (50 µg/mL)	This thesis
Mycobacterium smegmatis	mc^2155	pMV306-Rv1999c	Kanamycin (50 µg/mL)	This thesis

Mycobacterium smegmatis	mc²155	pMV306-Rv2434c	Kanamycin (50 µg/mL)	This thesis
Mycobacterium smegmatis	mc²155	pMV306-BCG0727	Kanamycin (50 µg/mL)	This thesis
Mycobacterium smegmatis	mc²155	pMV306-ClgR	Kanamycin (50 µg/mL)	This thesis
Mycobacterium smegmatis	mc²155	pMV306- NarK2	Kanamycin (50 µg/mL)	This thesis
Mycobacterium smegmatis	mc²155	pMV306-RibC	Kanamycin (50 µg/mL)	This thesis
Mycobacterium smegmatis	mc²155	pMV306-WhiB3	Kanamycin (50 µg/mL)	This thesis
Mycobacterium smegmatis	mc²155	pMV261 (empty)	Kanamycin (50 µg/mL)	(Kremer et al., 2000)
Mycobacterium smegmatis	mc²155	pMV261-FabH	Kanamycin (50 µg/mL)	(Kremer et al., 2000)
Mycobacterium smegmatis	mc²155	pMV261-KasA	Kanamycin (50 µg/mL)	(Kremer et al., 2000)
Mycobacterium smegmatis	mc²155	pMV261-KasAB	Kanamycin (50 µg/mL)	(Kremer et al., 2000)
Mycobacterium bovis	BCG - Pasteur			Lab strain
Mycobacterium bovis	BCG	pTIC6a (empty)	Kanamycin (50 µg/mL)	This thesis
Mycobacterium bovis	BCG	pVV16 (empty)	Kanamycin (50 µg/mL), Hygromycin (50 µg/mL)	This thesis
Mycobacterium bovis	BCG	pTIC6a-MtAroB	Kanamycin (50 µg/mL)	This thesis
Mycobacterium bovis	BCG	pVV16-MtAroB	Kanamycin (50 µg/mL), Hygromycin (50 µg/mL)	This thesis
Mycobacterium bovis	BCG	pSMT3-GFP	Hygromycin (50 µg/mL)	Lab strain
Mycobacterium bovis	BCG	ΔrecG Mutant		(Batt et al., 2015)
Mycobacterium bovis	BCG	pMV306 (empty)	Kanamycin (50 µg/mL)	This thesis
Mycobacterium bovis	BCG	pMV306-BCG0727	Kanamycin (50 µg/mL)	This thesis
Mycobacterium bovis	BCG	pMV306-ClgR	Kanamycin (50 µg/mL)	This thesis
Mycobacterium bovis	BCG	pMV306-NarK2	Kanamycin (50 µg/mL)	This thesis
Mycobacterium bovis	BCG	pMV306-RibC	Kanamycin (50 µg/mL)	This thesis
Mycobacterium bovis	BCG	pMV306-WhiB3	Kanamycin (50 µg/mL)	This thesis
Mycobacterium bovis	BCG	pMV261 (empty)	Kanamycin (50 µg/mL)	(Kremer et al., 2000)
Mycobacterium bovis	BCG	pMV261-DprE1	Kanamycin (50 µg/mL)	Lab Strain
Mycobacterium bovis	BCG	pMV261-InhA	Kanamycin (50 µg/mL)	Lab strain

Mycobacterium bovis	BCG	pMV261-MmpL3	Kanamycin (50 µg/mL)	(Cox et al., 2016)
Mycobacterium bovis	BCG	pMV261-Pks13	Kanamycin (50 µg/mL)	Lab strain
Mycobacterium bovis	BCG	pRH2102 + pRH2521	Kanamycin (50 µg/mL), Hygromycin (50 µg/mL)	This thesis
Mycobacterium bovis	BCG	pRH2102 + pRH2521-inhA+128	Kanamycin (50 µg/mL), Hygromycin (50 µg/mL)	This thesis
Mycobacterium bovis	BCG	pRH2102 + pRH2521-inhA+320	Kanamycin (50 µg/mL), Hygromycin (50 µg/mL)	This thesis
Mycobacterium bovis	BCG	pRH2102 + pRH2521-mmpL3+10	Kanamycin (50 µg/mL), Hygromycin (50 µg/mL)	This thesis
Mycobacterium bovis	BCG	pRH2102 + pRH2521-mmpL3+335	Kanamycin (50 µg/mL), Hygromycin (50 µg/mL)	This thesis
Mycobacterium bovis	BCG	pRH2102 + pRH2521-pknB+50	Kanamycin (50 µg/mL), Hygromycin (50 µg/mL)	This thesis
Mycobacterium bovis	BCG	pRH2102 + pRH2521-pknB+142	Kanamycin (50 µg/mL), Hygromycin (50 µg/mL)	This thesis
Mycobacterium bovis	BCG	pRH2102 + pRH2521-pknB+327	Kanamycin (50 µg/mL), Hygromycin (50 µg/mL)	This thesis
Mycobacterium bovis	BCG	pRH2102 + pRH2521-BCG3184c+29	Kanamycin (50 µg/mL), Hygromycin (50 µg/mL)	This thesis
Mycobacterium bovis	BCG	pRH2102 + pRH2521-BCG3184c+118	Kanamycin (50 µg/mL), Hygromycin (50 µg/mL)	This thesis
Mycobacterium bovis	BCG	pRH2102 + pRH2521-BCG3184c+196	Kanamycin (50 µg/mL), Hygromycin (50 µg/mL)	This thesis
Mycobacterium bovis	BCG	pRH2102 + pRH2521-clgR+104	Kanamycin (50 µg/mL), Hygromycin (50 µg/mL)	This thesis
Mycobacterium bovis	BCG	pRH2102 + pRH2521-narG+7	Kanamycin (50 µg/mL), Hygromycin (50 µg/mL)	This thesis
Mycobacterium bovis	BCG	pRH2102 + pRH2521-narG+196	Kanamycin (50 µg/mL), Hygromycin (50 µg/mL)	This thesis
Mycobacterium bovis	BCG	pRH2102 + pRH2521-narG+289	Kanamycin (50 µg/mL), Hygromycin (50 µg/mL)	This thesis
Mycobacterium bovis	BCG	pRH2102 + pRH2521-ribC+10	Kanamycin (50 µg/mL), Hygromycin (50 µg/mL)	This thesis
Mycobacterium bovis	BCG	pRH2102 + pRH2521-ribC+165	Kanamycin (50 µg/mL), Hygromycin (50 µg/mL)	This thesis
Mycobacterium bovis	BCG	pRH2102 + pRH2521-ribC+165	Kanamycin (50 µg/mL), Hygromycin (50 µg/mL)	This thesis
Mycobacterium bovis	BCG	pRH2102 + pRH2521-whiB3+30	Kanamycin (50 µg/mL), Hygromycin (50 µg/mL)	This thesis
Mycobacterium bovis	BCG	pRH2102 + pRH2521-whiB3+102	Kanamycin (50 µg/mL), Hygromycin (50 µg/mL)	This thesis
Mycobacterium bovis	BCG - Danish			Lab strain

Mycobacterium bovis	BCG Danish	-	ΔmmpL5	Kanamycin (25 µg/mL)	(Borgers et al., 2020)
Mycobacterium bovis	BCG Danish	-	ΔnarG	Kanamycin (25 µg/mL)	(Borgers et al., 2020)
Mycobacterium bovis	BCG Danish	-	ΔwhiB3	Kanamycin (25 µg/mL)	(Borgers et al., 2020)
C. glutamicum	13032				(Gande et al., 2004)
C. glutamicum	13032		Δpks13 mutant		(Gande et al., 2004)
Enterococcus faecium	64/3			Rifampicin, fusidic acid resistant	(Werner et al., 2003)
Enterococcus faecium	E745			Vancomycin, rifampicin, fusidic acid resistant	
Staphylococcus aureus	ATCC29213 (SA01)				
Klebsiella pneumoniae	Ecl8 (KP02)				
Acinetobacter baumannii	AYE (AC05)				
Pseudomonas aeruginosa	PA14				
Bacillus subtilis	168				

5.1.2.2. Broth Growth Conditions

Bacteria were grown in LB broth (*A. baumannii*, *E. coli, K. pneumoniae, P. aeruginosa, S. aureus, B. subtilis*), BHI broth (*C. glutamicum, E. faecium*), 7H9 broth (*M. smegmatis*) or 7H9 broth + OADC (Oleic Acid Albumin Dextrose Catalase, *M. bovis BCG*), unless otherwise stated. Single bacterial colonies were used to inoculate culture media. Bacterial cultures were grown at 37°C and 180 rpm, appropriate antibiotics were added when required, as outlined in Table 5.1.

5.1.2.3 Agar Growth Conditions

Bacteria were on LB agar (*A. baumannii*, *E. coli, K. pneumoniae, M. smegmatis, P. aeruginosa, S. aureus*), BHI agar (*C. glutamicum, E. faecium*), or 7H11 agar + OADC (*M. bovis BCG*), unless otherwise stated. Single bacterial colonies or glycerol stock aliquots were streaked onto agar plates and incubated at 37°C. Following bacterial growth, agar plates were stored at 4°C until required.

5.1.2.4. Glycerol Stocks

Strains were stored longer term as glycerol stocks. A fresh bacterial culture (OD_{600} 0.5-1.0, 750 µL) was added to glycerol (50%, 750 µL) in a cryovial, for a final glycerol concentration of 25%. The stock was flash frozen using liquid nitrogen and stored at -80°C until required.

5.1.2.5. Growth Curve Analysis

A mid-log culture (OD_{600} 0.5-1.0) of bacterial cells was diluted to OD_{600} 0.05 into suitable media and selective antibiotics, if required. If anhydrotetracycline (ATc, Sigma) was added, it was diluted to a final concentration of 200 ng/mL. At pre-determined intervals (3 hours for *M. smegmatis* and 24 hours for *M. bovis BCG*), samples (50-100 µL) were taken and added into a 96- or 384-well polystyrene plate. The OD_{600} (read using a BMG Labtech POLARstar Omega plate reader) was used to monitor growth over time (48 hours for *M. smegmatis,* and up to 10 days for *M. bovis BCG*). Alternatively, if a GFP expressing strain was used, fluorescence (excitation – 485 nm, emission – 520 nm) was measured as a proxy for growth.

5.1.3. Competent Cell Preparation

5.1.3.1. Chemically Competent *E. coli* XL10 cells

An overnight culture (1 mL) of *E. coli* XL10 cells was used to inoculate prewarmed LB media (100 mL) and incubated at 37°C until the OD_{600} reached 0.5. This culture was then cooled on ice for 5 minutes prior to being centrifuged (5 min, 4,000 g at 4°C). The supernatant was discarded and resuspend in TFB1 and left on ice for 90 minutes. The cells were then centrifuged (5 min, 4,000 g at 4°C) and resuspended in TBF2. Aliquots (200 µl) were dispensed into pre-chilled 1.5 mL Eppendorf tubes and flash frozen using liquid nitrogen, then stored at -80°C.

5.1.3.2. Electrocompetent *M. smegmatis cells*

A mid-log culture (1 mL) of *M. smegmatis* cells was used to inoculate prewarmed media and was grown overnight (37°C), until an OD_{600} 0.5-1.0 was reached. This culture was cooled on ice (10 min), centrifuged (10 min, 3,000 g at 4°C) and the supernatant discarded. Successive rounds of centrifugation (10 min, 3,000 g at 4°C) and pellet resuspension in cold TFB3 were undertaken, with a reduction in the volume of TFB3 used each round (10 mL, 5mL and 1 mL). Aliquots (100 µl) were dispensed into pre-chilled 1.5 mL Eppendorf tubes and flash frozen using liquid nitrogen, then stored at -80°C. Method adapted from (Parish, 2021).

5.1.3.3. Electrocompetent *M. bovis BCG* cells

A mid-log culture (1 mL) of *M. bovis BCG* was used to inoculate prewarmed 7H9-OADC-Tw (7H9 broth + 10% OADC + 0.05% Tween-80, 100 mL) and was grown, at 37°C statically, until an OD_{600} 0.8-1.0 was reached. The culture was centrifuged (10 min, 3,000 g at room temperature) and the supernatant discarded. Successive rounds of centrifugation (10 min, 3,000 g at room temperature) and pellet resuspension in 37°C TFB3 were undertaken, with a reduction in the volume of TFB3 in each round (10 mL, 5 mL, and 2 mL). Aliquots (200 µL) were dispensed into 1.5 mL Eppendorf tubes and either used immediately or flash frozen using liquid nitrogen, then stored at -80°C. Method adapted from (Parish, 2021).

5.1.4. Polymerase Chain Reactions (PCR)

All reagents were supplied by New England Biolabs or Qiagen and used without further purification, unless stated otherwise. All PCR reactions were undertaken in the Eppendorf Mastercycler® nexus GX2 PCR Thermal Cycler.

5.1.4.1. Gene Amplification PCR

A 3-step PCR was used to amplify the MtAroB gene from genomic DNA isolated from *Mycobacterium tuberculosis*. The PCR reactions (50 µL each) used Q5® High Fidelity 2X Master Mix and 30-cycles for DNA amplification. The primers used for gene amplification of MtAroB for traditional cloning into the pTIC6a plasmid are shown in Table 5.2.

Table 5.2: Primer sequences used for gene amplification PCRs

Primer	Species/Plasmid	Sequence
pTIC_AroB_F (Restriction)	*M. tuberculosis* /pTIC6a	AAGATCAAGCTTATGACCGATATCGGCGCACCCGTGAC
pTIC_AroB_R (Restriction)	*M. tuberculosis* /pTIC6a	AAGATCGCTAGCTCATGGGGCGCAAACTCCGGCGTAG

5.1.4.2. PCR for HiFi Cloning

Two PCR reactions (25 or 50 µL) were undertaken for each HiFi cloning reaction, to amplify the destination vector as a linear piece of DNA and to amplify the gene of interest. These comprised 25 reactions cycles, using a Q5® High Fidelity 2X Master Mix. The primers used for amplification of DNA for HiFi cloning are displayed in Table 5.3. These include those used for amplification of the MtAroB and GFP insert gene sequences and the amplification of the pET28a, pVV16 and pET28a-MtAroB vectors

Table 5.3: Primer sequences for HiFi cloning PCRs

Primer	Species/Plasmid	Sequence
pET_RFR1	pET28a	ATGATGATGATGATGGCTGCTGCCC
pET_RFF1	pET28a	CACAGCAGCGGCCTGGTG
AroB_pET_RFF1	*M. tuberculosis*	GCAGCCATCATCATCATCATATGACCGATATCGGC GCAC
AroB_pET_RFR1	*M. tuberculosis*	GGCACCAGGCCGCTGCTGTGTCATGGGGCGCAAA CTCC
pVV_RFR1	pVV16	CGAATTCTGCAGCTGGATCCGCAATTGTC
pVV_RFF1	pVV16	AAGCTTCACCACCACCACCACCACTG
AroB_pVV_RFF1	*M. tuberculosis*	GGATCCAGCTGCAGAATTCGATGACCGATATCGGC GCAC
AroB_pVV_RFR1	*M. tuberculosis*	CAGTGGTGGTGGTGGTGGTGAAGCTTTCATGGGG CGCAAACTCC
pET_AroB-GFP_HiFi_F	pET-MtAroB	TGACACAGCAGCGGCCTGGTG
pET_AroB-GFP_HiFi_R	pET-MtAroB	TGGGGCGCAAACTCCGGCG

GFP-AroB_HiFi_F	p-GFP	CGCCTACGCCGGAGTTTGCGCCCCAGAAAACCTTTATTTTCAGGGTAGTG
GFP-AroB_HiFi_R	p-GFP	GCGGCACCAGGCCGCTGCTGTGTCACTCGAGCTTGTAAAGCTC

5.1.4.3. PCR for Q5 Mutagenesis

PCR reactions were performed to introduce required mutations into the plasmid sequences, concurrently with DNA amplification and linearisation. These PCR reactions used Q5® High Fidelity 2X Master Mix (NEB), had 25-cycles and were 12.5 or 25 µL reactions. The primers used for Q5 mutagenesis of the pET28a-MtAroB plasmid are displayed in Table 5.4.

Table 5.4: Primer sequences for Q5 mutagenesis PCRs

Primer	Species/Plasmid	Sequence
pET_MtAroB_R97A_F	pET28a-MtAroB	CGGAATCGGCgcCAAAGACGCCCTGG
pET_MtAroB_R97A_R	pET28a-MtAroB	ATGCGGCCCAACACCTCC
pET_MtAroB_R122A_F	pET28a-MtAroB	CACCTGGCTGgcCGGCGTCTCGATTGTGCACCTGC
pET_MtAroB_R122A_R	pET28a-MtAroB	GCCGCCGCGAACCCGGCG
pET_MtAroB_R138A_F	pET28a-MtAroB	GGCATGGTCGcTGCGGCCGTC
pET_MtAroB_R138A_R	pET28a-MtAroB	CAGCAGTGTGGTGGGCAG
pET_MtAroB_R249A_F	pET28a-MtAroB	CAACTACGGCgcCACATTAGGCCACG
pET_MtAroB_R249A_R	pET28a-MtAroB	AGGATTTCGCGCAGCTCG
pET_MtAroB_R265A_F	pET28a-MtAroB	CCGGTGGCGCgcCGGCGCCGCC
pET_MtAroB_R265A_R	pET28a-MtAroB	TAGCGTTCCCGGCGCTCG
pET_MtAroB_R323A_F	pET28a-MtAroB	GGCCGGCGACgcGAAGACTCGG
pET_MtAroB_R323A_R	pET28a-MtAroB	ATGATTTCCAGCAGCTGG

5.1.4.4. Colony PCR

Colony PCR reactions were performed on transformant colonies from both traditional and HiFi based cloning techniques. The primers used for colony PCR are displayed in Table 5.5. In all cases, 12.5 or 25 µL reactions were performed, using a MyTaq™ Red Mix (2x, Bioline). The 3-step PCR reaction was cycled 30 times.

Table 5.5: Table of colony PCR primers

Primer	Species/Plasmid	Sequence
pET_Fw_Seq	pET28a Sequencing	GTGAGCGGATAACAATTCCC
pET_Rv_Seq	pET28a Sequencing	CCAACTCAGCTTCCTTTCG
pTIC6a_Fw	pTIC6a Sequencing	CAGCACGGCATACATCATTT
pTIC6a_Rv	pTIC6a Sequencing	TTGAGACACAACGTGGCTTT
pVV16_Fw	pVV16 Sequencing	CGAGTGGCAGCGAGGACAAC
pVV16_Rv	pVV16 Sequencing	TGTGCAATGTAACATCAGAG

5.1.5. Miraprep Plasmid Purification

The QIAprep Spin Miniprep kit (Qiagen) was used for plasmid extraction and purification from bacterial cells, using the following protocol. An overnight culture (5 mL) of *E. coli* was centrifuged (3,900 g, 5 min) and the supernatant was discarded. The pellet was resuspended in buffer P1 containing RNase A (250 µL). Then lysis buffer P2 (250 µL) was added, and the tube inverted 5 times. After 5 minutes, buffer N3 (350 µL) was added, and the tube inverted 5 times. The mixture was centrifuged (17,000 g, 10 min). The resulting supernatant was mixed with ethanol (250 µL, 96%, Fisher), before loading onto the QIAprep spin-column. The column was centrifuged (17,000 g, 1 min) and the flow-through discarded. Buffer PE (750 µL) was added, and the column centrifuged (17,000 g, 1 min). The flow-through was discarded and the column centrifuged again (17,000 g, 2 min), to remove residual buffer. The spin-column was transferred to a new 1.5 mL microcentrifuge tube. Elution buffer (35 µL,

10 mM Tris-HCl, pH 8.5) was added to the centre of the spin column. It was left to stand for 2 minutes, before being centrifuged (17,000 g, 2 min). The DNA concentration was measured at 260 nm using a Thermo Scientific NanoDrop™ 2000c spectrophotometer. Plasmid DNA was stored in elution buffer at -20°C. This method was adapted from Pronobis, Deuitch and Peifer, (2016).

5.1.6. Agarose Gel DNA Extraction

5.1.6.1. Agarose Gels

Agarose (1 g, Cleaver Scientific) was added into 1x TAE buffer (100 mL, 40 mM Tris, 20 mM acetic acid, 1 mM EDTA, National Diagnostics) and this mixture heated until the agarose dissolved. The solution was cooled, and Midori green (0.005% v/v, GENEFLOW) was added. The 1% agarose gel was cast and allowed to cool until solid. All DNA reaction products were combined with loading dye (6x, NEB) and samples (5-10 µL) were loaded. Gel electrophoresis (35 minutes, 120 V) was performed in 1x TAE buffer to separate the DNA by size and compared to a 1 kB DNA ladder (5 µL, NEB).

5.1.6.2. DNA Gel Extraction

The QIAquick® Gel Extraction kit (Qiagen) was used for DNA extraction from agarose gels. The DNA bands of interest were excised from the gel using a scalpel and weighed. For every 100 mg of gel, 300 µL of buffer QG was added. The mixture was incubated (50°C, 10 min) and then isopropanol (100 µL per 100 mg of gel, Fisher) was added. The solution was applied to a QIAquick spin column and centrifuged (17,000 g, 1 min) and flow-through discarded. Buffer PE (750 µL) was applied to the column and centrifuged (17,000 g, 1 min). The flow-through was discarded and the column re-centrifuged (17,000 g, 1 min), to remove residual PE buffer. The spin-column was transferred to a new 1.5 mL microcentrifuge tube. Elution buffer (35 µL, 10 mM Tris-

HCl, pH 8.5) was added to the centre of the spin column. It was left to stand for 2 minutes, before being centrifuged (17,000 g, 2 min). The DNA concentration was measured at 260 nm using a Thermo Scientific NanoDrop™ 2000c spectrophotometer and stored in elution buffer at -20°C.

5.1.7. Traditional Cloning

5.1.7.1. Digestion (insert and plasmid)

The DNA sample (500 ng) was combined with 10x CutSmart® buffer (2.5 µL, NEB) and required restriction endonucleases (1 µL of each, NEB), in water (up to 25 µL). The mixture was incubated (1 hour, 37°C), before the reaction was terminated. For plasmid digestion, DNA gel electrophoresis and DNA gel extraction were performed. For digestion of DNA inserts, the QIAquick® PCR Purification kit (Qiagen) was used.

5.1.7.2. Alkaline phosphatase (plasmid only)

The digested plasmid was combined with 10x CutSmart® buffer (5 µL, NEB), QuickCIP (1 µL, NEB) and water (up to 50 µL). The reaction mixture was incubated (37°C, 1 hour). Then the enzyme was heat inactivated (80°C, 2 minutes). This mixture was used without further purification.

5.1.7.3. Ligation

The concentration of insert required for ligation was calculated as follows:

$$\text{ng of insert (X)} = \frac{\text{ng of vector (ideal 50 ng)} \times \text{insert size (kb)}}{\text{vector size (kb)}} \times \frac{3}{1}$$

The Quick-Stick Ligase kit (Bioline) as used. For each reaction, vector DNA (~1 µL), insert DNA (X µL), water (14-X µL), QS-ligase (1 µL) and QS ligation buffer (4x, 5 µL) were combined. The reaction mixture was incubated (20°C, 20 minutes, or 0°C, 16 hours) and used to transform chemically competent cells.

5.1.8. Transformation

5.1.8.1. Chemical Transformation of *E. coli*

E. coli XL10 competent cells (100 µL) were thawed and combined with the ligase reaction (4 µL) and incubate at 4°C for 30 minutes. The cells were heat shocked (45 seconds at 42°C), before being returned to 4°C for 5 minutes. LB broth (750 µL) was added, and the cells incubated at 37°C for 1 hour. LB agar plates with required antibiotics (Table 1) were inoculated with the culture (100 or 200 µL aliquots). Colonies were screened by colony PCR and DNA sequencing.

5.1.8.2. Electroporation Transformation of *M. smegmatis*

M. smegmatis competent cells (100 µL) were thawed and combined with plasmid DNA (<500 ng, <5 µL), in an electroporation cuvette (1 mm, Geneflow, prechilled) and incubated (4°C, 30 minutes). Electroporation was undertaken (1,900 V, 600 Ω, 10 µF) using an Eppendorf Electroporator 2510, with the average time constant being 4.8 milliseconds. Immediately following electroporation, 7H9-Tw (7H9 broth + 0.05% Tween-80, 900 µL) was added. The cells were incubated (4 hours, 37°C, static), centrifuged (1 min, 3,000 g) and resuspended in fresh 7H9-Tw (300 µL). Two fractions (100 and 200 µL) were plated onto antibiotic selective agar and incubated (37°C, 3-4 days) until colonies grew. Method adapted from (Parish, 2021).

5.1.8.3. Electroporation Transformation of *M. bovis BCG*

M. bovis BCG competent cells (200 µL) were used following preparation, or thawed, and combined with plasmid DNA (<500 ng, <5 µL), in an electroporation cuvette (1 mm, Geneflow). This was incubated (room temperature, 15 minutes), before electroporation was undertaken (1,900 V, 600 Ω, 10 µF), using an Eppendorf Electroporator 2510. Immediately following electroporation, the cuvette's content was

washed into a 15 mL falcon tube using 7H9-OADC-Tw (7H9 broth + 10% OADC + 0.05% Tween-80, 3 mL total volume). The cells were incubated (24 hours, 37°C, 5% CO_2, static), centrifuged (10 min, 3,000 g) and resuspended in fresh 7H9-OADC-Tw (200 µL). This resuspension was plated onto antibiotic selective agar and incubated (37°C, 5% CO_2, 3-4 weeks), until colonies grew. Method adapted from (Parish, 2021).

5.1.9. HiFi Cloning

PCR was used to amplify the required vector and genes for HiFi cloning and these were gel extracted prior to use. The NEBuilder® HiFi DNA Assembly Cloning Kit (NEB) was used for HiFi cloning. The vector:insert ratio was 1:2 and 50 ng of either pET28a or pVV16 vector, to 20.04 ng MtAroB insert for each vector. The reaction mixture (vector DNA, insert DNA and HiFi DNA Assembly Master Mix) was incubated (50°C, 1 hour), then 2 µL was transformed into chemically competent cells (50 µL). The '5.1.8.1 Chemical Transformation of *E. coli*' protocol was used with the following exceptions: the cells were heat shocked for 30 seconds and allowed to recover for 2 minutes and SOC media (950 µL, NEB) was added to the recovering cells before one hour of incubation. Colony PCR was performed to confirm successful cloning, following by DNA sequencing for final confirmation.

5.1.10. Q5 Mutagenesis

The PCR products (0.5 µL) of the Q5 mutagenesis PCR reactions were added into the KLD reaction mixture of the Q5 Site-Directed Mutagenesis Kit (5 µL total volume, NEB). This reaction mixture was incubated at room temperature for 1 hour. Then the KLD mix (2.5 µL) was added to chemically-competent cells (25 µL). The '5.1.8.1 Chemical Transformation of *E. coli*' protocol was followed, with the following

exceptions: the cells were heat shocked for 30 seconds and the recovering cells had SOC media (950 µL) added.

5.1.11. DNA/Plasmid Sequencing

To confirm cloning was successful, following colony PCR analysis, the isolated plasmids (100 ng/µL) were sent for sequencing (Source Biosciences). The pairs of sequencing primers (3.2 pmol/µL) outlined in Table 5.6 were used in all cases. Sanger sequencing was performed across the multiple cloning site region of each plasmid. This sequencing data was analysed by aligning against the expected sequence.

Table 5.6: Table of sequencing primers

Primer	Purpose	Sequence
pET_Fw_Seq	pET28a Sequencing	GTGAGCGGATAACAATTCCC
pET_Rv_Seq	pET28a Sequencing	CCAACTCAGCTTCCTTTCG
pTIC6a_Fw	pTIC6a Sequencing	CAGCACGGCATACATCATTT
pTIC6a_Rv	pTIC6a Sequencing	TTGAGACACAACGTGGCTTT
pVV16_Fw	pVV16 Sequencing	CGAGTGGCAGCGAGGACAAC
pVV16_Rv	pVV16 Sequencing	TGTGCAATGTAACATCAGAG
KS	pRH2521 Sequencing	CCTCGAGGTCGACGGTATCG

5.1.12. CRISPR interference gene knockdowns

This approach used plasmids created by Singh et al., (2016), pRH2502 encoding an inactive version of the Cas9 protein and conferring kanamycin resistance and pRH2521 for expression of small guide RNA (sgRNA) and conferring hygromycin resistance. The following protocol was optimised for use by Dr Bala Madduri (University of Birmingham).

5.1.12.1. sgRNA sequence selection

The genes of interest from *M. smegmatis* (*aroB* only) and *M. bovis* BCG (were searched for 'CCX' motifs and then the CCX plus the next 20 nucleotide sequences were taken as potential target sequences. Blast was then used to search these 20 nucleotide sequences for uniqueness across the mycobacteria genome. Sequences with 14 or fewer nucleotides identical to any other sequence were taken forward. To allow cloning, the forward primer had 'GGGA' added to the start and the reverse primer had 'AAAC' added to the start. These meant for each gene location of interest, two DNA oligos were synthesised to order, show in Table 5.7.

Table 5.7: Primers for CRISPR interference

Primer	Gene location	Sequence
BCGAroB_Ci_8F	+8	GGGAGGTCACGGGTGCGCCGATAT
BCGAroB_Ci_8R		AAACATATCGGCGCACCCGTGACC
BCGAroB_Ci_139F	+139	GGGATCCGCGGTCTCGGCTAGTCC
BCGAroB_Ci_139R		AAACGGACTAGCCGAGACCGCGGA
BCGAroB_Ci_245F	+245	GGGACTCCCAGATGAATCCCACGA
BCGAroB_Ci_245R		AAACTCGTGGGATTCATCTGGGAG
MsAroB_Ci_37F	+37	GGGAAGCCCCGTCCCGATGACGAC
MsAroB_Ci_37R		AAACGTCGTCATCGGGACGGGGCT
MsAroB_Ci_137F	+137	GGGACAGGTGGCTTCGGATCGCCT
MsAroB_Ci_137R		AAACAGGCGATCCGAAGCCACCTG
MsAroB_Ci_269F	+269	GGGAGGCTCACGAGCGCGTCCTTA
MsAroB_Ci_269R		AAACTAAGGACGCGCTCGTGAGCC
BCG3184c_+29F	+29F	GGGACCAGGATGCGGAGTGCCGTT
BCG3184c_+29R		AAACAACGGCACTCCGCATCCTGG
BCG3184c_+118F	+118	GGGAGGCCGGCTGCTCCACCCCGA
BCG3184c_+118R		AAACTCGGGGTGGAGCAGCCGGCC
BCG3184c_+196F	+196	GGGACAGCTCAAGCGGCCACTCCA
BCG3184c_+196R		AAACTGGAGTGGCCGCTTGAGCTG
ClgR_+85F	+85	GGGAGAGGCTCACCCGCGCCGAAT
ClgR_+85R		AAACATTCGGCGCGGGTGAGCCTC
ClgR_+104F	+104	GGGACGATCTCCGACAGATACCCG
ClgR_+104R		AAACCGGGTATCTGTCGGAGATCG
ClgR_+148F	+148	GGGAAATCGCACTGAGCAGCTCGC
ClgR_+148R		AAACGCGAGCTGCTCAGTGCGATT
InhA_+128F	+128	GGGATGCGCTGAATCAGCCGCAGC
InhA_+128R		AAACGCTGCGGCTGATTCAGCGCA

InhA_+165F	+165	GGGATCGAGCAGCGGGGCCTTTGC
InhA_+165R		AAACGCAAAGGCCCCGCTGCTCGA
InhA_+320F	+320	GGGACGTAGGGCGCGTCGAAGAAC
InhA_+320R		AAACGTTCTTCGACGCGCCCTACG
Mmpl3_+10F	+10	GGGAGTACACAGTTCGACCCCACC
Mmpl3_+10R		AAACGGTGGGGTCGAACTGTGTAC
Mmpl3_+251F	+251	GGGACGACCTTCTTTGACCAGGCC
Mmpl3_+251R		AAACGGCCTGGTCAAAGAAGGTCG
Mmpl3_+335F	+335	GGGACGGTCGCCTGACTCGCTCTC
Mmpl3_+335R		AAACGAGAGCGAGTCAGGCGACCG
MmpS5_+25F	+25	GGGACAGGATGAGCAGCGGTATCC
MmpS5_+25R		AAACGGATACCGCTGCTCATCCTG
MmpS5_+86F	+86	GGGACTTCGGAACCAAAGAAAGTG
MmpS5_+86R		AAACCACTTTCTTTGGTTCCGAAG
MmpS5_+109F	+109	GGGAGTTGACGTAACTACCGGAGC
MmpS5_+109R		AAACGCTCCGGTAGTTACGTCAAC
NarG_+7F	+7	GGGATCCACCGACGTGAGGTGTAA
NarG_+7R		AAACTTACACCTCACGTCGGTGGA
NarG_+196F	+196	GGGAGATCTTCCATGAGCAGGATC
NarG_+196R		AAACGATCCTGCTCATGGAAGATC
NarG_+289F	+289	GGGAACAACCTCGTGGCTCGTATT
NarG_+289R		AAACAATACGAGCCACGAGGTTGT
PknB_+50F	+50	GGGACGGACATGCCCCCAAATCCA
PknB_+50R		AAACTGGATTTGGGGGCATGTCCG
PknB_+142F	+142	GGGAAAGGTAAAAACTGGGATCGC
PknB_+142R		AAACGCGATCCCAGTTTTTACCTT
PknB_+327F	+327	GGGAATGGCGCGTTTGGGCGTCAT
PknB_+327R		AAACATGACGCCCAAACGCGCCAT
RibC_+10F	+10	GGGATCCGCGTTCCTCAACAATTC
RibC_+10R		AAACGAATTGTTGAGGAACGCGGA
RibC_+80F	+80	GGGACGGCGGTAACCATCGGACCG
RibC_+80R		AAACCGGTCCGATGGTTACCGCCG
RibC_+165F	+165	GGGATCGGCGGTGAATTGGCCGTC
RibC_+165R		AAACGACGGCCAATTCACCGCCGA
WhiB3_+30F	+30	GGGACAGTTCCAGATGTCTGCGTT
WhiB3_+30R		AAACAACGCAGACATCTGGAACTG
WhiB3_+65F	+65	GGGAATGAGTCCATGCCGCGACAC
WhiB3_+65R		AAACGTGTCGCGGCATGGACTCAT
WhiB3_+102F	+102	GGGAGCACGGCCACGCTCGCCGTC
WhiB3_+102R		AAACGACGGCGAGCGTGGCCGTGC

5.1.12.2. Oligo annealing

The DNA oligos were diluted to 100 µM stock concentrations. For oligo annealing, T4 Buffer (10x, 1 µL, NEB), T4 PNK (1 µL, NEB), oligo 1 (1 µL) and oligo 2 (1 µL) were added to water (6 µL). This reaction mixed was held at 37°C (30 minutes), before heating to 95°C (5 minutes). The temperature was then reduced to 25°C, at a rate of 5°C per minute, the annealed oligo pair was then diluted 1:200.

5.1.12.3. Digestion and Ligation

For the reaction mixture, the pRH2521 plasmid (100 ng/mL, 1 µL), annealed oligos (1:200 dilution, 2 µL), Tango buffer (10x, 2 µL, Thermofisher), DTT (10 mM, 1 µL, Fisher), ATP (10 mM, 1 µL, NEB), BbsI (1 µL, NEB) and T7 ligase (0.5 µL, NEB) were added to water (12 µL). In an Eppendorf Mastercycler® nexus GX2 PCR Thermal Cycler, the reaction mixture was held at 37°C (5 minutes), followed by 21°C (5 minutes), six cycles of these two steps were undertaken.

5.1.12.4. Exonuclease (RecBCD) Treatment

The ligation product (11 µL) was combined with Buffer 4 (1.5 µL, NEB), ATP (10 mM, 1.5 µL, NEB) and RecBCD (1 µL, NEB). This mixture was heated to 37°C (30 minutes), followed by heating to 70°C (30 minutes). The product was then stored at -20°C until ready for transformation.

5.1.12.5 Transformation and Confirmation

The exonuclease treated product was transformed into *E. coli* T10 cells using the 'Chemical Transformation of *E. coli'* protocol, except hygromycin (200 µg/mL) containing LB agar plates were used for selection. The plasmids were extracted and sent for sequencing using the KS primer for sgRNA insertion confirmation.

Following sequencing confirmation, double electroporation of the pRH2502 and edited pRH2521 plasmids was undertaken into *M. smegmatis* and *M. bovis BCG*. These

followed the 'Electroporation Transformation of *M. smegmatis* and *M. bovis BCG*' protocol described above, the cells were plated onto kanamycin (50 µg/mL) and hygromycin (50 µg/mL) containing LB agar (*M. smegmatis*) or 7H11 + OADC agar (*M. bovis BCG*) plates. Growth curve analysis of colonies in the presence and absence of ATc was used to assess the impact of CRISPR interference knockdown.

5.1.13 SDS-PAGE Gels

Any kD™ Mini-PROTEAN® TGX™ precast gels (Bio-Rad) or Novex™ WedgeWell™ 8-16% Tris-Glycine precast gels (Invitrogen) were used within this work to perform sodium dodecyl sulphate-polyacrylamide gel electrophoresis (SDS-PAGE). Tris-glycine buffer was used during electrophoresis. Samples were prepared by addition of reducing SDS-Blue and boiled for 10 minutes. The samples were then loaded (5 µl) into each well on the precast gel and run (35 minutes, 200 V, 40 Ω). InstantBlue® protein stain (Expedeon) was used to stain the proteins on the gels, left for 1 hour, then water was used to de-stain the background.

5.1.14. Minimum Inhibitory Concentration (MIC) Testing

All fluorescence measurements were undertaken in black F-bottom 96-well micro-titre plates and used a BMG Labtech POLARstar Omega plate reader.

5.1.14.1 Drug Compounds

All drug compounds were dissolved into DMSO (100%), with the following exceptions. Ethambutol hydrochloride (Sigma), isoniazid (Sigma), kanamycin (BioBasic) and para-amino salicylic acid (PAS, Sigma) were all dissolved in water. Tetracycline (Sigma) was dissolved in ethanol (100%, Fisher).

5.1.14.2. Planktonic MICs

Bacterial cultures were grown to mid-log (OD_{600} 0.5-1.0) and then diluted (into appropriate broth + selective antibiotic if required) to a final cell OD_{600} 0.05. A compound plate was made of required drugs, performing a 2-fold (or 2:3) serial dilution into DMSO. Each drug concentration (1 µL) was transferred into a 96-well polystyrene plate, followed by addition of diluted cell culture (99 µL). The plates were wrapped in foil and incubated (37°C, 21 hours for *M. smegmatis*; 24 hours for *C. glutamicum, E. faecium* and *S. aureus*; 6 days for *M. bovis* BCG). For mycobacteria, resazurin (30 µL, 0.02%, Acros Organics) was added to each well and the plate re-incubated (37°C, 3 hours for *M. smegmatis* and 24 hours for *M. bovis BCG*). The resazurin fluorescence (excitation – 544 nm, emission - 590 nm) was measured, normalised and cell survival calculated. For other bacterial species, OD_{600} was measured immediately, normalised and cell growth calculated. For CRISPRi strains, ATc (2 ng/mL) was initially added and for *M. bovis* BCG, was then added every 48-hours.

5.1.15. Figure Production

Figure production was undertaken using both Chimera v.1.13.1 (Pettersen et al., 2004) and R v.3.6.2. The RStudio GUI (RStudio, 2020) was utilised for programming within R. Several R-packages were utilised within RStudio, including: Bio3d v.2.4-1 (Grant et al., 2006), Corrplot v.0.84 (Wei and Simko, 2017), ggplot2 v.3.2.1 (Wickham, 2009), ggpubr v.0.4.0. (Kassambara, 2019) and RColorBrewer v.1.1-2 (Neuwirth, 2014).

5.2. Chapter 2 Methods

5.2.1. AroB Protein Expression and Purification

All protein purification columns were supplied by GE Healthcare, unless otherwise stated.

5.2.1.1. MtAroB and MtAroB-GFP Protein Expression

An overnight culture (10 mL) of *E. coli* BL21 (DE3) was used to inoculate terrific broth (1 L) with kanamycin (50 µg/mL, BioBasic). This was grown (37°C, 180 rpm) until mid-log growth was reached. Then IPTG (1 mM, Generon) was added and grown overnight (25-37°C, 180 rpm). The cells were harvested by centrifugation (6,895 g, 10 minutes). The pelleted cells were stored at -20°C until required.

5.2.1.2. MtAroB Protein Purification

The pelleted cells were thawed and resuspended in buffer A (30 mL). The cells were lysed via sonication (3 minutes) and then centrifuged (31,360 g, 60 minutes). The clarified lysate was then loaded onto a Ni^{2+}-His Trap HP column, then washed with buffer A, followed by elution with increasing concentrations of buffer B. The fractions containing MtAroB were pooled and dialysed overnight into buffer C. The dialysed protein was then concentrated and loaded on to a HiLoad 26/600 Superdex 200 column and eluted with buffer C. The eluted fractions containing pure MtAroB were pooled and concentrated to 15 mg/mL. These were flash frozen using liquid nitrogen for storage at -80°C. Remaining fractions which contained some MtAroB were pooled and concentrated to 4.8 mg/mL and flash frozen for initial biochemicals assays.

5.2.1.3. MtAroB Mutant Protein Purification

The pelleted cells were thawed and resuspended in buffer A (20 mL). The cells were lysed via sonication (3 minutes) and the centrifuged (31,360 g, 20 minutes). The clarified lysate was filtered (0.22 µM) and then loaded onto a gravity-flow column

containing HisPur Ni-NTA Resin (5 mL, Generon). The resin was washed with buffer A, followed by elution with increasing concentrations of buffer B. The fractions containing MtAroB were pooled and dialysed overnight into buffer C. The protein was concentrated, and flash frozen for storage at -80°C, for future biochemical assays.

5.2.1.4. MtAroB-GFP Protein Purification

The pelleted cells were thawed and resuspended in buffer A (30 mL). The cells were lysed via sonication (3 minutes) and then centrifuged (31,360 g, 60 minutes). The clarified lysate was then loaded onto a Ni^{2+}-His Trap HP column, then washed with buffer A, followed by elution with increasing concentrations of buffer B. The fractions containing MtAroB-GFP were pooled and dialysed overnight into buffer D. The protein was flash frozen and stored at -80°C, at 2.415 mg/mL for future biochemical assays.

5.2.2. Protein Crystallography

All protein crystal screening conditions were obtained from Molecular Dimensions, unless otherwise stated. X-ray diffraction data was collected at Diamond Light source, on the i03, i04 and i04-1 beamlines.

5.2.2.1. MtAroB Protein Crystallography

Vapour-diffusion protein crystal trays were set-up, using JCSG plus and MIDAS plus screening conditions. The MtAroB protein (1.8 µL, 25 mg/mL in buffer C) was added to each buffer condition (1.8 µL) and sealed next to a reservoir of the same conditions (100 µL). The crystallisation trays were stored at 18°C. The drops were routinely monitored for protein crystal formation. Several conditions led to crystal formation, with two being taken forward for X-ray diffraction. 0.2 M magnesium chloride hexahydrate, 0.1 M HEPES, pH = 7.5, 30% (v/v) PEG 400 and 1 M succinic acid, 0.1 M HEPES, pH = 7.0, 1% (v/v) PEG 2000 MME.

5.2.2.2. Optimisation for XCHEM

Optimisation was required to convert the above conditions for use within a SwissCi-3-drop midi crystal tray, with the volume of drop and reservoir reducing significantly. Crystal trays were set up using a Mosquito robot, using the JCSG Plus screening conditions. The MtAroB (13 mg/mL, 100 nL) was added to each buffer condition (100 nL) and sealed next to a reservoir of the same condition (30 µL). The crystal trays were stored at 18°C. The drops were routinely checked for crystal formation, several crystals formed within 2 days. Crystallography consistency was assessed by setting up 2 rows (24 wells) per buffer condition. The conditions tested are listed in Table 5.8. In addition, an additive screen was tested against G6 (0.2 M sodium malonate dibasic monohydrate, 20% w/c PEG3350), using the Additive Screen from Molecular dimensions, and screening around the G6 to test for increased consistency.

Table 5.8: Crystallography conditions tested for reproducibility

Identifier	Condition
B8 (JCSG Plus)	0.2 M magnesium chloride hexahydrate, 0.1 M Tris, pH 7, 10% (w/v) PEG 8,000
E11 (JCSG Plus)	0.16 M calcium acetate hydrate, 0.08 M sodium cacodylate, pH6.5, 14.4% (w/v) PEG 8,000, 20% (w/v) glycerol
G6 (JCSG Plus)	0.2 M sodium malonate dibasic monohydrate, 20% (w/v) PEG 3,350
G8 (JCSG Plus)	0.15 M DL-malic acid, 20% (w/v) PEG 3,350
G6 + Isopropanol	0.2 M sodium malonate dibasic monohydrate, 20% (w/v) PEG 3,350, 5% isopropanol
Optimized G6	0.175 M sodium malonate dibasic hydrate, 28% (w/v) PEG 3,350.

5.2.3. MtAroB Activity Assay

All readings were undertaken using a BMG Labtech POLARstar Omega plate reader. The activity of purified MtAroB was monitored by coupling its rate of phosphate release

to the phosphorylase reaction of purine nucleoside phosphorylase (PNP) on 2-amino-6-mercapto-7- methylpurine ribonucleoside (MESG). The assay was performed in 384-well polypropylene plates (50 µL total per well, Greiner Bio-One). A standard assay mixture contained: nicotinamide adenine dinucleotide (NAD^+, 100 µM, SelleckChem); MESG (200 µM, ATT Bioquest); PNP (2.5 U/mL, EMD Millipore) and 3-Deoxy-D-arabino-heptulosonic acid 7-phosphate disodium salt (DAHP, 20-200 µM, Biosynth-Carbosynth), in AAB1. This was incubated for 10 minutes (30°C), followed by addition of MtAroB (48-480 µg/mL in Buffer C). The reaction was monitored, by reading the absorbance (360 nm) every minute for 30 minutes (30°C), for 2-amino-6-mercapto-7-methylpurine formation. The reaction rate was quantified. Method adapted from Dutra De Mendonça et al., (2007).

5.2.4 Circular Dichroism Spectroscopy

MtAroB and mutants of MtAroB were thawed and transferred into 20 mM $NaPO_4$, pH 7.4 buffer, using spin-protein concentrators. The proteins were then diluted to 0.021 mg/mL in the same buffer and added to a 1 cm quartz cuvette. All measurements were undertaken on a JD-1500 circular dichroism spectrophotometer. N_2 was used to purge the chamber of the CD spectrometer prior to reading samples. A buffer only baseline reading was undertaken. Data collection was performed at 50 nm/min, at 0.5 nm intervals between 190 and 340 nm. Ten accumulations were taken for every sample. Following data accumulation, the buffer baseline was subtracted, the baseline was corrected if it did not reach zero by 340 nm and the spectra were smoothed using the Savitzky-Golay method, with a convolution width of 15.

5.2.5. Fluorimetry Assay for MtAroB Binding

5.2.5.1 Cuvette-based Fluorimetry

MtAroB protein (3 µL, 4.6 mg/mL) was added to buffer C (400 µL) in a 1 cm quartz cuvette. This was equilibrated for 10 minutes (25°C), before tryptophan fluorescence (excitation - 280 nm, emission – 340 nm) measurements were undertaken. Compounds of interest were added (1 µL per minute, 1-10 mM) and fluorescence was measured using a PTI QuantaMaster™ 40 spectrofluorometer. The changes in fluorescence were compared to buffer C and DMSO (10% in Buffer C) only controls.

5.2.5.2 Plate-reader Fluorimetry

A 96-well plate was set-up containing drug concentrations in a 2:3 serial dilution from 8 µM as the highest concentration. The final DMSO concentration was 1%. MtAroB protein (1 µM, 99 µL) in buffer C was added to each well, except the no protein conditions. The plate was incubated (24-hours, 4°C), before the tryptophan fluorescence (excitation - 280 nm, emission – 340 nm) was measured using a BMG Labtech PHERAstar FSX plate reader. The change in fluorescence was compared to the DMSO-only background.

5.2.6. Microscale Thermophoresis (MST)

All experiments were undertaken using the Monolith NT.115 (NanoTemper), at 25°C, with 20% excitation power (NANO-Blue) and 40% MST power. Monolith NT.115 Capillary tubes were used in all cases.

5.2.6.1. Protein and Ligand check

The protein and ligand were diluted to assay concentration in MST buffer, protein (80 nM), ligand (500 µM, 5% DMSO). They were added to separate capillary tubes and inserted into the Monolith. The protein was checked for self-aggregation in the MST

buffer and adherence to the capillary tubes. The ligand was checked for auto-fluorescence that would interfere with binding assessment.

5.2.6.2 Binding analysis

A 1:2 serial dilution (10 µL per tube) of the ligand was performed into the MST buffer, to produce 16 concentrations of ligand. Then protein (160 nM, 10 µL) was added to each tube and mixed. The mixture was incubated (room temperature, 30 minutes), before being added to the capillary tubes. The fluorescence of the capillary tubes was measured before and after each run, to check for photobleaching. The response of any protein or protein-ligand complexes were measured and used to determine the Kd of binding.

5.2.7. Differential Scanning Fluorimetry

All compounds were added to a 96-well PCR plate (100 µM) in quadruplicate. The MtAroB protein was diluted into buffer C (39 µg/mL), added to the 96-well PCR plate (44.5 µL) and the plate incubated (room temperature, 30-min). The SYPRO orange dye was diluted 1,000-fold and added to the plate (5 µL). Immediately after, the plate was added to the Agilent Technologies Mx3000P qPCR machine and fluorescence (excitation – 580 nm, emission – 620 nm) was monitored as the temperature was increased from 25 to 95°C.

5.2.8. BlueBEAR

The computations described in this thesis were performed using the University of Birmingham's BlueBEAR HPC service, which provides a High-Performance Computing service to the University's research community. Compute and Storage for

Life Sciences (CaStLeS) resources were specifically used for computation (Thompson, Thompson and Cazier, 2019).

5.2.9. Molecular Docking

5.2.9.1. Classical Molecular Docking

Virtual screening of the Prestwick library against the MtAroB protein was undertaken using AutoDOCK Vina v.1.1.2 (Trott and Olson, 2010). This approach treated the protein as a rigid structure, whilst altering the drug's conformations to identify the strongest drug-protein binding interactions. PyRx v.0.8 (Dallakyan and Olson, 2015) and AutoDOCK Tools v1.5.6. (Morris et al., 2009) were used to generate the required input files. Initial unbiased approaches were used, specifying the search area as within the proteins' total volume and using an exhaustiveness of 8. The docking poses were analysed based on the docking score output, as a proxy for ligand binding energy. The higher-ranking compounds were then re-docked in a more comprehensive manner, focussing on the active site, generally within a ~30 $Å^3$ box, at a higher exhaustiveness. The strength and number of binding interactions, as well as the docking location's similarity to known binding components, were also analysed.

5.2.9.2. Cluster Ensemble docking

This method uses representative structures generated from clustering of MD trajectories (see 5.2.11.2/3.), to perform molecular docking of the same chemical compound against multiple conformers of the same protein. This also used AutoDOCK Vina v.1.1.2 (Trott and Olson, 2010), with an unbiased docking approach. An exhaustiveness of 10 was used. Both the average top and weighted average docking scores were calculated for each compound against all the protein conformations and used to rank each compound. This allowed the compounds which bound strongly to

multiple conformers of the protein to be selected for further evaluation. This methodology was adapted from Amaro, Baron and Mccammon, (2008).

5.2.9.3. Virtual Screening (work by Dr Daniel Moscoh (University of Ghana))

The compounds were docked to the crystal structure of the MtAroB protein (PDB: 3QBE). The Scigress version FJ 2.6 (SCIGRESS, 2016) was used to prepare the crystal structure for docking, i.e., hydrogen atoms were added, the co-crystallised ligand was removed as well as crystallographic water molecules. The centre of the binding pocket was defined as the active site zinc ion (x = -9.7070, y = -18.9160, z = 10.7260), with a radius of 10 Å. The virtual screen was conducted on the Hit2Lead Cambridge data base. For the initial screen 30% search efficiency was used, with ten runs per compound. For the second phase (re-dock) 100% efficiency was used in conjunction with fifty docking runs. The GoldScore (Jones et al., 1997), ChemScore (Eldridge et al., 1997; Verdonk et al., 2003), ChemPLP (Korb, Stützle and Exner, 2009), and ASP (Mooij and Verdonk, 2005) scoring functions were implemented to validate the predicted binding modes and relative energies of the ligands using the GOLD v5.2 software suite.

5.2.10. Molecular Dynamic Simulations

5.2.10.1. Classical Molecular Dynamic Simulations

Input files were prepared for NAMD simulations using the CHARMM-GUI server (Jo et al., 2008; Lee et al., 2016). The CHARMM-GUI input was the PDB code, 3QBE. The protein and active site zinc ion were solvated, in a cube, with 10 Å buffers of TIP3P water between the protein and each face of the cube, followed by addition of 0.15 M KCl to the solution. The total water-box size was 86$Å^3$ for MtAroB. CHARMM parameters files were generated.

Molecular dynamic simulations were then performed using NAMD v.2.14 (Phillips et al., 2005), on the University of Birmingham's BlueBEAR HPC service. For every simulation, an initial minimization and equilibration step was performed. The solvent/ions were relaxed for 10,000 steps, followed by equilibration of the protein at NVT for 250 ps. Following equilibration, a production step was undertaken at NPT, 1 atm and 303.15 K, for up to 50 nanoseconds. The protein's trajectories were acquired every 50 ps.

5.2.10.2. Accelerated Molecular Dynamic Simulations

The accelerated MD (aMD) simulation method (Hamelberg, Mongan and McCammon, 2004), is an adaptation of the classical MD simulations described above, with the purpose of increasing the conformational space a protein can explore across the same simulation timeframe. The aMD runs were undertaken following a production run of the protein, as described above. Dihedral aMD was undertaken, applying a boost potential (E_{dihed}, α_{dihed}) to all dihedral angles within the simulation (Wang et al., 2012). These parameters were calculated using the following equation, adapted from Miao *et al*. 2016 (Miao et al., 2016) and using data acquired from the previous production run:

$E_{dihed} = V_{dihed_avg} + 0.3 \times V_{dihed_avg}$ and $\alpha_{dihed} = 0.3 \times V_{dihed_avg} \div 5$

V_{dihed_avg} is the average dihedral angle energy. The protein's trajectories were acquired every 50 ps.

5.2.11. Molecular Dynamic Trajectory Analysis

5.2.11.1. VMD Analysis

The trajectory outputs were analysed using VMD v.1.9.4.(Humphrey, Dalke and Schulten, 1996) The root-mean-square-deviation (RMSD) values for the overall protein and root-mean-square fluctuations (RMSF) of individual residues were used to

analyse the modelling. The VMD clustering plugin was also used to assess the simulations. To analyse the protein-ligand interactions, the contact frequency was determined and the VMD plugin hbond1.2 were utilised.

5.2.11.2. Cluster analysis

The MD trajectories of the proteins were clustered to generate ensembles of potential protein conformations. The GROMACS based g_cluster (Abraham et al., 2015), clustered by RMSD similarity to generate the largest clusters possible. This was controlled by a user-specified cut-off values, which was varied depending on the RMSD range of the simulation. Several clustering methods were available, with the gromos algorithm being used within this thesis (Daura et al., 1999). The alpha-carbon atoms of the protein were used for RMSD comparison and clustering, unless specified otherwise.

For the top ten clusters generated, an average structure was generated for further evaluation. AutoDockTools v1.5.6. (Morris et al., 2009) was used to convert the pdb files to the required pdbqt files for docking.

5.2.11.3. Principal Component Analysis

Bio3D v.2.4-1 is an R package which was used to analyse MD trajectories and protein structures (Grant et al., 2006). It was utilised to perform Principal Component Analysis (PCA) on clustering generated structures and MD trajectories. This allowed analysis of structural features of the proteins that differed the most across the structures or simulation timeframe. Analysis was based on C-α atoms of the protein, unless stated otherwise.

5.2.12. Compound Property Correlations

All Prestwick Library compounds and associated control compounds were uploaded to the ChemMine tools webserver (Backman, Cao and Girke, 2011) and 38 physiochemical descriptors were determined using the JOELib tool for all compounds. Associated docking scores against MtAroB were incorporated into this dataset. Alongside known *in vivo M. smegmatis* and *M. bovis BCG* survival information from Kanvatirth et al., (2019) for most compounds. Correlation analysis was undertaken utilising the R package Corrplot v.0.84 (Wei and Simko, 2017).

5.3. Chapter 3 Methods

5.3.1. Resistant Mutant Generation

5.3.1.1 Spontaneous resistant mutants

Agar plates (5 mL, 7H11 + OADC for *M. bovis BCG*, LB for *M. smegmatis*) containing 2.5x, 5x and 10x MIC of compound of interest were each inoculated with $1x10^8$ cells. The plates were then incubated at 37°C until colonies grew, or the plates dried out, whichever occurred first. Any colonies were then grown in liquid culture containing the same concentration of compound, then the cells were pelleted and sent for genome sequencing.

5.3.1.2 Induced resistant mutants (Agar method)

The following method was adapted from Ismail et al., (2018). Agar plates (5 mL, 7H11 + OADC for *M. bovis BCG*, LB for *M. smegmatis*) containing 0.5x, 1x and 2x MIC of compound of interest were poured, alongside a control plate with no compound. From a plate containing growing bacteria, 3 loopfuls (5 µL each) of cells were added to media (7H9+0.05% Tween-80 for Mycobacteria) containing four glass beads (5 mm).

This suspension was vortexed (5 minutes) and allowed to stand (10 minutes), before the OD_{600} was measured. To each agar plate, this bacteria culture (100 µL, OD_{600} 0.2-0.4) was added and spread out. The plates were then incubated (37°C, 5% CO_2) until growth was observed. This process was repeated, using bacteria growing on the highest compound concentration plate, and replating on the same concentration, 2x and 4x this highest concentration. The maximum number of cycles undertaken was five. Any colonies possessing 2x MIC or greater were sent for genome sequencing.

5.3.1.3. E. faecium resistant mutants

E. faecium was grown to mid-log (OD_{600} 0.5 to 1.0), then diluted to OD_{600} 0.05 in BHI broth, containing either DMSO or drug compounds. The cultures were grown (37°C, 24 hours), before being sub-cultured (5 µL) into fresh broth. Initially, drug concentrations of 0.5x, 1x and 2x MIC_{99} were used, then following each 24-hour period; the highest drug concentration with growth was used instead of the initial MIC_{99}, representing 1x, 2x and 4x that drug concentration. Glycerol stocks of every resistance culture were made (500 µL culture with 500 µL 50% glycerol).

5.3.1.4. Genome sequencing

Resistant mutants were cultured in liquid broth (7H9 + OADC + 0.05% Tween-80 + drug) until between 4 to 6 x 10^9 cells could be harvested. The cell pellets were then washed with PBS, before being resuspended in a DNA/RNA shield buffer. All genomic DNA extraction and genome sequencing was then undertaken by MicrobesNG.

5.3.2 MICs Methods

5.3.2.1. Planktonic MICs with No Efflux

Cells were cultured and diluted as described above, except verapamil (50 µg/mL) was added into the diluted bacterial cultures before addition to the assay plate.

5.3.2.2. Checkerboard MICs

Cells were cultured and diluted as described above. The plate set-up was different, in one direction a 2:3 serial dilution of vanoxerine was added, in the orthogonal direction, a 1:2 serial dilution of another drug of interest was added. The final DMSO concentration in the assay was 2%. The fractional inhibitory concentration (FIC) was calculated (MIC_{99}A in combination/MIC_{99}A alone + MIC_{99}B in combination/MIC_{99}B alone) = FIC. If the FIC < 0.5, this represents synergy, 0.5 < FIC < 4, is indifference and FIC > 4, is antagonism (Odds, 2003).

5.3.3. RNA Sequencing

M. bovis BCG was cultured to an OD_{600} of 0.4 before exposure to 1× or 2x MIC_{99} concentrations of vanoxerine (15 or 30 µg/mL) for eight hours in four biological replicates, then compared to carrier control-treated bacilli. Cells were pelleted, flash frozen in liquid nitrogen and stored at −80°C. Then sent to Genewiz (Azenta Life Sciences) for RNA extraction, sequencing, and data processing. The significantly dysregulated genes were functionally annotated and clustered using the DAVID server (Huang, Sherman and Lempicki, 2009; Sherman et al., 2022). The transcriptomic data was submitted and is available online in the European Nucleotide Archive, accession number PRJEB57729.

5.3.4. Propidium Iodide Membrane Permeabilisation Assay

Bacterial cultures were grown until mid-log (OD_{600} 0.7-1.0), before being diluted (7H9 + 0.05% Tween-80) to OD_{600} 0.5 or 1.0. Propidium iodide (PI, 15 µM) was added to the diluted bacterial culture. This was immediately added to a 96-well plate (99 µL per well) containing drug compounds being tested, with SDS (1 µL, 5%) serving as a

positive control. The plate was sealed with a clear film, before being added to a BMG Labtech POLARstar Omega plate reader. The fluorescence (excitation – 544 nm, emission – 620 nm), was measured for 16 hours to follow dye entering the cells.

5.3.5. Ethidium Bromide Assays

5.3.5.1. Accumulation Assay

Strains were grown to mid log (OD_{600} 0.5-1.0), before being washed and resuspended in PBS (4 mL, OD_{600} 0.8) with glucose (0.4% (w/v)) and ethidium bromide (0.625 µg/mL), for mycobacteria Tween-80 (0.05%) was also added. The cell dilution (99 µL) was immediately added to a 96-well plate, with wells containing 1 µL of either DMSO, verapamil or vanoxerine, to achieve final concentrations of 1%, 50 µg/mL and 12.5-100 µM, respectively. The plate was added to a BMG Labtech POLARstar and the fluorescence was measured every 60 seconds for 1 hour (emission – 544 nm, excitation – 590 nm), at 37°C. Method adapted from Rodrigues, Aínsa and Viveiros, (2021).

5.3.5.2. Efflux Assay

Strains were grown to mid log (OD_{600} 0.5-1.0), before being washed and resuspended in PBS (4 mL, OD_{600} 0.8) with ethidium bromide (0.625 ug/mL) and verapamil (50 ug/mL), for mycobacteria Tween-80 (0.05%) was added. The culture was then incubated for 1 hour at 37°C. A 96-well plate was prepared, containing 1 µL of either DMSO, verapamil or vanoxerine, to achieve final concentrations of 1%, 50 µg/mL and 12.5-100 µM, respectively. The ethidium bromide loaded cells were centrifuged (3000 g, 8 min, 4°C), the supernatant discarded and replaced with cold PBS (4 mL, OD_{600} 0.8) with Tween-80 (0.05%). The cells were either added directly or supplemented with glucose (final concentration 0.4% (w/v)) before addition. The plate was then

added to a BMG Labtech POLARstar and the fluorescence was measured every 60 seconds for 1 hour (emission – 544 nm, excitation – 590 nm), at 37°C. Method adapted from Rodrigues, Aínsa and Viveiros, (2021).

5.3.6. Membrane Potential Assay

5.3.6.1. $DiOC_2(3)$ concurrent drug treatment

A 96-well plate was prepared, with each well containing 1 µL of either DMSO, CCCP, verapamil or vanoxerine (final concentrations = 1%, 25 µM, 50 µg/mL or between 25-100 µM, respectively). Strains were grown to mid log (OD_{600} 0.5-1.0), before being washed and resuspended in PBS (3 mL, OD_{600} 0.5) with $DiOC_2(3)$ (30 µM), for mycobacteria Tween-80 (0.05%) was added. The cell dilution (99 µL) was immediately added to a 96-well plate and added to a BMG Labtech POLARstar and the fluorescence was measured every 90 seconds for 90 minutes (excitation – 485 nm, emission – 520 nm, 620 nm), at 37°C. Method adapted from (Chawla et al., 2012; Hudson, Siegele and Lockless, 2020).

5.3.6.2. $DiOC_2(3)$ pre-incubation, then drug treatment

Strains were grown to mid log (OD_{600} 0.5-1.0), before being washed and resuspended in PBS (3 mL, OD_{600} 0.5) with $DiOC_2(3)$ (30 µM), for mycobacteria Tween-80 (0.05%) was added. The diluted culture was incubated (37°C, 2 hours), before being dispensed (99 µL) into a 96-well plate. The plate was added to a BMG Labtech POLARstar, and the fluorescence was measured every 90 seconds for 9 minutes (excitation – 485 nm, emission – 520 nm, 620 nm), at 37°C. The plate was then removed, 1 µL of either DMSO, CCCP, verapamil, vanoxerine or bedaquiline (final concentrations = 1%, 25 µM, 50 µg/mL, between 25-100 µM or 0.5 µg/mL, respectively), was added to each

well. The plate was then returned to the plate reader and readings continued for a further 50 minutes. Method adapted from (Chen et al., 2018; Li et al., 2019).

5.3.7. Real Time Glo™ Assay

The RealTime-Glo™ MT Cell Viability Assay kit (Promega) was used. *M. smegmatis* was grown until mid-log (OD_{600} 0.5-1.0). The bacterial culture was diluted to OD_{600} 0.1 and combined with pre-warmed 7H9 containing RealTime Glo™ enzyme/substrate. The diluted culture was added to a pre-warmed 96-well plate, containing drug compounds. The plate was added to a BMG Labtech POLARstar Omega plate reader, and the luminescence monitored every 5 minutes for 10 hours, at 37°C.

5.3.8. ATP monitoring using Firefly Luciferase

M. smegmatis was transformed with a pMV306 plasmid containing FFLucRT (sequence used from Andreu et al., (2010)), in front of the *hsp60* promoter (synthesised by Twist Biosciences). This strain was grown to mid-log (OD_{600} 0.5-1.0), before being diluted to OD_{600} 0.05 in 7H9 Broth. D-Luciferin (0.15 mM, Cambridge Biosciences) was added to the diluted culture and mixed. This was immediately added (99 µL) to a 96-well plate, with wells containing 1 µL of either DMSO, vanoxerine, rifampicin or kanamycin (final concentrations of 1%, between 2.6 to 100 µM, 100 µg/mL and 15.625 µM, respectively). The plate was added to a BMG Labtech POLARstar Omega plate reader, and the luminescence monitored every 5 minutes for 17 hours, at 37°C.

5.3.9. Protein pull-down assay using 482

5.3.9.1. Click reaction – adding 482 onto azide agarose resin

Compound 482 (Vanoxerine with an alkyne group added) was conjugated to azide agarose beads (Jena Biosciences), using the CuAAC Biomolecule Reaction Buffer Kit (Jena Biosciences). The azide agarose beads (100 µL, 1 µmol) and compound 482 (100 µL, 1 µmol) were added to Na-Phosphate buffer (100 mM, 620 µL). Then $CuSO_4$ (100 mM, 18 µL) and tris-hydroxylpropyltriazolylmethylamine (THPTA, 250 mM, 18 µL) were pre-mixed and then added (30 µL) to the azide-alkyne mix. To initiate the reaction, sodium ascorbate (100 mM, 150 µL) was added. The reaction was incubated (room temperature, 3+ hours) and the endpoint confirmed by UV inspection. EDTA (250 mM, 12 µL) was added to quench the reaction. The conjugated beads were washed in water (2x 1 mL) and then stored in 20% EtOH at 4°C until required.

5.3.9.2. Protein Pull-down

This protocol was optimised for use by Dr Alice Lanne (University of Birmingham). Mycobacteria were grown to mid-log (OD_{600} 0.5-1.0), then pelleted (7.5 mL if 0.5) and resuspended in Buffer E (1 mL). The suspension was lysed by bead beating (4.5 m/sec, 5-10 x 45 seconds, with 60 seconds on ice in-between), before being centrifuged (2 min, 17,000 g). The clarified lysate was kept on ice until required.

The conjugated 482-agarose resin was washed with water (2x 1 mL), centrifuged at 17,000 g for 2 minutes, supernatant removed, and then washed in Buffer E (2x 1 mL), before being incubated at room temperature for 1 hour with 5% BSA in Buffer E. After washing twice with Buffer E, the clarified lysate was added to the resin and incubated at room temperature for 2 hours. The resin was washed six times with Buffer E, before protein was eluted, first with vanoxerine (100 µM), then with SDS (0.5%). The samples

were combined with SDS-Blue (4:1 ratio of sample to SDS-Blue), for loading on an SDS-PAGE gel.

5.3.10. Lipid Extraction and TLC analysis

5.3.10.1. Drug Treatment

Mycobacteria were grown to mid-log (OD_{600} 0.5-1.0) and then split into cultures (5-10 mL) containing either no drug, 0.5, 0.75, 1, 2.5 or 5x MIC. These cultures were incubated at 37°C for between 6-24 hours, before cells were harvested by centrifugation (3,000 g, 10 minutes). The cell samples were stored at -20°C until required.

5.3.10.2. Total Lipid Extractions

The pelleted cells were thawed and CH_3Cl/MeOH/H_2O (10:10:3, v/v/v, 2 mL) was added. This solution was incubated for 2 hours at 50°C, followed by addition of CH_3Cl (1.75 mL, Fisher) and H_2O (0.75 mL). The lower organic phase was taken and washed twice with CH_3Cl/MeOH/H_2O (3:47:48, v/v/v, 2 mL). Then the lower organic phase was transferred to a new tube and dried. For TLC analysis, the lipids were resuspended in CH_3Cl/MeOH (2:1, v/v, 200-500 µL).

5.3.10.3. Thin-Layer Chromatography (TLC) analysis systems

The resuspended lipids (5-20 µL per spot) were spotted onto silica TLC plates and the solvent allowed to evaporate. TLCs were run using the solvent systems specified in Table 5.9. The compounds were visualised by spraying with either molybdophosphoric acid (MPA, 5% w/v in ethanol) or alpha-naphthol (5% w/v in ethanol) before heating.

Table 5.9: TLC solvent systems

System	Solvents	Ratio (v/v/v)
	1-Dimension TLCS	
Inner/Outer Lipids	Chloroform/Methanol/Water	60:16:2
TMM/TDM	Chloroform/Methanol/Water	80:20:2
Phospholipids	Chloroform/Methanol/Water/Ammonium hydroxide	65:25:3.6:0.4
Free Mycolates	Hexane/Diethyl-ether/Acetic acid	70:30:1
	2-Dimension TLCs	
C	Direction 1 – Chloroform/Methanol	96:4
	Direction 2 – Toluene/Acetone	80:20
D	Direction 1 – Chloroform/Methanol/Water	100:14:0.8
	Direction 2 – Chloroform/Acetone/Methanol/Water	50:60:2.5:3
E	Direction 1 – Chloroform/Methanol/Water	60:30:6
	Direction 2 – Chloroform/Acetic acid/Methanol/Water	40:25:3:6

5.3.10.4. C^{14} labelling of lipids

Mycobacteria were grown to mid-log (OD_{600} 0.5-1.0) and then split into cultures (5-10 mL), before C^{14} acetic acid (0.5 µCi/ml) was added, alongside vanoxerine (0, 0.5x, 1x and 2x MIC). These cultures were incubated for 24-hours, before cells were harvested by centrifugation (3,000 g, 10 minutes). Identical extractions were performed. TLCs were loaded with 10,000 counts per sample and visualised by exposing to an X-ray film for 1 week. Alternatively, TLCs were exposed to a Phosphor screen for 1 week, to allow densiometric analysis.

5.3.11. Dopamine Transporter assay

This work was performed by Eurofins Discovery. The transfected Chinese hamster ovary cells ($2.5x10^3$ cells/well) were incubated (90-min, room temperature) with [^{3}H] dopamine (0.3 µM) in the absence or presence of the test compound or the reference

compound in a buffer containing 5 mM Tris-HCl pH 7.4, 7.5 mM HEPES/Tris, 120 mM NaCl, 5.4 mM KCl, 1.2 mM $CaCl_2$, 1.2 mM $MgSO_4$, 5 mM glucose and 1 mM ascorbic acid. Basal control activity was determined in the presence of 10 µM vanoxerine to block the uptake. Following incubation, the amount of [^{3}H] dopamine was quantified with a scintillation counter (Topcount, Packard). The results were expressed as a percent inhibition of the control uptake of [^{3}H] dopamine. The standard inhibitory reference compound was vanoxerine, which was tested in each experiment at several concentrations to obtain an inhibition curve from which its IC_{50} value is calculated. Method adapted from Janowsky et al., (1986).

5.3.12. *B. subtilis* reporter strain assay

This work was performed by Anne Wochele (University of Tübingen), as outlined in Wex et al., (2021). *B. subtilis* cultures were grown in LB broth containing spectinomycin (100 µg/mL) until OD_{600} 1.0. Cells were used to inoculate LB soft agar (P_{ypuA}-lacZ, P_{liaI}-lacZ and P_{yorB}-lacZ, 3 x 10^7 CFU/mL) or Beliztky minimal soft agar (P_{yppS}-lacZ P_{fabHb}-lacZ, and P_{yheI}-lacZ, 3 x 10^7 CFU/mL, (Stülke, Hanschke and Hecker, 1993)) containing $MgCl_2$ (5 mM) and X-Gal (150 µg/mL). For positive controls, vancomycin (30 µg, P_{ypuA}-lacZ), teicoplanin (30 µg, P_{liaI}-lacZ), ciprofloxacin (5 µg, P_{yorB}-lacZ), rifampicin (30 µg, P_{yppS}-lacZ), triclosan (5 µg, P_{fabHb}-lacZ) and chloramphenicol (10 µg, P_{yheI}-lacZ), were used. To test vanoxerine, drops of 10 mM vanoxerine (DMSO, 5 or 15 µL), were added to agar inoculated with each reporter strain.

6. References

Abraham, M.J., Murtola, T., Schulz, R., Páll, S., Smith, J.C., Hess, B. and Lindahl, E. (2015) GROMACS: High performance molecular simulations through multi-level parallelism from laptops to supercomputers. *SoftwareX*, 1–2: 19–25. doi:10.1016/J.SOFTX.2015.06.001.

Abrahams, K.A. and Besra, G.S. (2020) Mycobacterial drug discovery. *RSC Medicinal Chemistry*, 11: 1354–1365. doi:10.1039/d0md00261e.

Abrahams, K.A., Cox, J.A.G., Fütterer, K., Rullas, J., Ortega-Muro, F., Loman, N.J., Moynihan, P.J., Pérez-Herrán, E., Jiménez, E., Esquivias, J., Barros, D., Ballell, L., Alemparte, C. and Besra, G.S. (2017) Inhibiting mycobacterial tryptophan synthase by targeting the inter-subunit interface. *Scientific Reports*, 7 (9430): 1–15. doi:10.1038/s41598-017-09642-y.

Abrahams, K.A., Cox, J.A.G., Spivey, V.L., Loman, N.J., Pallen, M.J., Constantinidou, C., Fernández, R., Alemparte, C., Remuiñán, M.J., Barros, D., Ballell, L. and Besra, G.S. (2012) Identification of Novel Imidazo[1,2-*a*]pyridine Inhibitors Targeting *M. tuberculosis* QcrB. *PLoS ONE*, 7 (12): e52951. doi:10.1371/journal.pone.0052951.

Alangaden, G.J., Kreiswirth, B.N., Aouad, A., Khetarpal, M., Igno, F.R., Moghazeh, S.L., Manavathu, E.K. and Lerner, S.A. (1998) Mechanism of Resistance to Amikacin and Kanamycin in *Mycobacterium tuberculosis*. *Antimicrobial Agents and Chemotherapy*, 42 (5): 1295–1297. doi:10.1128/AAC.42.5.1295.

Alemparte-Gallardo, C., Encinas, L. and Esquivias Provencio, J. (2021) *Novel tetrazole compounds and their use in the treatment of tuberculosis*. Available at: https://patents.google.com/patent/EP3668856B1/da%20US4325121.pdf (Accessed: 28 October 2022).

Alhaji Isa, M., Singh Majumdhar, R. and Haider, S. (2018) In silico docking and molecular dynamics simulation of 3-dehydroquinate synthase (DHQS) from *Mycobacterium tuberculosis*. *Journal of Molecular Modeling*, 24 (132): 1–12. doi:10.1007/s00894-018-3637-4.

Amaro, R.E., Baron, R. and Mccammon, J.A. (2008) An improved relaxed complex scheme for receptor flexibility in computer-aided drug design. *J Comput Aided Mol Des*, 22: 693–705. doi:10.1007/s10822-007-9159-2.

Ananthan, S., Faaleolea, E.R., Goldman, R.C., Hobrath, J.V., Kwong, C.D., Laughon, B.E., Maddry, J.A., Mehta, A., Rasmussen, L., Reynolds, R.C., Secrist, J.A., Shindo, N., Showe, D.N., Sosa, M.I., Suling, W.J. and White, E.L. (2009) High-throughput screening for inhibitors of *Mycobacterium tuberculosis* H37Rv. *Tuberculosis*, 89 (5): 334–353. doi:10.1016/j.tube.2009.05.008.

Andersen, C.L., Holland, I.B. and Jacq, A. (2006) Verapamil, a Ca^{2+} channel inhibitor acts as a local anesthetic and induces the sigma E dependent extra-cytoplasmic stress response in *E. coli*. *Biochimica et Biophysica Acta*, 1758: 1587–1595. doi:10.1016/j.bbamem.2006.05.022.

Andreu, N., Zelmer, A., Fletcher, T., Elkington, P.T., Ward, T.H., Ripoll, J., Parish, T., Bancroft, G.J., Schaible, U., Robertson, B.D. and Wiles, S. (2010) Optimisation of Bioluminescent Reporters for Use with Mycobacteria. *PLoS ONE*, 5 (5): e10777. doi:10.1371/journal.pone.0010777.

Andreu, N., Zelmer, A., Sampson, S.L., Ikeh, M., Bancroft, G.J., Schaible, U.E., Wiles, S. and Robertson, B.D. (2013) Rapid in vivo assessment of drug efficacy against *Mycobacterium tuberculosis* using an improved firefly luciferase. *Journal of Antimicrobial Chemotherapy*, 68 (9): 2118–2127. doi:10.1093/jac/dkt155.

Andries, K., Verhasselt, P., Guillemont, J., Göhlmann, H.W.H., Neefs, J.-M., Winkler, H., Gestel, J.V., Timmerman, P., Zhu, M., Lee, E., Williams, P., de Chaffoy, D., Huitric, E., Hoffner, S., Cambau, E., Truffot-Pernot, C., Lounis, N. and Jarlier, V. (2005) A Diarylquinoline Drug Active on the ATP Synthase of *Mycobacterium tuberculosis*. *Science*, 307 (5707): 223–227. doi:10.1126/science.1106753.

Andries, K., Villellas, C., Coeck, N., Thys, K., Gevers, T., Vranckx, L., Lounis, N., Jong, B.C. de and Koul, A. (2014) Acquired Resistance of *Mycobacterium tuberculosis* to Bedaquiline. *PLOS ONE*, 9 (7): e102135. doi:10.1371/journal.pone.0102135.

Arrow Therapeutics (2001) Bissulfonamides as inhibitors of the dehydroquinate synthetase enzyme AroB and of the Type II dehydroquinase enzyme AroQ. *Expert Opinion on Therapeutic Patents*, 11 (11): 1797–1799. doi:10.1517/13543776.11.11.1797.

Arulanandam, C.D., Ragothaman, P. and Kaveriyappan, G.R. (2021) Repurposing of an Antifungal Drug against Gastrointestinal Stromal Tumors. *J Exp Pathol.*, 2 (4): 151–163. doi:10.33696/pathology.2.026.

Bachmann, N.L., Salamzade, R., Manson, A.L., Whittington, R., Sintchenko, V., Earl, A.M. and Marais, B.J. (2020) Key Transitions in the Evolution of Rapid and Slow Growing Mycobacteria Identified by Comparative Genomics. *Frontiers in Microbiology*, 10: 3019. doi:10.3389/fmicb.2019.03019.

Backman, T.W.H., Cao, Y. and Girke, T. (2011) ChemMine tools: an online service for analyzing and clustering small molecules. *Nucleic Acids Research*, 39: W486–W491. doi:10.1093/nar/gkr320.

Baker, S.J., Zhang, Y.-K., Akama, T., Lau, A., Zhou, H., Hernandez, V., Mao, W., Alley, M.R.K., Sanders, V. and Plattner, J.J. (2006) Discovery of a New Boron-Containing Antifungal Agent, 5-Fluoro-1,3-dihydro-1-hydroxy-2,1- benzoxaborole (AN2690), for the Potential Treatment of Onychomycosis. *Journal of Medicinal Chemistry*, 49 (15): 4447–4450. doi:10.1021/jm0603724.

Ballell, L., Bates, R.H., Young, R.J., Alvarez-Gomez, D., Alvarez-Ruiz, E., Barroso, V., Blanco, D., Crespo, B., Escribano, J., Gonzµlez, R., Lozano, S., Huss, S., Santos-Villarejo, A., Martín-Plaza, J.J., Mendoza, A., Rebollo-Lopez, M.J., Remuiçan-Blanco, M., Lavandera, J.L., Perez-Herran, E., Gamo-Benito, F.J., García-Bustos, J.F., Barros, D., Castro, J.P. and Cammack, N. (2013) Fueling Open-Source Drug Discovery: 177 Small-Molecule Leads against Tuberculosis. *ChemMedChem*, 8: 313–321. doi:10.1002/cmdc.201200428.

Ballester, P.J. (2019) Selecting machine-learning scoring functions for structure-based virtual screening. *Drug Discovery Today: Technologies*, 32: 81–87. doi:10.1016/J.DDTEC.2020.09.001.

Banerjee, A., Dubnau, E., Quemard, A., Balasubramanian, V., Um, K.S., Wilson, T., Collins, D., de Lisle, G. and Jacobs, W.R. (1994) *inhA* , a Gene Encoding a Target for Isoniazid and Ethionamide in *Mycobacterium tuberculosis*. *Science*, 263 (5144): 227–230. doi:10.1126/science.8284673.

Bansal-Mutalik, R. and Nikaido, H. (2014) Mycobacterial outer membrane is a lipid bilayer and the inner membrane is unusually rich in diacyl phosphatidylinositol dimannosides. *Proceedings of the National Academy of Sciences*, 111 (13): 4958–4963. doi:10.1073/pnas.1403078111.

Bañuls, A.-L., Sanou, A., Thi Van Anh, N. and Godreuil, S. (2015) *Mycobacterium tuberculosis*: ecology and evolution of a human bacterium. *Journal of Medical Microbiology*, 64: 1261–1269. doi:10.1099/jmm.0.000171.

Barberis, I., Bragazzi, N.L., Galluzzo, L. and Martini, M. (2017) The history of tuberculosis: from the first historical records to the isolation of Koch's bacillus. *J Prev Med Hyg*, 58 (1): E9–E12. doi:10.15167/2421-4248/jpmh2017.58.1.728.

Barry III, C.E. (2009) Unorthodox Approach to the Development of a New Antituberculosis Therapy. *The New England Journal of Medicine*, 360 (23): 2466–2467. doi:10.1056/NEJMe0903012.

Barry III, C.E. (2011) Lessons from Seven Decades of Antituberculosis Drug Discovery. *Current Topics in Medicinal Chemistry*, 11 (10): 1216–1225. doi:10.2174/156802611795429158.

Barry III, C.E., Boshoff, H., Dartois, V., Dick, T., Ehrt, S., Flynn, J., Schnappinger, D., Wilkinson, R.J. and Young, D. (2009) The spectrum of latent tuberculosis: rethinking the goals of prophylaxis. *Nat Rev Microbiol*, 7 (12): 845–855. doi:10.1038/nrmicro2236.

Barry, V.C., Belton, J.G., Conalty, M.L., Denneny, J.M., Edward, D.W., O'sullivan, J.F., Twomey, D. and Winder, F. (1957) A New Series of Phenazines (Rimino-Compounds) With High Antituberculosis Activity. *Nature*, 179 (4568): 1013–1015. doi:10.1038/1791013a0.

Barry, V.C. and Conalty, M.L. (1965) The Antimycobacterial Activity of B 663. *Leprosy Review*, 36 (1). doi:10.5935/0305-7518.19650002.

Batt, S.M., Burke, C.E., Moorey, A.R. and Besra, G.S. (2020) Antibiotics and resistance: the two-sided coin of the mycobacterial cell wall. *The Cell Surface*, 6: 100044. doi:10.1016/j.tcsw.2020.100044.

Batt, S.M., Cacho Izquierdo, M., Castro Pichel, J., Stubbs, C.J., Vela-Glez Del Peral, L., Pérez-Herrán, E., Dhar, N., Mouzon, B., Rees, M., Hutchinson, J.P., Young, R.J., McKinney, J.D., Barros Aguirre, D., Ballell, L., Besra, G.S. and Argyrou, A. (2015) Whole Cell Target Engagement Identifies Novel Inhibitors of *Mycobacterium tuberculosis* Decaprenylphosphoryl-β- D -ribose Oxidase. *ACS Infectious Diseases*, 1 (12): 615–626. doi:10.1021/acsinfecdis.5b00065.

Batt, S.M., Jabeen, T., Bhowruth, V., Quill, L., Lund, P.A., Eggeling, L., Alderwick, L.J., Fütterer, K., Besra, G.S. and Brenner, M.B. (2012) Structural basis of inhibition of *Mycobacterium tuberculosis* DprE1 by benzothiazinone inhibitors. *Proceedings of the National Academy of Sciences*, 109 (28): 11354–11359. doi:10.1073/pnas.1205735109.

Batt, S.M., Minnikin, D.E. and Besra, G.S. (2020) The thick waxy coat of mycobacteria, a protective layer against antibiotics and the host's immune system. *Biochemical Journal*, 477 (10): 1983–2006. doi:10.1042/BCJ20200194.

Baulard, A.R., Betts, J.C., Engohang-Ndong, J., Quan, S., McAdam, R.A., Brennan, P.J., Locht, C. and Besra, G.S. (2000) Activation of the Pro-drug Ethionamide Is Regulated in

Mycobacteria. *Journal of Biological Chemistry*, 275 (36): 28326–28331. doi:10.1074/jbc.M003744200.

Bellon, S., Parsons, J.D., Wei, Y., Hayakawa, K., Swenson, L.L., Charifson, P.S., Lippke, J.A., Aldape, R. and Gross, C.H. (2004) Crystal Structures of *Escherichia coli* Topoisomerase IV ParE Subunit (24 and 43 Kilodaltons): a Single Residue Dictates Differences in Novobiocin Potency against Topoisomerase IV and DNA Gyrase. *Antimicrobial Agents and Chemotherapy*, 48 (5): 1856–1864. doi:10.1128/AAC.48.5.1856-1864.2004.

Benedetto Tiz, D., Kikelj, D. and Zidar, N. (2018) Overcoming problems of poor drug penetration into bacteria: challenges and strategies for medicinal chemists. *Expert Opinion on Drug Discovery*, 13 (6): 497–507. doi:10.1080/17460441.2018.1455660.

Benkovic, S.J., Baker, S.J., Alley, M.R.K., Woo, Y.-H., Zhang, Y.-K., Akama, T., Mao, W., Baboval, J., Rajagopalan, P.T.R., Wall, M., Kahng, L.S., Tavassoli, A. and Shapiro, L. (2005) Identification of Borinic Esters as Inhibitors of Bacterial Cell Growth and Bacterial Methyltransferases, CcrM and MenH. *Journal of Medicinal Chemistry*, 48 (23): 7468–7476. doi:10.1021/jm050676a.

Bernstein, J., Lott, W.A., Steinberg, B.A. and Yale, H.L. (1952) Chemotherapy of Experimental Tuberculosis | V. Isonicotinic Acid Hydrazide (Nydrazid) and Related Compounds. *American Review of Tuberculosis*, 65 (4): 357–364. doi:10.1164/art.1952.65.4.357.

Berry, M. and Kon, O.M. (2009) Multidrug-and extensively drug-resistant tuberculosis: an emerging threat. *European Respiratory Review*, 18 (114): 195–197. doi:10.1183/09059180.00005209.

Bhardwaj, A.K. and Mohanty, P. (2012) Bacterial Efflux Pumps Involved in Multidrug Resistance and their Inhibitors: Rejuvinating the Antimicrobial Chemotherapy. *Recent Patents on Anti-Infective Drug Discovery*, 7 (1): 73–89. doi:10.2174/157489112799829710.

Bhusal, R.P., Patel, K., Kwai, B.X.C., Swartjes, A., Bashiri, G., Reynisson, J., Sperry, J. and Leung, I.K.H. (2017) Development of NMR and thermal shift assays for the evaluation of *Mycobacterium tuberculosis* isocitrate lyase inhibitors. *MedChemComm*, 8 (11): 2155–2163. doi:10.1039/C7MD00456G.

Bhutani, I., Loharch, S., Gupta, P., Madathil, R. and Parkesh, R. (2015) Structure, Dynamics, and Interaction of *Mycobacterium tuberculosis* (*Mtb*) DprE1 and DprE2 Examined by Molecular Modeling, Simulation, and Electrostatic Studies. *PLoS ONE*, 10 (3): 1–31. doi:10.1371/journal.pone.0119771.

Biuković, G., Basak, S., Manimekalai, M.S.S., Rishikesan, S., Roessle, M., Dick, T., Rao, S.P.S., Hunke, C. and Grüber, G. (2013) Variations of Subunit ε of the *Mycobacterium tuberculosis* F_1F_o ATP Synthase and a Novel Model for Mechanism of Action of the Tuberculosis Drug TMC207. *Antimicrobial Agents and Chemotherapy*, 57 (1): 168–176. doi:10.1128/AAC.01039-12.

Blower, T.R., Williamson, B.H., Kerns, R.J. and Berger, J.M. (2016) Crystal structure and stability of gyrase – fluoroquinolone cleaved complexes from *Mycobacterium tuberculosis*. *Proceedings of the National Academy of Sciences*, 113 (7): 1706–1713. doi:10.1073/pnas.1525047113.

Borgers, K., Vandewalle, K., Van Hecke, A., Michielsen, G., Plets, E., van Schie, L., Vanmarcke, S., Schindfessel, L., Festjens, N. and Callewaert, N. (2020) Development of a Counterselectable Transposon To Create Markerless Knockouts from an 18,432-Clone Ordered *Mycobacterium bovis* Bacillus Calmette-Guérin Mutant Resource. *mSystems*, 5 (4): e00180-20. doi:10.1128/mSystems.00180-20.

Bosch, B., Dejesus, M.A., Poulton, N.C., Zhang, W., Engelhart, C.A., Zaveri, A., Lavalette, S., Ruecker, N., Trujillo, C., Wallach, J.B., Li, S., Ehrt, S., Chait, B.T., Schnappinger, D. and Rock, J.M. (2021) Genome-wide gene expression tuning reveals diverse vulnerabilities of *M. tuberculosis*. *Cell*, 184: 1–14. doi:10.1016/j.cell.2021.06.033.

Boshoff, H.I. and Barry, C.E. (2006) Is the mycobacterial cell wall a hopeless drug target for latent tuberculosis? *Drug Discovery Today: Disease Mechanisms*, 3 (2): 237–245. doi:10.1016/j.ddmec.2006.06.002.

Boshoff, H.I.M., Myers, T.G., Copp, B.R., McNeil, M.R., Wilson, M.A. and Barry, C.E. (2004) The Transcriptional Responses of *Mycobacterium tuberculosis* to Inhibitors of Metabolism. *Journal of Biological Chemistry*, 279 (38): 40174–40184. doi:10.1074/jbc.M406796200.

Brigo, A., Lee, K.W., Iurcu Mustata, G. and Briggs, J.M. (2005) Comparison of Multiple Molecular Dynamics Trajectories Calculated for the Drug-Resistant HIV-1 Integrase T66I/M154I Catalytic Domain. *Biophysical Journal*, 88 (5): 3072–3082. doi:10.1529/BIOPHYSJ.104.050286.

Bruning, J.B., Murillo, A.C., Chacon, O., Barletta, R.G. and Sacchettini, J.C. (2011) Structure of the *Mycobacterium tuberculosis* D -Alanine: D -Alanine Ligase, a Target of the Antituberculosis Drug D -Cycloserine. *Antimicrobial Agents and Chemotherapy*, 55 (1): 291–301. doi:10.1128/AAC.00558-10.

Bvumbi, M.V. (2020) Activity of Riminophenazines against *Mycobacterium tuberculosis*: A Review of Studies that Might be Contenders for Use as Antituberculosis Agents. *ChemMedChem*, 15 (23): 2207–2219. doi:10.1002/cmdc.202000580.

Cakulev, I., Lacerda, A.E., Khrestian, C.M., Ryu, K., Brown, A.M. and Waldo, A.L. (2011) Oral Vanoxerine Prevents Reinduction of Atrial Tachyarrhythmias: Preliminary Results. *Journal of cardiovascular electrophysiology*, 22 (11): 1266–1273. doi:10.1111/j.1540-8167.2011.02098.x.

Calmette, A. (1931) Preventive Vaccination against Tuberculosis with BCG. *Proceedings of the Royal Society of Medicine*, 24 (11): 1481–1490. doi:10.1177/003591573102401109.

Campbell, E.A., Korzheva, N., Mustaev, A., Murakami, K., Nair, S., Goldfarb, A. and Darst, S.A. (2001) Structural Mechanism for Rifampicin Inhibition of Bacterial RNA Polymerase. *Cell*, 104 (6): 901–912. doi:10.1016/S0092-8674(01)00286-0.

Carlson, H.A. and McCammon, J.A. (2000) Accommodating Protein Flexibility in Computational Drug Design. *Molecular Pharmacology*, 57: 213–218.

Carpenter, E.P., Hawkins, A.R., Frost, J.W. and Brown, K.A. (1998) Structure of dehydroquinate synthase reveals an active site capable of multistep catalysis. *Nature*, 394: 299–302. doi:10.1038/28431.

Cava, C., Bertoli, G. and Castiglioni, I. (2021) Potential drugs against COVID-19 revealed by gene expression profile, molecular docking and molecular dynamic simulation. *Future Virology*, 16 (8): 527–542. doi:10.2217/fvl-2020-0392.

CDC (2003) Treatment of Tuberculosis American Thoracic Society, CDC, and Infectious Diseases Society of America. *MMWR Recommendations and Reports*, 52 (RR11): 1–77.

Centers for Disease Control and Prevention (2013) Provisional CDC Guidelines for the Use and Safety Monitoring of Bedaquiline Fumarate (Sirturo) for the Treatment of Multidrug-Resistant Tuberculosis. *MMWR Recommendations and Reports*, 62 (RR09): 1–12.

Chakraborty, S. and Rhee, K.Y. (2015) Tuberculosis Drug Development: History and Evolution of the Mechanism-Based Paradigm. *Cold Spring Harbor Perspectives in Medicine*, 5 (8): 1–11. doi:10.1101/cshperspect.a021147.

Chandran, S.S. and Frost, J.W. (2001) Aromatic inhibitors of dehydroquinate synthase: synthesis, evaluation and implications for gallic acid biosynthesis. *Bioorganic & Medicinal Chemistry Letters*, 11 (12): 1493–1496. doi:10.1016/S0960-894X(01)00065-8.

Chatterjee, D., Bozic, C.M., McNeil, M. and Brennan, P.J. (1991) Structural features of the arabinan component of the lipoarabinomannan of *Mycobacterium tuberculosis*. *Journal of Biological Chemistry*, 266 (15): 9652–9660. doi:10.1016/S0021-9258(18)92870-X.

Chatterjee, D., Lowell, K., Rivoire, B., McNeil, M.R. and Brennan, P.J. (1992) Lipoarabinomannan of *Mycobacterium tuberculosis*. Capping with mannosyl residues in some strains. *Journal of Biological Chemistry*, 267 (9): 6234–6239. doi:10.1016/S0021-9258(18)42686-5.

Chatterji, M., Shandil, R., Manjunatha, M.R., Solapure, S., Ramachandran, V., Kumar, N., Saralaya, R., Panduga, V., Reddy, J., KR, P., Sharma, S., Sadler, C., Cooper, C.B., Mdluli, K., Iyer, P.S., Narayanan, S. and Shirude, P.S. (2014) 1,4-Azaindole, a Potential Drug Candidate for Treatment of Tuberculosis. *Antimicrobial Agents and Chemotherapy*, 58 (9): 5325–5331. doi:10.1128/AAC.03233-14.

Chawla, M., Parikh, P., Saxena, A., Munshi, M., Mehta, M., Mai, D., Srivastava, A.K., Narasimhulu, K.V., Redding, K.E., Vashi, N., Kumar, D., Steyn, A.J.C. and Singh, A. (2012) *Mycobacterium tuberculosis* WhiB4 regulates oxidative stress response to modulate survival and dissemination in vivo. *Molecular Microbiology*, 85 (6): 1148–1165. doi:10.1111/j.1365-2958.2012.08165.x.

Chen, C., Gardete, S., Jansen, R.S., Shetty, A., Dick, T., Rhee, K.Y. and Dartois, V. (2018) Verapamil Targets Membrane Energetics in *Mycobacterium tuberculosis*. *Antimicrobial Agents and Chemotherapy*, 62 (5): e02107-17. doi:10.1128/AAC.02107-17.

Chen, J.M., Uplekar, S., Gordon, S.V. and Cole, S.T. (2012) A Point Mutation in cycA Partially Contributes to the D-cycloserine Resistance Trait of *Mycobacterium bovis* BCG Vaccine Strains. *PLoS ONE*, 7 (8): e43467. doi:10.1371/journal.pone.0043467.

Cholo, M.C., Steel, H.C., Fourie, P.B., Germishuizen, W.A. and Anderson, R. (2012) Clofazimine: current status and future prospects. *Journal of Antimicrobial Chemotherapy*, 67 (2): 290–298. doi:10.1093/jac/dkr444.

Cimermancic, P., Medema, M.H., Claesen, J., Kurita, K., Wieland Brown, L.C., Mavrommatis, K., Pati, A., Godfrey, P.A., Koehrsen, M., Clardy, J., Birren, B.W., Takano, E., Sali, A., Linington, R.G. and Fischbach, M.A. (2014) Insights into Secondary Metabolism from a Global Analysis of Prokaryotic Biosynthetic Gene Clusters. *Cell*, 158 (2): 412–421. doi:10.1016/j.cell.2014.06.034.

Coleman, M., Martinez, L., Theron, G., Wood, R. and Marais, B. (2022) *Mycobacterium tuberculosis* Transmission in High-Incidence Settings–New Paradigms and Insights. *Pathogens*, 11 (11): 1228. doi:10.3390/pathogens11111228.

Conradie, F., Diacon, A.H., Ngubane, N., Howell, P., Everitt, D., Crook, A.M., Mendel, C.M., Egizi, E., Moreira, J., Timm, J., McHugh, T.D., Wills, G.H., Bateson, A., Hunt, R., Van Niekerk, C., Li, M., Olugbosi, M. and Spigelman, M. (2020) Treatment of Highly Drug-Resistant Pulmonary Tuberculosis. *New England Journal of Medicine*, 382 (10): 893–902. doi:10.1056/NEJMoa1901814.

Cooper, C.B. (2013) Development of *Mycobacterium tuberculosis* whole cell screening hits as potential antituberculosis agents. *Journal of Medicinal Chemistry*, 56 (20): 7755–7760. doi:10.1021/jm400381v.

Corrêa, D.H.A. and Ramos, C.H.I. (2009) The use of circular dichroism spectroscopy to study protein folding, form and function. *Afr. J. Biochem. Res.*, 3 (5): 164–173. doi:10.5897/AJBR.9000245.

Corsello, S.M., Bittker, J.A., Liu, Z., Gould, J., McCarren, P., Hirschman, J.E., Johnston, S.E., Vrcic, A., Wong, B., Khan, M., Asiedu, J., Narayan, R., Mader, C.C., Subramanian, A. and Golub, T.R. (2017) The Drug Repurposing Hub: a next-generation drug library and information resource. *Nature Medicine*, 23: 405–408. doi:10.1038/nm.4306.

Cox, J.A.G., Abrahams, K.A., Alemparte, C., Ghidelli-Disse, S., Rullas, J., Angulo-Barturen, I., Singh, A., Gurcha, S.S., Nataraj, V., Bethell, S., Remuiñán, M.J., Encinas, L., Jervis, P.J., Cammack, N.C., Bhatt, A., Kruse, U., Bantscheff, M., Fütterer, K., Barros, D., Ballell, L., Drewes, G. and Besra, G.S. (2016) THPP target assignment reveals EchA6 as an essential fatty acid shuttle in mycobacteria. *Nature Microbiology*, 1 (2): 15006. doi:10.1038/nmicrobiol.2015.6.

Daffe, M., Brennan, P.J. and McNeil, M. (1990) Predominant structural features of the cell wall arabinogalactan of *Mycobacterium tuberculosis* as revealed through characterization of oligoglycosyl alditol fragments by gas chromatography/mass spectrometry and by ^{1}H and ^{13}C NMR analyses. *Journal of Biological Chemistry*, 265 (12): 6734–6743. doi:10.1016/S0021-9258(19)39211-7.

Dallakyan, S. and Olson, A.J. (2015) “Small-Molecule Library Screening by Docking with PyRx.” In Hempel, J., Williams, C. and Hong, C. (eds.) *Chemical Biology*. New York: Humana Press, New York, NY. pp. 243–250. doi:10.1007/978-1-4939-2269-7_19.

Daura, X., Gademann, K., Jaun, B., Seebach, D., Van Gunsteren, W.F. and Mark, A.E. (1999) Peptide folding: When simulation meets experiment. *Angewandte Chemie - International Edition*, 38 (1–2): 236–240. doi:10.1002/(sici)1521-3773(19990115)38:1/2<236::aid-anie236>3.0.co;2-m.

Davis, B.D. (1987) Mechanism of bactericidal action of aminoglycosides. *Microbiological Reviews*, 51 (3): 341–350. doi:10.1128/mr.51.3.341-350.1987.

DeBarber, A.E., Mdluli, K., Bosman, M., Bekker, L.-G. and Barry, C.E. (2000) Ethionamide activation and sensitivity in multidrug-resistant *Mycobacterium tuberculosis*. *Proceedings of the National Academy of Sciences*, 97 (17): 9677–9682. doi:10.1073/pnas.97.17.9677.

Degiacomi, G., Belardinelli, J.M., Pasca, M.R., De Rossi, E., Riccardi, G. and Chiarelli, L.R. (2020) Promiscuous Targets for Antitubercular Drug Discovery: The Paradigm of DprE1 and MmpL3. *Applied Sciences*, 10 (2): 623. doi:10.3390/app10020623.

DeJesus, M.A., Gerrick, E.R., Xu, W., Park, S.W., Long, J.E., Boutte, C.C., Rubin, E.J., Schnappinger, D., Ehrt, S., Fortune, S.M., Sassetti, C.M. and Ioerger, T.R. (2017) Comprehensive Essentiality Analysis of the *Mycobacterium tuberculosis* Genome via Saturating Transposon Mutagenesis. *mBio*, 8 (1): 1–17. doi:10.1128/mBio.02133-16.

Derrer, B., Macheroux, P. and Kappes, B. (2013) The shikimate pathway in apicomplexan parasites: Implications for drug development. *Frontiers in Bioscience*, 18 (3): 944–969. doi:10.2741/4155.

Di Modugno, E., Erbetti, I., Ferrari, L., Galassi, G., Hammond, S.M. and Xerri, L. (1994) In vitro activity of the tribactam GV104326 against gram-positive, gram-negative, and anaerobic bacteria. *Antimicrobial Agents and Chemotherapy*, 38 (10): 2362–2368. doi:10.1128/AAC.38.10.2362.

Diacon, A.H., van der Merwe, L., Barnard, M., von Groote-Bidlingmaier, F., Lange, C., García-Basteiro, A.L., Sevene, E., Ballell, L. and Barros-Aguirre, D. (2016) β-Lactams against Tuberculosis — New Trick for an Old Dog? *New England Journal of Medicine*, 375 (4): 393–394. doi:10.1056/NEJMc1513236.

Dookie, N., Rambaran, S., Padayatchi, N., Mahomed, S. and Naidoo, K. (2018) Evolution of drug resistance in *Mycobacterium tuberculosis*: a review on the molecular determinants of resistance and implications for personalized care. *Journal of Antimicrobial Chemotherapy*, 73 (5): 1138–1151. doi:10.1093/jac/dkx506.

Ducati, R., Basso, L. and Santos, D. (2007) Mycobacterial Shikimate Pathway Enzymes as Targets for Drug Design. *Current Drug Targets*, 8 (3): 423–435. doi:10.2174/138945007780059004.

Dulberger, C.L., Rubin, E.J. and Boutte, C.C. (2020) The mycobacterial cell envelope — a moving target. *Nature Reviews Microbiology*, 18: 47–59. doi:10.1038/s41579-019-0273-7.

Dutra De Mendonça, J., Adachi, O., Rosado, L.A., Ducati, R.G., Santos, D.S. and Basso, L.A. (2011) Kinetic mechanism determination and analysis of metal requirement of dehydroquinate synthase from *Mycobacterium tuberculosis* H37Rv: an essential step in the function-based rational design of anti-TB drugs. *Mol. BioSyst.*, 7 (1): 119–128. doi:10.1039/C0MB00085J.

Dutra De Mendonça, J., Ely, F., Palma, M.S., Frazzon, J., Basso, L.A. and Santos, S. (2007) Functional Characterization by Genetic Complementation of aroB-Encoded Dehydroquinate Synthase from *Mycobacterium tuberculosis* H37Rv and Its Heterologous Expression and Purification. *Journal of Bacteriology*, 189 (17): 6246–6252. doi:10.1128/JB.00425-07.

Dutta, N.K. and Karakousis, P.C. (2014) Latent Tuberculosis Infection: Myths, Models, and Molecular Mechanisms. *Microbiology and Molecular Biology Reviews*, 78 (3): 343–371. doi:10.1128/MMBR.00010-14.

Dutta, N.K., Mehra, S. and Kaushal, D. (2010) A *Mycobacterium tuberculosis* Sigma Factor Network Responds to Cell-Envelope Damage by the Promising Anti-Mycobacterial Thioridazine. *PLOS ONE*, 5 (4): e10069. doi:10.1371/journal.pone.0010069.

Eldridge, M.D., Murray, C.W., Auton, T.R., Paolini, G.V. and Mee, R.P. (1997) Empirical scoring functions: I. The development of a fast empirical scoring function to estimate the binding affinity of ligands in receptor complexes. *Journal of Computer-Aided Molecular Design*, 11: 425–445. doi:10.1023/a:1007996124545.

Evangelopoulos, D., Prosser, G.A., Rodgers, A., Dagg, B.M., Khatri, B., Ho, M.M., Gutierrez, M.G., Cortes, T. and de Carvalho, L.P.S. (2019) Comparative fitness analysis of D-cycloserine resistant mutants reveals both fitness-neutral and high-fitness cost genotypes. *Nature Communications*, 10 (1): 4177. doi:10.1038/s41467-019-12074-z.

Feng, X., Zhu, W., Schurig-Briccio, L.A., Lindert, S., Shoen, C., Hitchings, R., Li, J., Wang, Y., Baig, N., Zhou, T., Kyung Kim, B., Crick, D.C., Cynamon, M., McCammon, J.A., Gennis, R.B. and Oldfield, E. (2015) Antiinfectives targeting enzymes and the proton motive force. *Proceedings of the National Academy of Sciences*, 112 (51): E7073–E7082. doi:10.1073/pnas.1521988112.

Ferebee, S.H., Doster, B.E. and Murray, F.J. (1966) Ethambutol: A Substitute for Para-Aminosalicylic Acid in Regimens for Pulmonary Tuberculosis. *Annals of the New York Academy of Sciences*, 135 (2): 910–920. doi:10.1111/j.1749-6632.1966.tb45533.x.

Fox, H.H. (1952) The Chemical Approach to the Control of Tuberculosis. *Science*, 116: 129–134. doi:10.1126/science.116.3006.129.

Fullam, E. and Young, R.J. (2021) Physiochemical properties and *Mycobacterium tuberculosis* transporters: key to efficacious antitubercular drugs? *RSC Med. Chem*, 12: 43–56. doi:10.1039/d0md00265h.

Galina, L., Hopf, F.S.M., Abbadi, B.L., Sperotto, N.D. de M., Czeczot, A.M., Duque-Villegas, M.A., Perello, M.A., Matter, L.B., de Souza, E.V., Parish, T., Machado, P., Basso, L.A. and Bizarro, C.V. (2022) Evaluation of 3-Deoxy-D-Arabino-Heptulosonate 7-Phosphate Synthase (DAHPS) as a Vulnerable Target in *Mycobacterium tuberculosis* Cardona, S.T. (ed.). *Microbiology Spectrum*, 10 (4): e00728-22. doi:10.1128/spectrum.00728-22.

Gande, R., Gibson, K.J.C., Brown, A.K., Krumbach, K., Dover, L.G., Sahm, H., Shioyama, S., Oikawa, T., Besra, G.S. and Eggeling, L. (2004) Acyl-CoA Carboxylases (*accD2* and *accD3*), Together with a Unique Polyketide Synthase (*Cg-pks*), Are Key to Mycolic Acid Biosynthesis in *Corynebacterianeae* Such as *Corynebacterium glutamicum* and *Mycobacterium tuberculosis*. *Journal of Biological Chemistry*, 279 (43): 44847–44857. doi:10.1074/jbc.M408648200.

Garvin, R.T., Biswas, D.K. and Gorini, L. (1974) The Effects of Streptomycin or Dihydrostreptomycin Binding to 16S RNA or to 30S Ribosomal Subunits. *Proceedings of the National Academy of Sciences of the United States of America*, 71 (10): 3814–3818.

Geng, M., Lin, A. and Nguyen, T.P. (2020) Revisiting Antiarrhythmic Drug Therapy for Atrial Fibrillation: Reviewing Lessons Learned and Redefining Therapeutic Paradigms. *Frontiers in Pharmacology*, 11 (581837): 1–23. doi:10.3389/fphar.2020.581837.

Georghiou, S.B., Magana, M., Garfein, R.S., Catanzaro, D.G., Catanzaro, A. and Rodwell, T.C. (2012) Evaluation of Genetic Mutations Associated with *Mycobacterium tuberculosis* Resistance to Amikacin, Kanamycin and Capreomycin: A Systematic Review Via, L.E. (ed.). *PLoS ONE*, 7 (3): e33275. doi:10.1371/journal.pone.0033275.

Geppert, H., Vogt, M. and Bajorath, J. (2010) Current trends in ligand-based virtual screening: molecular representations, data mining methods, new application areas, and performance evaluation. *Journal of Chemical Information and Modeling*, 50 (2): 205–216. doi:10.1021/ci900419k.

Gibson, S.E.R., Harrison, J., Molloy, A. and Cox, J.A.G. (2022) Cholesterol-dependent activity of dapsone against non-replicating persistent mycobacteria. *Microbiology*, 168 (12): 1–8. doi:10.1099/mic.0.001279.

Gioia, D., Bertazzo, M., Recanatini, M., Masetti, M. and Cavalli, A. (2017) Dynamic docking: A paradigm shift in computational drug discovery. *Molecules*, 22 (11): 1–21. doi:10.3390/molecules22112029.

Glynn, J.R., Guerra-Assunção, J.A., Houben, R.M.G.J., Sichali, L., Mzembe, T., Mwaungulu, L.K., Mwaungulu, J.N., McNerney, R., Khan, P., Parkhill, J., Crampin, A.C. and Clark, T.G. (2015) Whole Genome Sequencing Shows a Low Proportion of Tuberculosis Disease Is Attributable to Known Close Contacts in Rural Malawi. *PLOS ONE*, 10 (7): e0132840. doi:10.1371/journal.pone.0132840.

González-Alemán, R., Hernández-Castillo, D., Rodríguez-Serradet, A., Caballero, J., Hernández-Rodríguez, E.W. and Montero-Cabrera, L. (2020) BitClust: Fast Geometrical Clustering of Long Molecular Dynamics Simulations. *Journal of Chemical Information and Modeling*, 60 (2): 444–448. doi:10.1021/acs.jcim.9b00828.

Gopal, M., Padayatchi, N., Metcalfe, J.Z. and O'Donnell, M.R. (2013) Systematic review of clofazimine for the treatment of drug-resistant tuberculosis. *The International Journal of Tuberculosis and Lung Disease*, 17 (8): 1001–1007. doi:10.5588/ijtld.12.0144.

Gopal, P., Sarathy, J.P., Yee, M., Ragunathan, P., Shin, J., Bhushan, S., Zhu, J., Akopian, T., Kandror, O., Lim, T.K., Gengenbacher, M., Lin, Q., Rubin, E.J., Grüber, G. and Dick, T. (2020) Pyrazinamide triggers degradation of its target aspartate decarboxylase. *Nature Communications*, 11 (1): 1661. doi:10.1038/s41467-020-15516-1.

Goude, R., Amin, A.G., Chatterjee, D. and Parish, T. (2009) The Arabinosyltransferase EmbC Is Inhibited by Ethambutol in *Mycobacterium tuberculosis*. *Antimicrobial Agents and Chemotherapy*, 53 (10): 4138–4146. doi:10.1128/AAC.00162-09.

Grant, B.J., Rodrigues, A.P.C., Elsawy, K.M., Mccammon, J.A. and Caves, L.S.D. (2006) *Bio3d: an R package for the comparative analysis of protein structures*., 22 (21): 2695–2696. doi:10.1093/bioinformatics/btl461.

Grillot, A.-L., Tiran, A.L., Shannon, D., Krueger, E., Liao, Y., O'Dowd, H., Tang, Q., Ronkin, S., Wang, T., Waal, N., Li, P., Lauffer, D., Sizensky, E., Tanoury, J., Perola, E., Grossman, T.H., Doyle, T., Hanzelka, B., Jones, S., Dixit, V., Ewing, N., Liao, S., Boucher, B., Jacobs, M., Bennani, Y. and Charifson, P.S. (2014) Second-Generation Antibacterial Benzimidazole Ureas: Discovery of a Preclinical Candidate with Reduced Metabolic Liability. *Journal of Medicinal Chemistry*, 57 (21): 8792–8816. doi:10.1021/jm500563g.

Grossman, T.H., Bartels, D.J., Mullin, S., Gross, C.H., Parsons, J.D., Liao, Y., Grillot, A.-L., Stamos, D., Olson, E.R., Charifson, P.S. and Mani, N. (2007) Dual Targeting of GyrB and ParE by a Novel Aminobenzimidazole Class of Antibacterial Compounds. *Antimicrobial Agents and Chemotherapy*, 51 (2): 657–666. doi:10.1128/AAC.00596-06.

Gul, S., Ozcan, O., Asar, S., Okyar, A., Barıs, I. and Kavakli, I.H. (2021) In silico identification of widely used and well-tolerated drugs as potential SARS-CoV-2 3C-like protease and viral RNA-dependent RNA polymerase inhibitors for direct use in clinical trials. *Journal of Biomolecular Structure and Dynamics*, 39 (17): 6772–6791. doi:10.1080/07391102.2020.1802346.

Gupta, S., Cohen, K.A., Winglee, K., Maiga, M., Diarra, B. and Bishai, W.R. (2014a) Efflux Inhibition with Verapamil Potentiates Bedaquiline in *Mycobacterium tuberculosis*. *Antimicrobial Agents and Chemotherapy*, 58 (1): 574–576. doi:10.1128/AAC.01462-13.

Gupta, S., Cohen, K.A., Winglee, K., Maiga, M., Diarra, B. and Bishai, W.R. (2014b) Efflux Inhibition with Verapamil Potentiates Bedaquiline in Mycobacterium tuberculosis. *Antimicrobial Agents and Chemotherapy*, 58 (1): 574–576. doi:10.1128/AAC.01462-13.

Guy, C.S., Tichauer, E., Kay, G.L., Phillips, D.J., Bailey, T.L., Harrison, J., Furze, C.M., Millard, A.D., Gibson, M.I., Pallen, M.J. and Fullam, E. (2017) Identification of the anti-mycobacterial functional properties of piperidinol derivatives. *British Journal of Pharmacology*, 174: 2183–2193. doi:10.1111/bph.v174.14/issuetoc.

Hamelberg, D., Mongan, J. and McCammon, J.A. (2004) Accelerated molecular dynamics: A promising and efficient simulation method for biomolecules. *Journal of Chemical Physics*, 120 (24): 11919–11929. doi:10.1063/1.1755656.

Hariguchi, N., Chen, X., Hayashi, Y., Kawano, Y., Fujiwara, M., Matsuba, M., Shimizu, H., Ohba, Y., Nakamura, I., Kitamoto, R., Shinohara, T., Uematsu, Y., Ishikawa, S., Itotani, M., Haraguchi, Y., Takemura, I. and Matsumoto, M. (2020) OPC-167832, a Novel Carbostyril Derivative with Potent Antituberculosis Activity as a DprE1 Inhibitor. *Antimicrobial Agents and Chemotherapy*, 64 (6): e02020-19. doi:10.1128/AAC.02020-19.

Hartkoorn, R.C., Uplekar, S. and Cole, S.T. (2014) Cross-Resistance between Clofazimine and Bedaquiline through Upregulation of MmpL5 in *Mycobacterium tuberculosis*. *Antimicrobial Agents and Chemotherapy*, 58 (5): 2979–2981. doi:10.1128/AAC.00037-14.

Hartmann, G., Honikel, K.O., Knüsel, F. and Nüesch, J. (1967) The specific inhibition of the DNA-directed RNA synthesis by rifamycin. *Biochimica et Biophysica Acta (BBA) - Nucleic Acids and Protein Synthesis*, 145 (3): 843–844. doi:10.1016/0005-2787(67)90147-5.

Hassan, M.M., Ranzoni, A., Phetsang, W., Blaskovich, M.A.T. and Cooper, M.A. (2017) Surface Ligand Density of Antibiotic-Nanoparticle Conjugates Enhances Target Avidity and Membrane Permeabilization of Vancomycin-Resistant Bacteria. *Bioconjugate Chemistry*, 28: 353–361. doi:10.1021/acs.bioconjchem.6b00494.

Hatfull, G.F. (1993) Genetic transformation of mycobacteria. *Trends in Microbiology*, 1 (8): 310–314. doi:10.1016/0966-842X(93)90008-F.

Heidel, K.M. and Dowd, C.S. (2019) Phosphonate prodrugs: an overview and recent advances. *Future Medicinal Chemistry*, 11 (13): 1625–1643. doi:10.4155/fmc-2018-0591.

Herrmann, J.L., O'Gaora, P., Gallagher, A., Thole, J.E. and Young, D.B. (1996) Bacterial glycoproteins: a link between glycosylation and proteolytic cleavage of a 19 kDa antigen from *Mycobacterium tuberculosis*. *The EMBO Journal*, 15 (14): 3547–3554. doi:10.1002/j.1460-2075.1996.tb00724.x.

Hoa, N.B., Sy, D.N., Nhung, N.V., Tiemersma, E.W., Borgdorff, M.W. and Cobelens, F.G.J. (2010) National survey of tuberculosis prevalence in Viet Nam. *Bull World Health Organ*, 88 (4): 273–280. doi:10.2471/BLT.09.067801.

Hospital, A., Goñi, J.R., Orozco, M. and Gelpí, J.L. (2015) Molecular dynamics simulations: advances and applications. *Advances and Applications in Bioinformatics and Chemistry*, 8: 37–47. doi:10.2147/AABC.S70333.

Huang, D.W., Sherman, B.T. and Lempicki, R.A. (2009) Systematic and integrative analysis of large gene lists using DAVID bioinformatics resources. *Nature Protocols*, 4 (1): 44–57. doi:10.1038/nprot.2008.211.

Huang, R., Ayine-Tora, D.M., Muhammad Rosdi, M.N., Li, Y., Reynisson, J. and Leung, I.K.H. (2017) Virtual screening and biophysical studies lead to HSP90 inhibitors. *Bioorganic & Medicinal Chemistry Letters*, 27 (2): 277–281. doi:10.1016/j.bmcl.2016.11.059.

Hudson, M.A., Siegele, D.A. and Lockless, S.W. (2020) Use of a Fluorescence-Based Assay To Measure *Escherichia coli* Membrane Potential Changes in High Throughput. *Antimicrobial Agents and Chemotherapy*, 64 (9): e00910-20. doi:10.1128/AAC.00910-20.

Humphrey, W., Dalke, A. and Schulten, K. (1996) VMD: Visual Molecular Dynamics. *Journal of Molecular Graphics*, 14 (1): 33–38. doi:10.1016/0263-7855(96)00018-5.

Hunter, S.W. and Brennan, P.J. (1990) Evidence for the presence of a phosphatidylinositol anchor on the lipoarabinomannan and lipomannan of *Mycobacterium tuberculosis*. *Journal of Biological Chemistry*, 265 (16): 9272–9279. doi:10.1016/S0021-9258(19)38843-X.

Ismail, N., Omar, S.V., Ismail, N.A. and Peters, R.P.H. (2018) *In vitro* approaches for generation of *Mycobacterium tuberculosis* mutants resistant to bedaquiline, clofazimine or linezolid and identification of associated genetic variants. *Journal of Microbiological Methods*, 153: 1–9. doi:10.1016/J.MIMET.2018.08.011.

Izenwasser, S., Werling, L.L. and Cox, B.M. (1990) Comparison of the effects of cocaine and other inhibitors of dopamine uptake in rat striatum, nucleus accumbens, olfactory tubercle, and medial prefrontal cortex. *Brain Research*, 520 (1–2): 303–309. doi:10.1016/0006-8993(90)91719-W.

Janowsky, A., Berger, P., Vocci, F., Labarca, R., Skolnick, P. and Paul, S.M. (1986) Characterization of Sodium-Dependent [^{3}H]GBR-12935 Binding in Brain: A Radioligand for Selective Labelling of the Dopamine Transport Complex. *Journal of Neurochemistry*, 46 (4): 1272–1276. doi:10.1111/j.1471-4159.1986.tb00649.x.

Jeon, A.B., Ackart, D.F., Li, W., Jackson, M., Melander, R.J., Melander, C., Abramovitch, R.B., Chicco, A.J., Basaraba, R.J. and Obregón-Henao, A. (2019) 2-aminoimidazoles collapse mycobacterial proton motive force and block the electron transport chain. *Scientific Reports*, 9 (1): 1513. doi:10.1038/s41598-018-38064-7.

Jeon, A.B., Obregón-Henao, A., Ackart, D.F., Podell, B.K., Belardinelli, J.M., Jackson, M., Nguyen, T.V., Blackledge, M.S., Melander, R.J., Melander, C., Johnson, B.K., Abramovitch, R.B. and Basaraba, R.J. (2017) 2-aminoimidazoles potentiate ß-lactam antimicrobial activity against *Mycobacterium tuberculosis* by reducing ß-lactamase secretion and increasing cell envelope permeability. *PLOS ONE*, 12 (7): e0180925. doi:10.1371/journal.pone.0180925.

Jo, S., Kim, T., Iyer, V.G. and Im, W. (2008) CHARMM-GUI: A Web-Based Graphical User Interface for CHARMM. *Journal of Computational Chemistry*, 29 (11): 1859–1865. doi:10.1002/jcc.

Johnson, E.O., Office, E., Kawate, T., Orzechowski, M. and Hung, D.T. (2020) Large-Scale Chemical-Genetic Strategy Enables the Design of Antimicrobial Combination Chemotherapy in *Mycobacteria*. *ACS Infectious Diseases*, 6 (1): 56–63. doi:10.1021/acsinfecdis.9b00373.

Jones, G., Willett, P., Glen, R.C., Leach, A.R. and Taylor, R. (1997) Development and validation of a genetic algorithm for flexible docking. *Journal of Molecular Biology*, 267 (3): 727–748. doi:10.1006/JMBI.1996.0897.

Kanvatirth, P., Jeeves, R.E., Bacon, J., Besra, G.S. and Alderwick, L.J. (2019) Utilisation of the Prestwick Chemical Library to identify drugs that inhibit the growth of mycobacteria. *PLoS ONE*, 14 (3): 1–21. doi:10.1371/journal.pone.0213713.

Kappel, K., Miao, Y. and Mccammon, J.A. (2017) Accelerated Molecular Dynamics Simulations of Ligand Binding to a Muscarinic G-protein Coupled Receptor. *Q Rev Biophys.*, 48 (4): 479–487. doi:10.1017/S0033583515000153.

Kassambara, A. (2019) *ggpubr: "ggplot2" Based Publication Ready Plots*. Available at: https://cran.r-project.org/package=ggpubr.

Kaur, P., Potluri, V., Ahuja, V.K., Naveenkumar, C.N., Krishnamurthy, R.V., Gangadharaiah, S.T., Shivarudraiah, P., Eswaran, S., Nirmal, C.R., Mahizhaveni, B., Dusthackeer, A., Mondal, R., Batt, S.M., Richardson, E.J., Loman, N.J., Besra, G.S., Shandil, R.K. and Narayanan, S. (2021) A multi-targeting pre-clinical candidate against drug-resistant tuberculosis. *Tuberculosis*, 129: 102104. doi:10.1016/j.tube.2021.102104.

Keane, J., Balcewicz-Sablinska, M.K., Remold, H.G., Chupp, G.L., Meek, B.B., Fenton, M.J. and Kornfeld, H. (1997) Infection by *Mycobacterium tuberculosis* Promotes Human Alveolar Macrophage Apoptosis. *Infection and Immunity*, 65 (1): 298–304. doi:10.1128/iai.65.1.298-304.1997.

Kelley, L.A., Gardner, S.P. and Sutcliffe, M.J. (1996) An automated approach for clustering an ensemble of NMR-derived protein structures into conformationally related subfamilies. *Protein Engineering*, 9 (11): 1063–1065. doi:10.1093/protein/9.11.1063.

Kelley, L.A., Mezulis, S., Yates, C.M., Wass, M.N. and E Sternberg, M.J. (2015) The Phyre2 web portal for protein modeling, prediction and analysis. *Nature Protocols*, 10 (6): 845–858. doi:10.1038/nprot.2015.053.

Kingdon, A.D.H. and Alderwick, L.J. (2021) Structure-based *in silico* approaches for drug discovery against *Mycobacterium tuberculosis*. *Computational and Structural Biotechnology Journal*, 19: 3708–3719. doi:10.1016/j.csbj.2021.06.034.

Kingdon, A.D.H., Meosa John, A.-R., Batt, S.M. and Besra, G.S. (2022) Repurposing Vanoxerine as a new antimycobacterial drug and its impact on the mycobacterial membrane. *bioRxiv*. doi:10.1101/2022.11.29.517118.

Kingdon, A.D.H., Meosa-John, A.-R., Batt, S.M. and Besra, G.S. (2023) Vanoxerine kills mycobacteria through membrane depolarization and efflux inhibition. *Frontiers in Microbiology*, 14: 1112491. doi:10.3389/fmicb.2023.1112491.

Kitchen, D.B., Decornez, H., Furr, J.R. and Bajorath, J. (2004) Docking and scoring in virtual screening for drug discovery: Methods and applications. *Nature Reviews Drug Discovery*, 3 (11): 935–949. doi:10.1038/nrd1549.

Klebe, G. (2000) Recent developments in structure-based drug design. *J Med Mol*, 78: 269–281. doi:10.1007/s001090000084.

Korb, O., Stützle, T. and Exner, T.E. (2009) Empirical Scoring Functions for Advanced Protein−Ligand Docking with PLANTS. *Journal of Chemical Information and Modeling*, 49 (1): 84–96. doi:10.1021/ci800298z.

Koul, A., Vranckx, L., Dendouga, N., Balemans, W., Van den Wyngaert, I., Vergauwen, K., Göhlmann, H.W.H., Willebrords, R., Poncelet, A., Guillemont, J., Bald, D. and Andries, K. (2008) Diarylquinolines Are Bactericidal for Dormant Mycobacteria as a Result of Disturbed ATP Homeostasis. *Journal of Biological Chemistry*, 283 (37): 25273–25280. doi:10.1074/jbc.M803899200.

Kremer, L., Douglas, J.D., Baulard, A.R., Morehouse, C., Guy, M.R., Alland, D., Dover, L.G., Lakey, J.H., Jacobs, W.R., Brennan, P.J., Minnikin, D.E. and Besra, G.S. (2000) Thiolactomycin and Related Analogues as Novel Anti-mycobacterial Agents Targeting KasA and KasB Condensing Enzymes in *Mycobacterium tuberculosis*. *Journal of Biological Chemistry*, 275 (22): 16857–16864. doi:10.1074/jbc.M000569200.

Lacerda, A.E., Kuryshev, Y.A., Yan, G.-X., Waldo, A.L. and Brown, A.M. (2010) Vanoxerine: Cellular Mechanism of a New Antiarrhythmic. *Journal of Cardiovascular Electrophysiology*, 21 (3): 301–310. doi:10.1111/j.1540-8167.2009.01623.x.

Lachance, H., Wetzel, S., Kumar, K. and Waldmann, H. (2012) Charting, Navigating, and Populating Natural Product Chemical Space for Drug Discovery. *Journal of Medicinal Chemistry*, 55 (13): 5989–6001. doi:10.1021/jm300288g.

Laguna Pharmaceuticals, Inc. (2015) *Randomized, Double-blind, Placebo-controlled Dose Modification Study to Evaluate the Safety and Efficacy of Single Doses of Vanoxerine for Conversion of Subjects With Recent Onset Atrial Fibrillation or Flutter to Normal Sinus Rhythm*. NCT01691313. clinicaltrials.gov. Available at: https://clinicaltrials.gov/ct2/show/NCT01691313 (Accessed: 4 October 2022).

Laws, M., Jin, P. and Rahman, K.M. (2022) Efflux pumps in *Mycobacterium tuberculosis* and their inhibition to tackle antimicrobial resistance. *Trends in Microbiology*, 30 (1): 57–68. doi:10.1016/j.tim.2021.05.001.

Leblanc, D.J. (2006) “Enterococcus.” In Dworkin, M., Falkow, S., Rosenberg, E., Schleifer, K.-H. and Stackebrandt, E. (eds.) *The Prokaryotes*. 3rd ed. New York, NY: Springer US. pp. 175–204. doi:10.1007/0-387-30744-3_6.

Lee, J., Cheng, X., Swails, J.M., Yeom, M.S., Eastman, P.K., Lemkul, J.A., Wei, S., Buckner, J., Jeong, J.C., Qi, Y., Jo, S., Pande, V.S., Case, D.A., Brooks, C.L., Mackerell, A.D., Klauda, J.B. and Im, W. (2016) CHARMM-GUI Input Generator for NAMD, GROMACS, AMBER, OpenMM, and CHARMM/OpenMM Simulations Using the CHARMM36 Additive Force Field. *Journal of Chemical Theory and Computation*, 12: 405–413. doi:10.1021/acs.jctc.5b00935.

Lee, R.E., Brennan, P.J. and Besra, G.S. (1996) "*Mycobacterium tuberculosis* cell envelope." In Shinnick, T.M. (ed.) *Tuberculosis*. Current Topics in Microbiology and Immunology. Berlin, Heidelberg: Springer. pp. 1–27. Available at: https://doi.org/10.1007/978-3-642-80166-2_1.

Lee, R.E., Protopopova, M., Crooks, E., Slayden, R.A., Terrot, M. and Barry, C.E. (2003) Combinatorial Lead Optimization of [1,2]-Diamines Based on Ethambutol as Potential Antituberculosis Preclinical Candidates. *Journal of Combinatorial Chemistry*, 5 (2): 172–187. doi:10.1021/cc020071p.

Letunic, I. and Bork, P. (2016) Interactive tree of life (iTOL) v3: an online tool for the display and annotation of phylogenetic and other trees. *Nucleic Acids Research*, 44 (W1): W242–W245. doi:10.1093/nar/gkw290.

Leung, E., Ayine-Tora, D.M., Santos-Ledo, A., Korolchuk, V.I. and Reynisson, J. (2021) Identification of novel Atg3-Atg8 inhibitors using virtual screening for autophagy modulation. *Bioorganic Chemistry*, 114: 105092. doi:10.1016/j.bioorg.2021.105092.

Lewis, D.B., Matecka, D., Zhang, Y., Hsin, L.-W., Dersch, C.M., Stafford, D., Glowa, J.R., Rothman, R.B. and Rice, K.C. (1999) Oxygenated Analogues of 1-[2-(Diphenylmethoxy)ethyl]- and 1-[2-[Bis(4-fluorophenyl)methoxy]ethyl]-4-(3-phenylpropyl)piperazines (GBR 12935 and GBR 12909) as Potential Extended-Action Cocaine-Abuse Therapeutic Agents. *Journal of Medicinal Chemistry*, 42: 5029–5042. doi:10.1021/jm990291q.

Lewis, K.N., Liao, R., Guinn, K.M., Hickey, M.J., Smith, S., Behr, M.A. and Sherman, D.R. (2003) Deletion of RD1 from *Mycobacterium tuberculosis* Mimics Bacille Calmette-Guérin Attenuation. *The Journal of Infectious Diseases*, 187 (1): 117–123. doi:10.1086/345862.

Ley, S.D., de Vos, M., Van Rie, A. and Warren, R.M. (2019) Deciphering Within-Host Microevolution of *Mycobacterium tuberculosis* through Whole-Genome Sequencing: the Phenotypic Impact and Way Forward. *Microbiology and Molecular Biology Reviews : MMBR*, 83 (2): e00062-18. doi:10.1128/MMBR.00062-18.

Li, H., Peng, J., Leung, Y., Leung, K.-S., Wong, M.-H., Lu, G. and Ballester, P. (2018) The Impact of Protein Structure and Sequence Similarity on the Accuracy of Machine-Learning Scoring Functions for Binding Affinity Prediction. *Biomolecules*, 8 (1): 12. doi:10.3390/biom8010012.

Li, M., Chen, R., Lin, S., Lu, Y., Liu, H., Li, G., Liu, Z., Zhao, X., Zhao, L. and Wan, K.-L. (2020) Detecting Ethambutol Resistance in *Mycobacterium tuberculosis* Isolates in China: A Comparison Between Phenotypic Drug Susceptibility Testing Methods and DNA Sequencing of embAB. *Frontiers in Microbiology*, 11: 781. doi:10.3389/fmicb.2020.00781.

Li, W., Stevens, C.M., Pandya, A.N., Darzynkiewicz, Z., Bhattarai, P., Tong, W., Gonzalez-Juarrero, M., North, E.J., Zgurskaya, H.I. and Jackson, M. (2019) Direct Inhibition of MmpL3 by Novel Antitubercular Compounds. *ACS Infectious Diseases*, 5 (6): 1001–1012. doi:10.1021/acsinfecdis.9b00048.

Li, X., Hernandez, V., Rock, F.L., Choi, W., Mak, Y.S.L., Mohan, M., Mao, W., Zhou, Y., Easom, E.E., Plattner, J.J., Zou, W., Pérez-Herrán, E., Giordano, I., Mendoza-Losana, A., Alemparte, C., Rullas, J., Angulo-Barturen, I., Crouch, S., Ortega, F., Barros, D. and Alley, M.R.K. (2017) Discovery of a Potent and Specific *M. tuberculosis* Leucyl-tRNA Synthetase Inhibitor: (*S*)-3-(Aminomethyl)-4-chloro-7-(2-hydroxyethoxy)benzo[*c*][1,2]oxaborol-1(3*H*)-ol (GSK656). *Journal of Medicinal Chemistry*, 60 (19): 8011–8026. doi:10.1021/acs.jmedchem.7b00631.

Libermann, D., Moyuex, M., Rist, N. and Grumbach, F. (1956) Sur la préparation de nouveaux thioamides pyridiniques actifs dans la tuberculose expérimentale. *Comptes rendus hebdomadaires des séances de l'Académie des sciences*, 242 (19): 2409–2412.

Lin, J.H., Perryman, A.L., Schames, J.R. and McCammon, J.A. (2003) The relaxed complex method: Accommodating receptor flexibility for drug design with an improved scoring scheme. *Biopolymers*, 68 (1): 47–62. doi:10.1002/bip.10218.

Ling, L.L., Schneider, T., Peoples, A.J., Spoering, A.L., Engels, I., Conlon, B.P., Mueller, A., Schäberle, T.F., Hughes, D.E., Epstein, S., Jones, M., Lazarides, L., Steadman, V.A., Cohen, D.R., Felix, C.R., Fetterman, K.A., Millett, W.P., Nitti, A.G., Zullo, A.M., Chen, C. and Lewis, K. (2015) A new antibiotic kills pathogens without detectable resistance. *Nature*, 517 (7535): 455–459. doi:10.1038/nature14098.

Liu, J.-S., Cheng, W.-C., Wang, H.-J., Chen, Y.-C. and Wang, W.-C. (2008) Structure-based inhibitor discovery of *Helicobacter pylori* dehydroquinate synthase. *Biochemical and Biophysical Research Communications*, 373 (1): 1–7. doi:10.1016/J.BBRC.2008.05.070.

Locher, C.P., Jones, S.M., Hanzelka, B.L., Perola, E., Shoen, C.M., Cynamon, M.H., Ngwane, A.H., Wiid, I.J., van Helden, P.D., Betoudji, F., Nuermberger, E.L. and Thomson, J.A. (2015) A Novel Inhibitor of Gyrase B Is a Potent Drug Candidate for Treatment of Tuberculosis and Nontuberculosis Mycobacterial Infections. *Antimicrobial Agents and Chemotherapy*, 59 (3): 1455–1465. doi:10.1128/AAC.04347-14.

Lohning, A.E., Levonis, S.M., Williams-Noonan, B. and Schweiker, S.S. (2017) A practical guide to molecular docking and homology modelling for medicinal chemists. *Current Topics in Medicinal Chemistry*, 17 (18): 2023–2040. doi:10.2174/1568026617666170130110827.

Madacki, J., Orgeur, M., Mas Fiol, G., Frigui, W., Ma, L. and Brosch, R. (2021) ESX-1-Independent Horizontal Gene Transfer by Mycobacterium tuberculosis Complex Strains Sloan Siegrist, M. (ed.). *mBio*, 12 (3): e00965-21. doi:10.1128/mBio.00965-21.

Mahairas, G.G., Sabo, P.J., Hickey, M.J., Singh, D.C. and Stover, C.K. (1996) Molecular analysis of genetic differences between *Mycobacterium bovis* BCG and virulent *M. bovis*. *Journal of Bacteriology*, 178 (5): 1274–1282. doi:10.1128/jb.178.5.1274-1282.1996.

Maitra, A., Munshi, T., Healy, J., Martin, L.T., Vollmer, W., Keep, N.H. and Bhakta, S. (2019) Cell wall peptidoglycan in *Mycobacterium tuberculosis*: An Achilles' heel for the TB-causing pathogen. *FEMS Microbiology Reviews*, 43: 548–575. doi:10.1093/femsre/fuz016.

Makarov, V., Manina, G., Mikusova, K., Möllmann, U., Ryabova, O., Saint-Joanis, B., Dhar, N., Pasca, M.R., Buroni, S., Lucarelli, A.P., Milano, A., De Rossi, E., Belanova, M., Bobovska, A., Dianiskova, P., Kordulakova, J., Sala, C., Fullam, E., Schneider, P., McKinney, J.D., Brodin, P., Christophe, T., Waddell, S., Butcher, P., Albrethsen, J., Rosenkrands, I., Brosch, R., Nandi, V., Bharath, S., Gaonkar, S., Shandil, R.K., Balasubramanian, V., Balganesh, T., Tyagi, S., Grosset, J., Riccardi, G. and Cole, S.T. (2009) Benzothiazinones Kill *Mycobacterium*

tuberculosis by Blocking Arabinan Synthesis. *Science (New York, N.Y.)*, 324 (5928): 801–804. doi:10.1126/science.1171583.

Malone, L., Schurr, A., Lindh, H., McKenzie, D., Kiser, J.S. and Williams, J.H. (1952) The Effect of Pyrazinamide (Aldinamide) on Experimental Tuberculosis in Mice. *American Review of Tuberculosis*, 65 (5): 511–518. doi:10.1164/art.1952.65.5.511.

Mangtani, P., Abubakar, I., Ariti, C., Beynon, R., Pimpin, L., Fine, P.E.M., Rodrigues, L.C., Smith, P.G., Lipman, M., Whiting, P.F. and Sterne, J.A. (2014) Protection by BCG Vaccine Against Tuberculosis: A Systematic Review of Randomized Controlled Trials. *Clinical Infectious Diseases*, 58 (4): 470–480. doi:10.1093/cid/cit790.

Manjunatha, U., Boshoff, H.I.M. and Barry, C.E. (2009) The mechanism of action of PA-824: Novel insights from transcriptional profiling. *Communicative & Integrative Biology*, 2 (3): 215–218. doi:10.4161/cib.2.3.7926.

Manjunatha, U.H., Boshoff, H., Dowd, C.S., Zhang, L., Albert, T.J., Norton, J.E., Daniels, L., Dick, T., Pang, S.S. and Barry, C.E. (2006) Identification of a nitroimidazo-oxazine-specific protein involved in PA-824 resistance in *Mycobacterium tuberculosis*. *Proceedings of the National Academy of Sciences of the United States of America*, 103 (2): 431–436. doi:10.1073/pnas.0508392103.

Margalith, P. and Beretta, G. (1960) Rifomycin. XI. taxonomic study on streptomyces mediterranei nov. sp. *Mycopathologia et mycologia applicata*, 13 (4): 321–330. doi:10.1007/BF02089930.

Masaoka, Y., Ueno, Y., Morita, Y., Kuroda, T., Mizushima, T. and Tsuchiya, T. (2000) A Two-Component Multidrug Efflux Pump, EbrAB, in *Bacillus subtilis*. *Journal of Bacteriology*, 182 (8): 2307–2310. doi:10.1128/JB.182.8.2307-2310.2000.

Matsumoto, M., Hashizume, H., Tomishige, T., Kawasaki, M., Tsubouchi, H., Sasaki, H., Shimokawa, Y. and Komatsu, M. (2006) OPC-67683, a Nitro-Dihydro-Imidazooxazole Derivative with Promising Action against Tuberculosis In Vitro and In Mice. *pLoS Medicine*, 3 (11): 2131–2144. doi:10.1371/journal.pmed.0030466.

McCammon, J.A., Gel, B.R. and Karplus, M. (1977) Dynamics of folded proteins. *Nature*, 267: 585–590. doi:10.1038/267585a0.

McNeil, M., Daffe, M. and Brennan, P.J. (1990) Evidence for the nature of the link between the arabinogalactan and peptidoglycan of mycobacterial cell walls. *Journal of Biological Chemistry*, 265 (30): 18200–18206. doi:10.1016/S0021-9258(17)44738-7.

McNeil, M., Daffe, M. and Brennan, P.J. (1991) Location of the mycolyl ester substituents in the cell walls of mycobacteria. *Journal of Biological Chemistry*, 266 (20): 13217–13223. doi:10.1016/S0021-9258(18)98826-5.

McNeil, M.R., Robuck, K.G., Harter, M. and Brennan, P.J. (1994) Enzymatic evidence for the presence of a critical terminal hexa-arabinoside in the cell walls of *Mycobacterium tuberculosis*. *Glycobiology*, 4 (2): 165–174. doi:10.1093/glycob/4.2.165.

Medley, J., Goff, A., Bettencourt, P.J.G., Dare, M., Cole, L., Cantillon, D. and Waddell, S.J. (2022) Dissecting the *Mycobacterium bovis* BCG Response to Macrophage Infection to Help

Prioritize Targets for Anti-Tuberculosis Drug and Vaccine Discovery. *Vaccines*, 10 (1): 113. doi:10.3390/vaccines10010113.

Miao, Y., Anne Goldfeld, D., Von Moo, E., Sexton, P.M., Christopoulos, A., Andrew McCammon, J. and Valant, C. (2016) Accelerated structure-based design of chemically diverse allosteric modulators of a muscarinic G protein-coupled receptor. *Proceedings of the National Academy of Sciences*, 113 (38): E5675-5684. doi:10.1073/pnas.1612353113.

Minato, Y., Gohl, D.M., Thiede, J.M., Chacón, J.M., Harcombe, W.R., Maruyama, F. and Baughn, A.D. (2019) Genomewide Assessment of *Mycobacterium tuberculosis* Conditionally Essential Metabolic Pathways. *mSystems*, 4 (4): 1–13. doi:10.1128/mSystems .00070-19.

Minato, Y., Thiede, J.M., Kordus, S.L., McKlveen, E.J., Turman, B.J. and Baughn, A.D. (2015) *Mycobacterium tuberculosis* Folate Metabolism and the Mechanistic Basis for para-Aminosalicylic Acid Susceptibility and Resistance. *Antimicrobial Agents and Chemotherapy*, 59 (9): 5097–5106. doi:10.1128/AAC.00647-15.

Minnikin, D.E., Lee, O.Y.-C., Wu, H.H.T., Nataraj, V., Donoghue, H.D., Ridell, M., Watanabe, M., Alderwick, L., Bhatt, A., Besra, G.S., Minnikin, D.E., Lee, O.Y.-C., Wu, H.H.T., Nataraj, V., Donoghue, H.D., Ridell, M., Watanabe, M., Alderwick, L., Bhatt, A. and Besra, G.S. (2015) "Pathophysiological Implications of Cell Envelope Structure in *Mycobacterium tuberculosis* and Related Taxa." In Ribon, W. (ed.) *Tuberculosis - Expanding Knowledge*. London: IntechOpen. pp. 145–175. doi:10.5772/59585.

Mitchison, D.A. (1979) Basic Mechanisms of Chemotherapy. *Chest*, 76 (6): 771–780. doi:10.1378/chest.76.6.771.

Mobley, D.L. and Dill, K.A. (2009) Binding of Small-Molecule Ligands to Proteins: "What You See" Is Not Always "What You Get." *Structure*, 17 (4): 489–498. doi:10.1016/J.STR.2009.02.010.

Mooij, W.T.M. and Verdonk, M.L. (2005) General and targeted statistical potentials for protein-ligand interactions. *Proteins: Structure, Function, and Bioinformatics*, 61 (2): 272–287. doi:10.1002/prot.20588.

Morris, G.M., Huey, R., Lindstrom, W., Sanner, M.F., Belew, R.K., Goodsell, D.S. and Olson, A.J. (2009) AutoDock4 and AutoDockTools4: Automated Docking with Selective Receptor Flexibility. *Journal of Computational Chemistry*, 30 (16): 2785–2791. doi:10.1002/jcc.21256.

Motamen, S. and Quinn, R.J. (2020) Analysis of Approaches to Anti-tuberculosis Compounds. *ACS Omega*, 5: 28529–28540. doi:10.1021/acsomega.0c03177.

Motta, S. and Bonati, L. (2017) Modeling Binding with Large Conformational Changes: Key Points in Ensemble-Docking Approaches. *Journal of Chemical Information and Modeling*, 57 (7): 1563–1578. doi:10.1021/acs.jcim.7b00125.

Motta, S., Callea, L., Giani Tagliabue, S. and Bonati, L. (2018) Exploring the PXR ligand binding mechanism with advanced Molecular Dynamics methods. *Scientific Reports*, 8 (16207): 1–12. doi:10.1038/s41598-018-34373-z.

Nagarajan, K., Shankar, R.G., Rajappa, S., Shenoy, S.J. and Costa-Pereira, R. (1989) Nitroimidazoles XXI 2,3-dihydro-6-nitroimidazo [2,1-b] oxazoles with antitubercular activity.

European Journal of Medicinal Chemistry, 24 (6): 631–633. doi:10.1016/0223-5234(89)90034-2.

Nahid, P., Dorman, S.E., Alipanah, N., Barry, P.M., Brozek, J.L., Cattamanchi, A., Chaisson, L.H., Chaisson, R.E., Daley, C.L., Grzemska, M., Higashi, J.M., Ho, C.S., Hopewell, P.C., Keshavjee, S.A., Lienhardt, C., Menzies, R., Merrifield, C., Narita, M., O'brien, R., Peloquin, C.A., Raftery, A., Saukkonen, J., Schaaf, H.S., Sotgiu, G., Starke, J.R., Migliori, G.B. and Vernon, A. (2016) Official American Thoracic Society/Centers for Disease Control and Prevention/Infectious Diseases Society of America Clinical Practice Guidelines: Treatment of Drug-Susceptible Tuberculosis. *Clinical Infectious Diseases*, 63 (7): 853–867. doi:10.1093/cid/ciw566.

Naik, M., Humnabadkar, V., Tantry, S.J., Panda, M., Narayan, A., Guptha, S., Panduga, V., Manjrekar, P., Jena, L. kumar, Koushik, K., Shanbhag, G., Jatheendranath, S., Manjunatha, M.R., Gorai, G., Bathula, C., Rudrapatna, S., Achar, V., Sharma, S., Ambady, A., Hegde, N., Mahadevaswamy, J., Kaur, P., Sambandamurthy, V.K., Awasthy, D., Narayan, C., Ravishankar, S., Madhavapeddi, P., Reddy, J., Prabhakar, K., Saralaya, R., Chatterji, M., Whiteaker, J., McLaughlin, B., Chiarelli, L.R., Riccardi, G., Pasca, M.R., Binda, C., Neres, J., Dhar, N., Signorino-Gelo, F., McKinney, J.D., Ramachandran, V., Shandil, R., Tommasi, R., Iyer, P.S., Narayanan, S., Hosagrahara, V., Kavanagh, S., Dinesh, N. and Ghorpade, S.R. (2014) 4-Aminoquinolone Piperidine Amides: Noncovalent Inhibitors of DprE1 with Long Residence Time and Potent Antimycobacterial Activity. *Journal of Medicinal Chemistry*, 57 (12): 5419–5434. doi:10.1021/jm5005978.

Nakamura, Y., Gojobori, T. and Ikemura, T. (2000) Codon usage tabulated from international DNA sequence databases: status for the year 2000. *Nucleic Acids Research*, 28 (1): 292–292. doi:10.1093/nar/28.1.292.

Ndjeka, N. and Ismail, N.A. (2020) Bedaquiline and clofazimine: successes and challenges. *The Lancet Microbe*, 1 (4): e139–e140. doi:10.1016/S2666-5247(20)30097-5.

Neetu, N., Katiki, M., Dev, A., Gaur, S., Tomar, S. and Kumar, P. (2020) Structural and Biochemical Analyses Reveal that Chlorogenic Acid Inhibits the Shikimate Pathway. *Journal of Bacteriology*, 202 (18): 1–19. doi:10.1128/JB.00248-20.

Neuwirth, E. (2014) *RColorBrewer: ColorBrewer Palettes*. Available at: https://cran.r-project.org/package=RColorBrewer.

Nguyen, P.P., Kado, T., Prithviraj, M., Siegrist, M.S. and Morita, Y.S. (2022) Inositol acylation of phosphatidylinositol mannosides: a rapid mass response to membrane fluidization in mycobacteria. *Journal of Lipid Research*, 63 (9): 100262. doi:10.1016/j.jlr.2022.100262.

Nichols, D., Cahoon, N., Trakhtenberg, E.M., Pham, L., Mehta, A., Belanger, A., Kanigan, T., Lewis, K. and Epstein, S.S. (2010) Use of Ichip for High-Throughput *In Situ* Cultivation of "Uncultivable" Microbial Species. *Applied and Environmental Microbiology*, 76 (8): 2445–2450. doi:10.1128/AEM.01754-09.

Nirmal, C.R., Rao, R. and Hopper, W. (2015) Inhibition of 3-deoxy-D-arabino-heptulosonate 7-phosphate synthase from *Mycobacterium tuberculosis*: *In silico* screening and in vitro validation. *European Journal of Medicinal Chemistry*, 105: 182–193. doi:10.1016/j.ejmech.2015.10.014.

Novo, D., Perlmutter, N.G., Hunt, R.H. and Shapiro, H.M. (1999) Accurate flow cytometric membrane potential measurement in bacteria using diethyloxacarbocyanine and a ratiometric technique. *Cytometry*, 35 (1): 55–63. doi:10.1002/(SICI)1097-0320(19990101)35:1<55::AID-CYTO8>3.0.CO;2-2.

Nuermberger, E.L., Martínez-Martínez, M.S., Sanz, O., Urones, B., Esquivias, J., Soni, H., Tasneen, R., Tyagi, S., Li, S.-Y., Converse, P.J., Boshoff, H.I., Robertson, G.T., Besra, G.S., Abrahams, K.A., Upton, A.M., Mdluli, K., Boyle, G.W., Turner, S., Fotouhi, N., Cammack, N.C., Siles, J.M., Alonso, M., Escribano, J., Lelievre, J., Rullas-Trincado, J., Pérez-Herrán, E., Bates, R.H., Maher-Edwards, G., Barros, D., Ballell, L. and Jiménez, E. (2022) GSK2556286 Is a Novel Antitubercular Drug Candidate Effective *In Vivo* with the Potential To Shorten Tuberculosis Treatment. *Antimicrobial Agents and Chemotherapy*, 66 (6): e00132-22. doi:10.1128/aac.00132-22.

Nunes, J.E.S., Duque, M.A., Freitas, T.F.D., Galina, L. and Ducati, R.G. (2020) *Mycobacterium tuberculosis* Shikimate Pathway Enzymes as Targets for the Rational Design of Anti-tuberculosis Drugs. *Molecules*, 25 (6): 1–36. doi:10.3390/molecules25061259.

Obejero-Paz, C.A., Bruening-Wright, A., Kramer, J., Hawryluk, P., Tatalovic, M., Dittrich, H.C. and Brown, A.M. (2015) Quantitative Profiling of the Effects of Vanoxerine on Human Cardiac Ion Channels and its Application to Cardiac Risk. *Scientific Reports*, 5: 17623. doi:10.1038/srep17623.

Odds, F.C. (2003) Synergy, antagonism, and what the chequerboard puts between them. *Journal of Antimicrobial Chemotherapy*, 52 (1): 1–1. doi:10.1093/jac/dkg301.

Offe, H.A., Siefken, W. and Domagk, G. (1952) The tuberculostatic activity of hydrazine derivatives from pyridine carboxylic acids and carbonyl compounds. *Zeitschrift für Naturforschung*, 7b: 462–468.

O'Neill, M.B., Mortimer, T.D. and Pepperell, C.S. (2015) Diversity of *Mycobacterium tuberculosis* across Evolutionary Scales Fortune, S.M. (ed.). *PLOS Pathogens*, 11 (11): e1005257. doi:10.1371/journal.ppat.1005257.

Pai, M., Behr, M.A., Dowdy, D., Dheda, K., Divangahi, M., Boehme, C.C., Ginsberg, A., Swaminathan, S., Spigelman, M., Getahun, H., Menzies, D. and Raviglione, M. (2016) Tuberculosis. *Nature Reviews Disease Primers*, 2: 1–23. doi:10.1038/nrdp.2016.76.

Palencia, A., Li, X., Bu, W., Choi, W., Ding, C.Z., Easom, E.E., Feng, L., Hernandez, V., Houston, P., Liu, L., Meewan, M., Mohan, M., Rock, F.L., Sexton, H., Zhang, S., Zhou, Y., Wan, B., Wang, Y., Franzblau, S.G., Woolhiser, L., Gruppo, V., Lenaerts, A.J., O'Malley, T., Parish, T., Cooper, C.B., Waters, M.G., Ma, Z., Ioerger, T.R., Sacchettini, J.C., Rullas, J., Angulo-Barturen, I., Pérez-Herrán, E., Mendoza, A., Barros, D., Cusack, S., Plattner, J.J. and Alley, M.R.K. (2016) Discovery of Novel Oral Protein Synthesis Inhibitors of *Mycobacterium tuberculosis* That Target Leucyl-tRNA Synthetase. *Antimicrobial Agents and Chemotherapy*, 60 (10): 6271–6280. doi:10.1128/AAC.01339-16.

Pantel, A., Petrella, S., Veziris, N., Brossier, F., Bastian, S., Jarlier, V., Mayer, C. and Aubry, A. (2012) Extending the Definition of the GyrB Quinolone Resistance-Determining Region in *Mycobacterium tuberculosis* DNA Gyrase for Assessing Fluoroquinolone Resistance in *M. tuberculosis*. *Antimicrobial Agents and Chemotherapy*, 56 (4): 1990–1996. doi:10.1128/AAC.06272-11.

Parish, T. (2021) “Electroporation of Mycobacteria.” In Parish, T. and Kumar, A. (eds.) *Mycobacteria Protocols*. Methods in Molecular Biology. New York, NY: Springer US. pp. 273–284. doi:10.1007/978-1-0716-1460-0_12.

Parish, T. and Stoker, N.G. (2002) The common aromatic amino acid biosynthesis pathway is essential in Mycobacterium tuberculosis. *Microbiology*, 148: 3069–3077. doi:10.1099/00221287-148-10-3069.

Patel, V.B. and Giles, N.H. (1979) Purification of the arom multienzyme aggregate from Euglena gracilis. *Biochimica et Biophysica Acta (BBA) - Enzymology*, 567 (1): 24–34. doi:10.1016/0005-2744(79)90168-2.

Patterson, B. and Wood, R. (2019) Is cough really necessary for TB transmission? *Tuberculosis*, 117: 31–35. doi:10.1016/j.tube.2019.05.003.

Paudel, S., Acharya, S., Yoon, G., Kim, K.-M. and Cheon, S.H. (2017) Design, synthesis and *in vitro* activity of 1,4-disubstituted piperazines and piperidines as triple reuptake inhibitors. *Bioorganic & Medicinal Chemistry*, 25 (7): 2266–2276. doi:10.1016/j.bmc.2017.02.051.

Petersen, G.O., Saxena, S., Renuka, J., Soni, V., Yogeeswari, P., Santos, D.S., Bizarro, C.V. and Sriram, D. (2015) Structure-based virtual screening as a tool for the identification of novel inhibitors against Mycobacterium tuberculosis 3-dehydroquinate dehydratase. *Journal of Molecular Graphics and Modelling*, 60: 124–131. doi:10.1016/j.jmgm.2015.05.001.

Peterson, N.D., Rosen, B.C., Dillon, N.A. and Baughn, A.D. (2015) Uncoupling Environmental pH and Intrabacterial Acidification from Pyrazinamide Susceptibility in *Mycobacterium tuberculosis*. *Antimicrobial Agents and Chemotherapy*, 59 (12): 7320–7326. doi:10.1128/AAC.00967-15.

Pethe, K., Bifani, P., Jang, J., Kang, S., Park, S., Ahn, S., Jiricek, J., Jung, J., Jeon, H.K., Cechetto, J., Christophe, T., Lee, H., Kempf, M., Jackson, M., Lenaerts, A.J., Pham, H., Jones, V., Seo, M.J., Kim, Y.M., Seo, M., Seo, J.J., Park, D., Ko, Y., Choi, I., Kim, R., Kim, S.Y., Lim, S., Yim, S.-A., Nam, J., Kang, H., Kwon, H., Oh, C.-T., Cho, Y., Jang, Y., Kim, J., Chua, A., Tan, B.H., Nanjundappa, M.B., Rao, S.P.S., Barnes, W.S., Wintjens, R., Walker, J.R., Alonso, S., Lee, S., Kim, J., Oh, S., Oh, T., Nehrbass, U., Han, S.-J., No, Z., Lee, J., Brodin, P., Cho, S.-N., Nam, K. and Kim, J. (2013) Discovery of Q203, a potent clinical candidate for the treatment of tuberculosis. *Nature Medicine*, 19 (9): 1157–1160. doi:10.1038/nm.3262.

Pettersen, E.F., Goddard, T.D., Huang, C.C., Couch, G.S., Greenblatt, D.M., Meng, E.C. and Ferrin, T.E. (2004) UCSF Chimera-A visualization system for exploratory research and analysis. *Journal of Computational Chemistry*, 25 (13): 1605–1612. doi:10.1002/jcc.20084.

Phillips, J.C., Braun, R., Wang, W., Gumbart, J., Tajkhorshid, E., Villa, E., Chipot, C., Skeel, R.D., Kalé, L. and Schulten, K. (2005) Scalable Molecular Dynamics with NAMD. *Journal of Computational Chemistry*, 26 (16): 1781–1802. doi:10.1002/jcc.20289.

Piccini, J.P., Pritchett, E.L.C., Davison, B.A., Cotter, G., Wiener, L.E., Koch, G., Feld, G., Waldo, A., Gelder, I.C. van, Camm, A.J., Kowey, P.R., Iwashita, J. and Dittrich, H.C. (2016) Randomized, double-blind, placebo-controlled study to evaluate the safety and efficacy of a single oral dose of vanoxerine for the conversion of subjects with recent onset atrial fibrillation or flutter to normal sinus rhythm: RESTORE SR. *Heart Rhythm*, 13 (9): 1777–1783. doi:10.1016/j.hrthm.2016.04.012.

Pickford, H., Alcock, E., Singh, A., Kelemen, G. and Bhatt, A. (2020) A mycobacterial DivIVA domain-containing protein involved in cell length and septation. *Microbiology*, 166 (9): 817–825. doi:10.1099/mic.0.000952.

Piton, J., Foo, C.S.-Y. and Cole, S.T. (2017) Structural studies of *Mycobacterium tuberculosis* DprE1 interacting with its inhibitors. *Drug Discovery Today*, 22 (3): 526–533. doi:10.1016/J.DRUDIS.2016.09.014.

Preti, A. (2000) Vanoxerine National Institute on Drug Abuse. *Current Opinion in Investigational Drugs*, 1 (2): 241–251.

Projan, S.J. (2002) New (and not so new) antibacterial targets – from where and when will the novel drugs come? *Current Opinion in Pharmacology*, 2 (5): 513–522. doi:10.1016/S1471-4892(02)00197-2.

Pronobis, M.I., Deuitch, N. and Peifer, M. (2016) The Miraprep: A Protocol that Uses a Miniprep Kit and Provides Maxiprep Yields Hayes, F. (ed.). *PLoS ONE*, 11 (8): 1–12. doi:10.1371/journal.pone.0160509.

Prosser, G.A. and de Carvalho, L.P.S. (2013) Metabolomics Reveal D -Alanine: D -Alanine Ligase As the Target of D -Cycloserine in *Mycobacterium tuberculosis*. *ACS Medicinal Chemistry Letters*, 4 (12): 1233–1237. doi:10.1021/ml400349n.

Protopopova, M., Hanrahan, C., Nikonenko, B., Samala, R., Chen, P., Gearhart, J., Einck, L. and Nacy, C.A. (2005) Identification of a new antitubercular drug candidate, SQ109, from a combinatorial library of 1,2-ethylenediamines. *Journal of Antimicrobial Chemotherapy*, 56 (5): 968–974. doi:10.1093/jac/dki319.

Pule, C.M., Sampson, S.L., Warren, R.M., Black, P.A., van Helden, P.D., Victor, T.C. and Louw, G.E. (2016) Efflux pump inhibitors: targeting mycobacterial efflux systems to enhance TB therapy. *Journal of Antimicrobial Chemotherapy*, 71 (1): 17–26. doi:10.1093/jac/dkv316.

Rajan, A., Freddolino, P.L. and Schulten, K. (2010) Going beyond Clustering in MD Trajectory Analysis: An Application to Villin Headpiece Folding. *PLoS ONE*, 5 (4): 1–12. doi:10.1371/journal.pone.0009890.

Ramón- García, S., Bates, R., González del Río, R., Gamallo, P., Mendoza-Losana, A., Ferrer-Bazaga, S., Thompson, C. and Barros, D. (2019) *Sanfetrinem, repurposing an oral beta-lactam with intracellular activity for the treatment of tuberculosis*. In 10 Hyderabad, India, 29 October 2019. The International Journal of Tuberculosis and Lung Disease. p. S591. Available at: https://araid.es/en/content/sanfetrinem-repurposing-oral-beta-lactam-intracellular-activity-treatment-tuberculosis (Accessed: 31 October 2022).

Rao, S.P.S., Alonso, S., Rand, L., Dick, T. and Pethe, K. (2008) The protonmotive force is required for maintaining ATP homeostasis and viability of hypoxic, nonreplicating *Mycobacterium tuberculosis*. *Proceedings of the National Academy of Sciences*, 105 (33): 11945–11950. doi:10.1073/pnas.0711697105.

Raymond, J.B., Mahapatra, S., Crick, D.C. and Pavelka, M.S. (2005) Identification of the namH Gene, Encoding the Hydroxylase Responsible for the N-Glycolylation of the Mycobacterial Peptidoglycan. *Journal of Biological Chemistry*, 280 (1): 326–333. doi:10.1074/jbc.M411006200.

Reichau, S., Jiao, W., Walker, S.R., Hutton, R.D., Baker, E.N. and Parker, E.J. (2011) Potent Inhibitors of a Shikimate Pathway Enzyme from *Mycobacterium tuberculosis*. *Journal of Biological Chemistry*, 286 (18): 16197–16207. doi:10.1074/jbc.M110.211649.

Remm, S., Earp, J.C., Dick, T., Dartois, V. and Seeger, M.A. (2022) Critical discussion on drug efflux in *Mycobacterium tuberculosis*. *FEMS Microbiology Reviews*, 46 (1): 1–15. doi:10.1093/femsre/fuab050.

Roberts, A.P. (2020) Swab and Send: a citizen science, antibiotic discovery project. *Future Science OA*, 6 (6): FSO477. doi:10.2144/fsoa-2020-0053.

Rock, F.L., Mao, W., Yaremchuk, A., Tukalo, M., Crépin, T., Zhou, H., Zhang, Y.-K., Hernandez, V., Akama, T., Baker, S.J., Plattner, J.J., Shapiro, L., Martinis, S.A., Benkovic, S.J., Cusack, S. and Alley, M.R.K. (2007) An Antifungal Agent Inhibits an Aminoacyl-tRNA Synthetase by Trapping tRNA in the Editing Site. *Science*, 316 (5832): 1759–1761. doi:10.1126/science.1142189.

Rodrigues, L., Aínsa, J.A. and Viveiros, M. (2021) "Measuring Efflux and Permeability in Mycobacteria." In Parish, T. and Kumar, A. (eds.) *Mycobacteria Protocols*. Methods in Molecular Biology. 4th ed. New York, NY: Springer US. pp. 231–245. doi:10.1007/978-1-0716-1460-0_9.

Rohde, K.H. and Sorci, L. (2021) The Prospective Synergy of Antitubercular Drugs With NAD Biosynthesis Inhibitors. *Frontiers in Microbiology*, 11: 634640. doi:10.3389/fmicb.2020.634640.

Rozwarski, D.A., Grant, G.A., Barton, D.H.R., Jacobs, W.R. and Sacchettini, J.C. (1998) Modification of the NADH of the Isoniazid Target (InhA) from *Mycobacterium tuberculosis*. *Science*, 279 (5347): 98–102. doi:10.1126/science.279.5347.98.

RStudio (2020) *RStudio: Integrated Development for R*. Available at: https://rstudio.com.

Sacksteder, K.A., Protopopova, M., Barry, C.E., Andries, K. and Nacy, C.A. (2012) Discovery and development of SQ109: a new antitubercular drug with a novel mechanism of action. *Future Microbiology*, 7 (7): 823–837. doi:10.2217/fmb.12.56.

Saha, S., Yeom, G.S., Nimse, S.B. and Pal, D. (2022) Combination Therapy of Ledipasvir and Itraconazole in the Treatment of COVID-19 Patients Coinfected with Black Fungus: An *In Silico* Statement Baig, M.H. (ed.). *BioMed Research International*, 2022: 1–10. doi:10.1155/2022/5904261.

Schatz, A., Bugle, E. and Waksman, S.A. (1944) Streptomycin, a Substance Exhibiting Antibiotic Activity Against Gram-Positive and Gram-Negative Bacteria.∗†. *Proceedings of the Society for Experimental Biology and Medicine*, 55 (1): 66–69. doi:10.3181/00379727-55-14461.

Schmitt, K.C., Zhen, J., Kharkar, P., Mishra, M., Chen, N., Dutta, A.K. and Reith, M.E.A. (2008) Interaction of cocaine-, benztropine-, and GBR12909-like compounds with wild-type and mutant human dopamine transporters: Molecular features that differentially determine antagonist-binding properties. *Journal of Neurochemistry*, 107 (4): 928–940. doi:10.1111/j.1471-4159.2008.05667.x.

SCIGRESS (2016). Available at: https://www.fqs.pl/en/chemistry/products/scigress.

Scorpio, A. and Zhang, Y. (1996) Mutations in pncA, a gene encoding pyrazinamidase/nicotinamidase, cause resistance to the antituberculous drug pyrazinamide in tubercle bacillus. *Nature Medicine*, 2 (6): 662–667. doi:10.1038/nm0696-662.

Sensi, P. (1983) History of the Development of Rifampin. *Reviews of Infectious Diseases*, 5 (Supplementary 3): S402-406. doi:10.1093/clinids/5.supplement_3.s402.

Shaker, B., Yu, M.-S., Lee, J., Lee, Y., Jung, C. and Na, D. (2020) User guide for the discovery of potential drugs via protein structure prediction and ligand docking simulation. *Journal of Microbiology*, 58 (3): 235–244. doi:10.1007/s12275-020-9563-z.

Shao, J., Tanner, S.W., Thompson, N. and Cheatham, T.E. (2007) Clustering molecular dynamics trajectories: 1. Characterizing the performance of different clustering algorithms. *Journal of Chemical Theory and Computation*, 3 (6): 2312–2334. doi:10.1021/ct700119m.

Sharma, A., Gupta, V.K. and Pathania, R. (2019) Efflux pump inhibitors for bacterial pathogens: From bench to bedside. *The Indian Journal of Medical Research*, 149 (2): 129–145. doi:10.4103/ijmr.IJMR_2079_17.

Sherman, B.T., Hao, M., Qiu, J., Jiao, X., Baseler, M.W., Lane, H.C., Imamichi, T. and Chang, W. (2022) DAVID: a web server for functional enrichment analysis and functional annotation of gene lists (2021 update). *Nucleic Acids Research*, 50 (W1): W216–W221. doi:10.1093/nar/gkac194.

Shi, L., Berg, S., Lee, A., Spencer, J.S., Zhang, J., Vissa, V., McNeil, M.R., Khoo, K.-H. and Chatterjee, D. (2006) The Carboxy Terminus of EmbC from *Mycobacterium smegmatis* Mediates Chain Length Extension of the Arabinan in Lipoarabinomannan. *Journal of Biological Chemistry*, 281 (28): 19512–19526. doi:10.1074/jbc.M513846200.

Shirude, P.S., Shandil, R., Sadler, C., Naik, M., Hosagrahara, V., Hameed, S., Shinde, V., Bathula, C., Humnabadkar, V., Kumar, N., Reddy, J., Panduga, V., Sharma, S., Ambady, A., Hegde, N., Whiteaker, J., McLaughlin, R.E., Gardner, H., Madhavapeddi, P., Ramachandran, V., Kaur, P., Narayan, A., Guptha, S., Awasthy, D., Narayan, C., Mahadevaswamy, J., Vishwas, K., Ahuja, V., Srivastava, A., Prabhakar, K., Bharath, S., Kale, R., Ramaiah, M., Choudhury, N.R., Sambandamurthy, V.K., Solapure, S., Iyer, P.S., Narayanan, S. and Chatterji, M. (2013) Azaindoles: Noncovalent DprE1 Inhibitors from Scaffold Morphing Efforts, Kill *Mycobacterium tuberculosis* and Are Efficacious in Vivo. *Journal of Medicinal Chemistry*, 56 (23): 9701–9708. doi:10.1021/jm401382v.

Shruthi, T.G., Eswaran, S., Shivarudraiah, P., Narayanan, S. and Subramanian, S. (2019) Synthesis, antituberculosis studies and biological evaluation of new quinoline derivatives carrying 1,2,4-oxadiazole moiety. *Bioorganic & Medicinal Chemistry Letters*, 29 (1): 97–102. doi:10.1016/j.bmcl.2018.11.002.

Simithy, J., Fuanta, N.R., Alturki, M., Hobrath, J.V., Wahba, A.E., Pina, I., Rath, J., Hamann, M.T., DeRuiter, J., Goodwin, D.C. and Calderón, A.I. (2018) Slow-Binding Inhibition of *Mycobacterium tuberculosis* Shikimate Kinase by Manzamine Alkaloids. *Biochemistry*, 57 (32): 4923–4933. doi:10.1021/acs.biochem.8b00231.

Singh, A.K., Carette, X., Potluri, L.P., Sharp, J.D., Xu, R., Prisic, S. and Husson, R.N. (2016) Investigating essential gene function in *Mycobacterium tuberculosis* using an efficient CRISPR interference system. *Nucleic Acids Research*, 44 (18): 1–13. doi:10.1093/nar/gkw625.

Singh, A.K., Netea, M.G. and Bishai, W.R. (2021) BCG turns 100: its nontraditional uses against viruses, cancer, and immunologic diseases. *Journal of Clinical Investigation*, 131 (11): e148291. doi:10.1172/JCI148291.

Singh, B.N., Ellrodt, G. and Peter, C.T. (1978) Verapamil: A Review of its Pharmacological Properties and Therapeutic Use. *Drugs*, 15 (3): 169–197. doi:10.2165/00003495-197815030-00001.

Sivaranjani, P., Naik, V.U., Madhulitha, N.R., Kumar, K.S., Chiranjeevi, P., Alex, S.P. and Umamaheswari, A. (2019) Design of Novel Antimycobacterial Molecule Targeting Shikimate Pathway of *Mycobacterium tuberculosis*. *Indian Journal of Pharmaceutical Sciences*, 81 (3): 438–447. doi:10.36468/pharmaceutical-sciences.528.

Skinner, M.A., Günel-Ozcan, A., Shafiq, M., Maskell, D.J. and Brown, K.A. (1998) Expression of recombinant aroB-encoded dehydroquinate synthase from pathogenic microorganisms. *Biochemical Society transactions*, 26 (3): S280. doi:10.1042/bst026s280.

Søgaard, U., Michalow, J., Butler, B., Laursen, A.L., Ingersen, S.H., Skrumsager, B.K. and Rafaelsen, O.J. (1990) A Tolerance Study of Single and Multiple Dosing of the Selective Dopamine Uptake Inhibitor GBR 12909 in Healthy Subjects. *International Clinical Psychopharmacology*, 5 (4): 237–252. doi:10.1097/00004850-199010000-00001.

Sohaskey, C.D. and Wayne, L.G. (2003) Role of *narK2X* and *narGHJI* inHypoxic Upregulation of Nitrate Reduction by *Mycobacteriumtuberculosis*. *Journal of Bacteriology*, 185 (24): 7247–7256. doi:10.1128/JB.185.24.7247-7256.2003.

Stover, C.K., de Ia Cruz, V.F., Fuerst, T.R., Burlein, J.E., Benson, L., Bennett, L.T., Bansal, G.P., Young, J.F., Lee, M.H., Hatfull, G.F., Snapper, S.B., Barletta, R.G., Jacobs Jr, W.R. and Bloom, B.R. (1991) New use of BCG for recombinant vaccines. *Nature*, 351: 456–460. doi: 10.1038/351456a0.

Stover, C.K., Warrener, P., VanDevanter, D.R., Sherman, D.R., Arain, T.M., Langhorne, M.H., Anderson, S.W., Towell, J.A., Yuan, Y., McMurray, D.N., Kreiswirth, B.N., Barry III, C.E. and Baker, W.R. (2000) A small-molecule nitroimidazopyran drug candidate for the treatment of tuberculosis. *Nature*, 405: 962–966. doi:10.1038/35016103.

Stülke, J., Hanschke, R. and Hecker, M. (1993) Temporal activation of β-glucanase synthesis in *Bacillus subtilis* is mediated by the GTP pool. *Journal of General Microbiology*, 139 (9): 2041–2045. doi:10.1099/00221287-139-9-2041.

Su, C.-C., Klenotic, P.A., Bolla, J.R., Purdy, G.E., Robinson, C.V. and Yu, E.W. (2019) MmpL3 is a lipid transporter that binds trehalose monomycolate and phosphatidylethanolamine. *Proceedings of the National Academy of Sciences*, 116 (23): 11241–11246. doi:10.1073/pnas.1901346116.

Swaney, S.M., Aoki, H., Ganoza, M.C. and Shinabarger, D.L. (1998) The Oxazolidinone Linezolid Inhibits Initiation of Protein Synthesis in Bacteria. *Antimicrobial Agents and Chemotherapy*, 42 (12): 3251–3255. doi: 10.1128/aac.42.12.3251

Swift, R.V., Jusoh, S.A., Offutt, T.L., Li, E.S. and Amaro, R.E. (2016) Knowledge-Based Methods To Train and Optimize Virtual Screening Ensembles. *Journal of Chemical Information and Modeling*, 56: 830–842. doi:10.1021/acs.jcim.5b00684.

Szumowski, J.D., Adams, K.N., Edelstein, P.H. and Ramakrishnan, L. (2013) Antimicrobial efflux pumps and *Mycobacterium tuberculosis* drug tolerance: Evolutionary Considerations. *Current topics in microbiology and immunology*, 374: 1–25. doi:10.1007/82_2012_300.

Tahlan, K., Wilson, R., Kastrinsky, D.B., Arora, K., Nair, V., Fischer, E., Barnes, S.W., Walker, J.R., Alland, D., Barry, C.E. and Boshoff, H.I. (2012) SQ109 Targets MmpL3, a Membrane Transporter of Trehalose Monomycolate Involved in Mycolic Acid Donation to the Cell Wall Core of *Mycobacterium tuberculosis*. *Antimicrobial Agents and Chemotherapy*, 56 (4): 1797–1809. doi:10.1128/AAC.05708-11.

Takayama, K. and Kilburn, J.O. (1989) Inhibition of synthesis of arabinogalactan by ethambutol in *Mycobacterium smegmatis*. *Antimicrobial Agents and Chemotherapy*, 33 (9): 1493–1499. doi:10.1128/aac.33.9.1493.

Telenti, A. (1998) Genetics of drug resistant tuberculosis. *Thorax*, 53 (9): 793–797. doi:10.1136/thx.53.9.793.

Thomas, J.P., Baughn, C.O., Wilkinson, R.G. and Shepherd, R.G. (1961) A New Synthetic Compound with Antituberculous Activity in Mice: Ethambutol (Dextro-2, 2′- (Ethylenediimino)-di-1-Butanol). *American Review of Respiratory Disease*, 83 (6): 891–893. doi:10.1164/arrd.1961.83.6.891.

Thompson, S.J., Thompson, S.E.M. and Cazier, J.-B. (2019) *CaStLeS (Compute and Storage for the Life Sciences): a collection of compute and storage resources for supporting research at the University of Birmingham*. University of Birmingham. doi:10.5281/zenodo.3250616.

Tian, F., Montchamp, J.-L. and Frost, J.W. (1996) Inhibitor Ionization as a Determinant of Binding to 3-Dehydroquinate Synthase. *J. R. Biochemistry*, 61 (21): 7373–7381. doi:10.1021/jo960709h.

Trott, O. and Olson, A.J. (2010) AutoDock Vina: improving the speed and accuracy of docking with a new scoring function, efficient optimization and multithreading. *Journal of Computational Chemistry*, 31 (2): 455–461. doi:10.1002/jcc.21334.

Umezawa, H., Mizuno, S., Yamazaki, H. and Nitta, K. (1968) Inhibition of DNA-Dependent RNA Synthesis By Rifamycins. *The Journal of Antibiotics*, 21 (3): 234–236. doi:10.7164/antibiotics.21.234.

Van Der Zee, P. and Hespe, W. (1973) Influence of orphenadrine HCl and its N-demethylated derivatives on the in vitro uptake of noradrenaline and 5-hydroxytryptamine by rat brain slices. *Neuropharmacology*, 12 (9): 843–851. doi:10.1016/0028-3908(73)90037-3.

Van Der Zee, P. and Hespe, W. (1978) A Comparison of the inhibitory effects of aromatic substituted benzhydryl ethers on the uptake of catecholamines and serotonin into synaptosomal preparations of the rat brain. *Neuropharmacology*, 17 (7): 483–490. doi:10.1016/0028-3908(78)90054-0.

Van Der Zee, P., Koger, H.S., Gootjes, J. and Hespe, W. (1980) Aryl 1,4-dialk(en)ylpiperazines as selective and very potent inhibitors of dopamine uptake. *European Journal of Medicinal Chemistry*, 15 (4): 363–370.

Varadi, M., Anyango, S., Deshpande, M., Nair, S., Natassia, C., Yordanova, G., Yuan, D., Stroe, O., Wood, G., Laydon, A., Žídek, A., Green, T., Tunyasuvunakool, K., Petersen, S.,

Jumper, J., Clancy, E., Green, R., Vora, A., Lutfi, M., Figurnov, M., Cowie, A., Hobbs, N., Kohli, P., Kleywegt, G., Birney, E., Hassabis, D. and Velankar, S. (2022) AlphaFold Protein Structure Database: massively expanding the structural coverage of protein-sequence space with high-accuracy models. *Nucleic Acids Research*, 50 (D1): D439–D444. doi:10.1093/nar/gkab1061.

Verdonk, M.L., Cole, J.C., Hartshorn, M.J., Murray, C.W. and Taylor, R.D. (2003) Improved protein-ligand docking using GOLD. *Proteins*, 52 (4): 609–23. doi:10.1002/prot.10465.

Vincent, A.T., Nyongesa, S., Morneau, I., Reed, M.B., Tocheva, E.I. and Veyrier, F.J. (2018) The Mycobacterial Cell Envelope: A Relict From the Past or the Result of Recent Evolution? *Frontiers in Microbiology*, 9: 2341. doi:10.3389/fmicb.2018.02341.

Wang, W. and MacKinnon, R. (2017) Cryo-EM Structure of the Open Human *Ether-à-go-go*-Related K^+ Channel hERG. *Cell*, 169 (3): 422-430.e10. doi:10.1016/j.cell.2017.03.048.

Wang, Y., Harrison, C.B., Schulten, K. and Mccammon, J.A. (2012) Implementation of Accelerated Molecular Dynamics in NAMD. *Comput Sci Discov*, 4 (1): 1–14. doi:10.1088/1749-4699/4/1/015002.

Wasserman, S., Louw, G., Ramangoaela, L., Barber, G., Hayes, C., Omar, S.V., Maartens, G., Barry, C., Song, T. and Meintjes, G. (2019) Linezolid resistance in patients with drug-resistant TB and treatment failure in South Africa. *Journal of Antimicrobial Chemotherapy*, 74 (8): 2377–2384. doi:10.1093/jac/dkz206.

Webb, M.R. (1992) A continuous spectrophotometric assay for inorganic phosphate and for measuring phosphate release kinetics in biological systems. *Proceedings of the National Academy of Sciences*, 89: 4884–4887. doi:10.1073/pnas.89.11.4884.

Webby, C.J., Jiao, W., Hutton, R.D., Blackmore, N.J., Baker, H.M., Baker, E.N., Jameson, G.B. and Parker, E.J. (2010) Synergistic Allostery, a Sophisticated Regulatory Network for the Control of Aromatic Amino Acid Biosynthesis in *Mycobacterium tuberculosis*. *Journal of Biological Chemistry*, 285 (40): 30567–30576. doi:10.1074/jbc.M110.111856.

Wei, T. and Simko, V. (2017) *R Package "corrplot": Visualisation of Correlation Matrix*. Available at: https://github.com/taiyun/corrplot.

Wen, S., Jing, W., Zhang, T., Zong, Z., Xue, Y., Shang, Y., Wang, F., Huang, H., Chu, N. and Pang, Y. (2019) Comparison of in vitro activity of the nitroimidazoles delamanid and pretomanid against multidrug-resistant and extensively drug-resistant tuberculosis. *European Journal of Clinical Microbiology & Infectious Diseases*, 38 (7): 1293–1296. doi:10.1007/s10096-019-03551-w.

Werner, G., Willems, R.J.L., Hildebrandt, B., Klare, I. and Witte, W. (2003) Influence of Transferable Genetic Determinants on the Outcome of Typing Methods Commonly Used for *Enterococcus faecium*. *Journal of Clinical Microbiology*, 41 (4): 1499–1506. doi:10.1128/JCM.41.4.1499–1506.2003.

Wex, K.W., Saur, J.S., Handel, F., Ortlieb, N., Mokeev, V., Kulik, A., Niedermeyer, T.H.J., Mast, Y., Grond, S., Berscheid, A. and Brötz-Oesterhelt, H. (2021) Bioreporters for direct mode of action-informed screening of antibiotic producer strains. *Cell Chemical Biology*, 28 (8): 1242-1252.e4. doi:10.1016/j.chembiol.2021.02.022.

WHO (2015) *Global tuberculosis report 2015*. 20th ed. Geneva: World Health Organization. Available at: https://apps.who.int/iris/handle/10665/191102 (Downloaded: 27 October 2022).

WHO (2017) *Prioritization of pathogens to guide discovery, research and development of new antibiotics for drug-resistant bacterial infections, including tuberculosis.* Geneva: World Health Organisation.

WHO (2019) *Global Tuberculosis Report 2019*. Geneva: World Health Organisation. Available at: http://apps.who.int/bookorders. (Accessed: 30 March 2020).

WHO (2021) *Global Tuberculosis Report 2021*. Geneva: World Health Organization. Available at: https://apps.who.int/iris/handle/10665/351784 (Accessed: 22 August 2022).

WHO (2022a) *Global tuberculosis report 2022*. Geneva: World Health Organization. Available at: https://apps.who.int/iris/handle/10665/363752 (Downloaded: 28 October 2022).

WHO (2022b) *Rapid communication: key changes to the treatment of drug-resistant tuberculosis*. Geneva: World Health Organisation. Available at: https://www.who.int/publications/i/item/WHO-UCN-TB-2022-2.

Wickham, Hadley. (2009) *ggplot2 : Elegant Graphics for Data Analysis*. 1st ed. New York: Springer. doi:10.1007/978-0-387-98141-3.

Wietzerbin, J., Das, B.C., Petit, J.F., Lederer, E., Leyh-Bouille, M. and Ghuysen, J.M. (1974) Occurrence of D-alanyl-(D)-meso-diaminopimelic acid and meso-diaminopimelyl-meso-diaminopimelic acid interpeptide linkages in the peptidoglycan of Mycobacteria. *Biochemistry*, 13 (17): 3471–3476. doi:10.1021/bi00714a008.

Williams, C.M., Abdulwhhab, M., Birring, S.S., De Kock, E., Garton, N.J., Townsend, E., Pareek, M., Al-Taie, A., Pan, J., Ganatra, R., Stoltz, A.C., Haldar, P. and Barer, M.R. (2020) Exhaled *Mycobacterium tuberculosis* output and detection of subclinical disease by face-mask sampling: prospective observational studies. *The Lancet Infectious Diseases*, 20 (5): 607–617. doi:10.1016/S1473-3099(19)30707-8.

Zaunbrecher, M.A., Sikes, R.D., Metchock, B., Shinnick, T.M. and Posey, J.E. (2009) Overexpression of the chromosomally encoded aminoglycoside acetyltransferase *eis* confers kanamycin resistance in *Mycobacterium tuberculosis*. *Proceedings of the National Academy of Sciences*, 106 (47): 20004–20009. doi:10.1073/pnas.0907925106.

Zhang, L., Zhao, Y., Gao, Y., Wu, L., Gao, R., Zhang, Q., Wang, Y., Wu, C., Wu, F., Gurcha, S.S., Veerapen, N., Batt, S.M., Zhao, W., Qin, L., Yang, X., Wang, M., Zhu, Y., Zhang, B., Bi, L., Zhang, X., Yang, H., Guddat, L.W., Xu, W., Wang, Q., Li, J., Besra, G.S. and Rao, Z. (2020) Structures of cell wall arabinosyltransferases with the anti-tuberculosis drug ethambutol. *Science*, 368 (6496): 1211–1219. doi:10.1126/science.aba9102.

Zhang, Y. (2005) The Magic Bullets and Tuberculosis Drug Targets. *Annual Review of Pharmacology and Toxicology*, 45 (1): 529–564. doi:10.1146/annurev.pharmtox.45.120403.100120.

Zhang, Y., Heym, B., Allen, B., Young, D. and Cole, S. (1992) The catalase-peroxidase gene and isoniazid resistance of. *Nature*, 358: 591–593. doi:10.1038/358591a0.

Zhang, Y., Shi, W., Zhang, W. and Mitchison, D. (2014) Mechanisms of Pyrazinamide Action and Resistance. *Microbiology Spectrum*, 2 (4): 2.4.03. doi:10.1128/microbiolspec.MGM2-0023-2013.

Zhang, Y., Wade, M.M., Scorpio, A., Zhang, H. and Sun, Z. (2003) Mode of action of pyrazinamide: disruption of *Mycobacterium tuberculosis* membrane transport and energetics by pyrazinoic acid. *Journal of Antimicrobial Chemotherapy*, 52 (5): 790–795. doi:10.1093/jac/dkg446.

Zhao, Y., Tian, Y., Cui, Y., Liu, W., Ma, W. and Jiang, X. (2010) Small Molecule-Capped Gold Nanoparticles as Potent Antibacterial Agents That Target Gram-Negative Bacteria. *Journal of the American Chemical Society*, 132: 12349–12356. doi:10.1021/ja1028843.

Zheng, J., Rubin, E.J., Bifani, P., Mathys, V., Lim, V., Au, M., Jang, J., Nam, J., Dick, T., Walker, J.R., Pethe, K. and Camacho, L.R. (2013) para-Aminosalicylic Acid Is a Prodrug Targeting Dihydrofolate Reductase in *Mycobacterium tuberculosis*. *The Journal of Biological Chemistry*, 288 (32): 23447–23456. doi:10.1074/jbc.M113.475798.

Zhu, N., Lin, Y., Li, D., Gao, N., Liu, C., You, X., Jiang, J., Jiang, W. and Si, S. (2015) Identification of an anti-TB compound targeting the tyrosyl-tRNA synthetase. *Journal of Antimicrobial Chemotherapy*, 70 (8): 2287–2294. doi:10.1093/jac/dkv110.

Zhu, N., Wang, X., Li, D., Lin, Y., You, X., Jiang, J., Xu, Y., Jiang, W. and Si, S. (2018) IMB-T130 targets 3-dehydroquinate synthase and inhibits *Mycobacterium tuberculosis*. *Scientific Reports*, 8 (1): 1–9. doi:10.1038/s41598-018-35701-z.

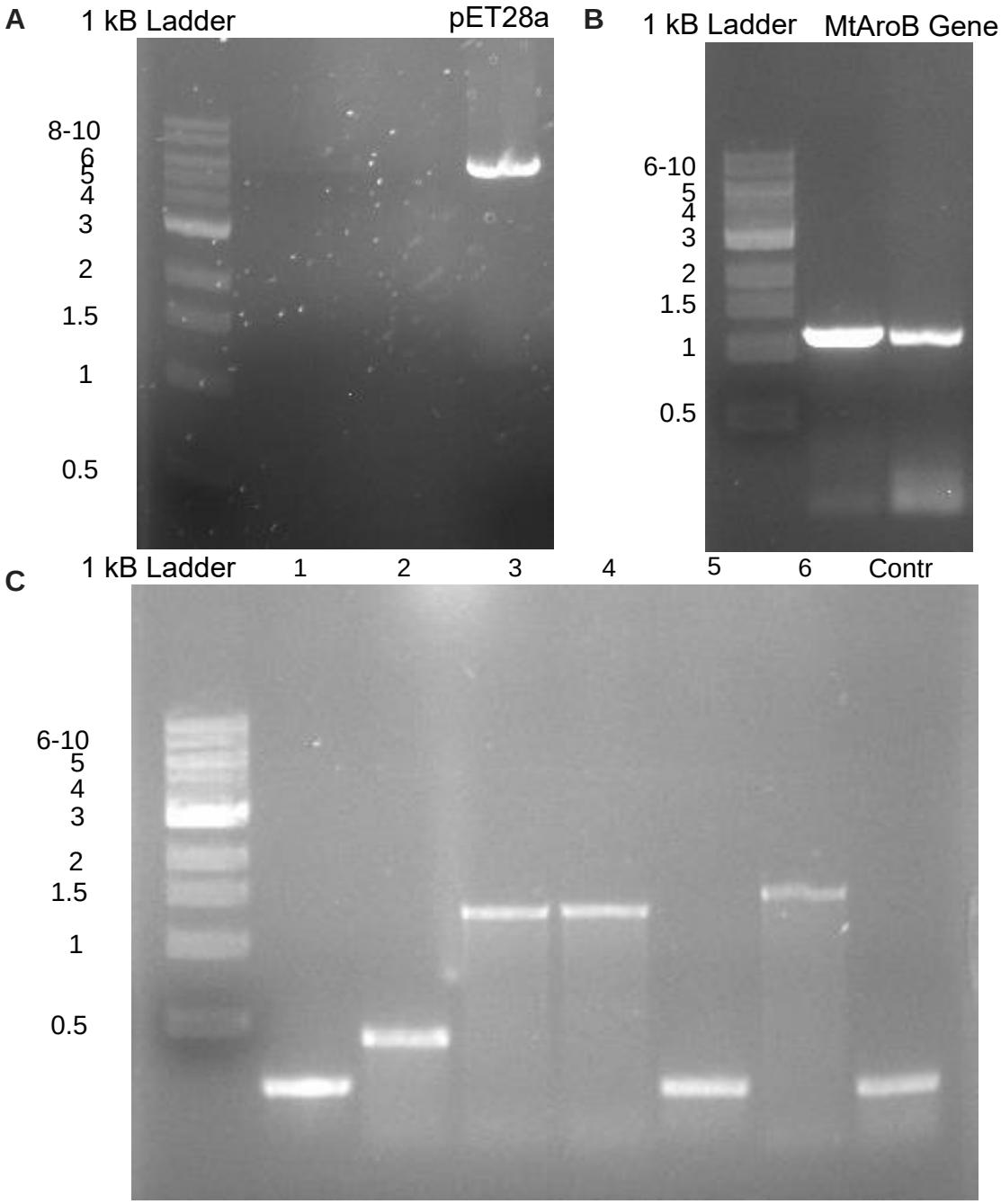
Zimenkov, D.V., Nosova, E.Yu., Kulagina, E.V., Antonova, O.V., Arslanbaeva, L.R., Isakova, A.I., Krylova, L.Yu., Peretokina, I.V., Makarova, M.V., Safonova, S.G., Borisov, S.E. and Gryadunov, D.A. (2017) Examination of bedaquiline- and linezolid-resistant *Mycobacterium tuberculosis* isolates from the Moscow region. *Journal of Antimicrobial Chemotherapy*, 72 (7): 1901–1906. doi:10.1093/jac/dkx094.

Zimmermann, S., Klinger-Strobel, M., Bohnert, J.A., Wendler, S., Rödel, J., Pletz, M.W., Löffler, B. and Tuchscherr, L. (2019) Clinically Approved Drugs Inhibit the *Staphylococcus aureus* Multidrug NorA Efflux Pump and Reduce Biofilm Formation. *Frontiers in Microbiology*, 10. doi:10.3389/fmicb.2019.02762.

Zumla, A., Nahid, P. and Cole, S.T. (2013) Advances in the development of new tuberculosis drugs and treatment regimens. *Nature Reviews Drug Discovery*, 12 (5): 388–404. doi:10.1038/nrd4001.

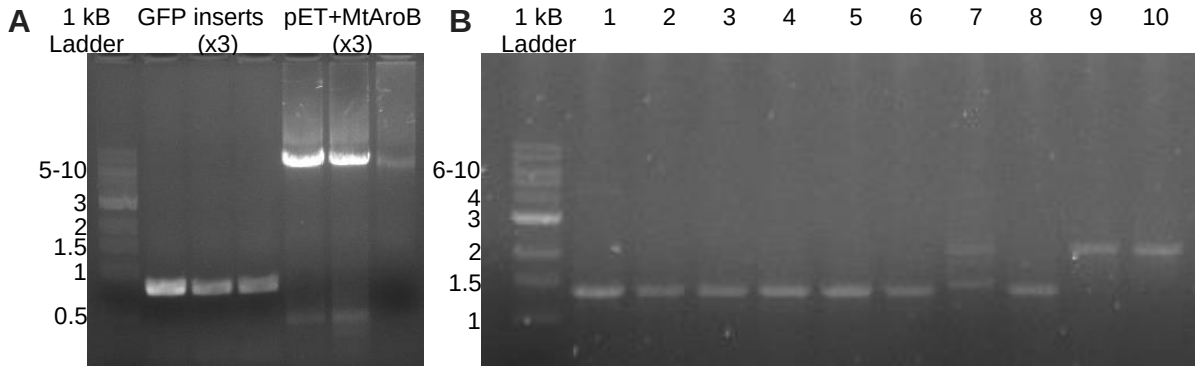
Appendix 1

Molecular cloning of plasmids

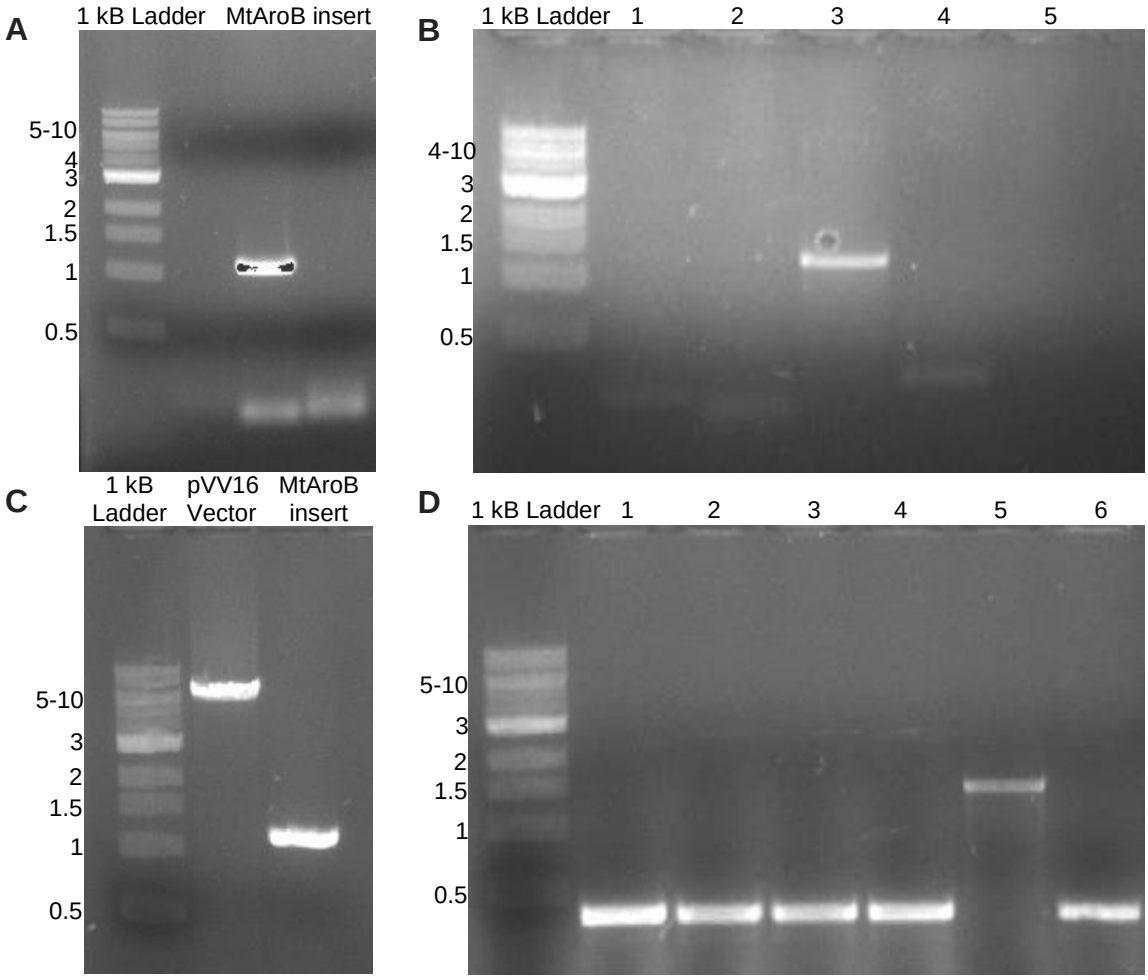


Appendix Figure 1.1: Cloning of the MtAroB gene into pET28a expression vector. (A) PCR amplification of the pET28a vector, opening it at the required insertion site. (B) PCR amplification of the MtAroB gene, including insertion of the overlapping regions for homologous recombination. (C) PCR amplification of the plasmids (amplifying expression region) generated following the HiFi cloning reaction. A 0.4 kB fragment is present in the original plasmid, if successful addition of the MtAroB gene occurs, this results in a 1.5 kB fragment. Contr = control empty pET28a vector.

The cloning of the MtAroB gene was performed three times, to add this sequence into the pET28a, pTIC6a and pVV16 expression vectors. The pET28a vector was for overexpression of the protein within *E. coli,* for downstream purification of the protein. The addition of the gene into pTIC6a and pVV16 was to allow native overexpression of the protein within mycobacteria. The former vector is for inducible overexpression, dependent on addition of ATc, while the latter is for constitutive overexpression. For all three vectors, restriction-based cloning was initially attempted for, however this was only successful for pTIC6a. The remaining plasmids were generated using HiFi cloning. Gels corresponding to the successful cloning of MtAroB into pET28a are displayed in Figure A1.1. This plasmid was further altered for down-stream assays by the addition of a GFP gene directly fused to the MtAroB gene sequence. This cloning attempt also used HiFi cloning to insert this gene, without the use of restriction sites, and the associated gels are displayed in Figure A2.1. Finally, gels corresponding to the successful cloning of the MtAroB gene into the pTIC6a and pVV16 vectors are displayed in Figure A1.3.



Appendix Figure A1.2: Cloning of the GFP gene into pET28a+MtAroB vector. (A) PCR amplification of both the GFP insert (lanes two to four) and pET28a+MtAroB vector (lanes five to seven). The former had regions required for homologous recombination added during PCR, while the latter was opened at the selected insertion site. (B) PCR amplification of the plasmids (amplifying expression region) generated from HiFi cloning, with plasmids 9 and 10 including the extra GFP coding sequence.

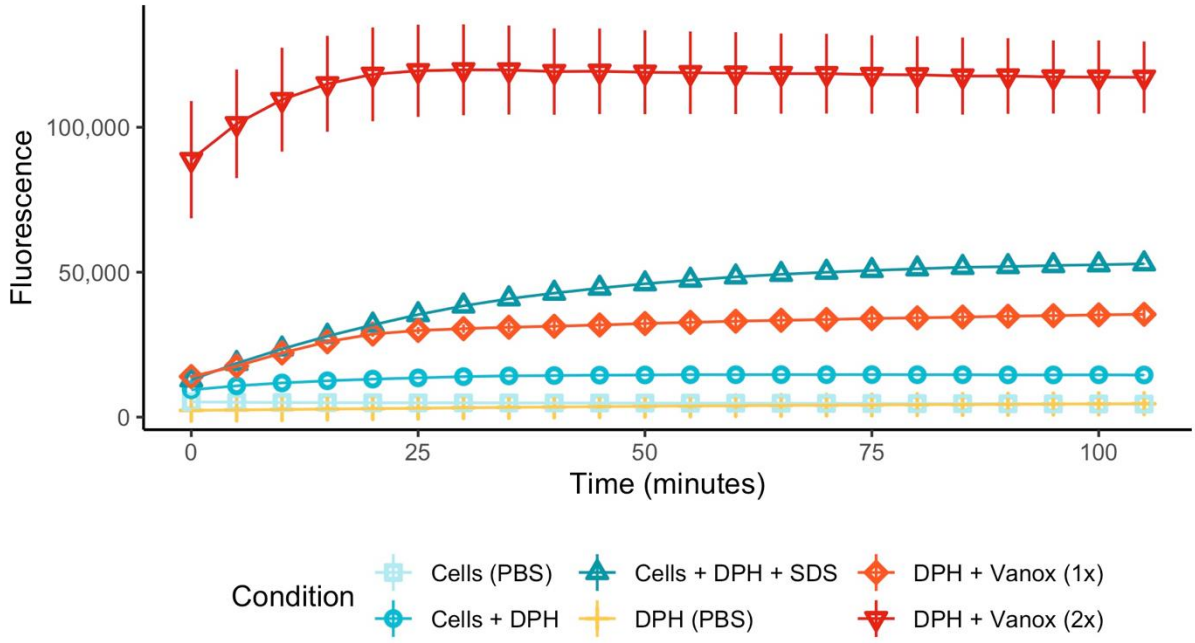


Appendix Figure A1.3: Cloning of the MtAroB gene into the pTIC6a and pVV16 overexpression vectors. (A) PCR amplification of MtAroB, adding required HindIII and NheI restriction sites. (B) PCR amplification of plasmids following ligation of MtAroB into pTIC6a (amplifying expression region), confirming plasmid 3 has the inserted MtAroB gene. (C) PCR amplification of both the pVV16 vector and MtAroB insert. The former was opened at the selected insertion site, while the latter had regions required for homologous recombination added during PCR. (D) PCR amplification of the plasmids (amplifying expression region) generated from HiFi cloning, with plasmids 5 including the extra MtAroB coding sequence.

Appendix 2

Vanoxerine's interactions with DPH

Vanoxerine was found to cause an increase in fluorescence of DPH (1,6-diphenyl-1,3,5-hexatriene), in the absence of cells (Figure A2.1). As displayed, there was a concentration dependent increase in the fluorescence of DPH when either 1x or 2x MIC_{99} of vanoxerine was incubated with the dye. The increase in fluorescence caused by 2x MIC_{99} vanoxerine was greater than found when lysing the *M. smegmatis* cells with SDS. This prevented this common dye from being used to study the impact of vanoxerine on the bacterial membrane.



Appendix Figure A2.1: Impact of vanoxerine on the fluorescence of DPH. For the assay, 96-well plates were prepared containing vanoxerine (26 or 52 µg/mL) or SDS (0.05%). DPH (0.25 µM) was diluted in PBS along or PBS containing *M. smegmatis* (OD_{600} 1.0) and was added to the 96-well plate (99 µL per well). The plates were then added to a BMG Labtech POLARstar Omega plate reader and the fluorescence (emission – 355 nm, excitation – 460 nm) was measured every 5-minutes for 2-hours. N=3. 1x MIC_{99} = 26 µg/mL.

Appendix 3

Crystallographic parameters for MtAroB structure

The parameters derived from the X-ray diffraction experiment to determine the structure of the MtAroB protein are outlined in Table A3.1.

Table A3.1. Crystallographic Parameters from MtAroB crystal structure

Protein	**Apo-MtAroB**
Beamline	Diamond i-03
Wavelength	0.979
Space group	$I4_1$
Asymmetric unit contents	1
Unit cell	a=141.89 Å, b=141.89 Å, c=38.53 Å, alpha=90.00, beta=90.00, gamma=90.00
Resolution range	70.94 - 2.27
Total reflections	17,719
Unique reflections	17719
Wilson B-factor	76.82
Reflections in refinement	17717
Reflections in free set	894
Rwork	0.241
Rfree	0.261
FSC average	0.9403
RMSD bonds (Å)	0.0169
RMSD angles (˚)	2.543
Ramachandran favoured (%)	94.1
Ramachandran allowed (%)	3.9
Ramachandran outliers (%)	2
Rotamer outliers	8.9
Clash score	5.3

Appendix 4

Docking scores for top 31 AroB hit compounds

The associated docking scores for the 31 compounds shown in Figure 2.26, are displayed in Table A4.1.

Table A4.1: Docking scores from each scoring function for the top compounds. ASP – Astex statistical potential, GS – GoldScore, CS – ChemScore, PLP – Chem PLP.

No	Compound ID	ASP	PLP	CS	GS
1	11654105	29.0	68.4	26.9	57.6
2	18077207	29.8	66.4	29.7	58.9
3	20530397	30.8	65.7	28.0	59.9
4	21487931	34.7	61.6	25.2	58.5
5	25761029	30.9	71.4	31.7	65.9
6	26694214	31.4	68.5	31.7	65.6
7	27313805	28.4	69.6	29.5	66.8
8	33782544	34.3	73.3	32.7	69.8
9	36875132	34.4	66.3	30.1	60.8
10	37560476	29.0	63.1	28.0	60.3
11	38571466	32.2	61.6	30.4	64.3
12	39181163	31.0	70.6	30.6	72.6
13	41172430	32.2	66.7	32.7	67.2
14	42501835	28.1	66.8	28.0	65.8
15	47431791	29.2	70.6	28.2	74.4
16	48979502	31.0	67.9	29.5	61.3
17	56169481	32.0	69.5	24.7	65.5
18	60757340	28.8	65.3	31.2	65.7
19	61362326	27.4	67.9	28.7	59.7
20	61451847	35.5	64.8	27.5	69.3
21	61486468	30.3	65.1	30.3	63.5
22	62706623	34.3	64.1	26.7	54.5
23	66325994	28.8	62.9	29.1	54.6
24	66993200	29.0	69.5	27.8	58.8
25	77463854	30.2	66.6	27.5	56.4
26	86160967	32.8	62.8	31.7	69.6
27	86399973	31.7	61.7	28.3	55.2
28	88440914	31.4	67.8	29.4	61.7
29	89177445	28.5	63.0	28.2	59.2
30	91125173	31.1	65.0	26.8	60.5
31	92455132	27.9	61.3	25.8	64.4

Appendix 5

List of SNPs present in laboratory *M. smegmatis* strain compared to reference

The laboratory *M. smegmatis* mc^{2}155 strain was WGS and compared to the reference *M. smegmatis* mc^{2}155 (GCA_000283295.1) and all differences in coding sequencing are displayed in Table A5.1.

Table A5.1: List of SNPs present within coding section of the *M. smegmatis* mc^{2}155 genome laboratory strains used within this work, compared to the reference *M. smegmatis* mc^{2}155 strain. NT_Pos = nucleotide position, AA_Pos = amino acid position. Alt = nucleotide in laboratory strain.

Position	Type	Ref	Alt	Strand	NT_Pos	AA_Pos	Effect	Locus_Tag	Product
575734	ins	G	GT	-	727/813	243/270	Frameshift	MSMEI_0483	hypothetical protein
676327	snp	G	A	+	366/435	122/144	Synonymous	MSMEI_0581	hypothetical protein
713730	ins	C	CT	-	1329/1398	443/465	Frameshift	MSMEI_0615	Sulfatase
736861	ins	T	TC	-	205/843	69/280	Frameshift	MSMEI_0636	hypothetical protein
860163	ins	A	AC	+	142/993	48/330	Frameshift	MSMEI_0758	Putative monooxygenase
927300	del	GC	G	-	1290/1341	430/446	Frameshift	MSMEI_0822	hypothetical protein
1449589	ins	C	CT	-	179/822	60/273	Frameshift	MSMEI_1316	hypothetical protein
1873625	ins	G	GC	+	2/441	1/146	Frameshift	MSMEI_1746	hypothetical protein
1903851	ins	G	GC	+	101/1122	34/373	Frameshift	MSMEI_1784	Mpg1 - Nucleotidyl transferase
2110478	del	TG	T	-	32/762	11/253	Frameshift	MSMEI_1984	Short-chain dehydrogenase
2118639	snp	T	G	+	946/1560	316/519	Missense	MSMEI_1992	Flavin-binding monooxygenase
2128071	del	GA	G	-	71/291	24/96	Frameshift	MSMEI_2003	EchA16 - Enoyl-CoA hydratase
2225484	del	GA	G	+	1194/1698	398/565	Frameshift	MSMEI_2097	HNH endonuclease
2225490	complex	TGGCCCA	CGCC	+	1198/1698	400/565	Missense + Indel	MSMEI_2097	HNH endonuclease
2225503	ins	A	AC	+	1216/1698	406/565	Frameshift	MSMEI_2097	HNH endonuclease

2323093	snp	C	T	-	835/1209	279/402	Missense	MSMEI_2186	Cyp187A4 - Cytochrome P450 187A4
2427114	del	GCC	G	-	212/264	71/87	Frameshift	MSMEI_2284	CrtYd - Lycopene cyclase
2450462	del	GA	G	+	920/1098	307/365	Frameshift	MSMEI_2306	PfkA - 6-phosphofructokinase
2597300	ins	A	AG	+	539/756	180/251	Frameshift	MSMEI_2450	DprA - DNA protecting protein
2788586	del	GA	G	+	128/210	43/69	Frameshift	MSMEI_2650	hypothetical protein
2818251	del	TC	T	-	995/1047	332/348	Frameshift	MSMEI_2678	conserved hypothetical protein
2820072	ins	G	GT	+	788/819	263/272	Frameshift	MSMEI_2679	Conserved hypothetical secreted protein
2825972	snp	A	G	-	753/993	251/330	Synonymous	MSMEI_2687	Conserved transmembrane protein
2827824	complex	ATC	GGCG	+	108/126	36/41	Frameshift + Missense	MSMEI_2689	hypothetical protein
3054639	ins	G	GT	-	948/1089	316/362	Frameshift	MSMEI_2912	Putative integral membrane protein
3107175	snp	G	A	+	844/1134	282/377	Missense	MSMEI_2957	AroB - 3-dehydroquinate synthase
3107182	snp	G	A	+	851/1134	284/377	Missense	MSMEI_2957	AroB - 3-dehydroquinate synthase
3107397	complex	T	GTG	+	1066/1134	356/377	Frameshift + Missense	MSMEI_2957	AroB - 3-dehydroquinate synthase
3107419	snp	T	C	+	1088/1134	363/377	Missense	MSMEI_2957	AroB - 3-dehydroquinate synthase
3110820	ins	A	ACG	-	94/633	32/210	Frameshift	MSMEI_2962	hypothetical protein
3264632	snp	C	G	-	777/2277	259/758	Synonymous	MSMEI_3103	TreY - Maltooligosyltrehalose synthase
3329854	complex	GCCCT	CC	+	1148/1425	383/474	Missense + Indel	MSMEI_3161	hypothetical protein
3420632	del	GC	G	+	319/405	107/134	Frameshift	MSMEI_3260	hypothetical protein
3420777	del	AC	A	-	74/102	25/33	Frameshift	MSMEI_3261	hypothetical protein
3487487	del	AG	A	+	274/303	92/100	Frameshift	MSMEI_3334	MerR-family transcriptional regulator
3581632	ins	G	GC	+	1015/1233	339/410	Frameshift	MSMEI_3436	Dihydrodipicolinate reductase
3813499	ins	C	CG	-	875/927	292/308	Frameshift	MSMEI_3657	hypothetical protein
4023519	del	GA	G	-	930/948	310/315	Frameshift	MSMEI_3862	3-oxoacyl-(Acyl-carrier protein) synthase
4031782	snp	T	C	+	633/873	211/290	Synonymous	MSMEI_3867	GntR family transcriptional regulator
4031824	del	CT	C	+	677/873	226/290	Frameshift	MSMEI_3867	GntR family transcriptional regulator
4054087	del	GA	G	-	825/942	275/313	Frameshift	MSMEI_3890	L-carnitine dehydratase/bile acid-inducible protein F

4134485	del	TG	T	+	779/936	260/311	Frameshift	MSMEI_3962	Aspartate aminotransferase
4160153	snp	A	G	-	1281/1416	427/471	Synonymous	MSMEI_3984	Putative monooxygenase
4299364	ins	C	CT	+	1186/1203	396/400	Frameshift	MSMEI_4115	Cytochrome P450
4563585	del	CG	C	+	57/144	19/47	Frameshift	MSMEI_4370	hypothetical protein
4563623	del	CT	C	+	95/144	32/47	Frameshift	MSMEI_4370	hypothetical protein
4717190	ins	A	AC	-	294/1569	98/522	Frameshift	MSMEI_4512	FolC - Folylpolyglutamate synthase protein
4717323	ins	A	AT	-	161/1569	54/522	Frameshift	MSMEI_4512	FolC - Folylpolyglutamate synthase protein
4717482	del	CA	C	-	2/1569	1/522	Frameshift	MSMEI_4513	Valyl-tRNA synthetase
5495482	ins	A	AC	-	1/492	1/163	Frameshift	MSMEI_5266	hypothetical protein
5500445	del	TG	T	+	1063/1209	355/402	Frameshift	MSMEI_5270	UPF0409 lipoprotein
5684083	ins	G	GT	-	1184/1629	395/542	Frameshift	MSMEI_5443	Ferredoxin-dependent glutamate synthase
5684091	del	GA	G	-	1176/1629	392/542	Frameshift	MSMEI_5443	Ferredoxin-dependent glutamate synthase
5834679	snp	G	A	+	372/1269	124/422	Synonymous	MSMEI_5601	hypothetical protein
5875661	del	GC	G	+	921/948	307/315	Frameshift	MSMEI_5650	ABC transporter ATP-binding protein
6062418	del	AG	A	-	277/1005	93/334	Frameshift	MSMEI_5833	FadE28 - Acyl-CoA dehydrogenase
6146884	ins	C	CG	-	486/786	162/261	Frameshift	MSMEI_5921	Conserved membrane protein
6146892	ins	A	AG	-	478/786	160/261	Frameshift	MSMEI_5921	Conserved membrane protein
6146897	ins	A	AG	-	473/786	158/261	Frameshift	MSMEI_5921	Conserved membrane protein
6305029	del	GC	G	-	100/1254	34/417	Frameshift	MSMEI_6077	sensory transduction histidine kinase
6468656	complex	TCGA	CTGACG	-	64/171	21/56	Frameshift + Missense	MSMEI_6229	hypothetical protein

Appendix 6

Vanoxerine's impact on other Mycobacterial lipids

As the C^{14} labelled lipid samples had been generated, both in the presence and absence of vanoxerine treatment, different solvent systems were used to separate these lipids, to gain more information on the changes induced by vanoxerine on *M. smegmatis*. All TLCs labelling was undertaken using (Stover et al., 1991; Pickford et al., 2020) as references. Initially, the same samples were loaded as Figure 3.20A, but equal sample volumes were loaded (Figure A6.1A)., rather than equal counts. This was to exclude sample enrichment through equal counts loading as a confounding factor. The loss of TMM following 1x MIC_{99} of vanoxerine remained clear. In Figure A7.1A, TDM also appeared to be enriched at 1x MIC_{99} vanoxerine, which could suggest conversion of TMM into TDM and no additional TMM was reaching the membrane. As loading equal counts did not affect the end result, this was used for the remaining TLCs.

To study the free mycolic acids extracted from the membrane, a TLC was run in hexane/diethyl-ether/acetic acid, 70:30:1 (Figure A6.1B). This has previously shown free mycolic acids about one-third up from the origin (Bansal-Mutalik and Nikaido, 2014), however, in this run, only triacylglycerol was visible. Triacylglycerol appears unaffected by vanoxerine treatment. System C (1^{st} direction – $CHCl_3$/MeOH, 96:4, v/v, 2^{nd} direction – toluene/acetone, 80:20, v/v) is a 2D-TLC system used to study free mycolic acids (Figure A6.1C). This has previously shown two spots, one corresponding to free fatty acids and one for free mycolic acid (Pickford et al., 2020). Nevertheless, the current TLC cannot be conclusively assigned, as only one main spot is present. Independent of the true lipid assignment, it was not affected by the addition of 1x MIC_{99}

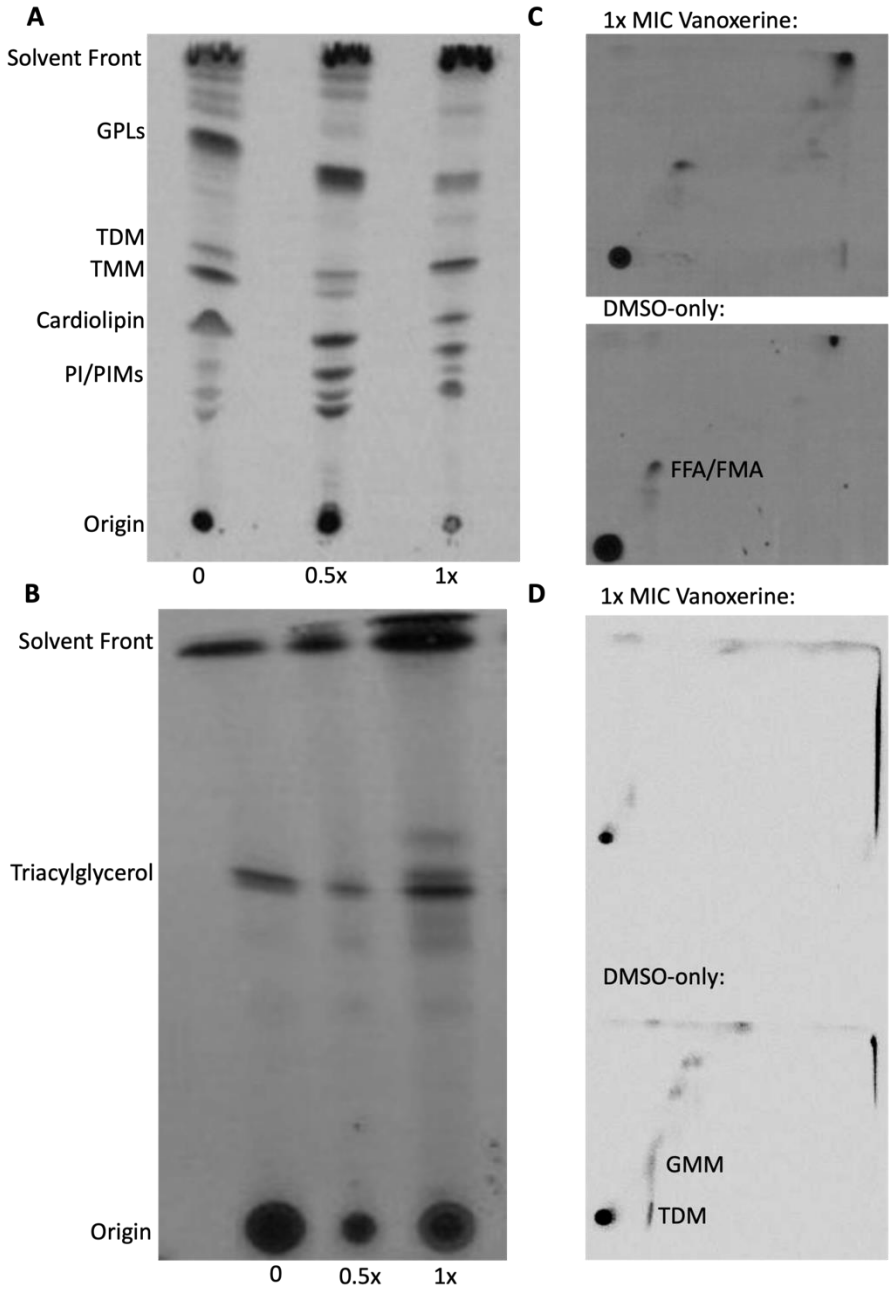


Figure A6.1: Analysis of C^{14} lipid samples using TLC, showing the loss of TMM, but limited effects on other Mycobacterial lipids. (A) Equal volume samples run in $CH_3Cl/MeOH/H_2O$, 80:20:2, v/v/v. (B) Samples run in hexane/diethyl-ether/acetic acid, 70:30:1, v/v/v. (C) System C, showing 1x MIC vanoxerine treated samples (top) and DMSO-only samples (bottom). (D) System D, showing 1x MIC treated samples (top) and DMSO-only samples (bottom). All TLCs were exposed to X-ray films, with representative images shown from N=2, MIC = 26 µg/mL vanoxerine. FFA = free fatty acids, FMA = free mycolic acids, GMM = glucose monomycolates, GPLs = glycopeptidolipids, PI = phosphatidylinositol, PIMs = phosphatidylinositol mannosides, TDM = trehalose dimycolate, TMM = trehalose mono-mycolate.

of vanoxerine. However, several spots appeared on the TLC following vanoxerine treatment, which could indicate other disruptions to lipid biosynthesis or incorporation into the membrane.

Finally, the same lipid samples were run in system D (1st direct – $CHCl_3$/acetone/MeOH/H_2O, 50:60:2.5:3, v/v/v/v, 2nd direction – $CHCl_3$/acetic acid/MeOH/H_2O, 40:25:3:6, v/v/v/v, Figure A6.1D). This suggested that TDM was lost at 1x MIC_{99} of vanoxerine, alongside more polar unknown lipids. In contrast, glucose monomycolates remained following vanoxerine treatment. Overall, this lipid analysis suggests that mycolic acids are affected by the treatment of vanoxerine, however, it is unknown if this is a direct or indirect effect of treatment.

Appendix 7

Percentage survival or growth curves following vanoxerine analogue treatment

The MIC_{99} values for each vanoxerine analogue were derived from percentage survival curves calculated following the treatment of either *M. smegmatis*, *M. bovis* BCG or *E. faecium*. These percentage survival curves are shown in Figure A7.1, with each curve being calculated based on the growth of the bacterial strains within a DMSO and rifampicin/Biocleanse control wells. The calculated MIC_{99} values are displayed in Table 3.9.

As previously described, the majority of analogues were less effective than vanoxerine, with many having no activity at the highest tested concentration (Figure A7.1). The exception to this rule was compound 486, which was more effective against both *M. bovis* BCG and *E. faecium*. In addition, EMK022 and compound 488 were equally affective against *M. bovis* BCG. The only other compounds which displayed antibacterial activity were EMK024, compound 482 and GBR12935.

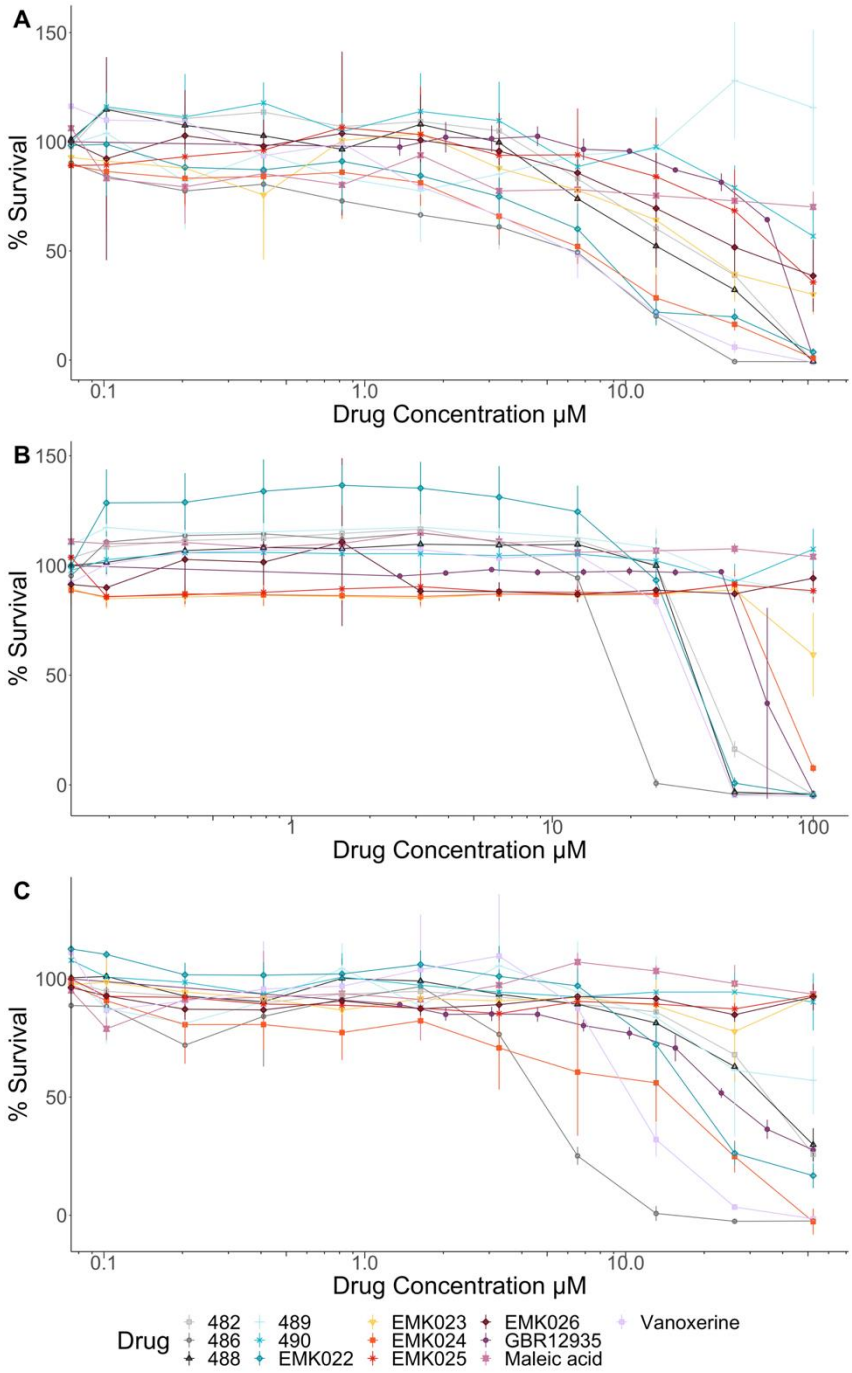


Figure A7.1. Percentage survival curves following treatment with vanoxerine analogues. (A) *M. smegmatis*. (B) *M. bovis* BCG. (C) *E. faecium* E745. Mid-log bacterial cultures were diluted to OD_{600} 0.05. A 96-well plate was prepared with 1:2 serial dilutions of the vanoxerine analogues, final DMSO concentration = 1%. The diluted cells were added to the plate and incubated for 21 (*M. smegmatis*), 24 (*E. faecium*) or 144 (*M. bovis* BCG) hours. For *E. faecium*, the OD_{600} was measured. For mycobacteria, resazurin (0.02%, 30 μL) was added and the plate re-incubated for 3 (*M. smegmatis*) or 24 (*M. bovis* BCG) hours. The fluorescence (excitation – 544 nm, emission – 590 nm) was measured. The %survival or growth was calculated relative to the DMSO and rifampicin/Biocleanse controls. N=3

Appendix 8

Comparison of lab *E. faecium* E745 WGS to reference strain

The laboratory *E. faecium* E745 strain was WGS and compared to the reference *E. faecium* E745 (GCA_000283295.1) and all differences in coding sequencing are displayed in Table A8.1.

Table A8.1: List of SNPs present within coding section of the *E. faecium* E745 genome laboratory strains used within this work, compared to the reference *E. faecium* E745 strain. NT_Pos = nucleotide position, AA_Pos = amino acid position. Alt = nucleotide in laboratory strain.

Position	Type	Ref	Alt	Strand	NT_Pos	AA_Pos	Effect	Locus Tag	Product
1031991	snp	T	G	+	340/1365	114/454	Missense	EfmE745_01043	Nox_1 - NADH oxidase
2174619	snp	G	A	-	56/1236	19/411	Missense	EfmE745_02193	FabF - 3-oxoacyl-[acyl-carrier-protein] synthase 2
2504870	del	CG	C	-	1089/1476	363/491	Frameshift	EfmE745_02528	Bmr3 - Multidrug resistance protein 3
2504878	complex	GTCTGGA	CGTTG	-	1082/1476	359/491	Frameshift + Missense	EfmE745_02528	Bmr3 - Multidrug resistance protein 3
9178	ins	T	TC	+	179/228	60/75	Frameshift	EfmE745_02806	hypothetical protein
30826	del	AC	A	-	324/363	108/120	Frameshift	EfmE745_03057	hypothetical protein
6095	ins	C	CT	+	145/759	49/252	Frameshift	EfmE745_03068	hypothetical protein
6665	del	CT	C	+	716/759	239/252	Frameshift	EfmE745_03068	hypothetical protein
8771	ins	A	ATG	+	586/603	196/200	Frameshift	EfmE745_03070	YxdL_2 - ABC transporter ATP-binding protein YxdL
9042	ins	G	GGA	+	127/147	43/48	Frameshift	EfmE745_03071	hypothetical protein
8075	ins	T	TA	+	879/897	293/298	Frameshift	EfmE745_03081	DinB_3 - DNA polymerase IV
8681	ins	T	TA	+	170/246	57/81	Frameshift	EfmE745_03083	hypothetical protein
10925	snp	C	A	+	314/327	105/108	Missense	EfmE745_03087	hypothetical protein
1470	del	CT	C	+	8/1824	3/607	Frameshift	EfmE745_03101	hypothetical protein
19988	snp	A	G	+	912/1086	304/361	Synonymous	EfmE745_03125	hypothetical protein

40962	snp	G	A	+	593/792	198/263	Missense	EfmE745_03147	TraM recognition site of TraD and TraG
41087	complex	CATC	ATCA	+	718/792	240/263	Missense	EfmE745_03147	TraM recognition site of TraD and TraG
41412	snp	T	G	+	255/2373	85/790	Synonymous	EfmE745_03148	hypothetical protein
41511	snp	T	C	+	354/2373	118/790	Synonymous	EfmE745_03148	hypothetical protein
41521	snp	A	G	+	364/2373	122/790	Missense	EfmE745_03148	hypothetical protein
49336	ins	G	GA	+	334/345	112/114	Frameshift	EfmE745_03161	hypothetical protein